

INVESTIGATION OF THE MECHANICAL CHARACTERISTICS OF MEDICAL  
DEVICE COMPONENTS, CONSTRUCTS AND DESIGN SUPPORT PACKAGES

A Dissertation

by

CHRISTINE MICHELLE BERGERSON

Submitted to the Office of Graduate and Professional Studies of  
Texas A&M University  
in partial fulfillment of the requirements for the degree of

DOCTOR OF PHILOSOPHY

Chair of Committee,  
Committee Members,

John C. Criscione  
Harry Hogan  
Brian Saunders

Head of Department,

Michael Madigan  
Anthony Guiseppi-Elie

December 2015

Major Subject: Biomedical Engineering

Copyright 2015 Christine Michelle Bergerson

## ABSTRACT

The field of biomechanics seeks to explain natural phenomena in the terms of classic engineering. Its theories are commonly applied to the motion and structure of an organism, and from that basis we can analyze and design complex medical components, multi-component constructs and even tools to make that design process or investigative effort easier. This portfolio dissertation concerns the application of biomechanics to the medical device community in six separate projects.

The first project concerns the development of a total knee replacement tibial tray bone-implant interface which will eventually be submitted for 510(k) clearance with the FDA. The second project details the proof of concept testing of a regenerative fracture fixation device on a sheep model that eventually biodegrades away, leaving no device left behind. The third project is the investigation of the effects of static and dynamic loading on the degradative properties of PLLA fibers, the information from which will be used to form a computational model simulating that degradation. The fourth project compares the gold standard LCDCP fracture fixation plate to a more versatile CRIF option gaining popularity in the veterinary community. The fifth and final project outlines the development of an electrospinning apparatus that is capable of spinning parallel fibers for investigation into cardiac stem cell therapies. All of these projects illustrate both simple and complex applications of the laws of classic mechanics to the field of medical devices and medical device support packages.

## DEDICATION

This thesis is dedicated to my husband Josh and our son Cohen. Josh, you never thought of failure as an option and your mindset was contagious. Life is so much better with you by my side, thank you for being there for me every step of the way. I can't wait to see what we get to do next. Cohen, you have made our lives so much more fulfilling. Thank you for all the snuggles, cuddles and kisses that got me through when I needed them the most. Study breaks are best when spent at the park with the quack-quacks, and Hand Hand Fingers Thumb gets better each time we read it.

Love you both.

## ACKNOWLEDGMENTS

I would like to thank my committee chair, Dr. Criscione, and my committee members, Dr. Saunders, Dr. Hogan, and Dr. Madigan, for their guidance and support throughout the course of this research. I would also like to thank Dr. Michael Moreno, who worked closely with me for the vast majority of this research. Your expertise, drive, patience and understanding have made me into the engineer I am today and I appreciate the time I had working with you.

Thanks also go to my friends and colleagues and the department faculty and staff for making my time at Texas A&M University a great experience. Finally, thanks to my mother, father, grandparents, aunts, uncles and cousins for their encouragement and support, and again to my husband for his patience and love.



## TABLE OF CONTENTS

	Page
ABSTRACT .....	ii
DEDICATION .....	iii
ACKNOWLEDGMENTS .....	iv
TABLE OF CONTENTS .....	v
LIST OF FIGURES .....	vii
LIST OF TABLES .....	xiii
CHAPTER I INTRODUCTION .....	1
CHAPTER II TOTAL KNEE REPLACEMENT TIBIAL TRAY INTERFACE .....	4
Preliminary Results .....	11
Methods .....	14
Approach .....	17
Summary .....	37
CHAPTER III REGENERATIVE FRACTURE FIXATION DEVICE .....	39
Nanocomposite Characterization .....	45
Bone Cuff Characterization .....	88
Gait Analysis .....	100
Conclusion .....	108
CHAPTER IV CONSTITUTIVE RELATIONS FOR A COMPUTATIONAL MODEL CAPABLE OF BIODEGRADATION .....	111
The Effect of Static and Dynamic Loading on Degradation of PLLA Stent Fibers ....	112
Materials and Methods .....	117
Results .....	124
Discussion and Conclusion .....	133
Conclusion .....	143
CHAPTER V CANINE FRACTURE FIXATION DEVICE COMPARISON .....	144
Materials and Methods .....	146
Results .....	158

	Page
Discussion.....	160
Conclusion.....	168
CHAPTER VI DEVELOPMENT OF AN ELECTROSPINNING SYSTEM FOR THE PRODUCTION OF PARALLEL FIBERS.....	170
Innovation .....	171
Design .....	174
CHAPTER VII CONCLUSION.....	184
REFERENCES .....	186
APPENDIX I NOMENCLATURE AND GREEK SYMBOLS .....	210
APPENDIX II BNS NANOCOMPOSITE SURFACE DEFECT ANALYSIS.....	211
APPENDIX III INDIVIDUAL FRACTURE ANALYSIS OF BNS NANOCOMPOSITES .....	236

## LIST OF FIGURES

	Page
Figure 1. Three views of the 4Web Load Transferring Implant Interface. ....	10
Figure 2. Stress distribution on the tray and on the bone. ....	14
Figure 3. A computational view of our SawBones analogs sized according to the poly insert. ....	20
Figure 4. The 50 N pre-load was applied for approximately 15 seconds before linearly increasing load to 115 N in compression, followed by the start of the cyclic testing. ....	21
Figure 5. The LVDTs interfaced with the tibial tray via a 5/8" cube, mounted 3/4" away from the edge of the tray. ....	22
Figure 6. Micromotion measured by the six LVDTs.....	23
Figure 7. The 4Web LTI tibial tray mounted in epoxy for fatigue testing. ....	25
Figure 8. Tray deflection at the beginning and end of testing. No signs of failure were evident in the data or via close visual inspection. ....	26
Figure 9. A single lap specimen has one shear joint between two pieces of material. ....	30
Figure 10. Conceptual rendering of the fixturing for the antero-posterior draw and medio-lateral shear testing. ....	35
Figure 11. Conceptual rendering of the fixturing for the rotary-laxity testing.....	37
Figure 12. Comparison of the different densities present throughout the groups.....	49
Figure 13. Comparisons of the four types of load deformation behavior exhibited by the samples during compressive testing.....	55
Figure 14. Compressive ultimate strength comparison across the different formulations ....	57
Figure 15. Compressive yield point comparison across the different formulations .....	60
Figure 16. Compressive modulus comparison across the different formulations.....	64
Figure 17. Resilience comparison across the different formulations.....	69

Figure 18. Manufacturing defects' influence on ultimate strength where blue points had bubbles only, red points had cracks only and orange points had both.....	72
Figure 19. Manufacturing defects' influence on yield point where blue points had bubbles only, red points had cracks only and orange points had both.....	73
Figure 20. Manufacturing defects' influence on compressive modulus. Blue points had bubbles only, red points had cracks only and orange points had both.....	73
Figure 21. Manufacturing defects' influence on resilience. Blue points had bubbles only, red points had cracks only and orange points had both.....	74
Figure 22. The influence of percent surface defect on the ultimate strength of the individual samples of the formulations.....	74
Figure 23. The influence of percent surface defect on the ultimate strength of the averaged formulation groups.....	75
Figure 24. The influence of percent surface defect on the yield point of the individual samples of the formulations.....	75
Figure 25. The influence of percent surface defect on the yield point of the averaged formulation groups.....	76
Figure 26. The influence of density on the yield point of the individual samples of the formulations.....	77
Figure 27. The influence of density on the ultimate strength of the averaged formulation groups.....	77
Figure 28. The influence of density on the yield point of the individual samples of the formulations.....	78
Figure 29. The influence of density on the yield point of the averaged formulation groups.....	78
Figure 30. Example graph depicting the failure mode analysis study.....	81
Figure 31. Comparison of the total number of fragments per group .....	82
Figure 32. Comparison of the total number of fragments, broken down by size. ....	83

	Page
Figure 33. Comparison of the total number of small fragments .....	83
Figure 34. Comparison of the total number of medium fragments .....	84
Figure 35. Comparison of the total number of large fragments .....	84
Figure 36. Comparison of the total number of extra-large fragments. ....	85
Figure 37. Classic four-point bend.....	89
Figure 38. Modified four-point bend. ....	90
Figure 39. Initial setup for mechanical testing. ....	91
Figure 40. Left – Load configuration for the classic four-point bend. Right – Load configuration for the modified four-point bend. ....	92
Figure 41. Locations of force application within the shell. Left – Classic four-point bend. Right – Modified four-point bend.....	93
Figure 42. Samples I and IV were subjected to unintended compressive loads due to insufficient clearance between the device and fixture throughout the range of the bending cycle. This was corrected for future tests. ....	96
Figure 43. Sample II. ....	97
Figure 44. Sample V. ....	98
Figure 45. Sample III. ....	99
Figure 46. Comparison of failed devices. Left – Device subjected to classic four-point bend in vitro. Right – Device explanted from sheep study. ....	100
Figure 47. Two AMTI force plates embedded in the walkway in a staggered configuration and covered with thin rubber mats to prevent slipping during locomotion. ....	103
Figure 48. A still frame from the marker data gathered and processed via Nexus software. The marker highlighted in blue is directly over the implanted device. ....	105
Figure 49. A still frame showing the marker data overlayed on the DV2 Bonita video capture. Again, the blue marker is directly over the implanted device.....	105

	Page
Figure 50. A comparison of the peak forces associated with the hind right limb during normal walking, normalized by body weight. There is no statistical difference between the pre-op peak force and the peak force seen 111 and 161 days after cast removal. ....	106
Figure 51. Three representative trials taken at the three time points and normalized by body weight. The waveform characteristics and duration of the stance phase indicate that the sheep is not favoring the limb. ....	107
Figure 52. A still frame of the sheep running across the walkway. The corresponding video shows this event at normal speed, 1/2 speed and 1/4 speed. ....	108
Figure 53. A still frame of the sheep beginning to run around the handler. A high speed video of this event can be seen in sheep run circle. ....	109
Figure 54. A still shot of the sheep climbing onto the wall of the pen. This behavior was common prior to the surgery and was often seen during both time points in between data capture sessions. A high speed video of this event can be seen in sheep stand3. ....	110
Figure 55. Illustration of the device used to apply a dynamic axial load to fibers. The load fluctuated between 0.125N and 0.25N at a frequency of 1 Hz while the fibers were submerged in PBS maintained at 45°C. ....	120
Figure 56. Average stress versus strain curves for the elastic regions of fibers exposed to (a) dynamic load, (b) no load, (c) small static load and (d) large static load at 0,6,9,12 and 15 months. ....	125
Figure 57. Illustration of the effect of varying $\beta$ while keeping $\mu$ and $m$ constant. An increase in $\beta$ indicates a softer material at higher strains. ....	127
Figure 58. $\beta$ , a Knowles model constant, increases with degradation time. * $p < 0.05$ compared to the no load group at 15 months. # $p < 0.05$ compared to the same loading group at 9 and 12 months. ....	128
Figure 59. The degradation model is fitted to the values of $\beta$ to obtain values for the degradation constants $K(F)$ . ....	130
Figure 60. The percent crystallinity ( $X_c$ ) changes with equivalent degradation time. ....	135

	Page
Figure 61. As the fiber degrades and percent crystallinity increases, the rigidity of the fiber also decreases. There is an approximate linear relationship between $X_c$ and $\beta$ .....	137
Figure 62. The model parameter $K_\beta$ for each static loading group was fitted to a linear model. The values for the dynamic load are also shown (red square) but not included when determining the linear relationship between $K_\beta$ and degradation stress. ....	138
Figure 63. Representative photograph of paired canine femora implanted with either CRIF/rod (A) or LC-DCP/rod (B) fixation before potting for mechanical testing. ....	150
Figure 64. Four-point bending fixture. ....	153
Figure 65. Geometry of the 4-point bending testing device.....	154
Figure 66. Torsion testing fixture. Specimens were potted in PVC housings using a jig designed to center the long axis of the IM pin within the torsional axis. ....	156
Figure 67. Representative photograph of a CRIF/Rod specimen upon completion of torsional testing. ....	157
Figure 68. Four-point bend load deformation curve.....	162
Figure 69. Torque deformation curve.....	165
Figure 70. Generation 1 of the electrospinning set-up. Very generally, this setup contains a high voltage power supply on the left, a syringe pump in the middle and a collector plate on the right.....	176
Figure 71. Generation 2 of the electrospinning set-up as seen from two views: directly in front (top) and from behind the collector (bottom). ....	178
Figure 72. 12% PCL/DMF/DCM solution spun at 24 kV with a feed rate of 4.0 mL produces continuous fibers with significant beading.....	179
Figure 73. 16% PCL/DCM/DMF solution spun at 7.2 kV with a feed rate of 4.0 mL produces the ideal fiber geometry. ....	180

	Page
Figure 74. Solidworks model of the electrospinning wheel, for use in the creation of aligned fibers. ....	181
Figure 75. The completed spinning wheel system. ....	182
Figure 76. Generation 3 of the electrospinning setup, capable of creating aligned fibers. .	183
Figure 77. An example of fiber alignment possible with the Generation 3 setup. ....	183



## LIST OF TABLES

	Page
Table 1. Group Labels .....	46
Table 2. Visual Examination for Defects .....	47
Table 3. Maximum Percent Variation Within the Groups as Compared to the Mean .....	50
Table 4. Individual Sample Densities .....	50
Table 5. Density Mean and Standard Deviation .....	52
Table 6. Table Categorizing Each Sample by its Representative Curve Type .....	56
Table 7. Individual Sample Ultimate Strength.....	58
Table 8. Ultimate Strength Mean and Standard Deviations .....	59
Table 9. Individual Sample Yield Points.....	61
Table 10. Yield Point Mean and Standard Deviation .....	62
Table 11. Individual Compressive Modulus Data .....	65
Table 12. Compressive Modulus Mean and Standard Deviation .....	67
Table 13. Individual Sample Resilience Data .....	70
Table 14. Resilience Mean and Standard Deviation.....	71
Table 15. Fragment Study Mean and Standard Deviation .....	86
Table 16. Small Fragment Mean and Standard Deviation .....	86
Table 17. Medium Fragment Mean and Standard Deviation.....	87
Table 18. Large Fragment Mean and Standard Deviation .....	87
Table 19. Extra-Large Fragment Mean and Standard Deviation.....	88
Table 20. Shell Thickness, Which Varied by Over 2mm in Some Cases.....	94
Table 21. Loads Applied to the Shell at Failure.....	95

	Page
Table 22. Average Values for the Knowles Model Material Constants for all Static (n=2) and Dynamic (n=3) Loading Groups.....	126
Table 23. $K(F)_\beta$ Values for the Degradation Models of $\beta$ .....	129
Table 24. Average Values for the Yield Stress, Yield Strain, Fail Stress and Fail Strain for all static (n=2) and Dynamic (n=3) Loading Groups.....	134
Table 25. Average Values for Crystallinity and Peak Melting Temperature for all Static (n=2) and Dynamic (n=3) Loading Groups .....	136
Table 26. Mean $\pm$ SD Values for 4-Point Bending.....	160
Table 27. Mean $\pm$ SD Values for Torsional Testing.....	164

## CHAPTER I

### INTRODUCTION

Biomechanics is a field dedicated to understanding the mechanical principles of living organisms, with much of the emphasis on those organism's movement and structure. Many complex natural phenomena can be explained or approximated by careful application of classic engineering theories. Socrates emphasized knowing ourselves before attempting to know the world around us (Martin 1999). Plato began forming the elegant mathematics that would allow such investigations. Aristotle gave the field deductive reasoning in addition to Plato's mathematical reasoning and could be argued to have been the first biomechanician with his novel *De Motu Animalium* discussing the movement of animals. Da Vinci applied his classic engineering principles to muscles and Galileo gave us the scientific method as he reasoned out the structure of bones. Motion analysis was introduced in the 19<sup>th</sup> century and the 20<sup>th</sup> century saw the formation of Wolff's Law of bone regeneration.

After the 20<sup>th</sup> century the field began to specialize. Just as biomechanics is a subfield of biomedical engineering; orthopedics, cardiac mechanics, vascular mechanics and kinematics are all subfields of biomechanics. This dissertation aims to use the principles of biomechanics to investigate problems in these subfields, to use the principles of classic engineering to develop medical devices, create computational models and provide a basic experimental system on which complex problems can be solved.

This dissertation concerns the mechanical investigation and characterization of novel medical devices and support packages to medical device development when the technology is still in the proof-of-concept stage, as well as the development of benchtop systems to assist in the study of biomechanically based topics. It is a study of biomechanics in a general sense, with many different types of projects coming together beneath that expansive topic.

The second chapter involves the design, verification and validation of a novel bone-implant interface for a total knee replacement tibial tray. This exploratory study goes through proof of concept validation work to designing the experiments necessary for submission of a 510(k) to the FDA. The third chapter concerns a novel fracture fixation device that regenerates the bone before biodegrading away. First the biomechanical environment the device is experiencing is investigated, then studies are run to find the best nanocomposite material to create the device from and a sheep study shows this proof of concept work solves the problem it was intended to solve. The fourth chapter details the generation of a computational model for the biodegradation of materials *in vivo*. Constitutive relations for biodegradable polymers vary as time progresses and in the presence of mechanical loads, and this accurate computational model conveying the mechanical integrity of different medical devices exposed to physiologic conditions will allow engineers to design structures such as stents appropriately. The fifth chapter is an investigation of fracture fixation technology for the veterinary field. The gold standard fixation plate is compared to a more versatile and cost-effective option with increasing popularity in the surgical suite. The sixth

chapter details the iterative development of an electrospinning system for the lab. Stem cell treatments have not appreciated the success they were anticipated to have, and this system will allow verifiable answers to poignant questions as to why not.

## CHAPTER II

### TOTAL KNEE REPLACEMENT TIBIAL TRAY INTERFACE

Knee arthritis is a debilitating condition that currently leads to over 700,000 knee replacements per year (MN Community Measurement 2010). Osteoarthritis causes extensive damage to the articulating surfaces of the knee. The knee replacement procedure is expensive and currently represents approximately 8% of all Medicare spending. Total hospital charges for these procedures reached \$4.5 billion in 2013. Revision rates for current TKR procedures are significant – 10% at 10 years and 20% at 20 years (MN Community Measurement 2010, Fitzgerald 2011). Significant revision rates add more costs to the healthcare system while leaving patients dissatisfied. This revision rate is driven by the deficiencies of legacy manufacturing technologies, including machining and cast molding, which limit the ability to produce sophisticated knee implant designs. As a result, predicate devices have relatively basic designs such as single intramedullary stems. Furthermore, promising concepts such as cementless interfaces that have potential for improved outcomes and reduced hospital costs are currently limited by the boundaries of conventional implant development as well. These current designs, while acceptable, leave significant room for improved clinical benefits and market differentiation.

This research is focused on the development of an innovative knee replacement component that employs state-of-the-art manufacturing processes and structural engineering design principles to improve the bone/implant interface in total knee replacement (TKR) systems. Revision procedures are often more complicated than the initial TKR; for example,

autologous bone grafts may be required to compensate for damage to the bone and bone loss caused by the TKR components. Current devices typically include “keeled” or “pegged” tibial trays, which may contribute to uplift, loosening, and related complications requiring revision. 4Web’s innovative design incorporates unique geometric and mechanical properties that have been optimized to address the problems associated with initial and long-term fixation. Specifically, the device is a novel bone-implant interface that incorporates a unique truss-like configuration, based on structural engineering principles, that is designed to improve initial fixation and facilitate bone through-growth, and thereby improve long-term fixation and load transfer/distribution. It is expected that the improvements in fixation and overall TKR performance will significantly improve patient quality of life, as well as reduce and potentially eliminate the need for revision procedures.

The knee joint experiences dynamic forces from all directions. These dynamic forces represent a simultaneous ‘rolling and gliding’ effect. If only a rolling motion were present, the knee would disarticulate during flexion, same with only gliding. Axial rotation of the tibia seats the tibial plateau into the femoral condyles during extension and is referred to as the ‘screw-home mechanism’. The combination of motions maintains the integrity of the knee joint. If initial fixation into the tibia is not stable, the implant can experience liftoff as the knee moves from flexion to extension. Liftoff happens when force is applied to one portion of the implant causing other portions of the implant to pull away from the adjacent bone, or see-saw. In this situation, the implant typically experiences micromotion exceeding 50  $\mu\text{m}$  (Bhimji 2012) which prevents the bone from being able to integrate into

the implant properly. This causes soft connective tissue to form in the device space, instead of the desired bone, which does not possess the structural integrity to support long-term fixation. Ultimately, this leads to loosening of the implant and possible revision.

The current design of TKR devices does not encourage osseointegration to the degree necessary for life-long fixation. TKR devices were historically fixed in place with the use of bone cement. The cement initially provides solid fixation but loosens over time due to a reduction in the amount of trabecular interlock. During implantation, the doughy bone cement flows around the trabecula and forms a mold as it polymerizes. Through years of use and because of imperfect designs, the interdigitated trabecula resorb, leaving cavities where they originally existed and decreasing the area of contact between the bone and the cement. After ten years of use, the amount of interlock loss was found to be roughly 75% with contact between the bone and the cement occurring at only 6.2% of the original interface surface area with a stemmed design (Goodheart 2014). Though cemented fixation remains the gold standard, porous coatings have been explored as the potential solution to non-biologic fixation for years. They can be successful in implants that receive continual compressive forces that constantly squeeze the bone and implant together. Examples of these devices are femoral TKR components and femoral stems for hip implants. Limited success has been seen with the tibial TKR component. This is mainly due to the dynamic forces that are applied to the device during the healing process. Without some sort of complimentary support, the bone does not have time to grow into the micro pores in the porous coating and establish a firm fixation. While cemented tibial components benefit



from a strong initial fixation, cementless porous-coated tibial components have a weaker hold directly following implantation. Both cemented and porous-coated components migrate following implantation, but the porous-coated components stabilize roughly 24 months into recovery while cemented components continue to migrate (Carlsson 2005). For this reason, early failures are seen with porous-coated tibial components while later failures are seen with cemented tibial components. Cementless tibial components relying on biologic fixation would benefit from solid initial implantation which would allow osseointegration and long term stability. The 4Web device establishes a firm initial fixation at depth in the bone which allows for the bone to grow throughout the web structure, eventually becoming fully incorporated in the implant.

Current post designs do not allow for uniform distribution of load induced stress to the adjacent bone surface (Scott 2012). Wolff's Law states that bone in a healthy person or animal will adapt to the loading conditions, i.e. the mechanical environment. If loading on a particular bone increases, the bone will remodel itself over time to become stronger, thereby more capable of supporting that loading condition. The converse is true as well; if the loading on the bone decreases, the bone will become weaker due to turnover. Thus, bone remodeling is based upon the exposure to stress in load bearing, organized bone.

Micromotion immediately following implantation, i.e. when no ingrowth has occurred, has been reduced by the use of stems to anchor the tibial implant into the tibia (Rawlinson 2005). Stress transfer through the stem is a function of both stem length and stiffness of the

material (Murase 1982). If the stem is too short or in the case of a pegged design, a large amount of stress is transferred to the trabecular bone supporting the implant after the cortical bone resection. The ideal stem length will engage the cortical bone as the metaphyseal flare narrows into the diaphysis, which will transmit the load from the stem to the cortical bone (Reilly 1982). As such, the current gold standard for interfacing the tibial component with the native tibia is a central stem ranging in length from 35 to 50 mm (National Joint Registry 2010). However, finite element analysis shows that these stems absorb much of the stress at the bone/implant contact surface (Completo 2008). This stress shielding effect causes artificial bone density reduction over time due to the implant. This results in lower pull out strength and ultimately loosening of the implant. The stiffness of the material is inversely proportional to the amount of stress transferred through the stem, meaning the stiffer the material, the larger the amount of stress shielding that occurs. For example, greater stress shielding is seen with a titanium stem as compared to an entirely polyethylene stem (Callister 2010). Tapering the stem also has an effect on the amount of stress shielding seen with a design, as well as decreasing the amount of shear stress seen at the bone-stem interface (Au 2005).

The geometry under investigation provides small struts that can be pressed into bone without the need for time consuming bone preparation and removal of excess host bone which naturally provides better stability than foreign body implants. These struts may also provide initial fixation that would prevent migration and micromotion of the implant immediately following implantation, thereby allowing for quicker healing and a more stable construct.

The webbed structures connecting the struts form large pores, which allow for significant osseointegration. The improved biomechanical cooperation between the implant and bone may protect against liftoff and the adverse development of soft connective tissue between the implant and bone. The struts are configured to enable favorable load distribution and transfer from the implant to the bone, which may cause the remodeled bone to be stronger, thereby increasing bone density at the bone implant interface over time. Finally, the web structure provides for equal distribution of force across the entire bone/implant contact area, thus avoiding a microenvironment conducive to bone resorption or atrophy which may lead to implant loosening.

The 4Web LTI interface has been designed to optimize the mechanical environment the bone sees after implantation. The network of struts features a central peak long enough to engage the cortical bone at the neck of the metaphysis for load transfer, which also anchors the tibial component to minimize micromotion. Stems made from polyethylene are too compliant and experience premature backside wear. Titanium alloy or cobalt chromium stems shield the cancellous bone, eventually leading to bone density reduction, aseptic loosening and revision surgery. The webbed frames are constructed from a series of struts which are less stiff than the solid titanium alloy or cobalt chromium stems typically seen in tibial tray designs. Additive manufacturing techniques allow the 4Web trusses to provide the durability of a metal while allowing the creation of thin, complex truss structures. The tapered shape of the trusses decrease the amount of shear stress seen at the bone-strut interface, as well as further reduce the amount of stress shielding. 4Web's LTI Tibial Tray

Interface was designed to promote equal stress distribution across the entire bone contact area in order to promote the growth of strong, mechanically appropriate bone and can be seen in Figure 1. It should be noted that while the structure of the interface is referred to as a truss, it is only truss-like in its geometry. Despite the triangular design, this is not a structure comprised of two force members joined by revolute joints with one degree of freedom; the members are capable of transferring moments.

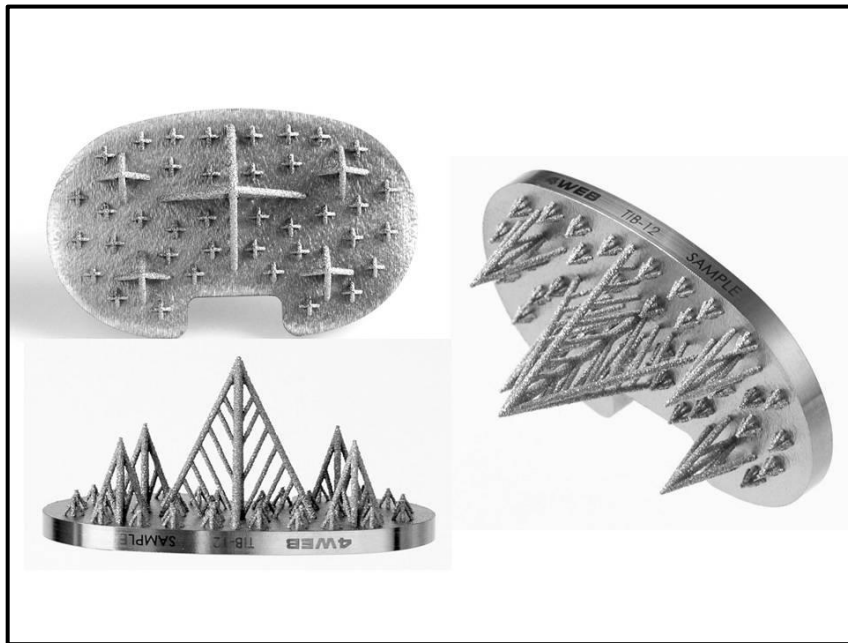


*Figure 1.* Three views of the 4Web Load Transferring Implant Interface.

A network of varying sized trusses work to reduce stress shielding, stabilize the implant and encourage osseointegration.

This research incorporated structural and civil engineering principles to design TKR devices. The inspiration for this interface came from the principles of creating foundations for buildings in sandy soil, how long keels extending into the ground have been replaced with the more favorable multi-fixation type designs. In order to produce the more elegant designs necessary for progress in this field, the use of additive manufacturing techniques in combination with legacy machining practices is being investigated. The truss fixtures were manufactured using an Electron Beam Melting additive manufacturing machine which prints them on to solid blocks of titanium. After the titanium bases were milled, the raw implants were subjected to hot isotonic pressing in order to remove any surface holes and increase the fatigue life of the parts. The implants were then ground down and polished to their final form. Additive manufacturing has made it possible to design, develop and manufacture TKR implants with a bone interface that is optimized to improve the structural stability of the implant and provide an environment for continued device-induced therapy to the bone/implant interface over time.

### **Preliminary Results**

Animal studies have demonstrated that the geometries implemented in the 4Web device allow for a large degree of bone integration and through-growth. Finite element analysis found that the 4Web LTI Tibial Tray produced a more uniform stress distribution on the underlying bone than current devices, and also had improved construct stiffness as a result of the advanced structural design. Observations made by a surgeon who implanted the device

in a cadaveric specimen confirmed that the 4Web design has multiple advantages over comparable devices, including removal of less native bone and an improved initial stability.

The design was verified using finite element analysis. The system then underwent complete FEA and empirical testing to demonstrate the input requirements, including acceptable fit to the anatomy, proper kinematics to simulate the normal knee, appropriate radius-radius surface articulation and feasibility of performance requirements, were satisfied. The system was modeled with the tibial tray implanted in the tibia with the poly insert locked in place. A FE model of tibial bone was constructed using CT images of a cadaver leg. The images were converted into CAD model and were then taken into FEA package for computational modeling. The bone model incorporated both the cortical shell and cancellous core and heterogeneous material properties were assigned based on the anatomical location at each transverse layer within the tibia (Beillas 2004, Donahue 2002). The simulation was run using a 3000N axial compressive load, a 1500N anterior to posterior shear force and 50 Nm of medial to lateral abductive moment. The loading conditions imposed during FE analysis represented the worst case scenarios for climbing stairs and landing from a jump (Kiapour 2014 A, B, C). The shank of the tibia was constrained in all degrees of freedom in all loading scenarios.

Three different implant configurations were tested. Design A featured 36 short pyramids each made of 4 trusses, four medium height pyramids each made of one central pole and four surrounding slants, and one tall central pyramid comprised of a central pole and 4 slants

each interconnected to the tray using trusses. Design C was similar to Design A but with wider medium and large size pyramids. Design B is similar to Design C but has a perpendicular orientation of the interconnecting trusses. These designs can be found in Figure 2, as can the stresses the implants imparted onto the tibia. The FEA predicted the implant stresses under these physiological loads were well below the known endurance limits for Ti-6Al-4V titanium alloy and showed that Design C was the most efficient at diffusing the stresses within the bone.

As evidenced by good performance in these preliminary studies, the technology has great potential as an effective therapeutic option for TKR. The proof of concept *in vitro* testing was therefore designed to quantitatively assess and characterize the fixation capabilities of the technology since that is the source of the majority of complications seen after knee arthroplasties using current fixation methods. Furthermore, in order to move forward on a path toward commercialization of this technology, an experimental design for FDA mandated mechanical testing was created to meet 510(k) submission requirements.

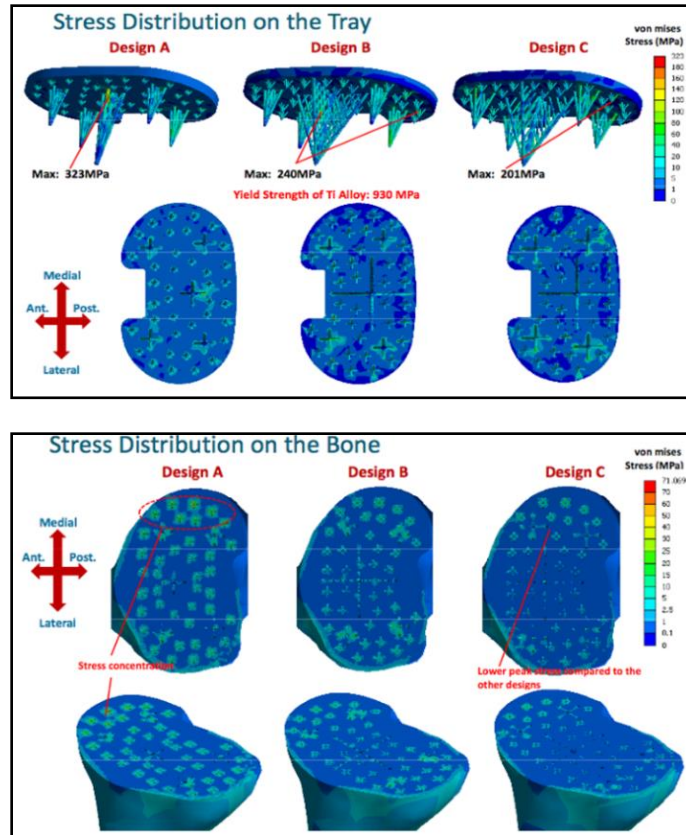


Figure 2. Stress distribution on the tray and on the bone.

(Top) The FEA results of a 3000N axial compressive load on the implant. The three designs with varying sized trusses were tested and all had peak stresses far below the yield strength of Ti-6Al-4V titanium alloy. (Bottom) The stress distribution on the bone after a simulated 50 Nm abductive bending moment was applied. Design C displayed the lowest peak stresses of the three designs.

## Methods

Long-term outcome data confirms that the Total Knee Replacement (TKR) procedure is successful and provides significant quality of life improvement. This device utilizes



structural engineering principles such as load transfer and truss design to improve osseointegration of a TKR implant; such a device is likely to be more efficacious than current designs and yield better patient outcomes. 4Web has employed additive layer manufacturing technology to produce a TKR implant with an innovative approach to the bone-implant interface of the tibial component. The web structure should provide improved initial fixation, reduced micromotion, and eliminate aseptic loosening. The research plan vetted and characterized the novel bone-implant interface in terms of fixation and fatigue as the incorporation of this technological advancement into a complete total knee replacement system, with the eventual goal of submitting this device for FDA approval.

### **Proof of Concept Testing**

I investigated and characterized the fixation and fatigue capabilities of the 4Web tibial tray using in vitro testing methods. Problems of fixation are the source of the majority of complications seen after TKR using current methods. Currently, there are no standard methods (ISO, ASTM) for investigating the fixation of a tibial tray, however, this is of great concern to the industry and researchers have published several different methods for exploring fixation in vitro. This technology is a good candidate for 510(k) approval assuming FDA guidelines are met. Thus, in accordance with the FDA Class II Special Controls Guidance Document: Knee Joint Patellofemoral and Femoral Tibial Metal/Polymer Porous-Coated Uncemented Prostheses, we conducted cyclic fatigue testing on the tibial tray as specified in ASTM F1800-07 and ISO 14879.

**Design of porous coating characterization testing.** *I designed a battery of tests to evaluate the characteristics of the porous coating covering the interface system of the tibial tray with respect to mechanical performance in accordance with ASTM F1044 and ASTM F1160. These mechanical tests are required for 510(k) approval, as per the FDA's Document: Class II Special Controls Guidance Document: Knee Joint Patellofemoral and Femoral Tibial Metal/Polymer Porous Coated Uncemented Prostheses. This novel interface was created using computer aided fused titanium alloy rapid prototyping, then finished with a titanium plasma spray. This manufacturing process created a porous surface for osteointegration of the surrounding bone. In order to quantify the surface characteristics, shear strength investigations and fixturings were designed, with implementation to be performed by another student.*

**Design of range of motion testing.** *I designed a Geometric Assessment battery of tests including Range of Motion (ROM) and Constraint Testing in Accordance with ASTM F1223-08. These mechanical tests are required for 510(k) approval, as per the FDA's Document: Class II Special Controls Guidance Document: Knee Joint Patellofemoral and Femoral Tibial Metal/Polymer Porous Coated Uncemented Prostheses. This research was designed to develop a database of the complete total knee replacement system's functional capabilities with the aim of identifying the range of motion and constraint characteristics of the system. Motion data on internal/external rotation and medial/lateral as well as anterior/posterior translation were the focus of this investigation.*

The proof of concept research performed and the additional protocols and fixturings designed will contribute towards advancing the technology of total knee replacement systems. This novel approach towards the bone-implant interface has the potential to significantly reduce the number of revision procedures of knee arthroplasties by creating a stable tibial component without the use of bone cement.

### **Approach**

This section details the theories and protocols employed during the proof of concept testing, as well as the design process for the porous coating and range of motion battery of tests.

### **Proof of Concept Approach**

This special aim investigates and characterizes the fixation and fatigue capabilities of the 4Web tibial tray using in vitro testing methods.

The objective of this proof of concept investigation was to develop and evaluate the operating parameters and durability of the device through mechanical testing designed to satisfy the recommendations outlined in the FDA's Guidance Document for TKR implants. This work is necessary prior to any in-vitro safety and efficacy testing. This research was intended to evaluate whether this design could represent a significant advancement in knee replacement technology due to the enhanced stability and resistance to failure, which would reduce the need for costly and damaging revision surgeries.

**Fixation.** Currently, there are no standard methods (ISO, ASTM) for investigating the fixation of a tibial tray, however, this is of great concern to the industry and researchers have published several different methods for exploring fixation in-vitro. In performing our fixation tests, we based our methods on recent studies, specifically the protocol employed by Bhimji, et al. 2012, and compared our results with their findings for currently used devices.

The fixation of the tibial tray immediately following implantation is crucial to determining the stability of the implant and the amount of osseointegration that can be expected to occur. The micromotion was analyzed by measuring movements seen at different locations around the tibial tray when physiologically relevant loading conditions were applied. This motion was quantified as the measurement of the in-plane movement at the tray edge relative to the adjacent supporting bone using six linear variable differential transformers mounted to the test sample. The trays were subjected to sinusoidal compressive loading from 115 to 1150N at 2 Hz for 100 cycles. This can be seen graphically in Figure 3.

The testing profile consisted of a sinusoidal compressive load applied to the posterior third of the condyle, first the lateral condyle, then the medial. The polymer insert was initially subjected to a 50 N pre-load to verify placement on the tibial tray baseplate prior to proceeding with the testing protocol. An orthopedic surgeon specializing in arthroplasty implanted the tibial trays in SawBones (Pacific Research Laboratories, Washington) tibial analogs, which were used instead of human tibias in order to reduce cost and variability seen among cadaveric specimens. These bone analogs are commonly used in the literature and

have been validated as models of human long bone in torsion, under axial loading and under antero-posterior/medio-lateral bending load (Cristofolini 2000, Heiner 2001). The SawBones analogs were custom designed to match the size of the tibial trays, which were manufactured to mate with the largest poly insert and femoral component set commercially available. The largest sizes were chosen to represent the worst-case scenario mechanically by maximizing the moment arm between the fixed end of the implant and the line of action of the force. The SawBones analogs are models of an 8 mm resection of the tibial head, the standard resection taken during an implantation procedure. A computational view of our SawBones analogs sized according to the poly insert can be seen in Figure 4, compared with an example of the ideal fit taken from Bhimji 2012. Micromotion was reported as peak-to-peak motion (ie, recoverable motion) from each LVDT, calculated every 10 cycles for each sample and then averaged over the 100 cycles of the test. The data was then averaged across samples for each loading condition (lateral vs medial). Eight samples were tested via the fixation protocol with the micromotion analyzed for all of the directions of interest.

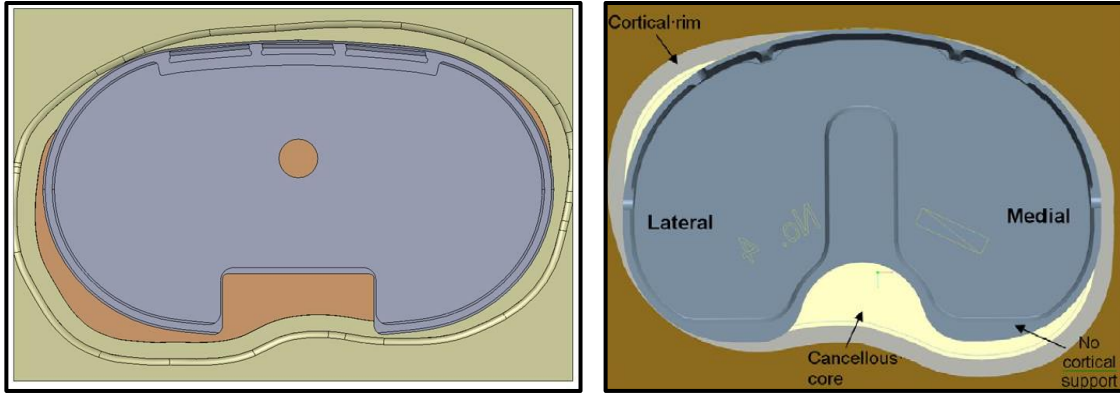


*Figure 3.* A computational view of our SawBones analogs sized according to the poly insert.

(Left) Our custom SawBones tibial analog sized to the largest poly insert commercially available with the medial condyle on the left. (Right) A graphic illustrating ‘ideal fit’ supplied by Bhimji et al. 2012. When fitting a tibial tray, the orthopedic surgeon looks for cortical rim support along the anterior rim of the tray and extended around the medial condyle.

**Results of completed testing.** Eight samples were tested in the described manner. From Bhimji, et al. 2012, the approximate lateral liftoff value for the keeled device tested according to the same loading protocol was 150  $\mu\text{m}$  and 125  $\mu\text{m}$  for the pegged device. Under the same loading conditions, the 4Web LTI device had an average measured motion of 54  $\mu\text{m}$ . From the same source, the approximate medial liftoff value for the keeled device was 240  $\mu\text{m}$  and 60  $\mu\text{m}$  for the pegged device. The 4Web LTI device had an average measured motion of 53  $\mu\text{m}$ . The experimental setup can be found in Figure 5 and a graphical representation of the results from each point of measurement as well as a quantitative comparison of the 4Web LTI device and the fixation values for pegged and keeled devices can be seen in Figure 6.

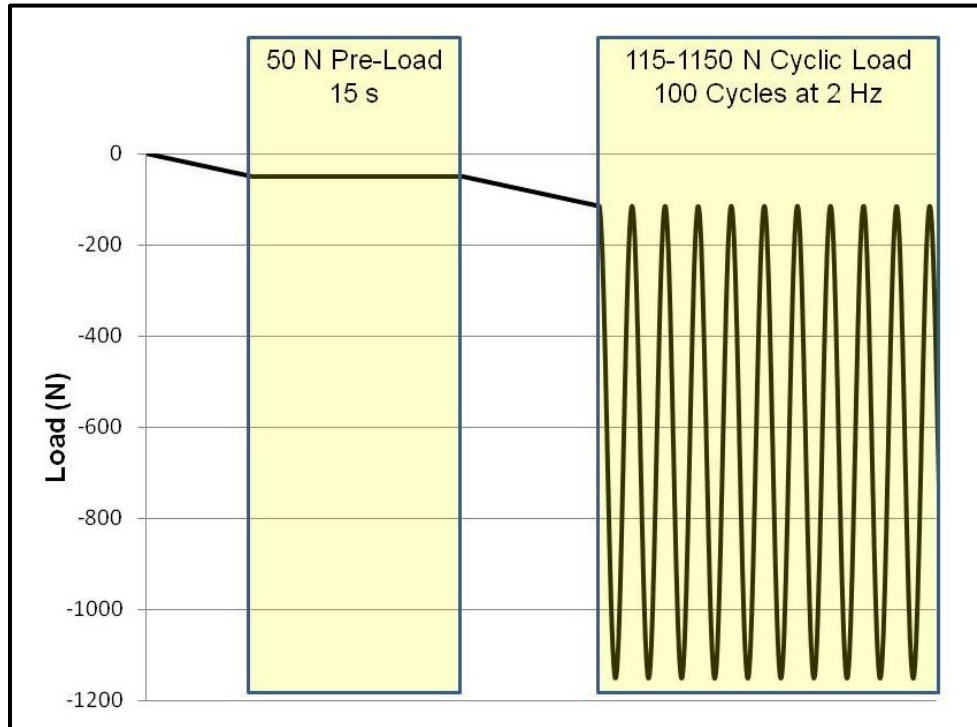


*Figure 4.* The 50 N pre-load was applied for approximately 15 seconds before linearly increasing load to 115 N in compression, followed by the start of the cyclic testing.

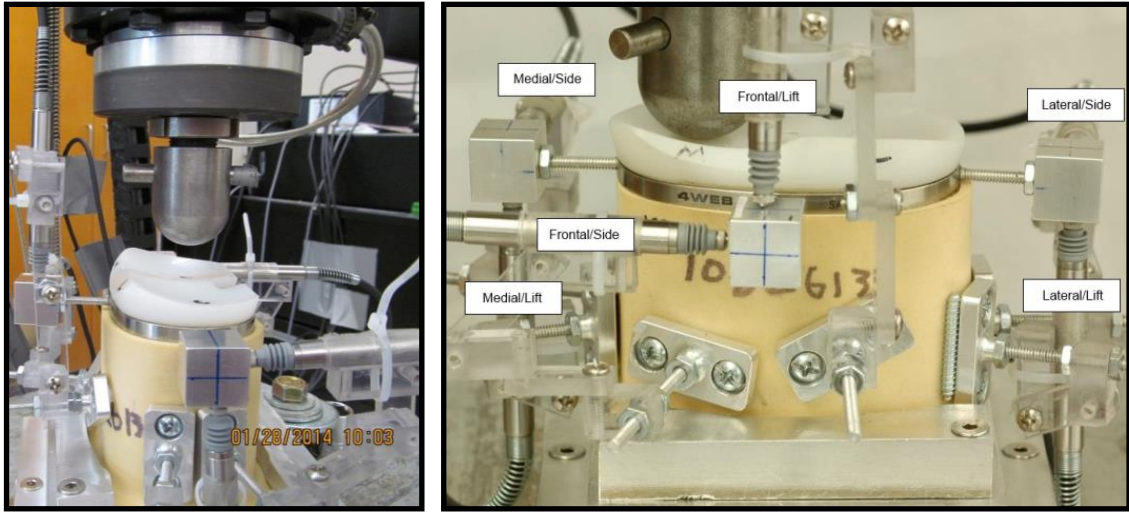


*Figure 5.* The LVDTs interfaced with the tibial tray via a 5/8" cube, mounted 3/4" away from the edge of the tray.

The transducers were mounted at three locations: the anterior, medial, and lateral sides of the tibial tray. At each location, one LVDT measured the motion in the axial direction and the second measured the transverse motion. Load was applied by a TestResources (Shakopee, MN) Dual Column Load Frame using a round indenter to apply compression on the polymer insert at the lowest point of either the medial or lateral condyle.



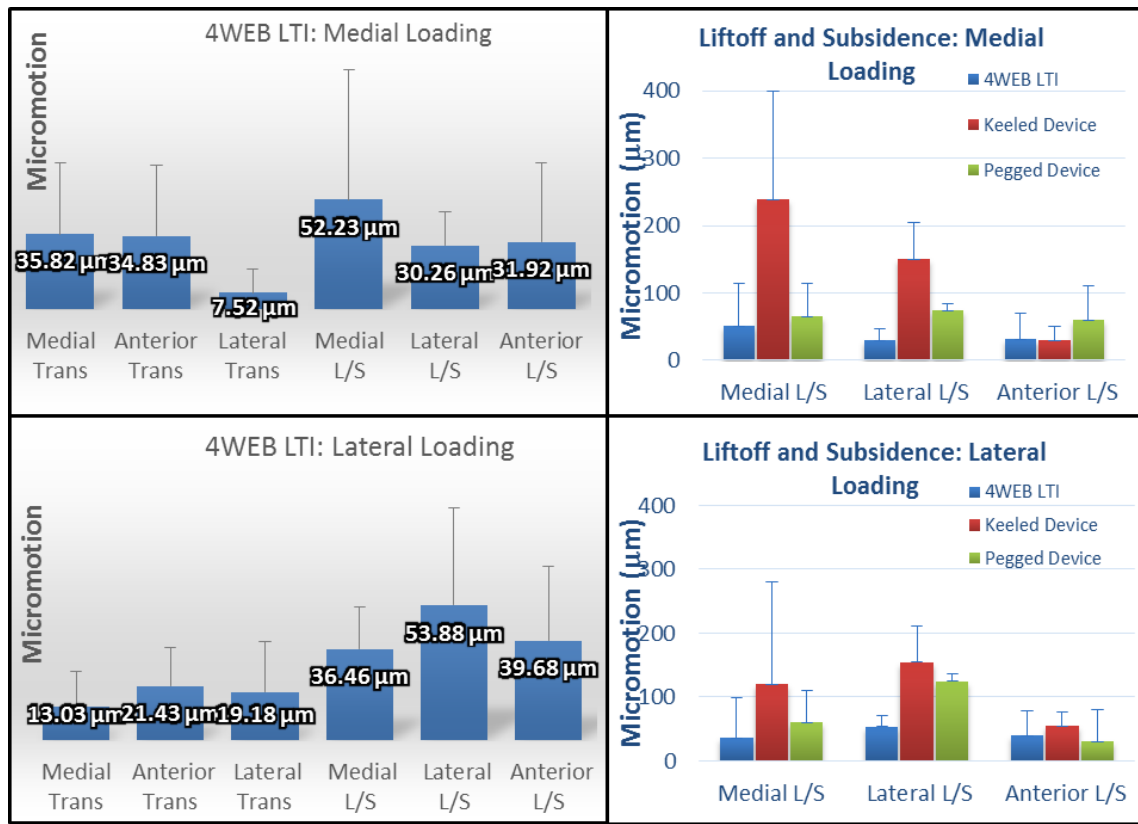


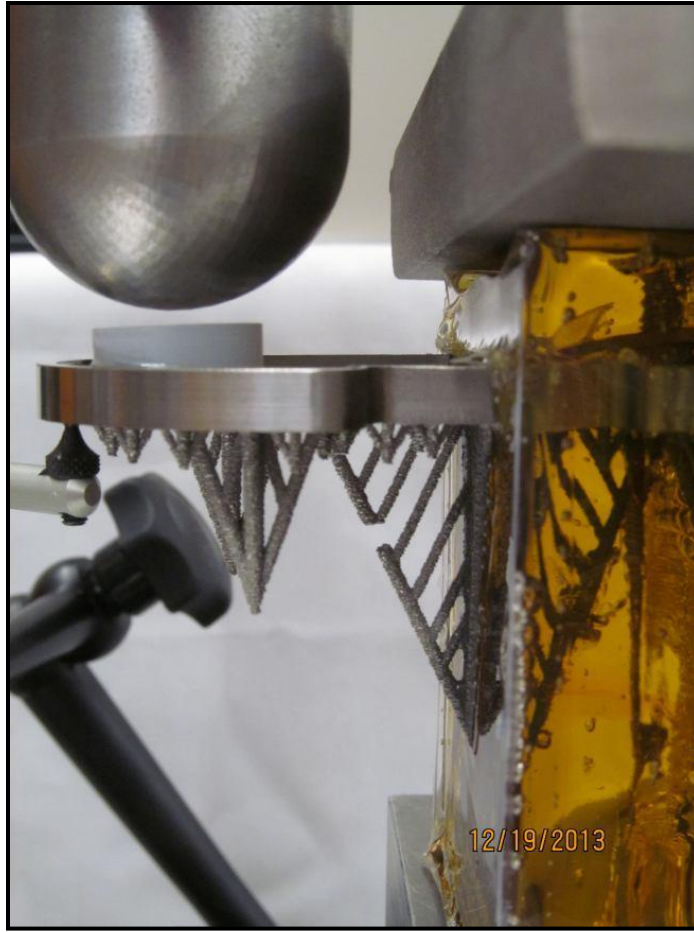
Figure 6. Micromotion measured by the six LVDTs

Micromotion measured by the six LVDTs during the fixation testing under the medial condyle loading condition (top left) and the lateral condyle loading condition (bottom left). At each location, the observed micromotion in the 4Web tibial tray was lower than the micromotion reported in Bhimji, et al. for keeled and pegged TKR devices (top and bottom right). The 4Web device compares favorably to currently-used devices according to this measure of fixation.

**Fatigue.** Cyclic fatigue testing was performed to ensure the novel design of the tibial tray did not hamper its ability to withstand the repetitive loading conditions experienced in vivo. The testing protocol followed ASTM F1800-07 and ISO 14879 as required for FDA approval. Briefly, the tibial tray was mounted as a cantilever beam with care taken to ensure that the fixation of the tibial tray did not produce abnormal stress concentrations that could

change the failure mode of the part. A spacer of plastic possessing sufficient stiffness and creep resistance was placed between the tibial tray and the load applicator on the unsupported condyle. The fixturing was designed and constructed so that the load is applied perpendicular to the undeflected superior surface of the tibial tray. A Test Resources (Shakopee, MN) Dual Column Load Frame was used to apply the load which cycled from 50 to 500 N, five million times at 10 Hz. The purpose of this testing was to evaluate the fatigue behavior of the baseplate alone, independent of the in vivo environment. Plastic deformation or catastrophic failure mode are the data of interest for this study. Evidence of failure was evaluated visually at specified points throughout the fatigue protocol and after completion of the study via examination of the displacement data. Peak to peak deflection was measured at the beginning and the end of the test using a displacement transducer (Epsilon Technology Corp, Jackson, WY). Six samples were tested via the fatigue protocol and the samples have been analyzed for evidence of failure.

**Results of completed testing.** Six samples were tested in the described manner. No evidence of device failure was observed during the test and close visual inspection of the devices both during and following testing also revealed no evidence of failure. Failure is defined as a sudden drop in load, cracking along the tray base or a statistically significant difference in deflection. The testing set up can be seen in Figure 7. The deflection measured before and after fatigue testing was measured and compared. The results can be seen in Figure 8.



---

*Figure 7.* The 4Web LTI tibial tray mounted in epoxy for fatigue testing.

In accordance with ASTM Standard F1800-12, the central truss strut was cut prior to testing to allow the tray to freely deflect under load. At the conclusion of testing no signs of failure of the baseplate were evident in the data or by close visual inspection.

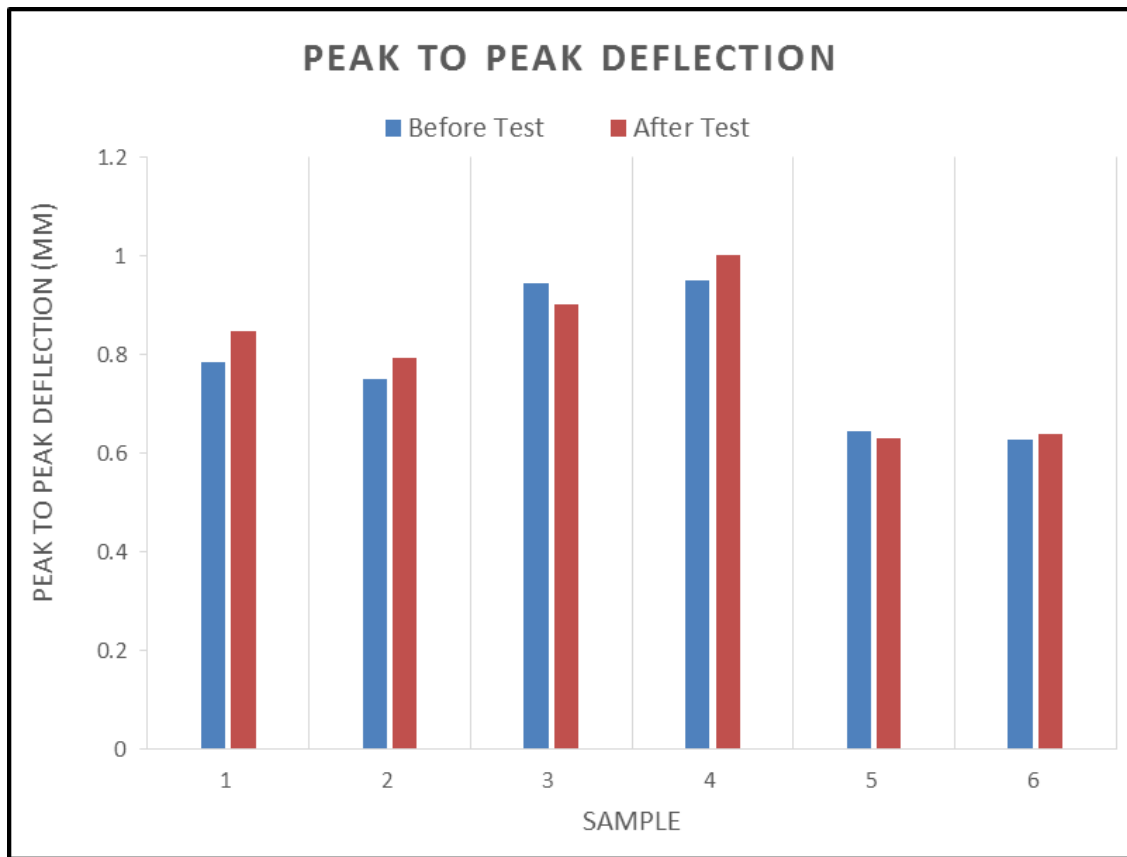


*Figure 8.* Tray deflection at the beginning and end of testing. No signs of failure were evident in the data or via close visual inspection.

**Conclusions for proof of concept testing based on results.** The results of the mechanical testing performed in Specify Aim 1 provide evidence of the improved fixation and durability of the 4Web device as compared to current technology. The results of this investigation provide validation of both the design and the additive manufacturing techniques used by 4Web to produce the Load Transferring Implant (LTI) Tibial Tray. The device performed well in the tests it underwent. The fixation/micromotion testing showed that, at all measured locations, the micromotion of the 4Web device was less than that of comparable keeled and

pegged devices in both liftoff\subsidence and transverse movement. This demonstrates better initial fixation and less potential for loosening, offering a major advantage over current TKR devices. This represents the potential to significantly reduce the necessity of revision surgery for patients receiving TKRs using 4Web's technology. The fatigue testing demonstrates the ability of the device to resist plastic deformation over long periods of cyclic loading. As TKR implants are expected to experience millions of loading cycles throughout the lifetime of the device, permanent deformation could lead to device failure and complications requiring revision. Because of this relevance, the FDA requires survival of such cyclic fatigue testing prior to approval. The 4Web device concept has been validated.

**Problems encountered and methods of resolution.** It was originally proposed that the in-vitro testing to assess the fixation would be done according to protocols found in current literature because there are no standard methods (such as ASTM or ISO) for investigating the fixation of a tibial tray. The proposed testing was to follow the protocol described in Chong, et al. 2010, implanting the tibial trays into cadaveric specimens and applying loads to the medial and lateral sides of the tibial tray simultaneously via a femoral component. However, polyurethane foam constructs were substituted for biological specimen for two reasons. First, it became apparent that bone analogs would be a more appropriate testing tool that would produce less inconsistency between trials, due to the inherent variability that exists between cadaveric specimens. Second, because of the increased difficulties associated with using explanted tissue (handling care, storage, training), it was decided that bone

analog would also be a more cost-efficient test source. For these reasons the test was modified, but this meant the results from the 4-Web LTI tibial tray fixation testing could not be directly compared to the results of the devices reported in Chong, et al. Therefore, the testing protocol was modified to conform to the procedure reported in Bhimji, et al. 2012. In that study, researchers implanted keeled and pegged tibial trays from TKR devices into a polyurethane bone construct, and measured micromotion during cyclic loading on either the medial or lateral condyle after an initial pre-load. The testing for the 4Web tibial tray duplicated this procedure, including the loading regime, loading location, and bone analog density, material and manufacturer. Also as in Bhimji, et al., six LVDTs were used to measure the micromotion between the tray edge and its adjacent supporting bone; however one of the measurement locations was altered to try and provide a more accurate representation of device movement throughout the loading protocol. Bhimji, et al. used four LVDTs to measure liftoff from the bone analog and two to measure movement in the transverse plane. The test setup was adjusted so that three LVDTs would measure liftoff and three would measure movement in the transverse plane. Modifying the test procedure to recreate the same testing conditions used by Bhimji, et al. allowed direct comparison between published testing results from currently accepted devices and micromotion observed in the 4-Web tibial tray. Thus, evidence was provided to show that the fixation capabilities of the 4-Web tibial tray meet or exceed that of current technology.

To accomplish this proof of concept testing, it was proposed that fatigue testing would be performed according to the standard ASTM F1800-07. This was modified to also

incorporate lower loading values recommended in the ISO 14879 standard. The tests still conformed to the ASTM F1800 standard because the ratio of maximum to minimum load (R) was still 10, as the ASTM standard specified. Therefore, the objective to perform cyclic fatigue testing according to this standard was met.

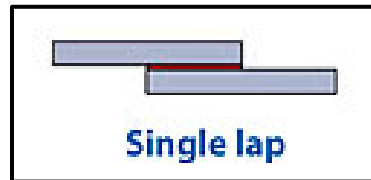
### **Porous Coating Characterization Approach**

This specific aim concerns the design a battery of tests to evaluate the characteristics of the porous coating covering the interface system of the tibial tray with respect to mechanical performance in accordance with ASTM F1044 and ASTM F1160.

These mechanical tests are required for 510(k) approval, as per the FDA's Document: Class II Special Controls Guidance Document: Knee Joint Patellofemoral and Femoral Tibial Metal/Polymer Porous Coated Uncemented Prostheses. 4-Web, Inc. employs computer-aided fused titanium rapid prototyping to produce the truss system on its orthopedic implants. The truss struts are then finished with a titanium plasma spray. This manufacturing process creates a porous surface for osseointegration of the surrounding bone. In order to quantify the surface characteristics, the shear strength was investigated in accordance with ASTM F1044. Below described are experiments to be carried out subsequent to the publication of this dissertation.

The adhesive and cohesive strength of the coating is assessed using a lap shear test which consists of two parallel plates epoxied together, one of which has the surface modification

while the other does not. A single lap specimen is used for this shear test and is a specimen consisting of two pieces joined by a single shear joint. An example of a single lap specimen can be found in Figure 9.



---

*Figure 9.* A single lap specimen has one shear joint between two pieces of material.

The plates are subjected to a shearing force and the mode of surface failure is noted. The adhesive used to bond the coated and the uncoated specimens together for the lap shear test must have a minimum bulk shear strength equal to the minimum adhesion strength of the coating. FM 1000 Adhesive Film supplied by Cytec Engineered Materials in Havre de Grace, MD, is commonly used as the adhesive for this test (Wei 1999) though bone cement and 3M Scotch-Weld 2214 are also acceptable (ASTM F1044-87). As this is a shear test, the fixturing was designed such that loading of the specimen in tension occurs in line with the central axis of the specimen, and that no eccentric loads or bending moments are introduced. This fixture was constructed of hardened steel having a Rockwell hardness test of greater than 60 on the ‘C’ scale, namely SS316L.

The bars to be tested are recommended to be 3”x1”x1” with the coated bars having the last 1” of the length treated with the surface modification. A 9/16” diameter hole accommodates



the dowel pin which connects the sample to the fixturing on the testing machine. The coating was visually inspected for all specimens prior to testing then the thickness was measured in the center as well as the four corners of the treated area. The tolerance for varying the coating measurement may be up to 15% of that measured at the center. Five specimens were tested. A 0.01" thick coating of the adhesive will be used to glue the uncoated bar to the coated bar. The specimens will be tested with a crosshead rate of 0.25 cm/min (0.1 in/min) until the bars have separated completely. The maximum tensile load applied will be recorded and used to calculate the adhesive strength, which will be reported along with the mode of failure for each specimen.

Since the coating is porous in an effort to encourage osseointegration, it is a concern that the adhesive will penetrate through the coating to the substrate beneath, thus compromising the validity of the findings. Each specimen will be inspected after testing and any compromised samples will not be included in the study. SEM will be used to evaluate the failure mode of the coating in more detail and energy dispersive spectroscopy (EDS) will be used to analyze the composition of the fracture surface to ensure no epoxy resin is present. The presence of epoxy resin at the fracture site would indicate that either the epoxy had penetrated through the coating to bond with the substrate, or that the fracture occurred within the coating instead of at the coating/substrate interface. Either of these situations would produce invalid results and prohibit the inclusion of the affected sample in the study. This investigation has not occurred at the time of this publication but will be completed prior to submission to the FDA via a 510(k).

### **Range of Motion Evaluation Approach**

This specific aim concerns designing the protocol and fixturing for a complete geometric assessment including range of motion (ROM) and constraint testing in accordance with ASTM F1223-08.

Range of motion testing involves characterizing the implant using antero-posterior draw, medio-lateral shear and rotary laxity to determine constraint. The ultimate purpose of this testing is to create a database of information on these parameters which characterize the implant and give physicians adequate information to choose the appropriate implant for their patient. While investigating the implant in vitro does not directly predict the in vivo behavior primarily due to the lack of soft tissue interaction, FDA mandate of this battery of tests allows for direct comparison of all total knee replacement systems that are FDA approved. The protocols will follow ASTM F1223-08. The author has designed all fixturing and optimized the protocol to allow this testing to be performed, but construction and testing have not occurred at the time of this publication.

All samples will be at room temperature for a minimum of 24 hours prior to testing. Once implanted, each protocol will be run three times to condition the sample. Data will be collected on the fourth trial.

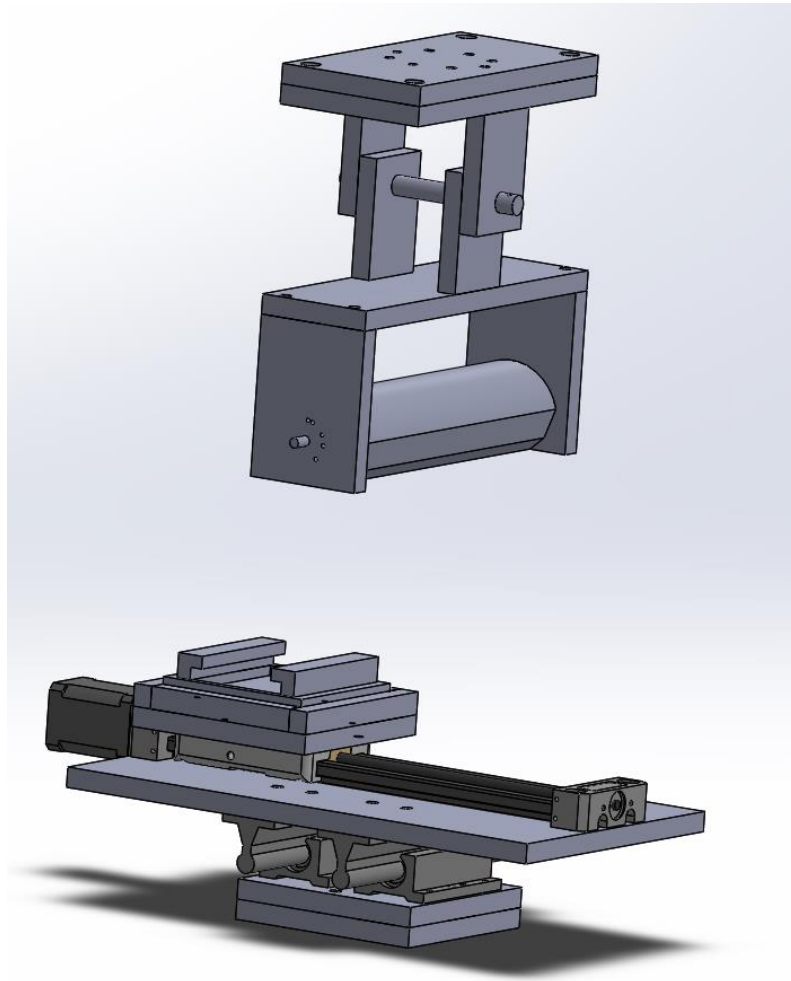
The **anterio-posterior draw test** is testing the tibia's ability to slide A/P relative to the femur, meaning the tibia will be pulled towards or pushed away from the patella. The knee

should be at a 90° angle and the femoral component should be able to move along the x-axis only. The construct experiences a constant axial load mimicking a joint reaction force of 710 N, or one body-weight (Haider 2005). The limits for the test will be determined by moving the tibial component back and forth along the x-axis until the two points of maximal force, one anterior and one posterior, are found. Because of deformation of the poly insert, the limits for testing will be established by finding the displacement associated with the maximal force, then reducing the distance travelled by 0.5mm on each side (Haider 2005). Actual testing will involve ramping between these displacement set points five times at a rate of 1 mm/s. The test should be completed within two minutes of the start of the applied load and the load will be applied gradually. Test termination will occur if the dislocation of the parts is imminent, if a mechanical stop prevents further motion or if a dangerous or unrealistic situation is about to occur. The A/P displacement in millimeters and corresponding force in Newtons are of interest when conducting this test and will be measured using LVDTs (Solartron Metrology). The test will first be run with force displacing the tibia anteriorly, then it will be reset to the neutral position and force will be applied that will displace it posteriorly.

The **medio-lateral shear test** is testing the tibia's ability to slide M/L relative to the femur, meaning the tibia will be pulled towards or pushed away from the other knee. With reference to the load frame, this testing can be seen as similar to the anterior-posterior draw test, but the knee is now free to move along the y-axis as opposed to the x. All of the other information pertaining to the test is the same, including the 710 axial load, method for

obtaining the limits, and testing protocol. The M/L displacement in millimeters and corresponding force in Newtons are of interest when conducting this test and will be measured using LVDTs (Solartron Metrology). The test will first be run with force displacing the tibia medially, then it will be reset to the neutral position and force will be applied that will displace it laterally.

The concept for the fixturing for both the antero-posterior draw and medio-lateral shear testing can be seen in Figure 10 below. Briefly, all the degrees of freedom are maintained open if they are not prescribed by the protocol (Haider 2005, Moran 2008, Willing 2012). To restate, during antero-posterior draw the medio-lateral displacement, varus-valgus rotation and internal-external rotations are open. During medio-lateral displacement, the antero-posterior displacement, varus-valgus rotation and internal-external rotations are open. A six degree of freedom load cell measures the axial load applied, as well as the loads seen by the tibial component as it is translated along either the x or the y axis.

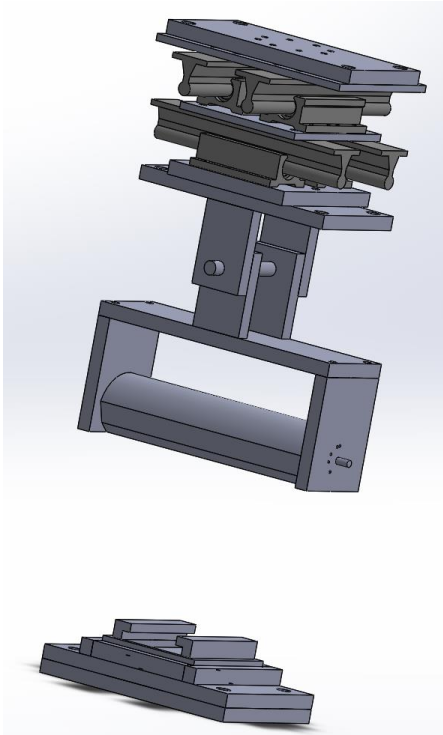


---

*Figure 10.* Conceptual rendering of the fixturing for the antero-posterior draw and medio-lateral shear testing.

The tibial component translates via a linear actuator in displacement control. Linear bearings allow the orthogonal displacement to be free, while a hinge joint located above the femoral component allows the varus-valgus joint to be free. The load frame has a torsion motor which will remain unlocked during testing to allow internal/external rotation.

The **rotary-laxity test** is testing the tibia's ability to rotate while the femur is stationary. The tibial component should be able to move in angular displacements parallel to the z-axis only. The construct experiences a constant axial load mimicking a joint reaction force of 710 N, or one body-weight (Haider 2005). The limits for the test will be determined by moving the tibial component back and forth about the z-axis until the two points of maximal force, one internal and one external, are found. Because of deformation of the poly insert, the limits for testing will be established by finding the displacement associated with the maximal force, then reducing the distance travelled by  $0.5^\circ$  on each side (Haider 2005). Actual testing will involve ramping between these displacement set points five times at a rate of 1 degree/s. Rotary torque will be applied gradually, and the test will terminate when a rotation of  $20^\circ$  is reached, a torque of 25 Nm is reached, if disarticulation of the components is imminent or if a mechanical stop prevents further motion. The test will be completed within two minutes of the start of the applied load. The ending internal or external rotation in degrees as well as the corresponding torque in Nm will be recorded by interfacing with the load cell. The test will first be run with force rotating the tibia internally, then it will be reset to the neutral position and force will be applied to rotate it externally. The concept for the fixturing for this protocol can be seen in Figure 11. The medio-lateral displacement, varus-valgus rotation and internal-external rotation are all free (Haider 2005, Moran 2008, Willing 2012).




---

*Figure 11.* Conceptual rendering of the fixturing for the rotary-laxity testing.

The tibial component translates about the z axis via a torsional motor on the load frame located directly below the tibial component clamp, the bottommost fixture. Linear bearings allow the antero-posterior and medio-lateral displacement to be free, while a hinge joint located above the femoral component allows the varus-valgus joint to be free.

### **Summary**

This dissertation details the design of the experimentation and fixturing of the porous coating evaluation and range of motion characterization for the TKR tibial tray bone-implant interface. The implementation of the protocols and the analysis of the results remaining in

the NSF SBIR Phase II grant will be completed by a student in the Biomechanical Environment Lab and/or 4Web, Inc.



### CHAPTER III

#### REGENERATIVE FRACTURE FIXATION DEVICE

Despite new stabilization techniques and improved wound care, open long bone fractures still result in high rates of infection, delayed union, non-union, and – in major limb trauma – amputation. Patient morbidity, partial functional recovery, and poor quality of healing have long-term impact on quality of life after injury. Rehabilitation is slow, painful, and the costs emotionally, physically, and economically are prohibitive. These types of injuries and subsequent challenges exist both for the civilian and military patient populations and underscores the pressing need to address the complexities of bone regeneration in the extremities.

There were approximately 1,620,000 surgical bone graft procedures in the United States in 2005 and 672,000 fracture reductions in 2006 (Meling et al. 2009). The estimated economic costs for orthopedic injuries to upper and lower extremities collectively account for 17%, or \$68 billion, of total lifetime costs that originated in 2000. Over the past 15 years, significant efforts have focused on the development of bioactive, load-bearing polymeric materials designed to restore function within critical-sized bone defects. Traditional reconstructive approaches use autografting of the defects, but these approaches have significant limitations (Boerckel et al. 2011). As a result, transfer of grafts greater than 2 cm are associated with an unacceptably high complication rate. Thus, the optimal skeletal extremity reconstruction would be one in which the reconstruction is performed with material that may be taken “off

the shelf” to eliminate donor site morbidity, but is degradable and resorbable affording incorporation into the host.

Guided tissue regeneration is based on the biological principle that the different tissues of the body have different tendencies and therefore abilities to occupy a wound. By providing a mechanical hindrance, such as a membrane, preference for certain types of cells to repopulate the open space can be achieved (Nyman et al. 1995). Bone’s ability to grow into isolated cavities was first documented in the late 1950’s. In 1982, Sture Nyman and Thorkild Karring established the field using cellulose acetate filters as barriers in animal and clinical trials. By 1989, clinical trials for periodontal applications using expanded PTFE membranes saw success. Guided tissue regeneration is now the gold standard for regenerating bone in over 40% of dental implant placements performed today (Scantlebury et al. 2012).

Guided tissue regeneration principles and practices have been well established with regard to intramembranous bones such as the mandible and maxilla and are starting to branch into the endochondral bone space, which includes the long bones. The regenerative successes seen previously have not been appreciated in studies involving long and weight bearing bone regeneration. This may be due to differences in the healing patterns between the two types of bone. When used as bone grafts, endochondral bone appears to be resorbed with time whereas the intramembranous bone has been known to maintain or even expand its volume (Smith and Abramson 1974).

Because of the differences in natural bone growth between these two subsets of bone, the types of membranes used for guided tissue regeneration will have to be modified from those successful with intramembranous bones to ones more suitable for endochondral bone. A study in rabbits suggested that the mechanical cues created by the solid surface of the membrane used to guide the tissue formation is one of the more important factors in bone regeneration of endochondral bone and recommended the use of scaffolding to increase the amount of mature bone regenerated (Nyman et al. 1995).

Histologically, the presence of a membrane increases the number of newly formed bone trabeculae during the early stages of healing as compared to a defect left to heal spontaneously (Lysiak-Drwal et al. 2008). Cortical bone caps the end of these control defects (Nyman et al. 1995, Lysiak-Drwal et al. 2008). Many types of scaffolds have been tested in vivo, including ceramic (Gao et al. 1997, Bloemers et al. 2003, Mastrogiacomo et al. 2006), polymeric (Hutmacher 2000, Puppi et al. 2010) and composite scaffolds (Ramakrishna et al. 2001, Hutmacher et al. 2007, Lickorish et al. 2007). Because synthetic polymers exhibit predictable and reproducible mechanical properties and degradation profiles, we have chosen this subset of material to create our cylindrical cuff, which will be used as our membrane. Poly(propylene fumarate) (PPF) is a linear polyester which undergoes bulk degradation by hydrolysis, splitting the ester linkages to produce propylene glycol and fumaric acid, both of which are easily cleared by the body (Rezwan et al. 2006). Varying the polymer molecular weight or the crosslinker content has been shown to alter the mechanical properties and degradation rate (Peter et al. 1999), though issues of

biocompatibility with the use of the crosslinker PPF-diacrylate do exist (Timmer et al. 2003). PPF composites utilizing ceramic fillers are of interest given their suitable mechanical properties for bone regeneration as scaffold, and their potential to lend these properties to the membrane itself. Specifically, PPF and spherical  $\text{CaSO}_4/\text{TCP}$  granules have been shown to have compressive mechanical properties similar to that of cancellous bone (Cai et al. 2009). Controlling the degradation rate to match the tissue formation rate is an important factor to consider when developing a membrane for guided bone regeneration. PLGA microspheres have been successfully added to PPF membranes to tailor the degradation rate as well as promote the osteoconductivity of the membrane itself (Hedburg et al. 2005) and mesoporous silica nanoparticles are receiving attention for their potential in biomedical applications due to their excellent biocompatibility and in vivo biodegradation (Park et al. 2009). Surface-functionalized and peptide conjugated silica nanoparticles are readily internalized by animal and plant cells without any cytotoxic response (Radu et al. 2004, Slowing et al. 2006). For these reasons we have chosen silica nanoparticles for our PPF-based nanocomposites. PPF has not been investigated for use as a load bearing membrane, only as the scaffold on which the bone regenerates. Our investigation will be a novel application of the polymer.

The most popular animal models for orthopedic investigations are rats, mice and rabbits, likely due to their inexpensive care and the fact that they are easy to handle (Martini et al. 2001). Because of their small size, investigations using these species are typically limited to basic orthopedics, including toxicological tests on biomaterials. The rate of bone repair is

inversely proportional to the position of the species on the phylogenic scale, thus these smaller animals have much higher capacity for regeneration than do humans (Klienschmidt et al. 1992). This will be true for any animal model, though to varying degrees. Large sized animals are used for the final evaluation of orthopedic devices, prosthetics and surgical tools, the most popular of which is dogs, followed by non-human primates and finally sheep (Martini et al. 2001). Sheep are currently cited in 12% of publications reviewed in 2001, while dogs are cited as the animal model in 35%. While non-human primates provide an excellent model for human bone growth, they are expensive, strictly regulated, have the capacity to cause severe zoonotic diseases and are associated with heated ethical debate. Dogs are a popular choice mainly because of the extensive background knowledge associated with this animal model. For the past 50 years, orthopedic researchers have preferred the use of scientific findings of the veterinary community and thus the dog has become the only large animal species to be studied extensively in the lab. The use of dogs and primates is declining in the European community due to the emotional impact and legal complications associated with their use (Martini et al. 2001, Mills et al. 2012). Current general consensus is that there is no reason to use dogs when sheep are available (An Yuehwei et al. 1998).

Sheep are acceptable for use as an orthopedic animal model when investigating the load bearing long bones because their body weight, complexity of bone architecture and secondary bone remodeling characteristics are similar to those of humans (Viateau et al. 2004, Martini et al. 2001, Mills et al. 2012). Sheep cortical bone has fewer Haversian canals

than human bone does (Viateau et al. 2004, Martini et al. 2001, Mills et al. 2012), though the rate of healing does approximate humans' (Den Boer et al. 1999). Similarities between human and sheep trabecular bone exist, though cortical bone differs in ash, hydroxyproline, extractable protein and insulin-like growth factor content (Aerssens et al. 1998).

Between 2008 and 2013, under the Fracture Putty Program at DARPA, Methodist Hospital Research Institute designed, engineered, and tested a biodegradable polymeric shell capable of providing mechanical stability to a critically size segmental tibial defect without metallic hardware or external fixation. They demonstrated the efficacy of this construct and showed conclusively full functional recovery of the treated animals. The biodegradable polymeric shell was used in combination with an implantable biomimetic collagen scaffold capable of instructing surrounding tissues and guiding the cells of the periosteum and the marrow cavity toward an osteogenic fate. The implant induced unprecedented bone growth that encased the polymeric shell and functional resolution of the defect as early as 4 weeks after surgery. In this study, the author was the primary student involved with completing the preliminary assessment of a L-phenylalanine-based poly(ester urea)s (PEU) shell effectiveness in critical size osteo-regeneration. These studies will be instrumental in achieving Food and Drug Administration (FDA) approval. Data generated by the investigation will be collected and used for a pre-IND regulatory filing. We have worked together with industry, regulatory experts and FDA policy makers to identify an accelerated and straightforward path to the clinic, and design the structure of the necessary clinical trials to be conducted with the shell on both the civilian and military populations. The target

patient that will benefit from our study will be the soldiers or civilians with highly unstable long bone fractures usually treated with external skeletal fixation (segmental defects of high severity that exceed 1cm). In clinical practice, the application of our novel fracture fixation shell will result in rapid and safe bone formation, avoidance of amputation, absence of permanent hardware that are prone to infection, a faster return to duty for military personnel and normal routine for civilians and an overall higher quality of life after injury. Healthcare costs will be dramatically decreased given lesser need for reconstructive surgery, repeated surgeries or hospitalizations, and extensive rehabilitation.

### **Nanocomposite Characterization**

This aspect of the project involved characterizing the mechanical properties of poly(propylene fumarate) (PPF) reinforced with three different types of nanoparticles (MSN, 3.5 SiO<sub>2</sub> Rod, 7.5 SiO<sub>2</sub> Rod) in two differing concentrations (0.5%, 1.0%) and comparing the effects of that reinforcement on the behavior of the polymer under compressive loading. The spherical nanoparticles have a diameter of  $100 \pm 15$  nm, the short rod nanoparticles (labelled the 3.5 rods) have a length of  $300 \pm 11$  nm and an aspect ratio of 2 and the long rods (labelled the 7.5 rods) have a length of  $375 \pm 11$  nm and an aspect ratio of 3.5.

The mechanical testing protocol was based on ASTM D695-02a Standard Test Method for Compressive Properties of Rigid Plastics. The standard calls for specimens with an aspect ratio of 4, ideally cylinders 0.5” in diameter by 2” in length. Our samples were 0.25” in diameter with a length of 0.75”, giving an aspect ratio of 3.

The samples were supplied to us by Methodist Hospital Research Institute. We received seven groups of samples, with five samples in each group. The groups are delineated in Table 1 below, according to the labels fixed to the tubes they were received in.

Table 1. *Group Labels*

Group Number	Group Name
Group 1	Control, unfilled PPF
Group 2	0.5% (wt) MSN, 0.5% 100 nm SiO <sub>2</sub>
Group 3	1.0% (wt) MSN, 1% 100 nm SiO <sub>2</sub>
Group 4	0.5% (wt) 3.5 Rod, 0.5% 3.5% Rod
Group 5	1.0% (wt) 3.5 Rod, 1.0% SiO <sub>2</sub> 3.5% Rod
Group 6	0.5% (wt) 7.5 Rod, 0.5% 7.5% Rod
Group 7	1.0% (wt) 7.5 Rod, 1.0% Rod-PPF 7.5% dcrg

The ends of the samples were inspected visually for any defects and on some required facing off to ensure good contact between the sample and the compression plate across the entire diameter. Facing off did not remove enough material to appreciably effect the total length of the sample, and lengths were taken after facing off, directly before compressive testing. One sample was compromised during the facing off process. This was a 1.0% 7.5 Rod sample with a large crack near one end, and during machining vibration caused this sample to split long the crack, thus significantly reducing the aspect ratio. This sample was removed from



the study. Preliminary work suggests machining does not affect the mechanical properties of the samples. This preliminary work was with samples of virgin PPF, 0.5% SiI<sub>2</sub>-PPF and 1.0% SiI<sub>2</sub>-PPF. In this study, the 1% 3.5 Rods were used as a control since no samples from that group were subjected to the machining. The standard deviations of the 1% 3.5 Rods were similar to the standard deviations of the other groups in every aspect examined in this study.

The samples were then visually inspected for defects present in the form of cracks on the surface and bubbles throughout. Table 2 lists the overall impressions of the samples, by group.

Table 2. *Visual Examination for Defects*

Group Name	Visual Inspection for Defects
Control	Some cracked, some smooth
0.5% MSN	Prevalent cracking, few bubbles
1.0% MSN	Minor bubbles
0.5% 3.5 Rods	Prevalent cracking, few bubbles
1.0% 3.5 Rods	Prevalent cracking, few bubbles
0.5% 7.5 Rods	Prevalent cracking, few bubbles
1.0% 7.5 Rods	Extreme cracking, no bubbles

The surface defects of the samples were quantified by rolling the samples in black ink, then across white paper. A perfect sample would leave a completely black signature while cracking on the surface of the sample would leave corresponding white spaces in the impression. A MATLAB code processed the images and returned the percent of the surface affected by cracking. This process was verified by a comparison to visual inspection.

The bubbles were quantified by calculating the density of the samples, with the thought that the air trapped inside the bubbles would weigh less than the polymer that would have been occupying that space. The density varied widely throughout the groups. There were large variations both between groups of different reinforcement categories, such as the 0.5% MSNs and the 0.5% 3.5 Rods, and within the same reinforcement category, as seen with the 0.5% and 1.0% 7.5 Rods. These variations in manufacturing likely influenced the mechanical properties and are thought to have contributed to the large standard deviations present in many of the graphs.

The largest change in density was found in each group and divided by the mean of that group to give the maximum percent density variation from mean. These values can be seen in Table 3. Of particular concern are the 0.5% MSNs and the 1.0% 7.5 Rods, as seen in Figure 12. The 1.0% 7.5 Rods had no bubbles present in the samples, yet has the largest standard deviation, suggesting manufacturing is influencing the variance of the density. The 1.0% MSNs contain an outlier; all the samples were within  $1 \text{ kg/m}^3$  except for one, which was  $26.1 \text{ kg/m}^3$  more dense. The individual densities for each sample can be found in

Table 4, and the group means and standard deviations follow in Table 5. While in theory this method of quantification achieved the intended result, the wide variation of densities present in the samples appears to have masked any effects the bubbles may have had. A sample by sample defect analysis has been included in Appendix II.

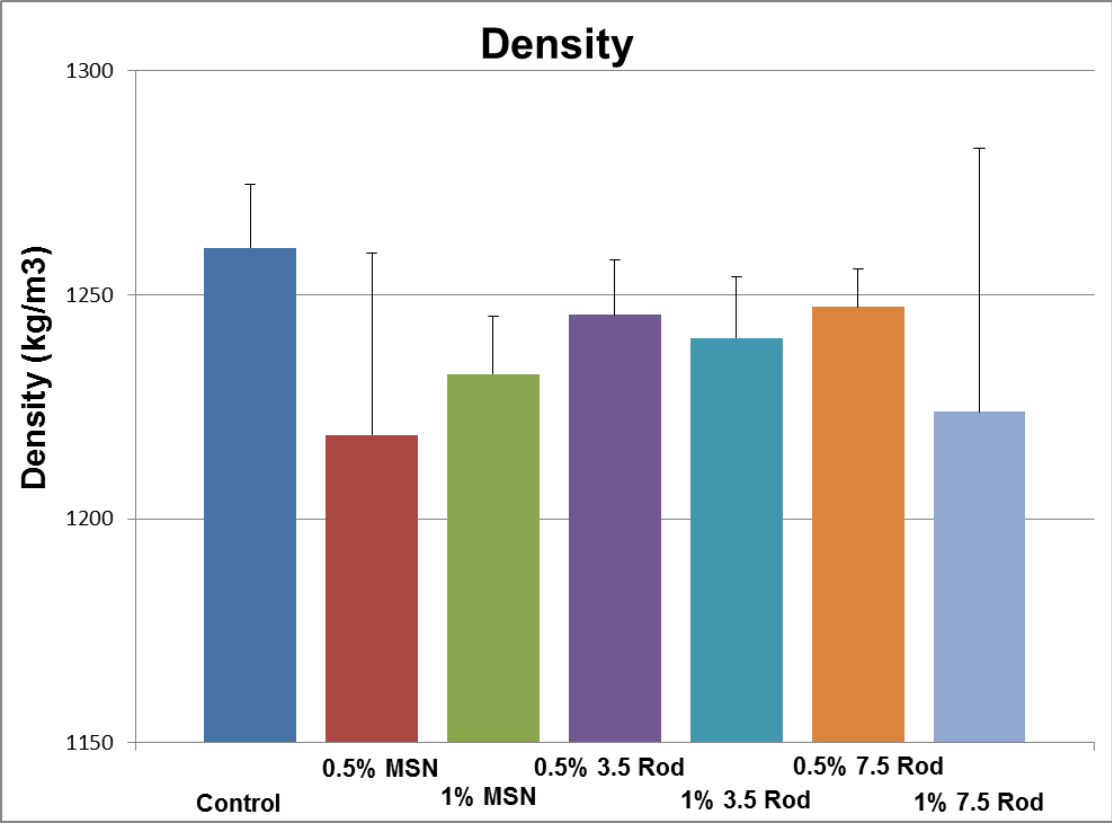


Figure 12. Comparison of the different densities present throughout the groups.

Table 3. *Maximum Percent Variation Within the Groups as Compared to the Mean*

Group	Max Percent Density Variation from Mean
Control	1.58%
0.5% MSN	6.64%
1.0% MSN*	2.12%
0.5% 3.5 Rods	2.41%
1.0% 3.5 Rods	2.23%
0.5% 7.5 Rods	1.65%
1.0% 7.5 Rods	9.45%

\**Outlier Present*

Table 4. *Individual Sample Densities*

Sample	Density [kg/m <sup>3</sup> ]
1E	1250.58
1F	1270.54
2C	1179.05
2D	1259.99
2E	1217.04
3B	1251.49
3C	1225.39

Table 4. Continued

Sample	Density [kg/m <sup>3</sup> ]
3D	1225.39
3E	1226.96
4B	1245.63
4C	1261.08
4D	1231.01
4E	1244.44
5B	1255.98
5C	1228.26
5D	1229.53
5E	1247.63
6A	1241.34
6B	1246.9
6C	1261.97
6D	1242.6
6E	1243.53
7B	1211.99
7C	1172.03
7D	1287.73

Table 5. *Density Mean and Standard Deviation*

Group	Average Density [kg/m <sup>3</sup> ]	Standard Deviation
1	1260.56	14.11
2	1218.69	40.5
3	1232.31	12.81
4	1245.54	12.3
5	1240.35	13.67
6	1247.27	8.47
7	1223.92	58.76

### **Mechanical Testing Protocol**

All mechanical testing was done at room temperature and after the samples were conditioned at 25°C and 50% humidity away from direct sunlight for a minimum of 40 hours. The lengths and widths of the sample were measured at three points along the axis and averaged. The sample was then photographed and the surface defects were quantified. The long axis of the sample was aligned with the compression axis of the testing machine. Smooth compression plates with no lip were used for fixturing. The sample was compressed at a rate of 0.05 +/- 0.01 in/min (1.3 +/- 0.3 mm/min) to failure. The data was sampled at a rate of 100 Hz.

## **Representative Raw Data**

In the raw data of the compressive testing, four distinct groups of load deformation curves became evident.

**Type I.** Some samples' graphs followed the form similar to sample 3E, where a toe region is present, followed by a ramp, then a decrease in stiffness and failure. The vast majority of samples fell into this group.

**Type II.** Other samples behaved more like sample 5B, where a toe region is present, followed by a ramp, then an inflection point, followed by a ramp of the same stiffness as the initial ramp, then a decrease in stiffness and failure. Two samples fell into this group, with the other being 7B.

**Type III.** A third group of samples are represented better by sample 6B's graph, where a toe region is present, followed by a ramp, then instabilities as the sample transitions from the elastic to plastic region of the graph, followed by a decrease in stiffness as compared to the initial ramp representative of a long plastic region, then failure. This was the second most popular behavior for the samples.

**Type IV.** The last group of samples are represented well by sample 7D's graph, where a toe region is present with a ramp, then an inflection point followed by an abbreviated plastic region and finally failure. The shorter region of plastic deformation is the distinguishing

feature of this group. Only two samples fell into this category, with the other being the control sample 1F.

All samples exhibited the toe region at the beginning of the load deformation curve. As these curves tended to span a wide range of loads and deformations while still maintaining similar shapes to the examples provided, the numbers were omitted from the load and deformation axes for clarity. The graphs can be seen in Figure 13 and the samples are organized into their representative curve types in Table 6.



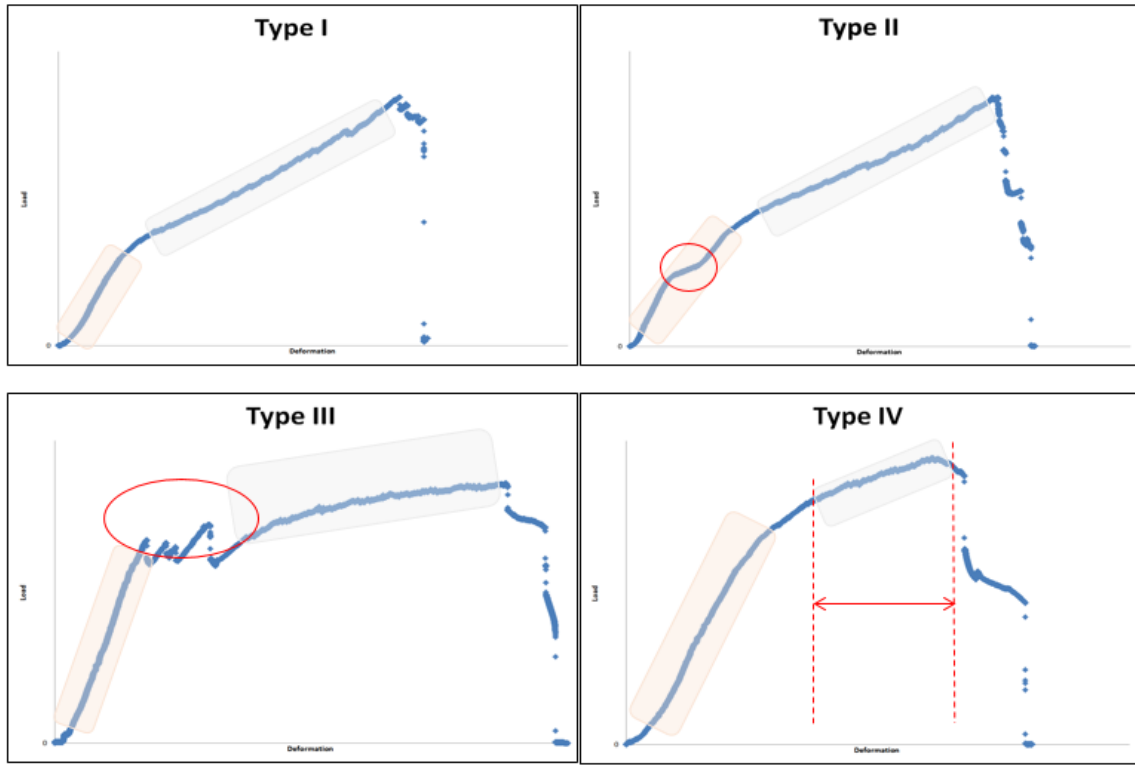


*Figure 13.* Comparisons of the four types of load deformation behavior exhibited by the samples during compressive testing.

The elastic region is denoted by a pink box and the plastic region is denoted by a green box. The toe region precedes the pink box in each case. The differences in types ii-iv as compared to type i are denoted by the red indicators.

Table 6. *Table Categorizing Each Sample by its Representative Curve Type*

Representative Curve Type	Samples Described By This Type
Type I	2D, 2E, 3B, 3C, 3D, 3E, 4B, 4C, 4D, 4E, 5C, 5D, 5E, 6C, 6D, 6E, 7C
Type II	5B, 7B
Type III	1E, 2C, 6A, 6B
Type IV	1F, 7D

**Compressive ultimate strength.** The compressive ultimate strength was calculated by finding the maximum compressive load experienced by the sample. These loads were averaged to find the ultimate strengths for each group. Standard deviations were calculated using Microsoft Excel's built in standard deviation function, STDEV.

The significance was found by running a two-tailed unequal variance Student's t-Test, where  $P < 0.05$  was found to be significant. The graphical comparison is shown in Figure 14. The individual ultimate strengths for each sample can be found in Table 7, and the group means and standard deviations follow in Table 8.

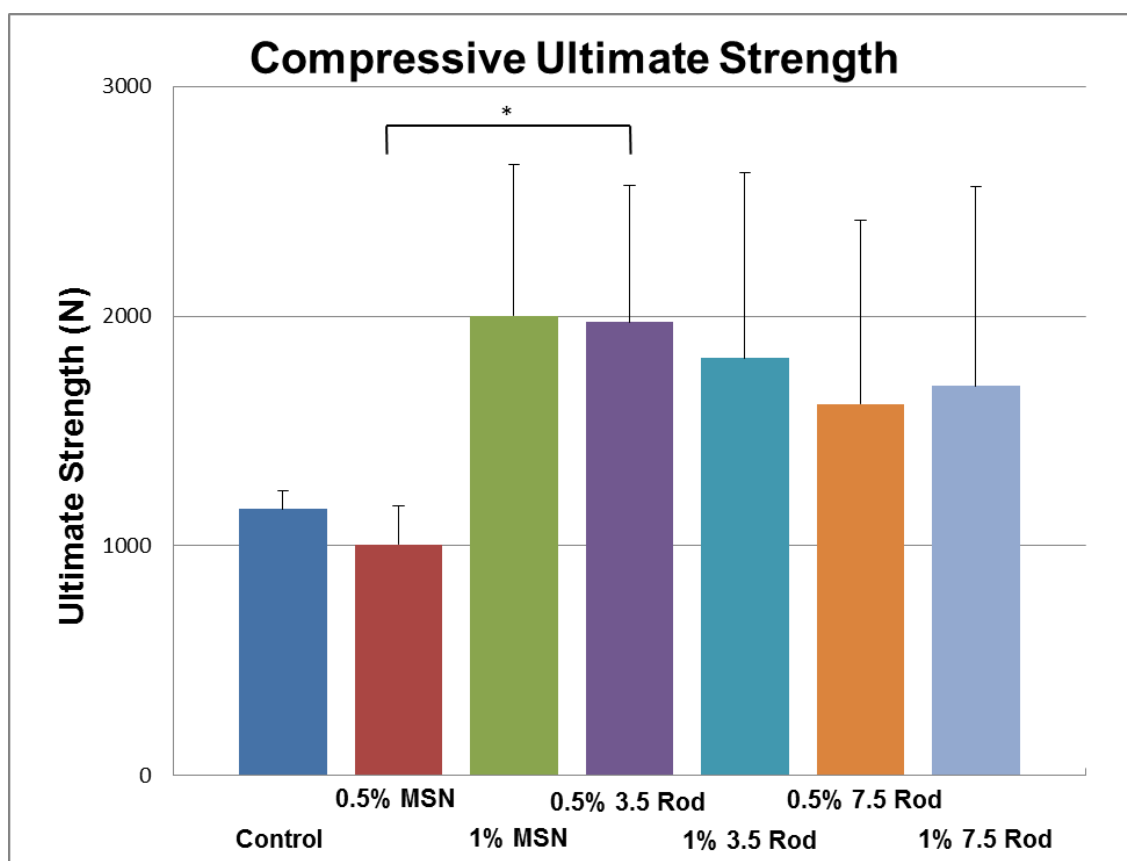


Figure 14. Compressive ultimate strength comparison across the different formulations

Table 7. *Individual Sample Ultimate Strength*

Sample	Ultimate Strength (N)
1E	1104.52
1F	1215.98
2C	822.545
2D	1038.28
2E	1153.86
3B	1184.85
3C	1751.48
3D	2527.7
3E	2538.96
4B	2022.62
4C	2590.42
4D	1156.51
4E	2119.57
5B	2112.95
5C	828.17
5D	2735.17
5E	1592.36
6A	807.26
6B	774.44
6C	2415.51

Table 7. Continued

Sample	Ultimate Strength (N)
6D	2362.34
6E	1724.46
7B	2693.92
7C	1256.87
7D	1132.95

Table 8. *Ultimate Strength Mean and Standard Deviations*

Group	Mean Ultimate Strength (N)	Standard Deviation
1	1160.25	78.81
2	1004.9	168.16
3	2000.75	657.06
4	1972.28	597.72
5	1817.16	808.06
6	1616.80	801.60
7	1694.58	867.67

**Compressive Ultimate Strength Summary.** The 0.5% 3.5 Rods show a statistically significant change in ultimate strength as compared to both the control and the other groups.

## Yield Point

The yield point was determined by estimating the intersection of the line described in the proportionality region of the load deformation curve and the beginning of the nonlinear region. Since the samples expressed several different types of load deformation curves, this was determined to be the most consistent way to quantify the yield. The yield points were averaged to get the group mean values and the standard deviations and statistical significance were calculated as described by Eq. 1. The graphical comparison is shown in Figure 15. The individual yield strengths for each sample can be found in Table 9, and the group means and standard deviations follow in Table 10.

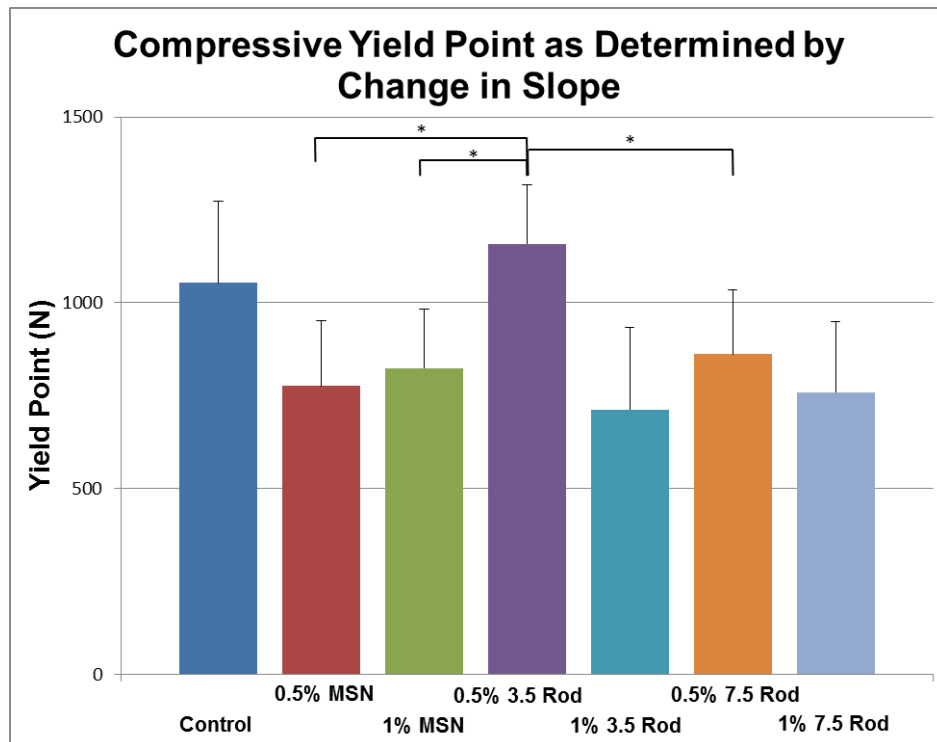


Figure 15. Compressive yield point comparison across the different formulations.

Table 9. *Individual Sample Yield Points*

Sample	Yield Point by Inspection (N)
1E	898.7
1F	1208.88
2C	622.4
2D	737.55
2E	966.78
3B	942.85
3C	709.71
3D	666.2
3E	976.37
4B	1241.29
4C	1327.42
4D	966.11
4E	1101.85
5B	560.6
5C	497.29
5D	963.61
5E	827.68
6A	792.66
6B	592.5
6C	911.01
6D	1007.91

Table 9. Continued

Sample	Yield Point by Inspection (N)
6E	1002.26
7B	639.9
7C	658.1
7D	979.38

Table 10. *Yield Point Mean and Standard Deviation*

Groups	Mean Yield Point (N)	Standard Deviation
1	1053.79	219.33
2	775.58	175.31
3	823.78	158.44
4	1159.17	158.75
5	712.29	220.39
6	861.27	173.78
7	759.13	190.96

**Compressive yield point summary.** The 0.5% 3.5 Rods show a statistically significant change in yield point as compared to both the control and the other groups.



## Compressive Modulus

The elastic modulus describes a materials tendency to deform elastically and is defined as the slope of the elastic region of a material's stress-strain curve. As our protocol called for purely compressive mechanical testing, we will refer to the modulus as the 'compressive modulus' to differentiate from parameters found during future work. To calculate the compressive modulus, we chose two points within the proportionality region of the load-deformation curve. The toe region was neglected in our analysis. Stress was calculated using the following formula (Eq.1):

$$\sigma = \frac{y_0}{(\pi(\frac{d}{2})^2)} \quad \text{Eq. 1}$$

where  $y_0$  equals the load at the point of interest in Newtons and  $d$  equals the sample's original diameter in meters. Strain was calculated using Equation 2 below.

$$\varepsilon = \frac{x_0}{l} \quad \text{Eq. 2}$$

where  $x_0$  equals the deformation at the point of interest in meters and  $l$  equals the sample's original length in meters. The deformation data reflects only the amount the sample has been compressed, thus the equation could be simplified to (change in length)/(original length), or the definition of engineering strain. Since the changes in cross sectional area and length remain small, the use of engineering strain for our calculations is acceptable. The

stress and strain for the two points were calculated and the slope, or modulus, was found using the traditional method as shown by Equation 3.

$$\epsilon = \frac{y_1 - y_0}{x_1 - x_0} \quad \text{Eq. 3}$$

A comparison by groups can be found in Figure 16 below. The individual compressive moduli of each sample are included in Table 11 and the group mean and standard deviations follow in Table 12.

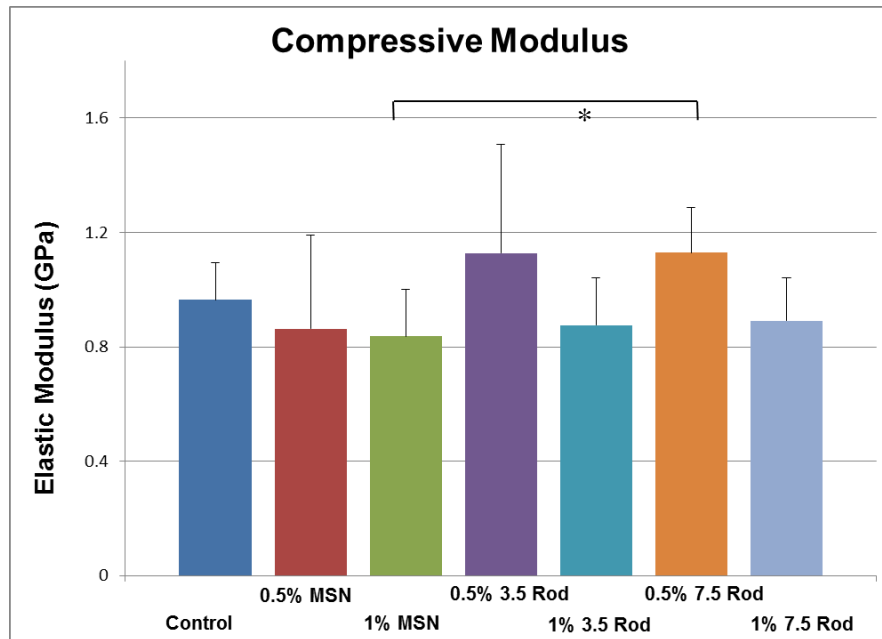


Figure 16. Compressive modulus comparison across the different formulations

Table 11. *Individual Compressive Modulus Data*

Sample	Strength 1 (y <sub>0</sub> ) [N]	Strength 2 (y <sub>1</sub> ) [N]	Stroke 1 (x <sub>0</sub> ) [m]	Stroke 2 (x <sub>1</sub> ) [m]	Diameter (m)	Length (m)	Stress (y <sub>0</sub> ) [Pa]	Stress (y <sub>1</sub> ) [Pa]	Strain (x <sub>0</sub> )	Strain (x <sub>1</sub> )	Modulus [GPa]
1E	348.95	491.15	0.0002	0.0003	0.006	0.02	11779768.26	16579837.81	0.01	0.02	1.06
1F	609.61	758.08	0.0004	0.0006	0.006	0.02	20801647.16	25868054.3	0.02	0.03	0.87
2C	240.76	363.56	0.0002	0.0004	0.006	0.02	7727547.73	11668677.47	0.01	0.02	0.6
2D	252.25	431.55	0.0002	0.0004	0.006	0.02	8635809.5	14774249.1	0.01	0.02	0.76
2E	297.9	419.24	0.0001	0.0003	0.006	0.02	9561242.95	13455782.31	0.01	0.01	1.23
3B	419.69	583.81	0.0003	0.0004	0.006	0.02	13908418.78	19347137.07	0.01	0.02	1.07
3C	271.59	420.1	0.0003	0.0004	0.006	0.02	9297901.22	14381186.48	0.02	0.02	0.73
3D	206.59	469.24	0.0002	0.0004	0.006	0.02	6630773.85	15060672.44	0.01	0.02	0.7
3E	426.24	727.96	0.0004	0.0006	0.006	0.02	13680594.67	23364498.43	0.02	0.03	0.85
4B	557.73	833.34	0.0003	0.0004	0.006	0.02	18483065.68	27616648	0.02	0.02	1.37
4C	530.5	864.7	0.0003	0.0004	0.006	0.02	17580688.24	28655633.4	0.01	0.02	1.33
4D	408.5	579.15	0.0003	0.0003	0.006	0.02	13537424.52	19192713.27	0.01	0.02	1.24
4E	431.25	694.62	0.0002	0.0005	0.006	0.02	14763694.44	23780279.6	0.01	0.03	0.57

Table 11. Continued

Sample	Strength 1 (y <sub>0</sub> ) [N]	Strength 2 (y <sub>1</sub> ) [N]	Stroke 1 (x <sub>0</sub> ) [m]	Stroke 2 (x <sub>1</sub> ) [m]	Diameter (m)	Length (m)	Stress (y <sub>0</sub> ) [Pa]	Stress (y <sub>1</sub> ) [Pa]	Strain (x <sub>0</sub> )	Strain (x <sub>1</sub> )	Modulus [GPa]
5B	212.39	361.37	0.0002	0.0003	0.006	0.02	7118666.63	12112081.96	0.01	0.02	0.85
5C	227.24	325.22	0.0002	0.0003	0.006	0.02	7744110.08	11083134.29	0.01	0.02	0.68
5D	346.86	622.21	0.0003	0.0004	0.006	0.02	11494694.35	20619640.5	0.01	0.02	1.08
5E	315.74	476.72	0.0003	0.0004	0.006	0.02	10809470.09	16320487.78	0.02	0.02	0.89
6A	378.25	506.22	0.0003	0.0003	0.006	0.02	12739618.05	17049835.11	0.01	0.02	1.24
6B	171.94	268.61	0.0002	0.0002	0.006	0.02	5742390.08	8970873.07	0.01	0.01	0.92
6C	228.02	485.69	0.0002	0.0003	0.006	0.02	7677510.19	16352959.16	0.01	0.02	1.25
6D	258.75	537.86	0.0001	0.0003	0.006	0.02	8489893.62	17647569.29	0.01	0.02	1.24
6E	286.15	418.58	0.0002	0.0003	0.006	0.02	9659788.46	14130274.14	0.01	0.02	1.0
7B	250.27	490.41	0.0002	0.0004	0.006	0.02	8219526.27	16106199.44	0.01	0.02	0.87
7C	278.55	393.82	0.0003	0.0004	0.006	0.02	9201267.47	13009142.18	0.02	0.02	0.75
7D	287.28	455.91	0.0003	0.0004	0.006	0.02	10031302.4	15919743.3	0.02	0.02	1.05

Table 12. *Compressive Modulus Mean and Standard Deviation*

Group	Average Modulus [GPa]	Standard Deviation
1	0.96	0.13
2	0.86	0.33
3	0.84	0.17
4	1.13	0.38
5	0.88	0.16
6	1.13	0.16
7	0.89	0.15

**Compressive Modulus Summary.** The 0.5% 3.5 Rods did not show a statistically significant change in compressive modulus as compared to both the control and the other groups. This could be due to an outlier present in that group which affected the standard deviation. The 0.5% MSNs showed a similar outlier. The 1.0% MSNs and 0.5% 7.5 Rods exhibited significantly different moduli.

## **Resilience**

The resilience of a material is a measure of the ability of the material to absorb energy while it is deforming elastically, then release that energy upon unloading. It is calculated using the equation below (Eq. 4):

$$U_r = \frac{\sigma^2}{2E} \quad \text{Eq. 4}$$

where  $U_r$  equals the modulus of resilience,  $\sigma$  equals the yield stress, determined by inspection in our case, and  $E$  equals the compressive modulus. For the proposed application of this material, the functionality of the material could be said to be compromised once that material has yielded. Functional toughness describes the amount of energy the material can absorb until it is no longer functional. In our case, functional toughness and resilience are synonymous, but we will use the term ‘resilience’ due to its prevalence in the field. The graphical comparison is shown in Figure 17. The individual resiliences of each sample are included in Table 13 and the group mean and standard deviations follow in Table 14.

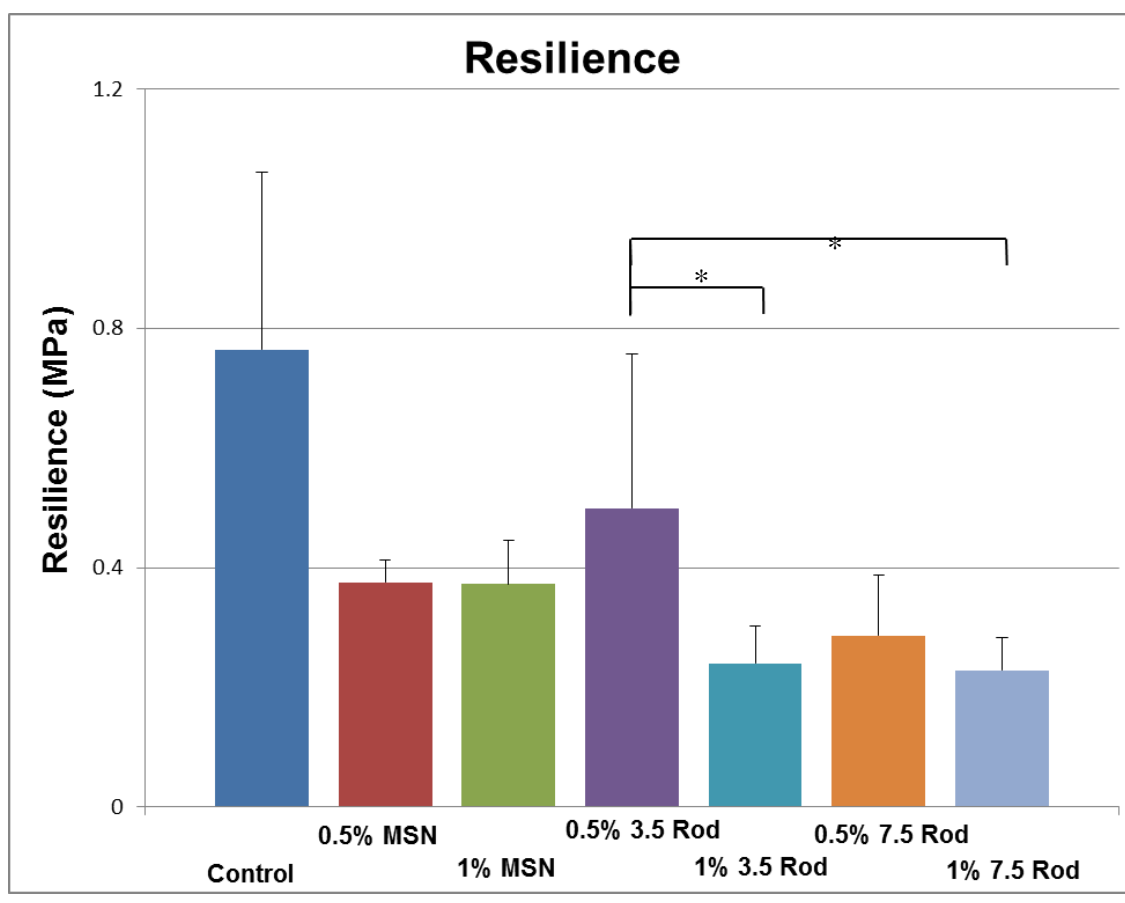


Figure 17. Resilience comparison across the different formulations

Table 13. *Individual Sample Resilience Data*

Sample	Traditional Resilience [Pa]
1E	554215.36
1F	974125.06
2C	333959.15
2D	400066.26
2E	394078.47
3B	411677.82
3C	328591.74
3D	298189.36
3E	453911.36
4B	172111.84
4C	544449.98
4D	478757.50
4E	800882.97
5B	191272.05
5C	180455.41
5D	280804.14
5E	306464.46
6A	180937.17
6B	170751.45
6C	377183.74
6D	348748.24



Table 13. Continued

Sample	Traditional Resilience [Pa]
6E	355349.08
7B	167831.33
7C	272168.03
7D	245010.32

Table 14. *Resilience Mean and Standard Deviation*

Group	Mean Resilience (MPa)	Standard Deviation
1	0.76	0.3
2	0.38	0.04
3	0.37	0.07
4	0.5	0.26
5	0.24	0.06
6	0.29	0.1
7	0.23	0.05

**Resilience summary.** The 0.5% 3.5 Rods show a statistically significant change in resilience as compared to both the control and the other groups.

## Influence of Material Defects on Mechanical Properties

The results of the compression testing did not show the doping having a strong effect on the mechanical properties of the polymers. It was suspected that this lack of trending was due to manufacturing defects present in the samples. The effect of different types of defects on the ultimate strength, yield point, resilience and compressive modulus of the samples was investigated, and the individual studies can be seen in Figures 18 through 29. Each point represents one sample and the blue shape represents a sample with just bubbles present, a red shape with just cracks present and an orange shape for both cracks and bubbles.

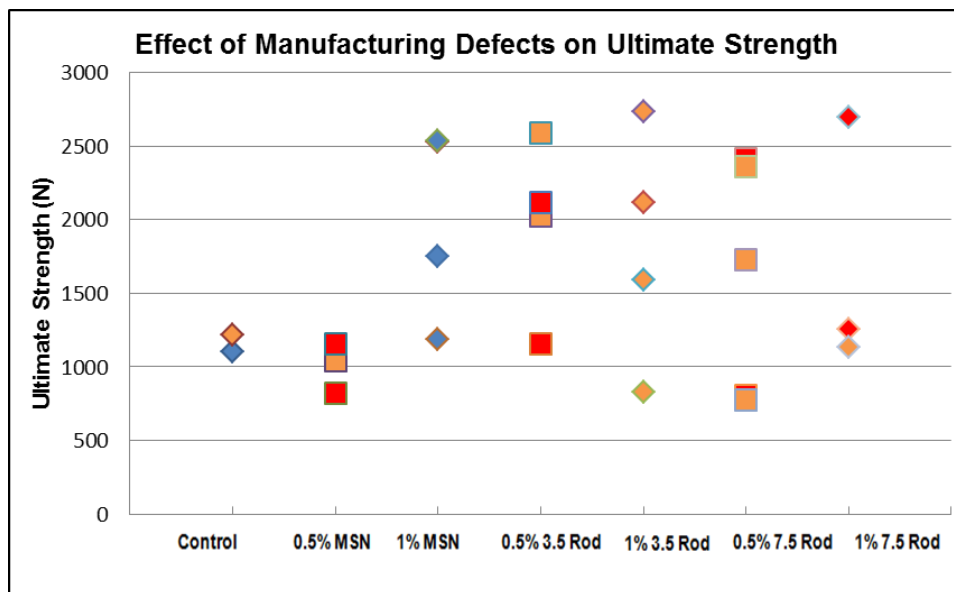


Figure 18. Manufacturing defects' influence on ultimate strength where blue points had bubbles only, red points had cracks only and orange points had both.

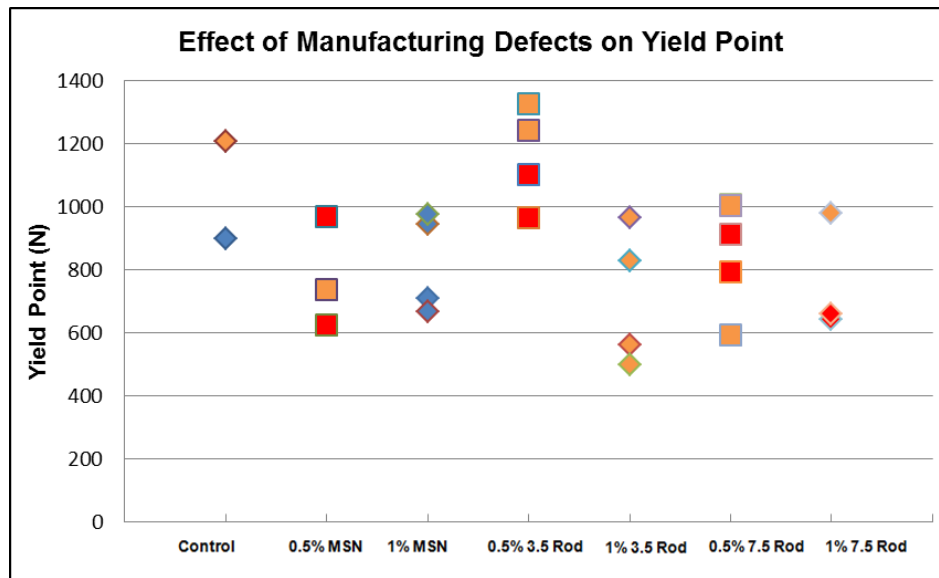


Figure 19. Manufacturing defects' influence on yield point where blue points had bubbles only, red points had cracks only and orange points had both.

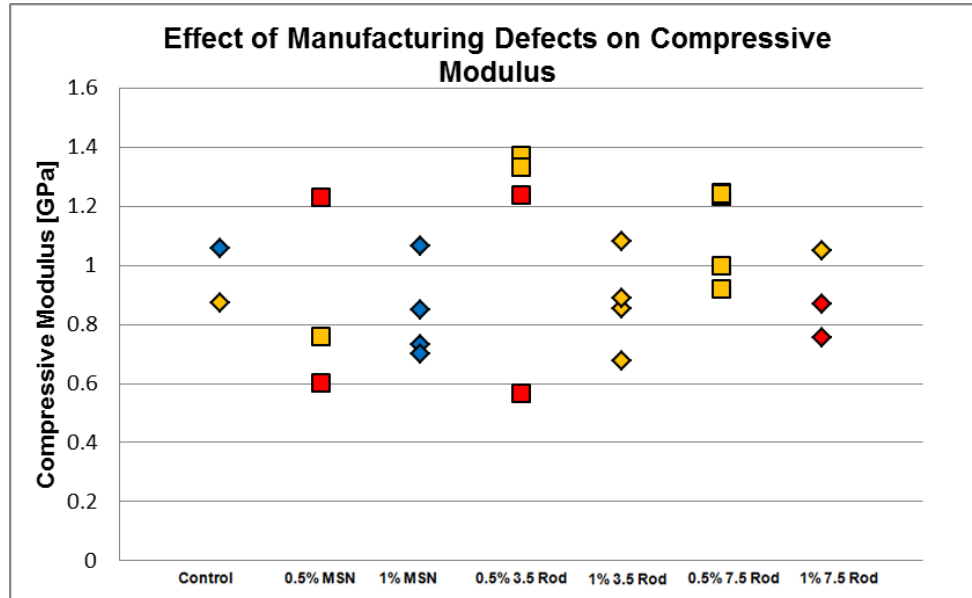


Figure 20. Manufacturing defects' influence on compressive modulus. Blue points had bubbles only, red points had cracks only and orange points had both.

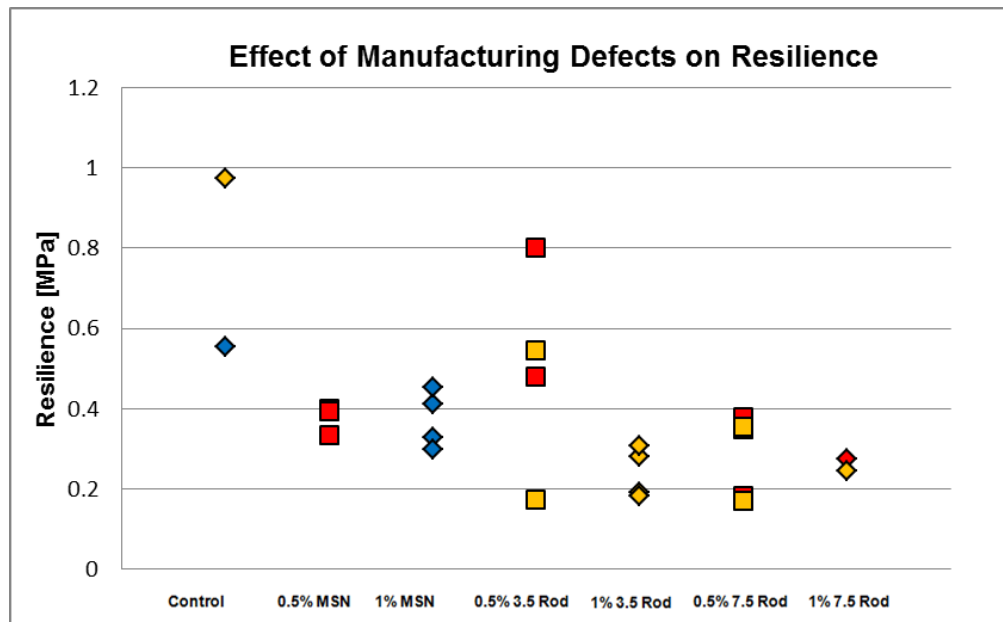


Figure 21. Manufacturing defects' influence on resilience. Blue points had bubbles only, red points had cracks only and orange points had both.

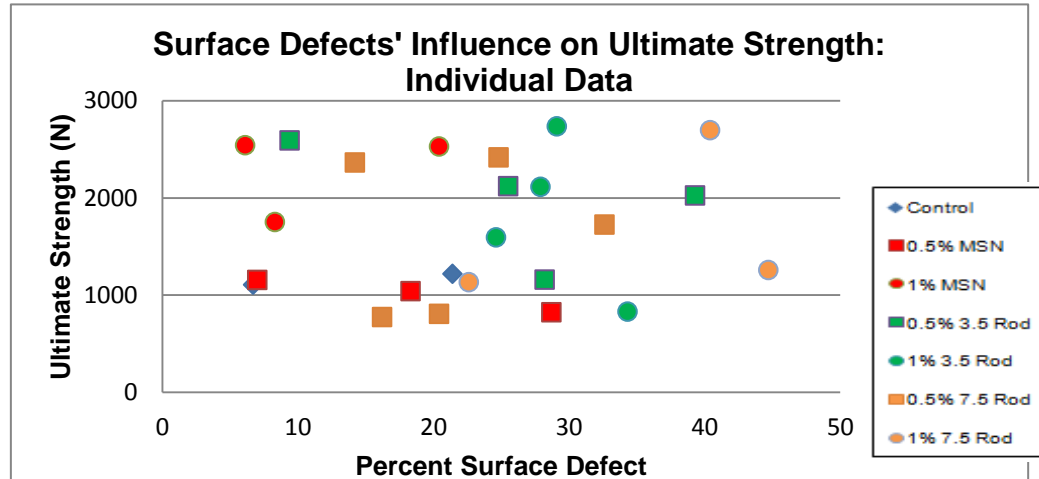


Figure 22. The influence of percent surface defect on the ultimate strength of the individual samples of the formulations.

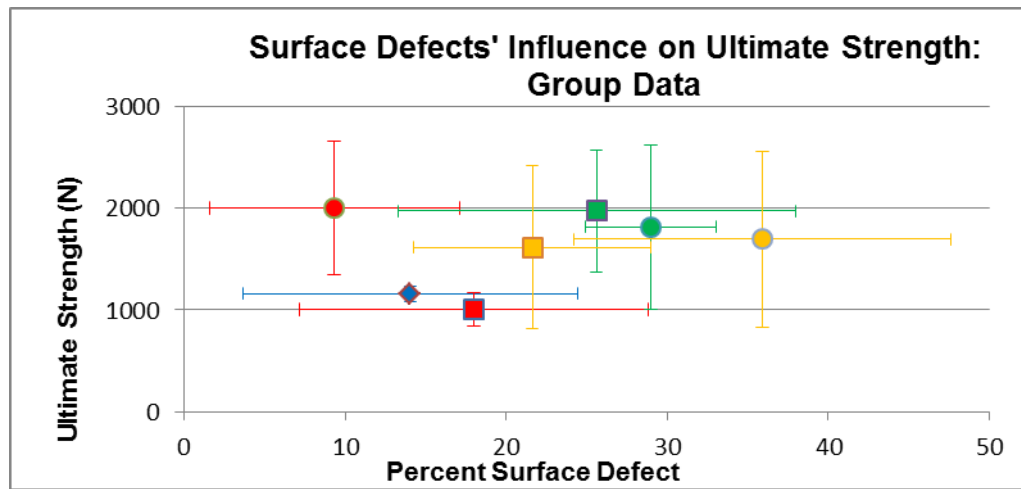


Figure 23. The influence of percent surface defect on the ultimate strength of the averaged formulation groups.

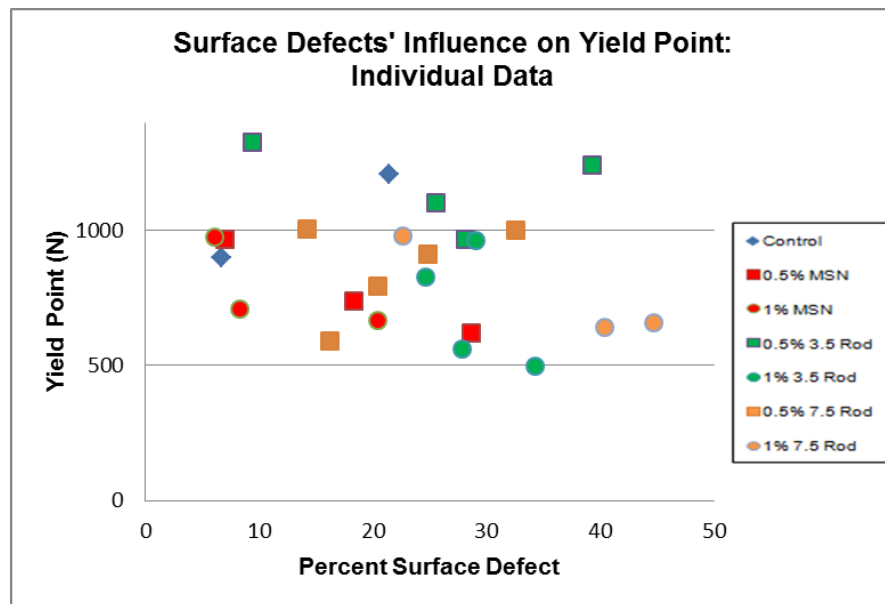


Figure 24. The influence of percent surface defect on the yield point of the individual samples of the formulations.

The percent surface defect as determined by our quantification test was then compared to the ultimate strength and yield points to see if any trends emerged. The same was done with the density to see if this factor had any effect on ultimate strength or yield point. This can be seen in Figures 25 through 29, where the legend in the individual graph serves for the group data graph.

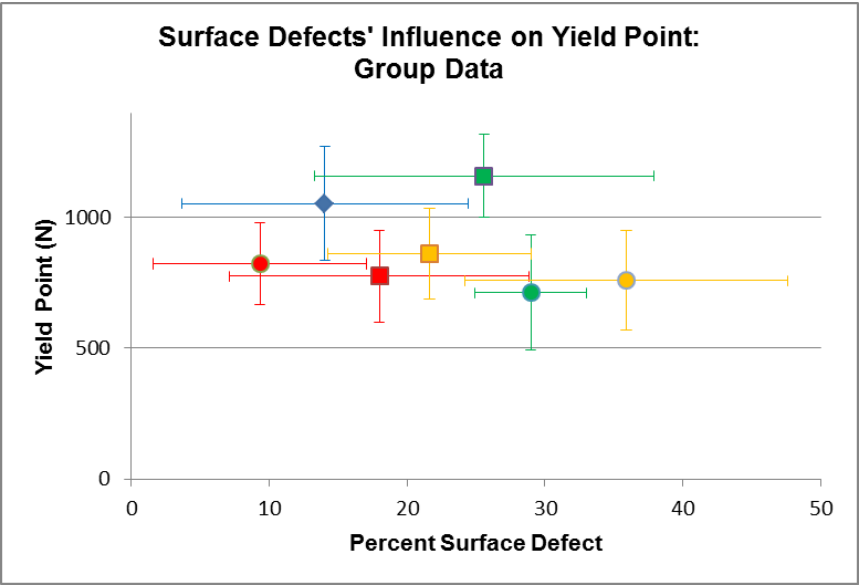


Figure 25. The influence of percent surface defect on the yield point of the averaged formulation groups.

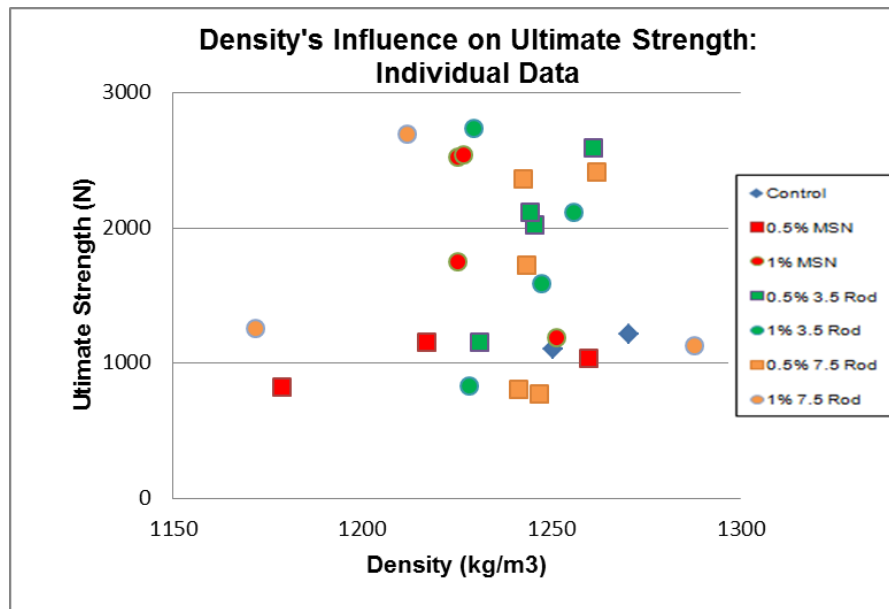


Figure 26. The influence of density on the yield point of the individual samples of the formulations.

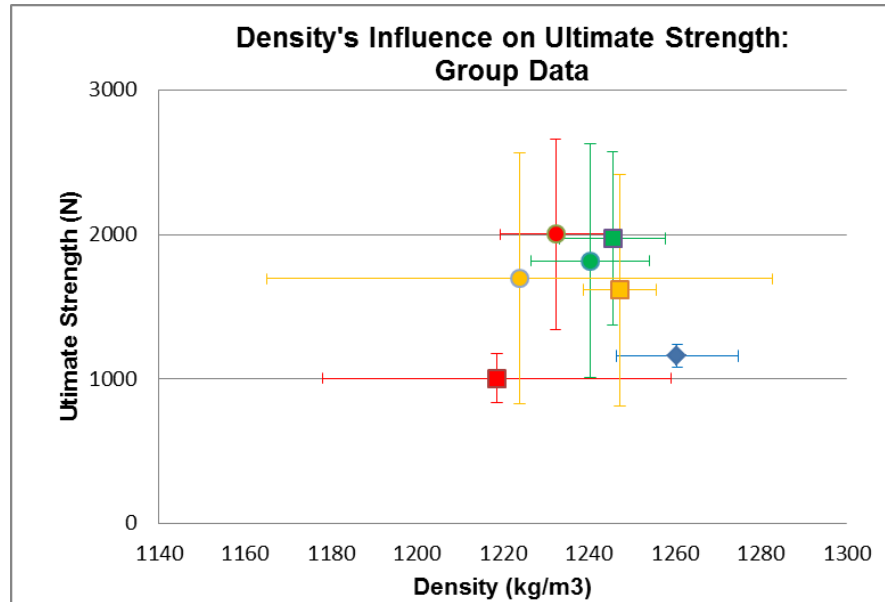


Figure 27. The influence of density on the ultimate strength of the averaged formulation groups.

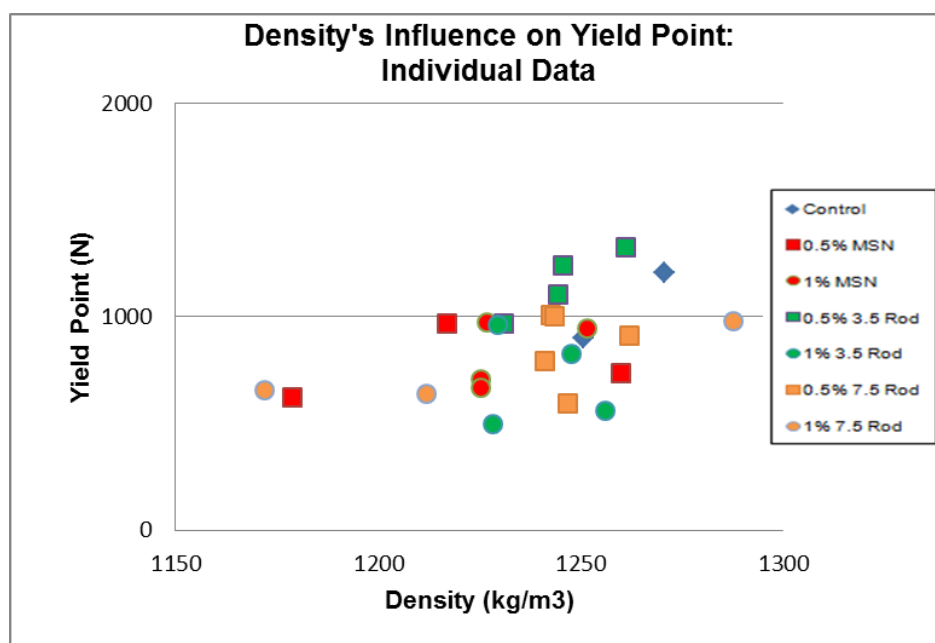


Figure 28. The influence of density on the yield point of the individual samples of the formulations.

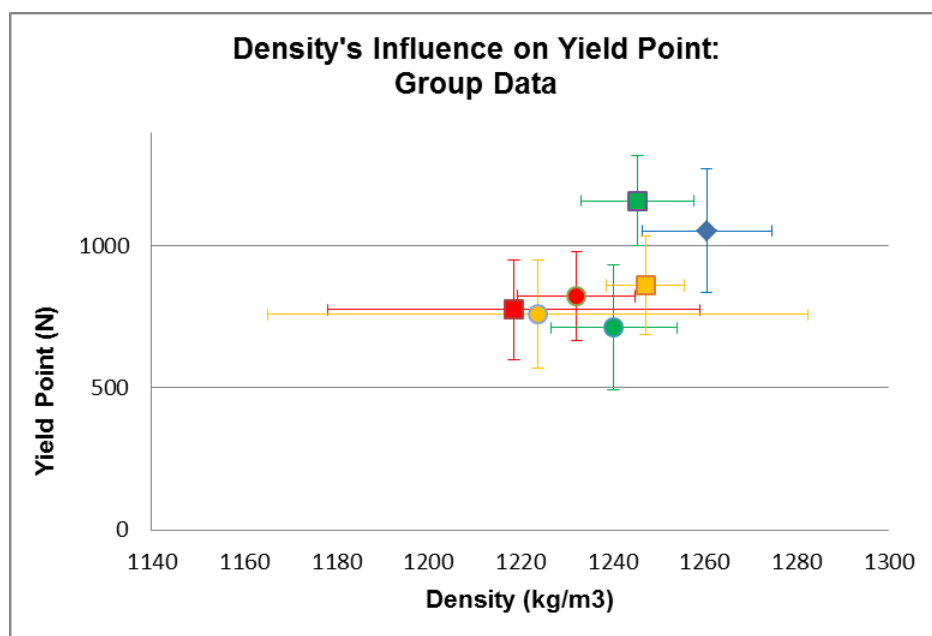


Figure 29. The influence of density on the yield point of the averaged formulation groups.



The percentage of the surface of the samples affected by defects were quantified by first coating the samples in ink, then rolling them across a white sheet of paper. Images taken of the result of this ink smear were analyzed via a Matlab code written by the author that quantifies black versus white pixels within the area of interest. A sample free of defects would have a completely black signature, whereas a sample with many defects would have a great deal of white. The results were used to produce the above graphs. The code can be seen below.

```
clc; clear all; close all;

%Read the picture in and make the array doubles
image_name=input('Which file would you like to analyze? ','s');
original=imread(image_name,'jpeg');

% original=imread('Test1 ImageJ.jpg','jpeg');
original=double(original);

%Denote the border width (in pixels) and find the size of the image
[amt_totalx, amt_totaly, amt_totalz]=size(original);
original_bool=original;

%Divide up the RGB triplet, arbitrarily choose to work with red
im_red=original_bool(:,:,1);
im_red_bool=im_red;

%Make the parts with red above the background threshold one, others zero
for a=1:amt_totalx
    for b=1:amt_totaly
        if im_red_bool(a,b)>=100
            im_red_bool(a,b)=1;
        else
            im_red_bool(a,b)=0;
        end
    end
end
end
```

```

a=0;
b=0;
red_total=0;

%Count the total number of red pixels above the threshold
for a=1:amt_totalx
    for b=1:amt_totaly
        red_total=red_total+im_red_bool(a,b);
    end
end

%Calculate total area of polymer
area_total=amt_totalx*amt_totaly;

%Calculate percent area of overlap
defect=red_total/area_total*100;

%Print results
fprintf('\r\n%s\r\n%s\r\n\r\n%s%3.1f\r\n','Image  Analysis',image_name,'The
percent area of the defect is: ',defect);

```

## Mode of Failure

Video of the compressive tests was used to analyze the failure modes of the different groups. Using this footage, we were able to identify points on the load deformation curves which correspond to fragments breaking off of the sample. An example graph can be seen in Figure 30. The full collection of these graphs for each individual sample can be found in Appendix III.

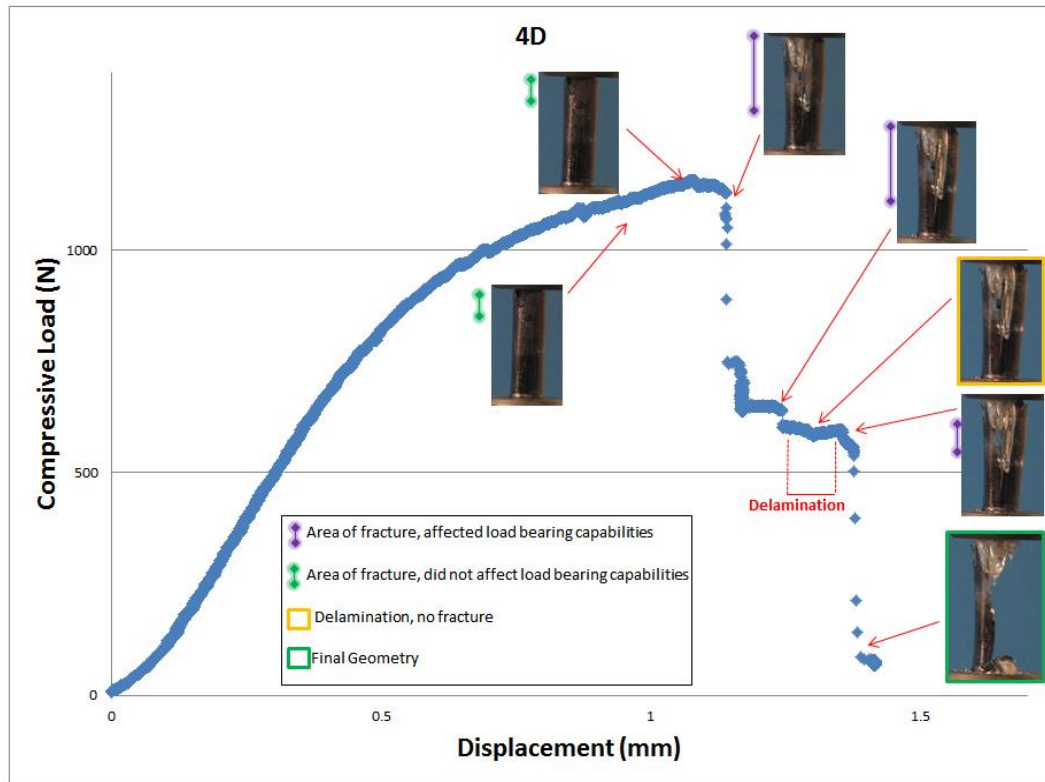


Figure 30. Example graph depicting the failure mode analysis study.

Using this information, we studied the effect of the nanoparticles on the fracturing tendencies of the PPF, specifically focusing on the number and size of the fragments produced. Small fragments are quantified as those  $<25\%$  of the total length at the time of fracture, medium fragments are  $25\% < x < 50\%$ , large fragments are  $50\% < x < 75\%$  and extra-large fragments are defined as those  $<75\%$  of the total length at fracture, but were typically seen to be 100%. The number of each of these size fragments were counted per sample, then averaged by groups with standard deviations. We looked at the total number of fragments of any size, and that information can be found in Figure 31.

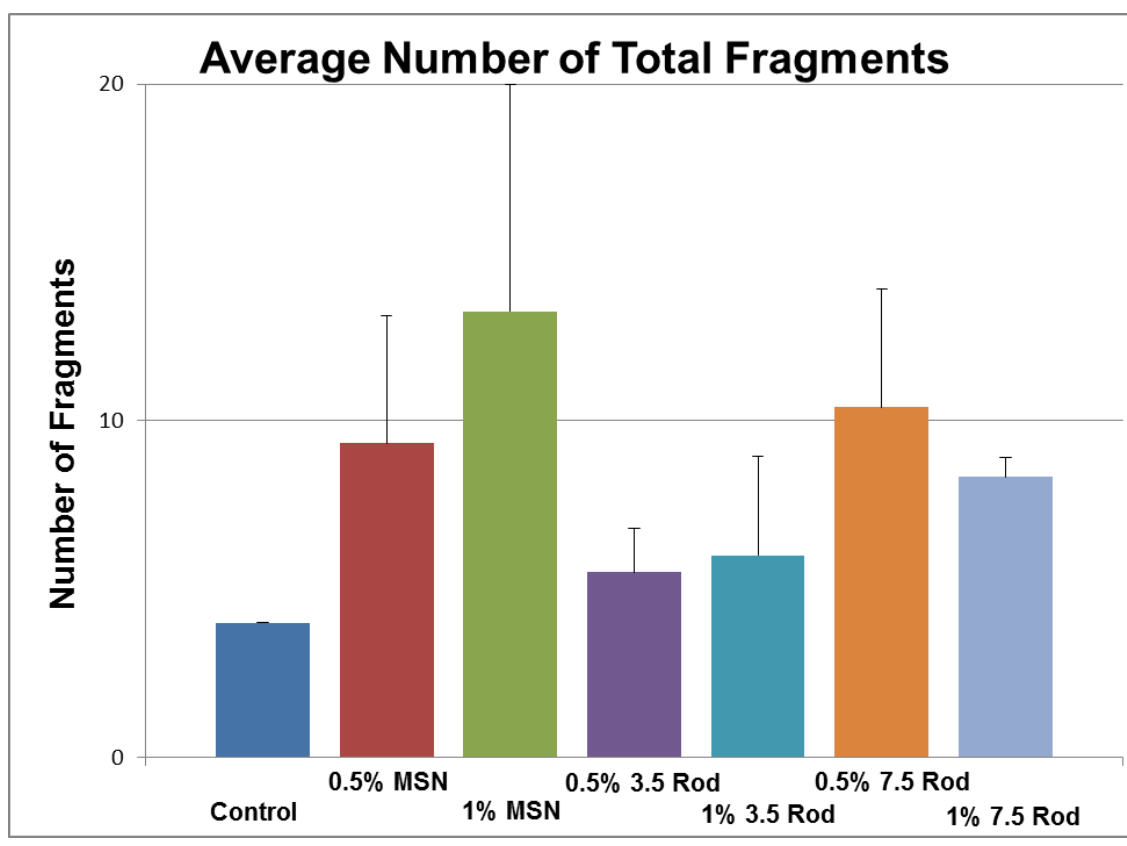


Figure 31. Comparison of the total number of fragments per group

The number of fragments was then broken down into size of fragments seen per group. This information is presented both as a comprehensive graph in Figure 32 and broken down by fragment size in Figures 33 through 36. Statistically significant data is denoted by an asterisk, with  $p < 0.05$ .

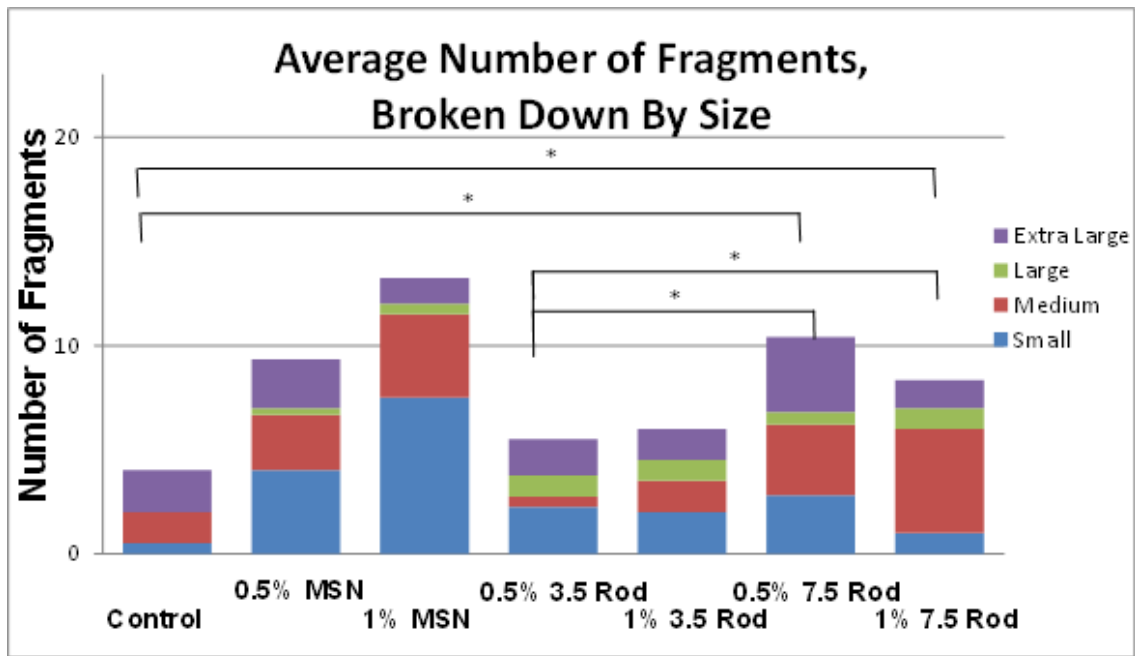


Figure 32. Comparison of the total number of fragments, broken down by size.

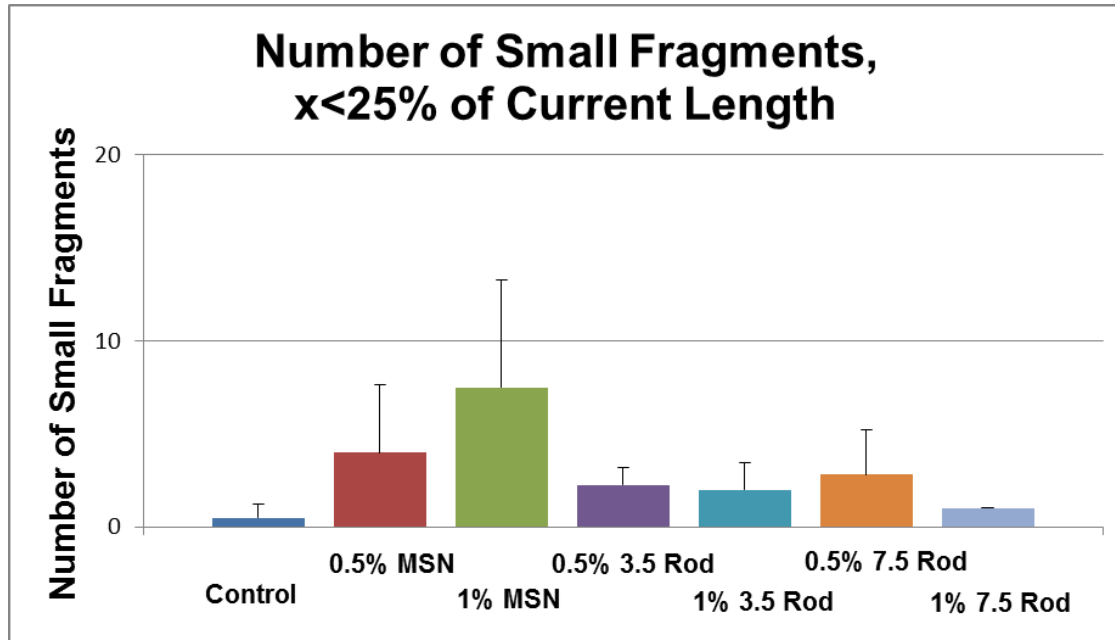


Figure 33. Comparison of the total number of small fragments

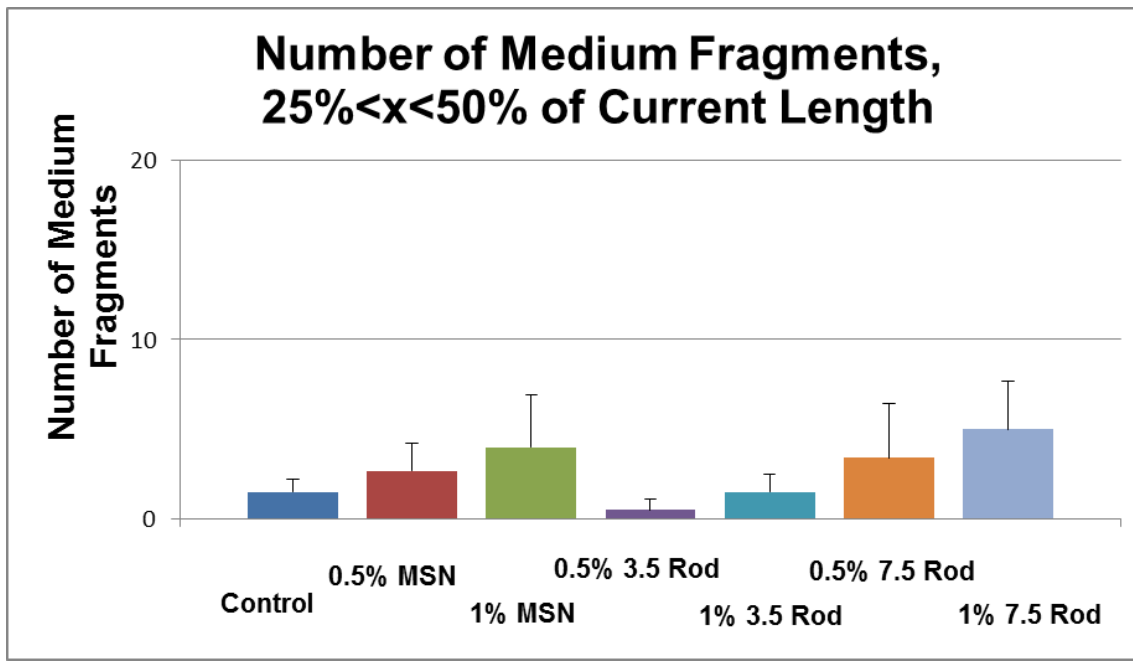


Figure 34. Comparison of the total number of medium fragments

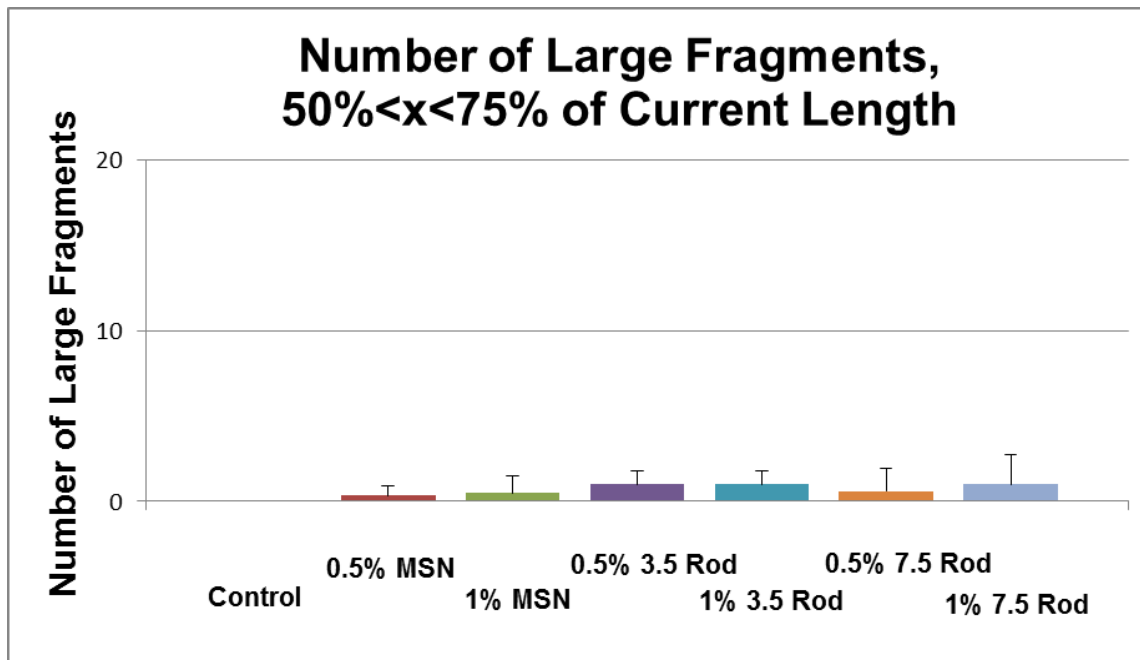


Figure 35. Comparison of the total number of large fragments

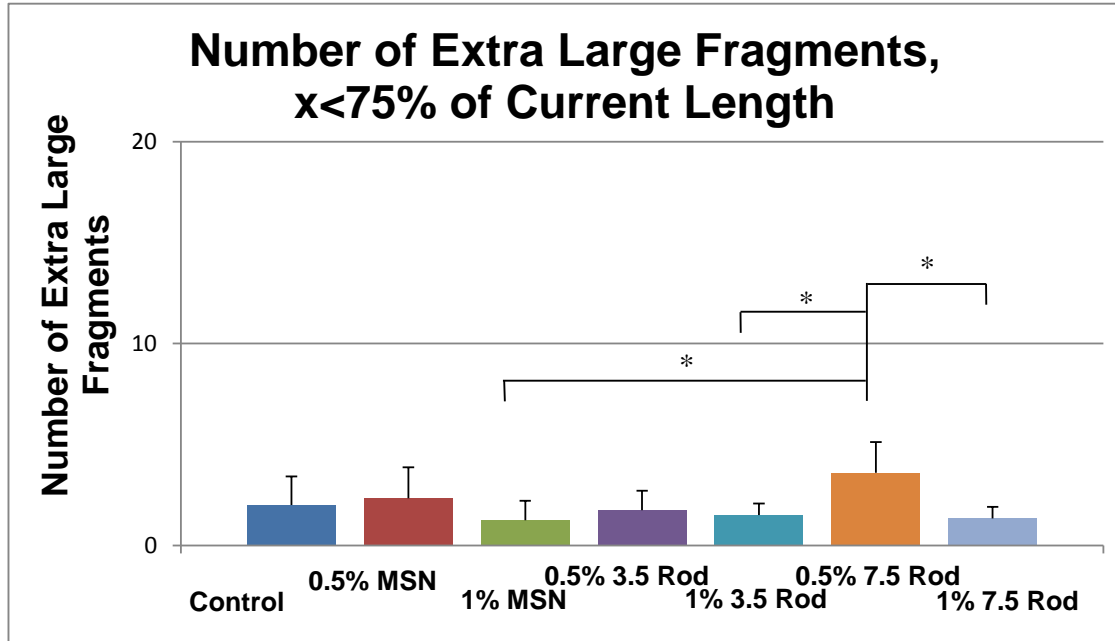


Figure 36. Comparison of the total number of extra-large fragments.

The group mean and standard deviation data in Table 15, with the small, medium, large and extra-large data following in Tables 16 through 19.

Table 15. *Fragment Study Mean and Standard Deviation*

Group	Average Number of Fragments	Standard Deviation
1	4	0
2	9.33	3.79
3	13.25	6.75
4	5.5	1.29
5	6	2.94
6	10.4	3.51
7	8.33	0.58

Table 16. *Small Fragment Mean and Standard Deviation*

Group	Average Number of Small Fragments	Standard Deviation
1	0.5	0.71
2	4	3.61
3	7.5	5.74
4	2.25	0.96
5	2	1.41
6	2.8	2.39
7	1	0



Table 17. *Medium Fragment Mean and Standard Deviation*

Group	Average Number of Medium Fragments	Standard Deviation
1	1.5	0.71
2	2.67	1.53
3	4	2.94
4	0.5	0.58
5	1.5	1
6	3.4	3.05
7	5	2.65

Table 18. *Large Fragment Mean and Standard Deviation*

Group	Average Number of Large Fragments	Standard Deviation
1	0	0
2	0.33	0.58
3	0.5	1
4	1	0.82
5	1	0.82
6	0.6	1.34
7	1	1.73

Table 19. *Extra-Large Fragment Mean and Standard Deviation*

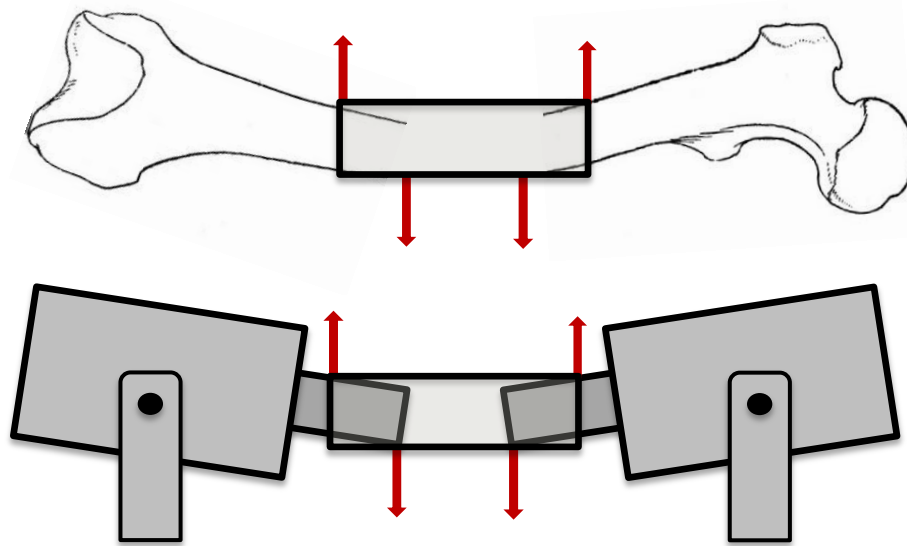
Group	Average Number of Extra-Large Fragments	Standard Deviation
1	2	1.41
2	2.33	1.53
3	1.25	0.96
4	1.75	0.96
5	1.5	0.58
6	3.6	1.52
7	1.33	0.58

**Fragment study summary.** The 0.5% 3.5 Rods, 0.5% 7.5 Rods and 1.0% 7.5 Rods show a statistically significant change in the total number of fragments as compared to both the control and the other groups. The 0.5% 7.5 Rods appear to have the most noticeable effect on the fragmentation of the sample, in that they produce a significantly higher number of extra-large fragments as compared to other reinforcement techniques.

### **Bone Cuff Characterization**

Evidence from previous animal studies suggests that a bending load sufficient to induce failure in the shell device is generated as the animal moves from a supine position to a standing position. When considering bending along the major axis of the bone-device construct it is apparent that two possibilities exist. The first case results when the bone segments experience moments such that a rotation in opposing directions is induced, i.e., the

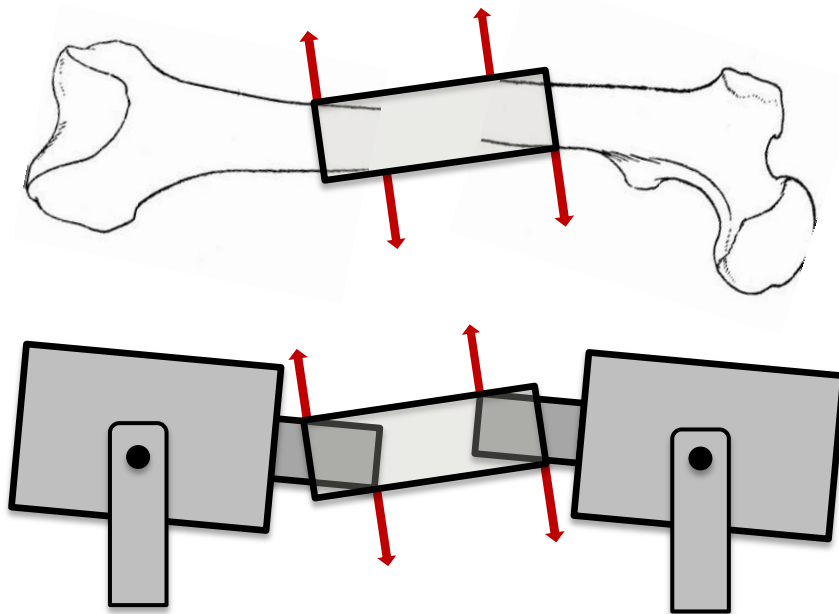
bone segment at one end of the device rotates in one direction (about an axis orthogonal to the long axis) and the bone segment at the other end of the device tends to rotate in the opposite direction. This scenario is similar to a classic four-point bend. Figure 37 illustrates this case and the load frame fixtures employed to model this potential mode of failure.



---

*Figure 37. Classic four-point bend.*

The second possibility occurs when moments are applied that cause the bone segments at each end of the device to rotate in the same direction. This also results in a four-point load that hereafter we will refer to as a Modified Four-Point Bend. Figure 38 illustrates this case and the orientation of the load frame fixtures in modeling this potential mode of failure.



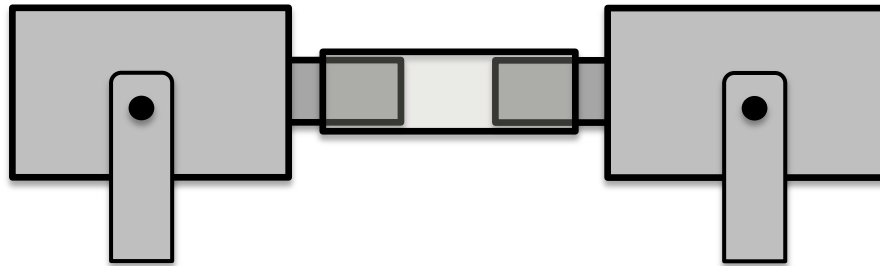
---

*Figure 38. Modified four-point bend.*

### **Mechanical Testing Protocol**

Prior to mechanical testing the dimensions of each shell device were measured and recorded. The devices were labeled so that the orientation during testing could be recorded for post-test analysis and inspection. In addition to labeling the ends, marks were made every 90 degrees about the circumference. The wall thickness was measured and recorded at these marks. The volume of each shell was determined by placing the device graduated cylinder and measuring the volume of water displaced. The mass was determined using an electronic balance and the density calculated and recorded.

For mechanical testing, the device was mounted to the fixtures as illustrated above. The fixture pins that are inserted in the shell are adjustable and can be retracted or extended from the fixture. The pins were oriented such that they extended into the shell one third of the length of the shell (Figure 39). For the classic four-point bend, the load frame prongs were oriented such that the centers of the prongs were both outside the fixture pivot point (Figure 40 - Left). For the modified four-point bend the load frame prongs were oriented such that the center of one prong was outside one fixture pivot point and the center of the other prong was inside the other fixture pivot point (Figure 40 - Right).



---

*Figure 39.* Initial setup for mechanical testing.

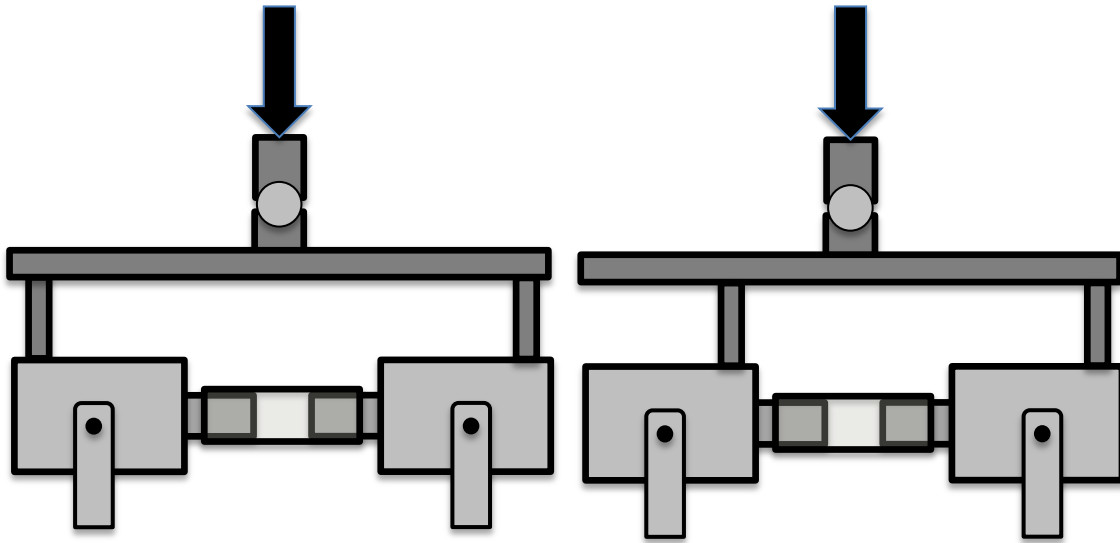


*Figure 40.* Left – Load configuration for the classic four-point bend. Right – Load configuration for the modified four-point bend.

Using a Test Resources 830 12kN Axial-Torsion load frame in stroke control, loads were applied at using a stroke rate of 0.5 mm/sec. The failure criteria were set to terminate the test with a 70% drop in the applied load. Load and stroke data were acquired at a sampling rate of 100 Hz. Upon completion of the test, data was exported to excel for processing and analysis.

As illustrated above, load was applied to the fixtures, which in turn induced a bending moment on the shell. All moment arms were measured and the forces on the shell were calculated. There are essentially four locations in the shell where forces are applied by the bone segments, or fixture pins, as they rotate. These are labeled from left to right, A, B, C, and D accordingly (Figure 41).

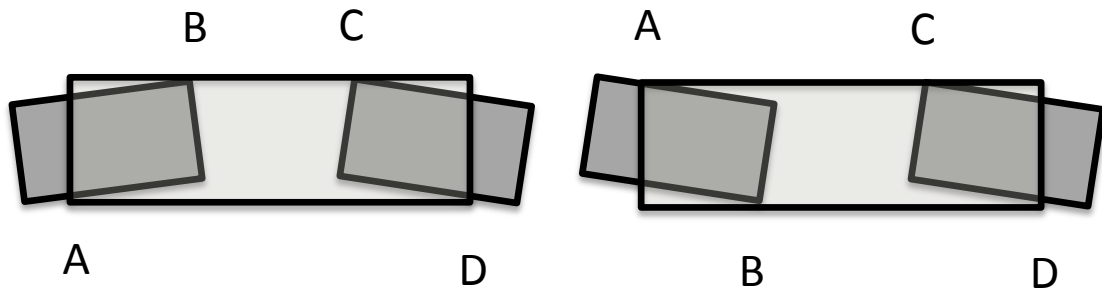


*Figure 41.* Locations of force application within the shell. Left – Classic four-point bend. Right – Modified four-point bend.

## Results

We have tested five samples; three with the classic four-point bend and two with the modified four-point bend. Visual inspection revealed the samples to have an irregular bore and a wall thickness that varied considerably about the circumference of the shells. The minimum and maximum wall thicknesses at each end of sample were recorded and are given in Table 20.

Table 20. *Shell Thickness, Which Varied by Over 2mm in Some Cases.*

Sample ID	End (left or right)	Minimum Thickness (mm)	Maximum Thickness (mm)	Difference (mm)
I	Left	4.3	6.55	2.25
	Right	4.24	5.7	1.46
II	Left	4.16	6.42	2.26
	Right	4.44	6.43	1.99
III	Left	4.56	6.19	1.63
	Right	4.07	5.49	1.42
IV	Left	3.77	5.27	1.5
	Right	3.57	5.13	1.56
V	Left	4.15	5.42	1.27
	Right	3.95	5.21	1.26

Based on the loading symmetry and Newton's 3<sup>rd</sup> Law, the loads at A, B, C, and D for the classic four-point scenario are assumed to be the same. In the modified four-point scenario the loads are also symmetrically applied however, the loading distribution results in a different symmetry such that the loads at A and D are the same, as are the loads at B and C. The loads at the points of interest upon failure are given in Table 21. In reviewing the video of the tests it was determined that samples I and IV were subjected to unintended compressive loads due to insufficient clearance between the sample and the test fixtures



throughout the bending cycle (Figure 42). This was corrected for future tests and these samples are thus denoted accordingly.

Table 21. *Loads Applied to the Shell at Failure*

Test Scenario	Sample ID	Load A and D (lbf)	Load B and C (lbf)
Classic 4pt	II	1063	1063
Classic 4pt	IV	313*	313*
Classic 4pt	V	696	696
Modified 4pt	I	91*	258*
Modified 4pt	III	173	506

\*Samples I and IV were subjected to unintended compressive loads due to insufficient clearance between the samples and the fixtures throughout the bending cycle.

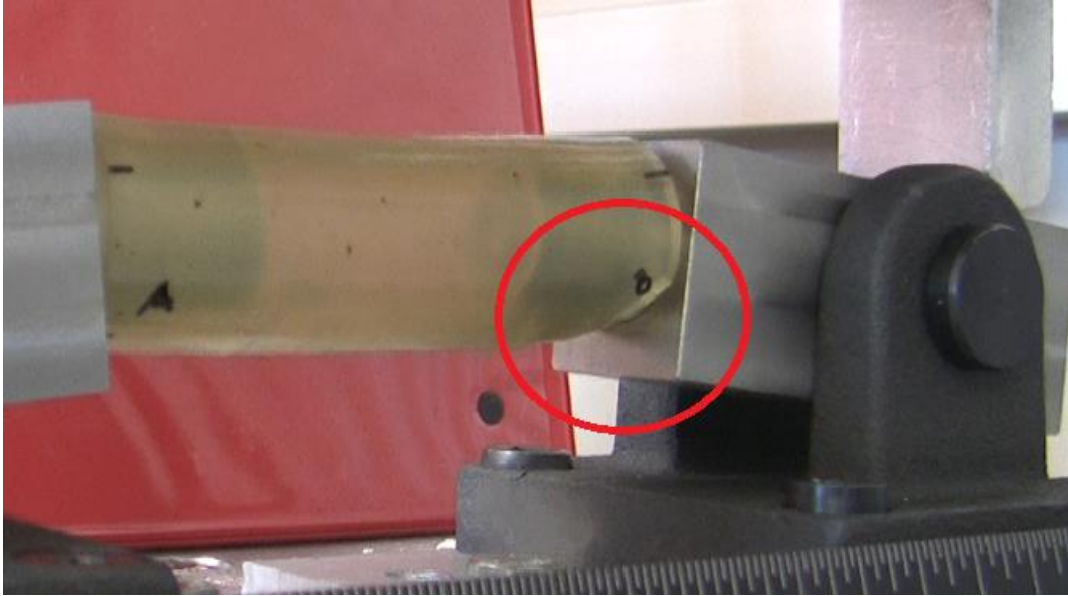


*Figure 42.* Samples I and IV were subjected to unintended compressive loads due to insufficient clearance between the device and fixture throughout the range of the bending cycle. This was corrected for future tests.

Following the tests, video of the mechanical testing was reviewed to determine the location and character of the failure. In reviewing the samples subjected to classic four-point bending, it was observed that sample II first failed at point B, about halfway between the thinnest and thickest regions of the shell wall with an applied load of over 1060 lbf. The failure propagated from there along the length of the shell until the entire device shattered catastrophically (Figure 43).

Video review of sample V revealed that points A and B seemed to fail simultaneously as that end of the device completely shattered when subjected to a load of just under 700 lbf. The other end of the device also failed and though it did not shatter, a crack originating from this

end propagated the length of the device. We were not able to tell from the video whether or not the thin or thick region of the wall failed first (Figure 44).

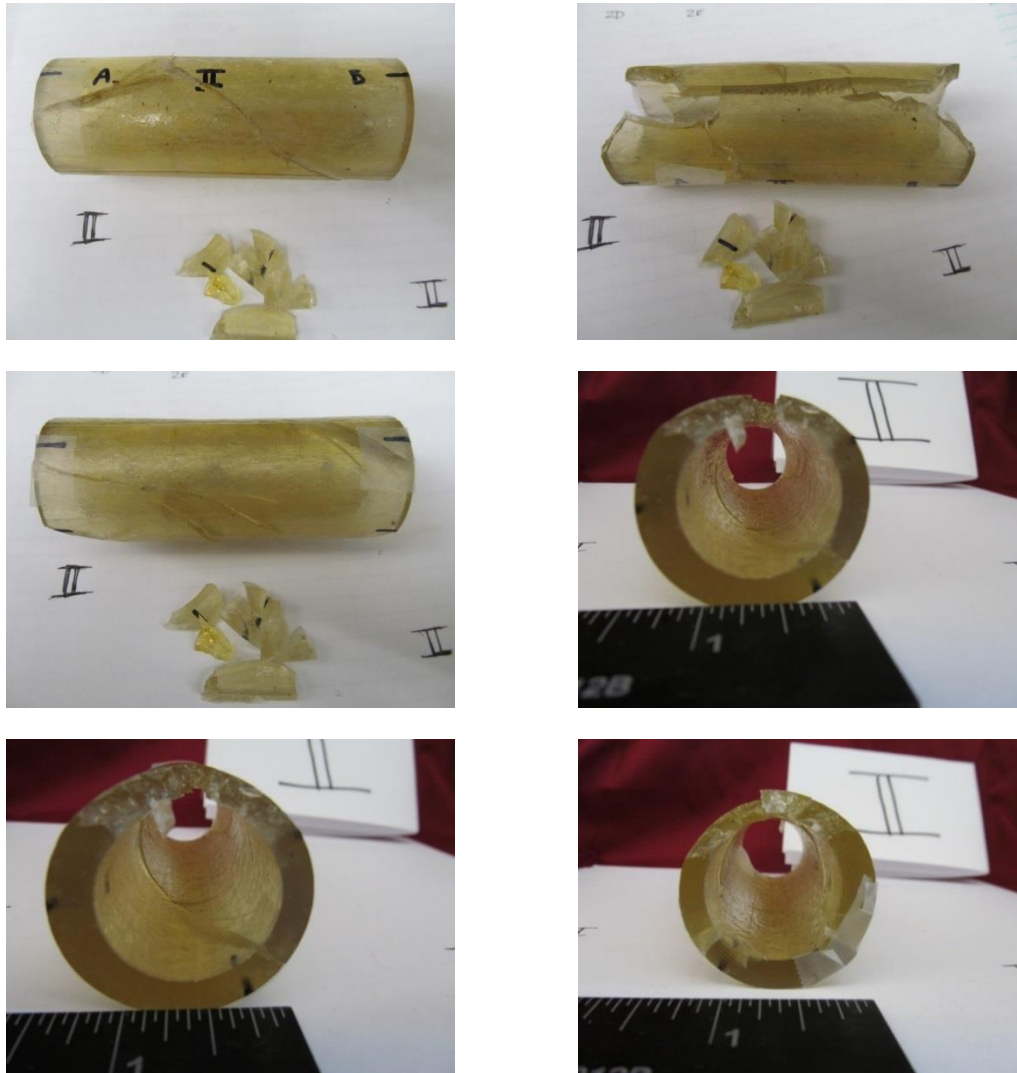


Figure 43. Sample II.

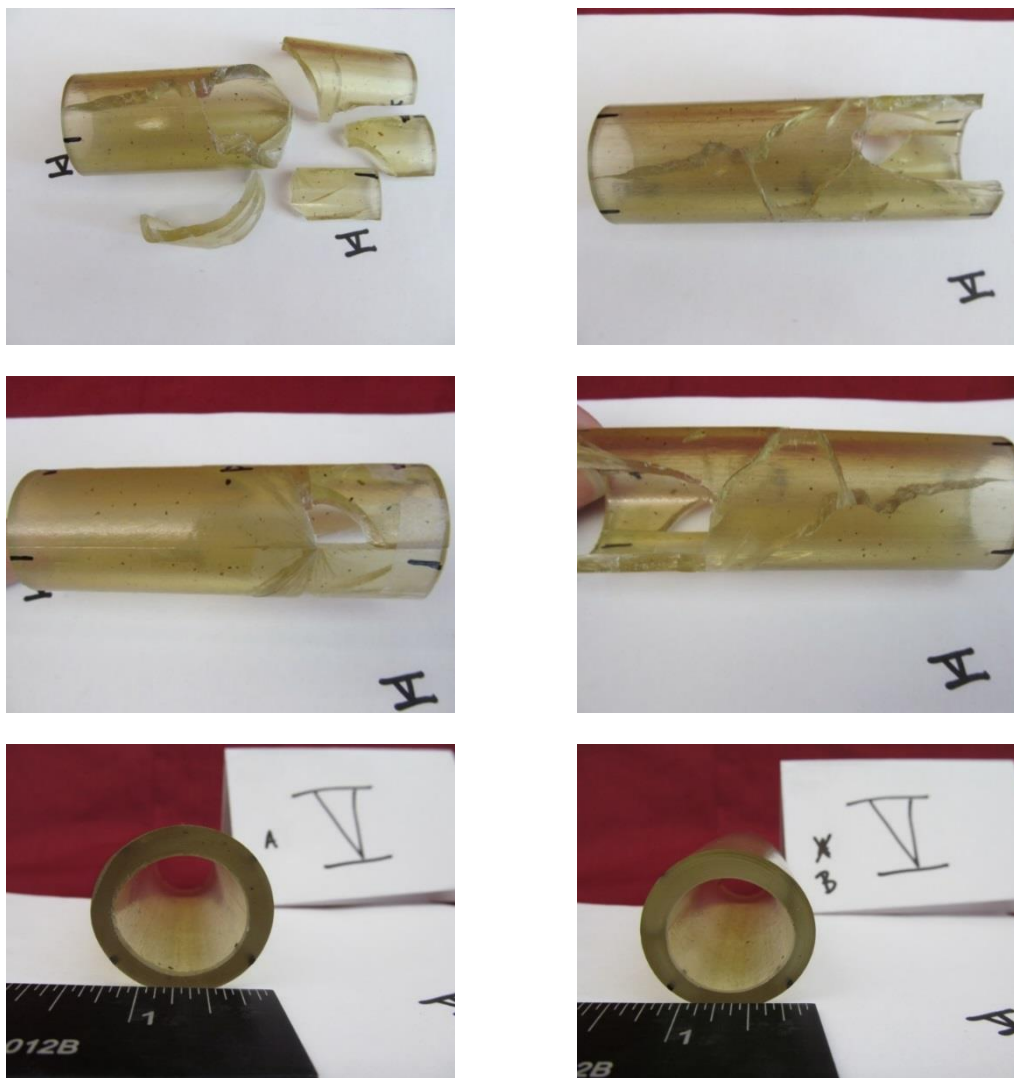


Figure 44. Sample V.

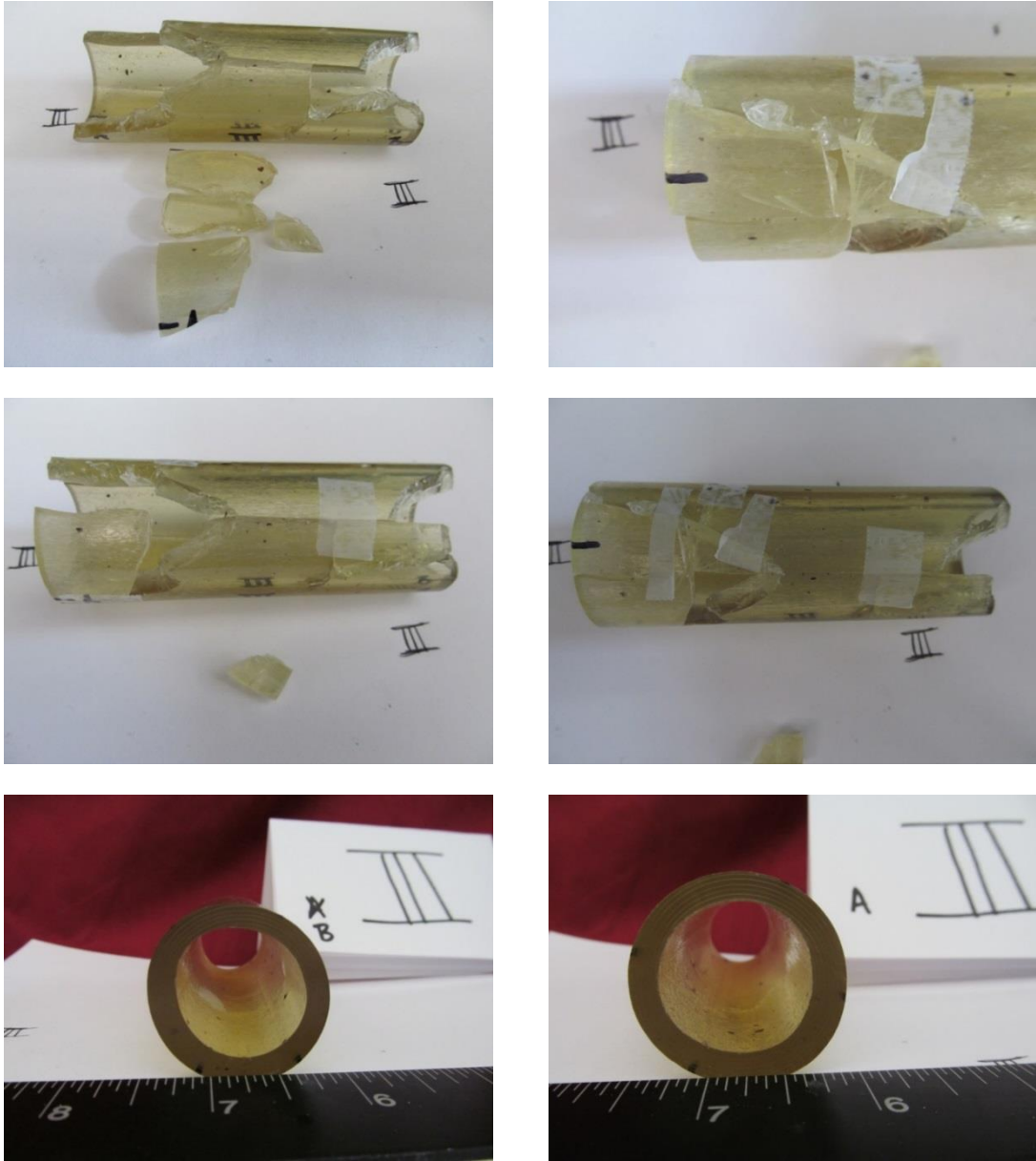
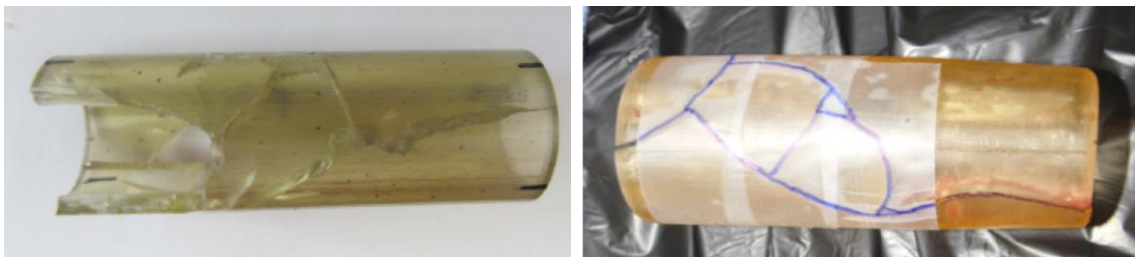


Figure 45. Sample III.

Sample III was subjected to the modified four-point bend and failed when subjected to a load of just over 500 lbf. The initial failure occurred in region B, followed by failure at region D. Cracks propagated along the length of the specimen with failure occurring halfway between the thick and thin regions of the shell (Figure 45).

Of particular interest was reproducing the failures observed in the previous animal studies. Visual comparison of images obtained from these mechanical tests with those obtained following explant from the previous sheep study suggest that a four-point loading scenario may have led to the prior failure (Figure 46). Note the similarity in the geometry of the fracture and the propagation of the crack along the length of the sample.



*Figure 46.* Comparison of failed devices. Left – Device subjected to classic four-point bend in vitro. Right – Device explanted from sheep study.

### **Gait Analysis**

The Biomechanical Environments Laboratory was contracted to work in collaboration with Methodist Hospital Research Institute and the Texas A&M Institute for Preclinical Studies

(TIPS) to evaluate the gait of sheep implanted with MHRI's PEU biodegradable polymeric shells indicated for osteoregeneration.

Gait analysis is an effective way to evaluate the performance of an orthopedic device as it passes through different healing phases in an animal model. Dogs are one of the most popular animal models used for orthopedic assessments, but sheep are rising in popularity due to the ethical issues concerning the use of dogs, their demeanor and the fact that they have a body weight similar to humans (Kim 2008, Martini 2001). Sheep appear to have a rate of bone healing which closely approximates that of humans and similarities between sheep and human trabecular bone have been documented, though sheep cortical bone contains fewer Haversian canals than is typically seen in human cortical bone (Martini 2001). Sheep do not have the extensive background of literature appreciated by dogs as an orthopedic model but with their recent rise in popularity, more on this subject is being published.

Both force plates and pressure walkways have been successfully used to evaluate ground reaction forces associated with gait. In this study, we opted for the use of force plates due to their high sampling rate, 1000 Hz for our system as compared to 60 Hz for most pressure walkways, and therefore their tendency to produce more accurate absolute values (Agostinho 2012).

We are examining the differences in peak vertical force and stance phase presentation before and after the implantation of a novel, biodegradable internal fixation device for the treatment of comminuted fractures in the long bones of load bearing limbs in the right rear limb of a sheep. We hypothesize that no differences will be present after allowing for a sufficient healing time.

### **Testing Protocol**

A Vicon (Vicon Systems, Oxford, UK) motion capture system with eight infrared cameras, one DV2 Bonita camera and two AMTI force plates were used to perform gait analysis on V251, a 75 kg, 1 year old male Suffolk mix sheep implanted with the device. Retroreflective markers which react to the infrared strobes of the cameras were placed at specific bony landmarks located on the sheep. Nexus software (Vicon Systems) was used to gather and analyze both the marker trajectory and force plate data. The force plates were embedded in a dense foam walkway approximately 17 feet long by two feet wide which began and ended with gradual ramps. A sufficient entry length preceding the force plates allowed the sheep to assume a normal gait prior to and during data capture. The walkway was made of dense foam to prevent slipping of the sheep during locomotion and the force plates were covered with thin rubber mats for the same reason. The arrangement of the force plates within the walkway, as well as the rubber mats covering them, can be seen in Figure 47.



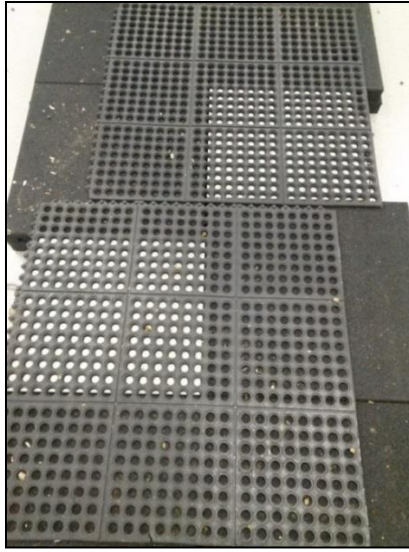
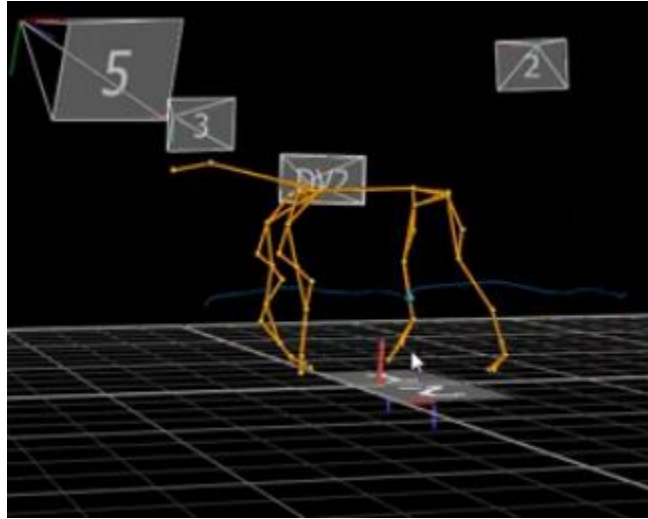


*Figure 47.* Two AMTI force plates embedded in the walkway in a staggered configuration and covered with thin rubber mats to prevent slipping during locomotion.

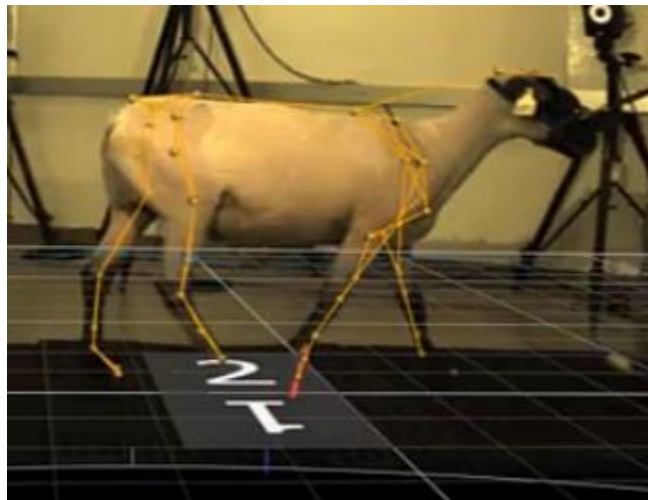
Gait analysis was performed in one of the ICU rooms located within the Texas Institute for Pre-clinical Studies (TIPS) in College Station, Texas for both Time Point 1, occurring 111 days after cast removal, and Time Point 2, occurring 161 days after cast removal. The sheep was acclimated to the environment via housing in a pen located in the corner of the room for a minimum of one night prior to the gait analysis data capture. The sheep became acclimated to walking with a handler on a halter via the duration of its stay at TIPS. The markers were attached via Velcro superglued to the shorn and shaved skin of the sheep. Shearing occurred four days prior and shaving occurred one day prior to the data capture for each time point. The same handler was used for each time point. Only the trials where the sheep hit squarely on the force plate with no overlap from either the handler or the sheep's other hooves touching the force plate simultaneously were included in the trial. To

accommodate the small amount of force dispersion caused by the rubber mats covering the force plates, only hoof strikes occurring more than an inch away from the edge of the force plates were considered. The sheep's velocity approximated a natural walk for all included trials. A video of a representative trial can be seen in *Time Point 2 Walking 16 Aerial*, with the marker data overlayed on the DV2 Bonita camera seen in the video *Time Point 2 Bonita Walking 16*. A still frame of each of these videos can be seen in Figures 48 and 49. The marker placed over the implanted device and its trajectory is highlighted in blue in both videos. Halfway through the capture period of Time Point 2, the force plate configuration was switched from staggered to side by side in an effort to increase the percentage of viable trials captured. This effort was successful with no difference seen in the quality of data gathered other than the greater probability of a successful data capture. The side-by-side configuration can be seen in Figures 48 and 49.



---

*Figure 48.* A still frame from the marker data gathered and processed via Nexus software. The marker highlighted in blue is directly over the implanted device.



---

*Figure 49.* A still frame showing the marker data overlayed on the DV2 Bonita video capture. Again, the blue marker is directly over the implanted device.

## Results

Figure 50 shows the comparison of the peak forces experienced by the limb receiving the therapy for all three time points; Pre Op, Time Point 1 and Time Point 2, depicted as a percentage of the sheep's body weight. No significant change in peak force occurred during this study. Figure 51 shows a comparison between the waveforms of the limb of interest, in our case the rear right limb, as normalized by body weight at the three time points. No significant changes in the duration of the stance phase of the gait cycle can be seen and the characteristic double hump of a sheep's back leg can clearly be distinguished.

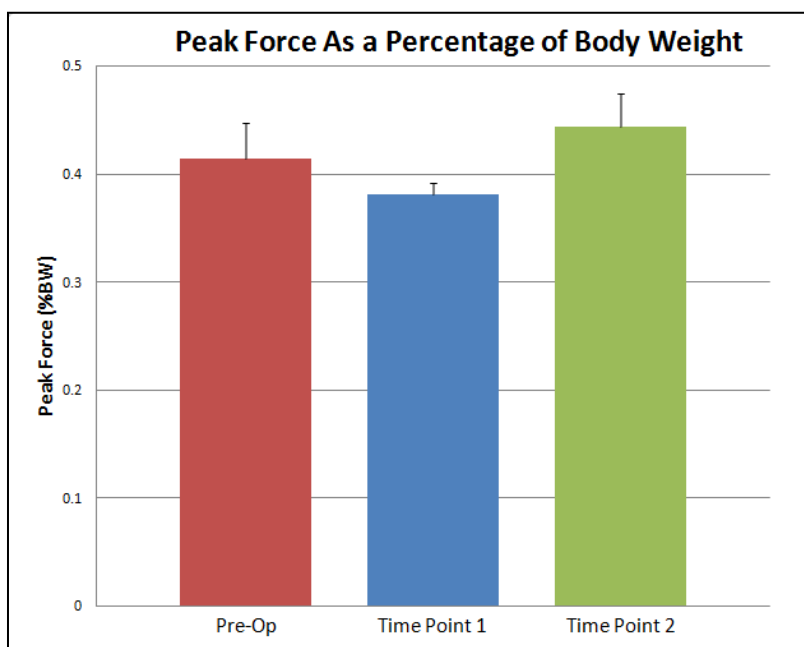


*Figure 50.* A comparison of the peak forces associated with the hind right limb during normal walking, normalized by body weight. There is no statistical difference between the pre-op peak force and the peak force seen 111 and 161 days after cast removal.

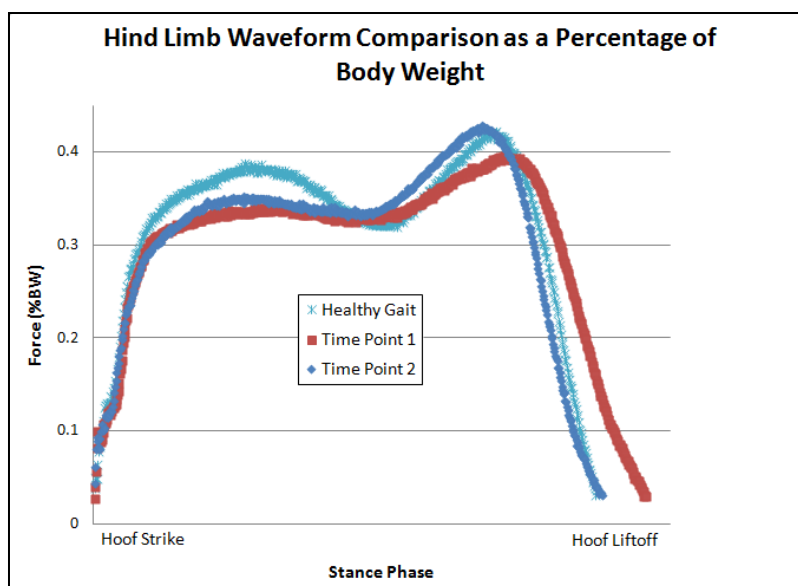


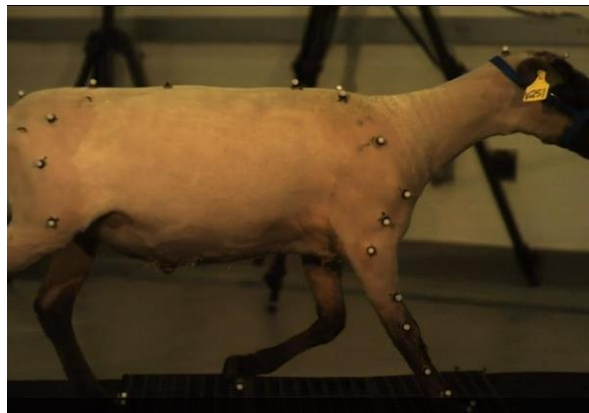
*Figure 51.* Three representative trials taken at the three time points and normalized by body weight. The waveform characteristics and duration of the stance phase indicate that the sheep is not favoring the limb.

These results show that the therapy did not significantly alter the gait of the sheep. We saw no shortening of the duration of contact during the stance phase of the gait cycle, nor did we see any reduction in the percentage of body weight applied to the limb during normal walking, both of which would imply the sheep favoring that limb.

### **Supplemental Data**

Using our high speed video camera, we were able to capture video of the sheep running on the walkway 161 days after cast removal. A still frame of this is included in Figure 52 and the video is titled *sheep run2*. From the motion of the sheep, it is evident that the sheep did not favor the affected limb, even when presented with this more strenuous loading condition.

Additional high speed videos of the sheep running in a circle in its pen and climbing onto the chicken wire fencing which comprises the walls of the pen, and thus applying a significantly higher percentage of its body weight to its rear limbs, can be seen in the videos *sheep run circle* and *sheep stand 3*, with stills included in Figures 53 and 54, respectively.



---

*Figure 52.* A still frame of the sheep running across the walkway. The corresponding video shows this event at normal speed,  $\frac{1}{2}$  speed and  $\frac{1}{4}$  speed.

## Conclusion

In conclusion, this study has shown that implantation of the novel, biodegradable internal fixation device can be done without causing any abnormalities in the sheep's ground reaction force in the affected limb or the load-bearing pattern during ambulation. As of the publication of this dissertation, DARPA recently announced funding a preclinical trial for this technology.



---

*Figure 53.* A still frame of the sheep beginning to run around the handler. A high speed video of this event can be seen in *sheep run circle*.



---

*Figure 54.* A still shot of the sheep climbing onto the wall of the pen. This behavior was common prior to the surgery and was often seen during both time points in between data capture sessions. A high speed video of this event can be seen in *sheep stand3*.



CHAPTER IV  
CONSTITUTIVE RELATIONS FOR A COMPUTATIONAL MODEL  
CAPABLE OF BIODEGRADATION<sup>1</sup>

The author was responsible for setting up and maintaining the static and dynamic testing rigs, collecting the samples and analyzing for peak crystallinity, peak temperature, ultimate stress and strain and yield stress and strain via differential scanning calorimetry (DSC) and tensile test to failure via the Instron 3345 Load Frame. Briefly, the degradation and mechanical properties of the fiber were evaluated at five points for both accelerated (45°C) and non-accelerated degradation (37°C). At each time point, for each loading condition, two whole fibers were collected, dried and weighed. Segments were allocated for instantaneous elastic response testing (3cm) or crystallinity testing (2cm). Each fiber was approximately 11 cm long.

After the degradation period ended, a fiber was collected and allowed to dry overnight under vacuum at room temperature or in drierite crystals at room temperature. The dry fiber weight was measured and recorded, and the sample was stored in drierite crystals until the testing was carried out. The weight of the fiber was taken with the clamps and silicone still

---

<sup>1</sup> Reprinted with permission from “The effect of static and dynamic loading on degradation of PLLA stent fibers” by Hayman, Bergerson, Miller, Moreno and Moore, 2014. *Journal of Biomechanical Engineering*, 136(8), 081006-1:081006-9, Copyright 2014 by American Society of Mechanical Engineers.

intact; however, the fishing line that attaches the weight was removed to easily compare the fiber to the initial weight, also taken with clamps and silicone intact but without fishing line.

Tensile testing to failure was performed on samples with a total length between 2.5 and 3 cm to give a gauge length of 1 cm, and to prevent slipping of the fiber inside the grips. The sample gauge length, width and thickness were recorded to allow stress and strain calculations and the displacement rate was set at 10% of the gauge length.

Testing with the DSC was performed on a sample between 5 and 10 mg, which corresponded to roughly 2 cm of PLLA. The fiber was heated at 5°C/min until it reached 230°C, then cooled to room temp at the same rate. The percent crystallinity is then calculated from the following equation:

$$X_c = \frac{\Delta H_m}{\Delta H_m^0} \quad \text{Eq. 5}$$

where  $\Delta H_m^0 = 140 \text{ J/g}$  and  $\Delta H_m$  is found using the integrated peak tool in the Universal Analysis software.

## **The Effect of Static and Dynamic**

### **Loading on Degradation of PLLA Stent Fibers**

The transient nature of biodegradable stents may decrease long-term complications associated with traditional stents such as restenosis and incomplete re-endothelialization

(Lanckhor et al. 2012). However, designing biodegradable stents that can maintain their mechanical integrity throughout the degradation process presents a new set of challenges.

Poly-L-lactic Acid (PLLA), a nontoxic polymer that is easily eliminated from the body, is often used in degradable devices. Clinical studies of PLLA stents such as the Igaki-Tamai stent and the BVS stent (Abbott Vascular) indicate that, although the stents are safe, they are prone to greater elastic recoil compared to bare metal stents (Nishio et al. 2012, Tamai et al. 2000, Okamura et al. 2010, Onuma et al. 2011). Attempts to correct this problem are addressed through changes in stent design. Currently, a second-generation BVS stent is undergoing clinical trials (ClinicalTrials.gov; NCT01425281), and additional designs are under investigation in animal models and in vitro (Diletti et al. 2012, Grabow et al. 2007, Venkatraman et al. 2006, Bunger et al. 2007, Vogt et al. 2004, Su et al. 2003, Wu et al. 2012). However, the design process is complicated by an incomplete understanding of how the PLLA degradation rate is impacted by its local mechanical environment.

PLLA has been used in a variety of medical devices and consumer products; so much is known about the effect of material and environmental properties on its degradation rate. The primary degradation mechanism of PLLA is passive hydrolysis of the ester bond (Li 1999); however, enzymatic degradation can also occur (Tsuji 2008). The degradation rate and erosion mechanism are affected by changes in characteristic material properties such as percent crystallinity (Tsuji et al. 2000) and geometry (Grizzi et al. 1995) or environmental factors such as pH (Yuan et al. 2002), water uptake (Yew et al. 2005) and temperature (Weir

et al. 2004). Given this information, it is possible to predict how changes in material properties or environment will alter the degradation rate (Lyu et al. 2007). However, very little is known about the effect of loading on the degradation rate as most in vitro degradation studies are performed in the absence of mechanical loads.

In vivo studies of biodegradable devices suggest that loading accelerates degradation in polymers. Specifically, the degradation rates are higher in devices experiencing high compressive loads such as spinal cord cages, bone screws and bone plates compared to unloaded in vitro controls (Van Dijk et al. 2002, Leenslag et al. 1987). However, it is difficult to extrapolate these results to stent designs as these loads are not comparable to those found in stents, the degradation rates have not been quantified, the changes in mechanical properties have not been well characterized, and the complex loading conditions in vivo make it difficult or impossible to quantify the relationship between load and degradation rate (Van Dijk et al. 2003, Bedoya et al. 2006).

In vitro studies offer more quantifiable results, however few degradation studies have been carried out under loaded conditions. One study that examined the effects of a tensile load and a dynamic tensile load on poly -D,L - lactic acid (PDLLA) foams found that both increased the degradation rate and decreased the molecular weight, elastic modulus and tensile strength after 3 months (Fan et al. 2010). Other studies of PLLA foams, composites and copolymers have also found an increase in degradation with load through a decrease in mechanical properties (Wan et al. 2001, Thompson et al. 1996). In one study of

dynamically compressed 50:50 PLA:PGA implants dynamic loading significantly increased material stiffness during the first 3 weeks (Thompson et al. 1996). These studies all indicate that load affects degradation rate; however, the polymer geometries and composition are too variable to compare between studies or define a quantitative relationship (Gopferich 1996).

Conversely, a study on the degradation of poly(glycolide-co-L-lactide) (PGLA) sutures suggests that smaller loads may have less effect on degradation. When a static load of less than 1 N was applied to braided sutures, no change was seen in the breaking strength retention, tensile modulus retention, or tensile breaking strain (Deng et al. 2005). These loads are much smaller than those described in the above studies, which suggests there may be a critical loading value below which the change in degradation is less pronounced. A rapid decrease in elastic modulus was observed within the first 5 days of degradation; this was followed by a 20-day period of elastic modulus stability. The authors attribute this initial decrease in elastic modulus to the plasticizing effect of water absorption in the PLLA sutures (Yew et al. 2005, Deng et al. 2005).

Despite the paucity of experimental data, material models have been developed, which predict degradation based on thermodynamic factors. Rajagopal et al. developed a model of polymer degradation as a function of deformation measured by the first strain invariant (Rajagopal et al. 2007). In this model, degradation is driven by strain alone so that, in the unloaded model, the degradation rate is zero. Degradation is introduced to the neo-Hookean

material model through a deformation dependent decrease in the shear modulus. Soares et al. further developed this model for use with PLLA stent fibers under tensile loading conditions (Soares et al. 2010, Soares et al. 2009, Soares et al. 2008, Soares 2008). The degradation model was applied with a neo-Hookean constitutive description to fibers loaded under uniaxial extension (Soares et al. 2008). In this model, the degradation rate is a function of deformation, which is quantified by the radius in the  $(I_B, II_B)$  plane. When the degradation model was applied to more complex strain energy functions, a better description of the mechanical behavior was obtained. The Knowles strain energy function, which provided a good description of PLLA behavior, was allowed to degrade through a decrease in the three characteristic material parameters (Soares et al. 2010). The Knowles model was chosen over the traditionally used Young's modulus because semicrystalline polymers such as PLLA exhibit nonlinear behavior, which extends to several percent strain. While the Young's modulus can provide a description of overall material behavior for small strains ( $\ll 1\%$ ) of linearly elastic materials, it would be inappropriate for use with these materials. Therefore, we chose an appropriate nonlinear model within a finite elasticity framework (Humphrey 2002). When the Knowles model is coupled with the degradation model, it predicts that greater deformation will induce a higher degree of degradation.

Although these models provide thermodynamically sound descriptions of the polymer behavior, they were developed in the absence of quantitative experimental data, and so it is difficult to evaluate how well they predict the degradation behavior of polymers. Soares et al. provided preliminary experimental data for PLLA fibers degraded in vitro under static

loading conditions (Soares 2008). The degradation of the mechanical properties was examined for 12 months; however, the results found that mechanical properties did not change significantly until 12 months; so, a longer degradation times are necessary to fully characterize this phenomenon.

The purpose of this study was to quantitatively define PLLA fiber degradation under static and dynamic loading conditions in vitro. Fiber degradation was quantified through changes in material properties over 15 months. These results were used to further define the degradation model.

### **Materials and Methods**

Degradation studies were performed on extruded PLLA fibers. The fibers used in this study were obtained from TissueGen (Dallas, TX) and are used in the production of biodegradable stents. The process used by TissueGen is described briefly. The fibers were produced by a wet extrusion process from PLLA pellets (Purasorb PL 38, Purac, The Netherlands). The polymer flow rate was 4.5 mL/min at room temperature with a maximum oven temperature in the draw line of 121°C. The fiber was annealed at 140°C for 1 h and drawn from the anneal state at a line tension of 2.6 kg. Fibers were degraded in phosphate buffered saline (PBS) at 45°C, to accelerate degradation and loaded axially. The degradation temperature was chosen to be lower than the glass transition temperature of PLLA (55°C) (Weir et al. 2004, Soares 2008, Agrawal et al. 1997). The rate of degradation acceleration was calculated using the Arrhenius equation:

$$k = Ae^{E_a/RT} \quad \text{Eq. 6}$$

where  $k$  is the rate constant,  $A$  the frequency factor,  $E_a$  the activation energy,  $R$  the universal gas constant and  $T$  the temperature (Weir et al. 2004).

The experimental protocol for static loading has been described previously (Soares 2008). Briefly, the fibers were mounted inside a plastic box and loaded axially with free hanging weights (the small static load and large static load were 50 g or 100 g, respectively). The loads were chosen so that the fibers would experience only recoverable (elastic) deformation. The stress experienced by the undegraded fiber under a 1-N load is approximately half of the yield stress ensuring that throughout degradation the fiber stays within its elastic range. Unloaded controls were mounted with no attached weight. The PBS was circulated and the temperature maintained by a model 210 heated recirculator (Polyscience). Two fibers from each group were collected at 73 days, 113 days, 147 days, and 183 days, which correspond with an equivalent degradation time of 6 months, 9 months, 12 months, and 15 months in a fiber degraded at 37°C (Weir et al. 2004). Afterward, the fibers were dried under vacuum overnight at room temperature and stored in drierite crystals.

Dynamic loading was applied to the fibers with a load-controlled device (Figure 55). One end of the fibers was mounted on a static stage in a biobath environmental chamber while the other end was attached to one of two force transducers mounted on the crosshead of the



Universal Test Machine (model 120R225; Test Resources). Four fibers were connected to each force transducer in parallel. While only one transducer controlled crosshead displacement, both collected force and extension data. Dynamically loaded fibers were cycled between 0.125 N and 0.25 N at 1 Hz using R Controller software. Five-centimeter segments of each fiber were collected and stored at the same time points listed for static loading. To quantify degradation, the mechanical properties of the fiber were measured at each time point. These data were used to define a degradation function, described below, for each loading group. A uniaxial tensile test to failure was performed with 3-cm long fiber segments on an Instron single column testing system (model 3345) to estimate the material properties of the fibers at each time point. The fibers have an oblong cross-sectional area with a width between 1.28 and 1.35 mm and a thickness between 0.18 and 0.22 mm. The cross-sectional dimensions were measured manually with calipers. The gauge length ranged between 0.95 and 1.05 mm. The displacement rate was 10% of the original length per minute (approximately 1 mm/min). One outlier had a fiber length of 11.95 mm; however, the stress–strain curve was similar to other fibers within the group. Axial force (N) versus extension (mm) was recorded for each fiber.

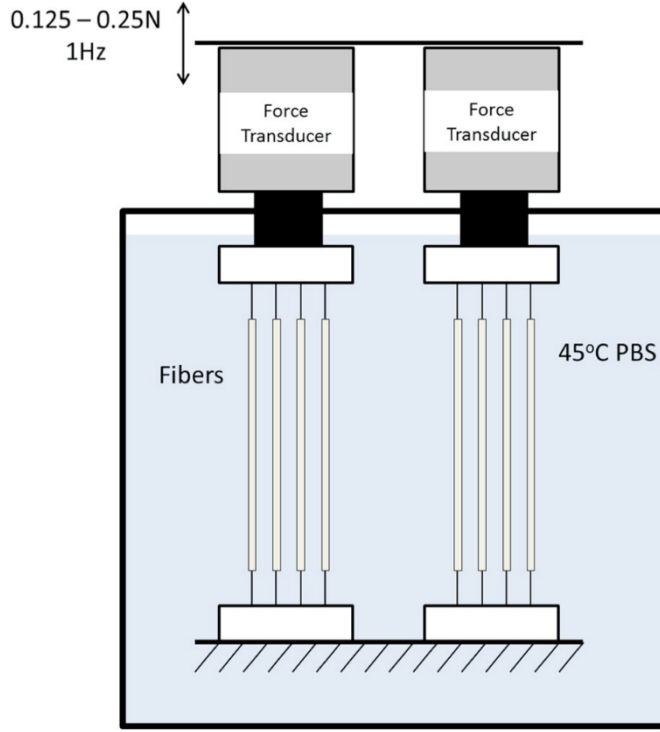


*Figure 55.* Illustration of the device used to apply a dynamic axial load to fibers. The load fluctuated between 0.125N and 0.25N at a frequency of 1 Hz while the fibers were submerged in PBS maintained at 45°C.

The fiber was modeled as a nonlinearly elastic incompressible material capable of finite deformation under uniaxial extension. The constitutive model, developed previously, was fitted to the uniaxial stress strain curves (Soares et al. 2010, Soares et al. 2009, Soares et al. 2008). The deformation tensor,  $F$ , is used to define the left Cauchy–Green stretch tensors,  $B = FF^T$ , and the first strain invariants,  $I_B = \text{tr}(B)$  and  $II_B = (1/2)[(\text{tr}(B))^2 - \text{tr}(B^2)]$  where  $III_B$  is 1 for an incompressible material. Although Cauchy stress,  $\sigma$ , is a better measure of the stress in a deformed body, it is difficult to calculate the cross-sectional area of the fiber

during loading accurately enough to justify its use with experimental data. Therefore, nominal stress ( $\sigma_n$ ) was used in this study

$$\sigma_n = JF^{-1} \left( -p1 + 2 \frac{\partial W}{\partial I_B} B - 2 \frac{\partial W}{\partial II_B} B^{-1} \right) \quad \text{Eq. 7}$$

Under uniaxial extension, the only nonzero stress component is the axial stress

$$\sigma_{n,33} = 2 \frac{\partial W}{\partial I_B} B - 2 \frac{\partial W}{\partial II_B} B^{-1} \quad \text{Eq. 8}$$

Where the strain energy function  $W$  is defined by the following equation:

$$W = \frac{\mu}{2\beta m} [(1 + \beta(I_B - 3))^m - 1] \quad \text{Eq. 9}$$

where  $\mu$  is the shear modulus and  $\beta$  and  $m$  are dimensionless material constants (Knowles 1977). The shear modulus is a measure of material stiffness, while  $\beta$  and  $m$  are markers of material softening, which occurs at larger strain levels within the elastic region. Using Eq. 8, the nonlinear model was fitted to the stress versus strain curve using the MATLAB function `lsqcurvefit` to determine the values of the constants using the default trust-region-reflective algorithm and a lower bound of zero for all constants.

The model incorporates fiber degradation by tracking the change in the material constants with respect to time (Soares et al. 2010). The degradation,  $d$ , of a material constant in the

model is defined as a function of time, current state of degradation, and the deformation dependent reaction rate,  $K_x = K(F)$

$$\dot{d} = (1 - d)K_x \quad \text{Eq. 10}$$

$$\frac{1}{\mu} = \frac{1}{\mu_0} (1 - d) = \frac{1}{\mu_0} e^{-K_\mu * t} \quad \text{Eq. 11a}$$

$$\frac{1}{\beta} = \frac{1}{\beta_0} (1 - d) = \frac{1}{\beta_0} e^{-K_\beta * t} \quad \text{Eq. 11b}$$

The effect of material constant degradation was evaluated by evaluating stress values at 5% strain at each time point when only one constant is allowed to degrade. The deformation dependent reaction rates were calculated for each loading group (no load, small static load, large static load, and dynamic load) and for each material constant ( $\mu$ ,  $\beta$  and  $m$ ) by fitting the values of the material constants to Eq. 11. Equation 11 was fitted to the data using a least squares fitting in JMP for a custom nonlinear model. Because of the tendency of the material to stiffen initially (see Results), two versions of the model were specified: one in which the material was assumed to degrade from the beginning of the experiment and one in which the material was assumed to begin degrading at  $t=6$  months. These are denoted as models M1 and M2, respectively. The relationship between  $K_\beta$  and degradation load was examined by fitting a linear model to the  $K_\beta$  versus degradation stress plot of the static groups. Degradation stress was calculated as the degradation load divided by the average cross sectional area measured for the uniaxial tensile tests described earlier.

Additional characteristic points on the stress versus strain curve were also examined at each time point as possible markers of degradation. The yield point, maximum stress, and strain at break were identified for each fiber. The yield point was identified by a manual examination of the stress versus strain curves, where a sudden decrease in the slope of the stress versus strain curve was observed. This yield point occurred slightly before that predicted by the 2% offset method. The yield point identified by this method included a portion of the curve where a slight decrease in the stress after yield occurred, which indicated that the fiber had likely undergone some plastic deformation. However, a 1% offset identified the yield point on all curves without including this decrease. Data are presented as the mean  $\pm$  the standard deviation.

Changes in fiber crystallinity and peak melting temperature were also examined using differential scanning calorimetry (DSC) at each time point. A segment of fiber (2.6 mg to 8.6 mg) was loaded into a DSC (DSC Q100; TA Instruments) and heated from 25°C to 230°C at a rate of 5°C/min. The enthalpy of fusion ( $\Delta H_m$ ) and peak melting temperature were measured using Universal Analysis software (TA Instruments). The percent crystallinity ( $X_c$ ) is calculated from the following equation:  $X_c = \Delta H_m / \Delta H_m^0$ , where  $\Delta H_m^0$ , the enthalpy of fusion for a completely crystalline PLLA sample, is 140 J/g (Soares 2008, Mano et al. 2005). The relationships between crystallinity and the material constants from the model were examined using regression analysis carried out with JMP. The strength of the relationships was evaluated with the Spearman's correlation coefficient ( $\rho$ ),  $R^2$  value, and significance of the relationship,  $p$ .

A two-way repeated measures ANOVA was used to determine significance ( $p < 0.05$ ) followed by a post hoc Tukey HSD comparison. A sphericity test was run to determine if univariate analysis could be used, and in each case, the  $\chi^2$  value was not significant, indicating that it could. The results from the uniaxial tensile tests ( $\mu$ ,  $\beta$ ,  $m$ , yield point, maximum stress, and strain at break) included some groups with  $n=1$ , which were removed from the statistical analysis. In these cases, the 6-month time point and the large static loading group could not be included in the analysis. Significant difference resulted from two independent factors: degradation time and loading condition, and the interaction between the two. All statistical analysis was performed with JMP Statistical Software (Cary, NC).

## Results

Changes in fiber rigidity were observed in the elastic regions of the stress versus strain curves during degradation, which were quantified by examining the change in values of  $\beta$  (Figure 56). Values of  $\beta$  ranged from 0.9 to 140.1 across all loads and degradation times (Table 22). These variations had a significant effect on the nonlinearity of the stress strain curve, where an increase in  $\beta$  decreased the rigidity of the model (Figure 57). Average  $\beta$  values at each time point (Figure 58) did not change significantly with load; however, average  $\beta$  values increased significantly with time ( $p = 0.0002$ ). At 15 months, the  $\beta$  value ( $100.4 \pm 40.1$ ) was higher than at 9 ( $32.7 \pm 9.1$ ) or 12 months ( $44.5 \pm 10.1$ ).

The  $\beta$  value also showed a significant interaction between time and load ( $p = 0.0137$ ). At 15 months, the dynamic group ( $134.0 \pm 1.3$ ) was significantly greater compared to the no load

( $62.2 \pm 44.5$ ) group. In addition, there were significant differences between time points within the dynamic loading group. After 15 months,  $\beta$  was significantly greater in the dynamic loading group compared to its 9- and 12-month counterparts. The observed changes in  $\beta$  resulted in a significant change in the behavior of the model (Figure 59). The largest increase in  $\beta$  was observed in the large static load group where values ranged from 12.9 to 140.1. This change resulted in roughly half the predicted stress at a strain of 5% when  $\mu$  and  $m$  are held constant.

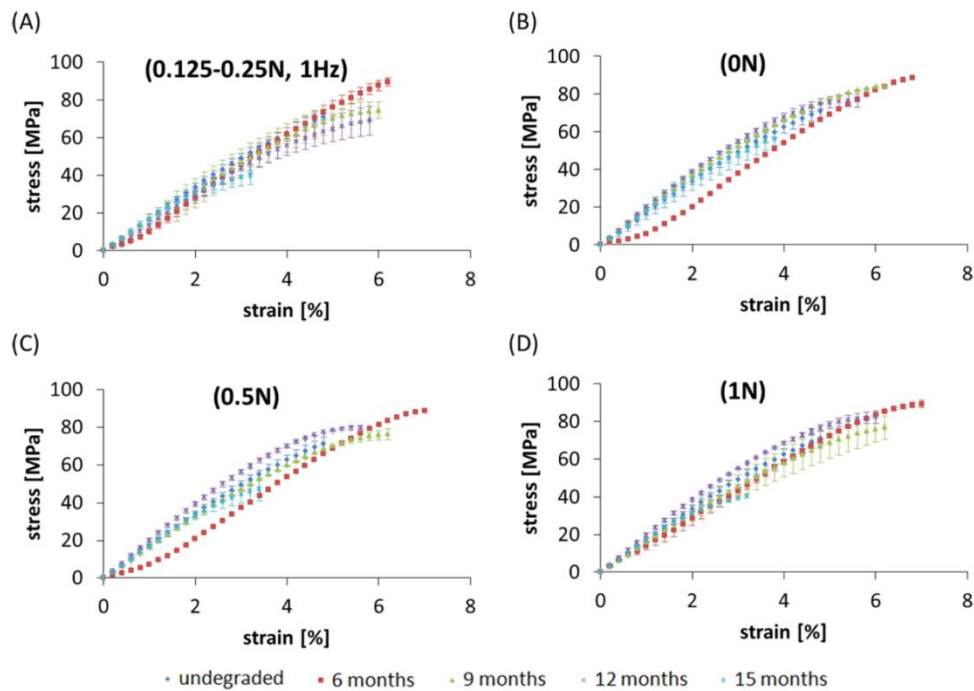


*Figure 56.* Average stress versus strain curves for the elastic regions of fibers exposed to (a) dynamic load, (b) no load, (c) small static load and (d) large static load at 0,6,9,12 and 15 months.

Table 22. *Average Values for the Knowles Model Material Constants for all Static (n=2) and Dynamic (n=3) Loading Groups*

	$t = 0$ months	6 months	9 months	12 months	15 months
No load (0 N)	$\mu = 612.5 \pm 30.6$ MPa ( $n = 4$ ); $\beta = 30.7 \pm 4.0$ (dimensionless); $m = 8.1 \times 10^{-5} \pm 1.3 \times 10^{-6}$ (dimensionless)	461.6 ( $n = 1$ ); 1.8; $6.6 \times 10^{-3}$	$663.2 \pm 1.0$ ; $35.0 \pm 0.4$ ; $5.9 \times 10^{-5} \pm 3.5 \times 10^{-6}$	$715.6 \pm 7.6$ ; $52.6 \pm 4.5$ ; $4.1 \times 10^{-5} \pm 1.9 \times 10^{-6}$	$636.3 \pm 133.8$ ; $62.2 \pm 44.5$ ; $5.7 \times 10^{-5} \pm 1.8 \times 10^{-5}$
Small static load (0.5 N)		456.0 ( $n = 1$ ); 0.9; $4.2 \times 10^{-2}$	$591.2 \pm 6.7$ ; $32.8 \pm 3.8$ ; $6.8 \times 10^{-5} \pm 5.8 \times 10^{-6}$	$732.7 \pm 24.3$ ; $51.0 \pm 6.0$ ; $4.3 \times 10^{-5} \pm 3.8 \times 10^{-6}$	$614.7 \pm 19.7$ ; $88.5 \pm 33.4$ ; $6.7 \times 10^{-5} \pm 8.3 \times 10^{-6}$
Large static load (1 N)		$535.9 \pm 34.0$ ; $12.9 \pm 6.3$ ; $6.8 \times 10^{-5} \pm 3.0 \times 10^{-5}$	$567.0 \pm 80.7$ ; $27.7 \pm 5.8$ ; $7.4 \times 10^{-5} \pm 7.2 \times 10^{-6}$	$706.8 \pm 17.3$ ; $44.3 \pm 8.6$ ; $6.4 \times 10^{-5} \pm 1.5 \times 10^{-5}$	$611.9$ ( $n = 1$ ); 140.1; $7.7 \times 10^{-5}$
Dynamic load (0.125–0.25 N, 1 Hz)		$549.5 \pm 38.6$ ; $10.1 \pm 3.4$ ; $6.5 \times 10^{-4} \pm 4.5 \times 10^{-4}$	$583.5 \pm 112.6$ ; $31.2 \pm 15.3$ ; $6.9 \times 10^{-5} \pm 2.4 \times 10^{-5}$	$550.8 \pm 49.6$ ; $34.8 \pm 5.6$ ; $7.2 \times 10^{-5} \pm 1.2 \times 10^{-5}$	$594.5 \pm 69.0$ ; $133.9 \pm 1.7$ ; $9.6 \times 10^{-5} \pm 4.4 \times 10^{-5}$



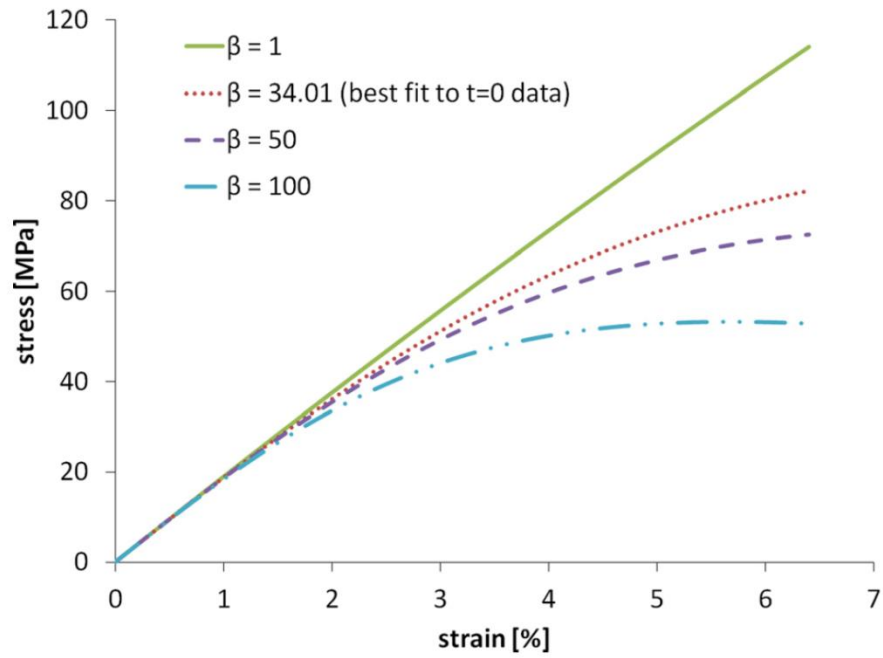


*Figure 57.* Illustration of the effect of varying  $\beta$  while keeping  $\mu$  and  $m$  constant. An increase in  $\beta$  indicates a softer material at higher strains.

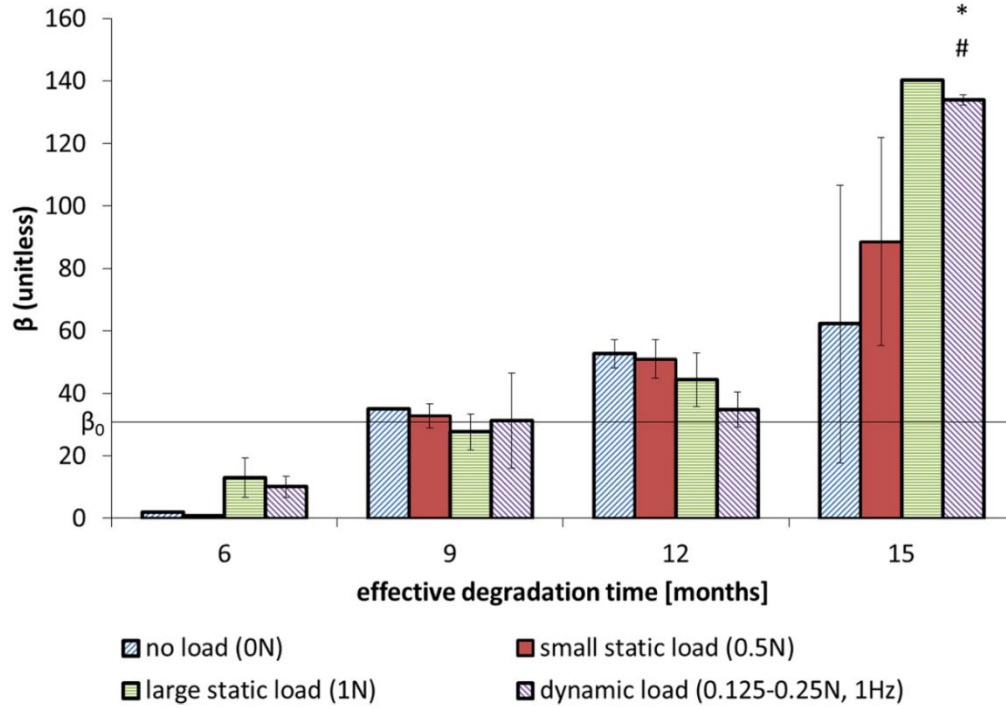


Figure 58.  $\beta$ , a Knowles model constant, increases with degradation time. \* $p < 0.05$  compared to the no load group at 15 months. # $p < 0.05$  compared to the same loading group at 9 and 12 months.

Table 23.  $K(F)_\beta$  Values for the Degradation Models of  $\beta$

	$\beta_{M1}$			$\beta_{M2}$		
	$K(F)_\beta$	Lower CI	Upper CI	$K(F)_\beta$	Lower CI	Upper CI
No load (0 N)	0.039	−0.017	0.071	0.406	0.258	0.468
Small static load (0.5 N)	0.055	0.007	0.084	0.516	0.436	0.562
Large static load (1 N)	0.062	−0.033	0.103	0.257	0.233	0.277
Dynamic load (0.125–0.25 N)	0.072	0.033	0.098	0.283	0.267	0.296

The confidence intervals (CI) are shown for each parameter estimate.

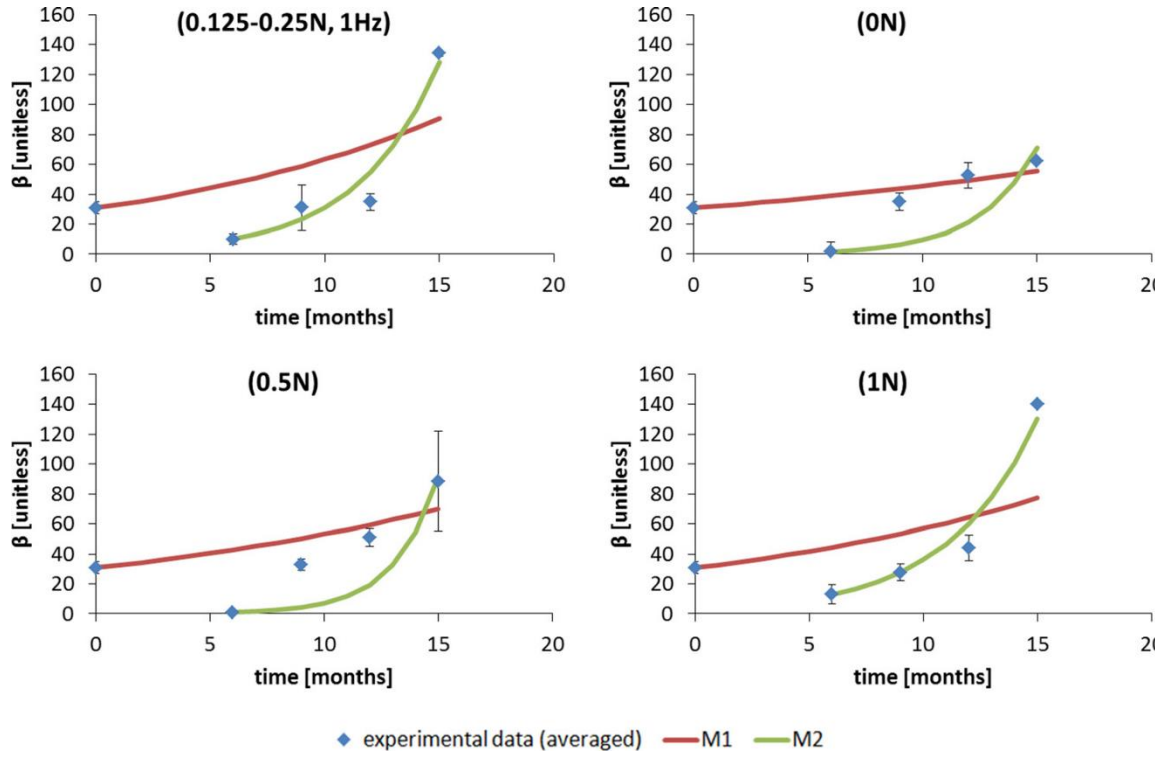


Figure 59. The degradation model is fitted to the values of  $\beta$  to obtain values for the degradation constants  $K(F)$ .

No change in the shear modulus was observed with respect to load or time. No significant interaction between load and time was observed. No significant changes were observed in the value of  $m$  with respect to time, load, or the interaction between the two (Table 23) despite the large variations observed in the data. The variations observed in  $m$  had very little effect on the shape of the stress versus strain curve when  $\mu$  and  $\beta$  were held constant (less than 1% change in predicted stress at 5% strain across all values of  $m$ ). These results suggest that, in this case, the degradation of  $m$  is not a significant factor when predicting the response to loading.

Other measures of fiber degradation were significantly affected by degradation time, but not all were affected by load. Specifically, the yield stress and strain decreased with time across all loading groups. The yield strain was significantly smaller after 15 months ( $0.0394 \pm 0.0063$ ) when compared to 9 ( $0.0633 \pm 0.0024$ ) and 12 months ( $0.0594 \pm 0.0018$ ). After 15 months, the yield strain was approximately half that in the nondegraded fiber ( $0.0657 \pm 0.0018$ ). At the same time, the yield stress decreased significantly after 15 months ( $49.7 \pm 10.9$  MPa) compared to both 9 ( $78.1 \pm 5.0$  MPa) and 12 months ( $74.7 \pm 6.7$  MPa). No significant interaction between time and load was observed in the yield stress.

The strain at break followed a similar trend to the yield strain where a significant decrease was observed with time, but load had no effect. Strain at break decreased significantly ( $p < 0.0001$ ) at each time point, with 12 ( $0.2271 \pm 0.1197$ ) months being significantly smaller than 9 ( $0.3697 \pm 0.0491$ ) months and 15 months ( $0.0569 \pm 0.0177$ ) being significantly smaller compared to 12 months (Table 24).

The maximum stress also decreased significantly ( $p < 0.0001$ ) with time. Significant decreases were observed for all time points with 9 months ( $127.0 \pm 14.0$  MPa) being significantly greater than ( $100.5 \pm 25.6$  MPa) months and 12 months being significantly greater than 15 ( $51.4 \pm 10.7$  MPa) months.

The percent crystallinity,  $X_c$ , increased significantly with degradation time (Figure 61). For these samples, all groups had an  $n$  of 2 with the dynamic groups at 9, 12, and 15 months

having an  $n$  of 3. In this case, the MANOVA was run for all groups and time points. The  $X_c$  of the fibers increased significantly between 9 ( $45.4 \pm 2.7\%$ ) and 12 ( $47.3 \pm 1.6\%$ ) months and again between 12 and 15 ( $49.0 \pm 3.4\%$ ) months. Although degradation load had no effect on  $X_c$ , a significant interaction between time and load was observed. Within the no load, large static load, and dynamic load groups  $X_c$  increased significantly with time and reached a maximum at 15 months (51.664.3%, 52.8%, and 48.660.8%, respectively). Within the small static load group, the crystallinity increased with time but reached a maximum value at 12 months ( $48.9 \pm 1.4\%$ ) before exhibiting a nonsignificant decrease in crystallinity. Within each time point, some differences between the loading groups were observed. After 6 months, the  $X_c$  in the large static load group ( $47.5 \pm 1.6\%$ ) was significantly greater than the dynamic load group ( $43.4 \pm 1.1\%$ ). After 9 months, the  $X_c$  in the no load group ( $41.8 \pm 1.1\%$ ) was significantly greater than the dynamic load group ( $47.2 \pm 3.0\%$ ). After 15 months, the  $X_c$  in the small static load group ( $45.0 \pm 0.9\%$ ) was significantly smaller than the other loading groups.

Changes in the peak melting temperature ( $T_m$ ) were also observed (Table 24).  $T_m$  decreased significantly between 9 ( $180.461.2$  °C) and 12 ( $178.561.3$  °C) months and again between 12 and 15 ( $174.761.7$  °C) months. No effect with respect to load was observed. No relationship was found between  $X_c$ , and  $\mu$  or  $m$ . However, a linear relationship between  $\beta$  and  $X_c$ , was observed (Figure 61). The slope and intercept are both significantly different from 0. In addition, the Spearman's correlation coefficient,  $\rho=0.6152$ , is significantly different from 0.

## Discussion and Conclusion

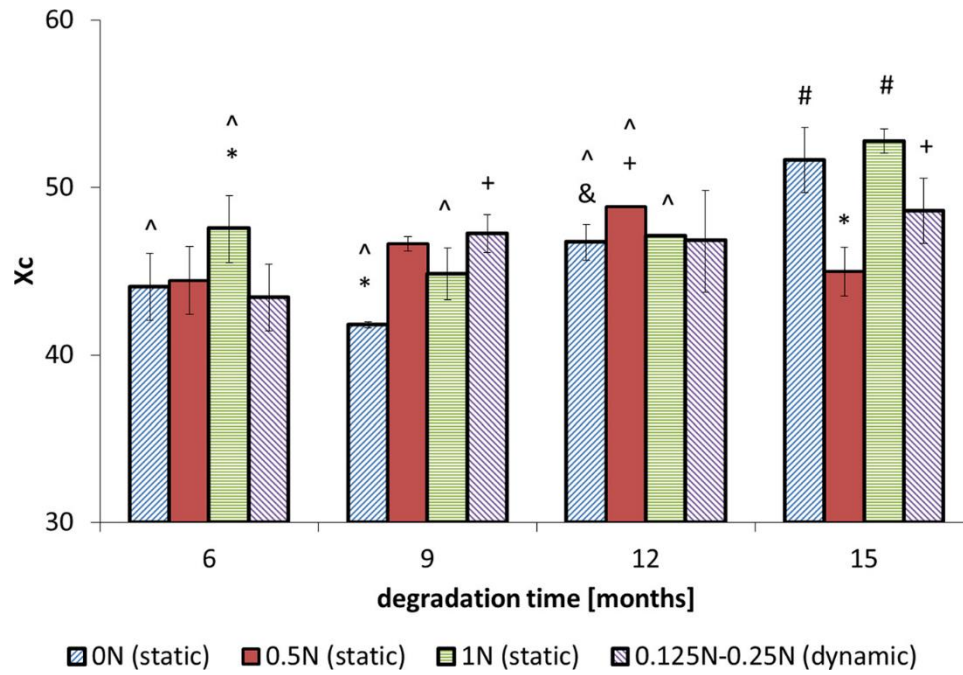
Mechanical property degradation increased with increasing static loading and dynamic loading. While the large static load resulted in an observed increase in  $\beta$  at 15 months, the small sample size in this group prevents a statistical comparison between groups. In addition, when the degradation model was fitted to the data, a decrease in the degradation constant  $K_\beta$  with static load was observed. Taken together, these results suggest that increased static loading increases fiber degradation. Our results agree with previous studies of PLLA copolymers and polyorthoesters, which indicate that static loading increases degradation rates (Wan et al. 2001, Deng et al. 2005, Fan et al. 2008).

Table 24. *Average Values for the Yield Stress, Yield Strain, Fail Stress and Fail Strain for all static (n=2) and Dynamic (n=3)*

*Loading Groups*

	$t = 0$ months	6 months	9 months	12 months	15 months
No load (0 N)	Yield stress = $82.6 \pm 6.9$ MPa ( $n = 4$ ); yield strain = $0.0657 \pm 0.0018$ (dimensionless); maximum stress = $152.0 \pm 8.9$ MPa;	89.0 ( $n = 1$ ); 0.0694; 159.7; 0.4504	84.2 $\pm$ 0.6; 0.0638 $\pm$ 0.0005; 145.3 $\pm$ 8.7; 0.4166 $\pm$ 0.0318	76.5 $\pm$ 3.7; 0.0581 $\pm$ 0.0003; 112.6 $\pm$ 21.7; 0.2996 $\pm$ 0.0907	62.6 $\pm$ 4.1; 0.0463 $\pm$ 0.0088; 64.3 $\pm$ 5.4; 0.0547 $\pm$ 0.0112
Small static load (0.5 N)	strain at break = $0.3454 \pm 0.0163$ (dimensionless)	88.8 ( $n = 1$ ); 0.0705; 139.6; 0.3382	76.5 $\pm$ 3.5; 0.0638 $\pm$ 0.0016; 117.5 $\pm$ 3.0; 0.3153 $\pm$ 0.0366	79.9 $\pm$ 1.1; 0.0582 $\pm$ 0.0008; 117.2 $\pm$ 17.4; 0.2882 $\pm$ 0.0841	49.7 $\pm$ 9.1; 0.0382 $\pm$ 0.0042; 51.0 $\pm$ 8.9; 0.0432 $\pm$ 0.0024
Large static load (1 N)		89.5 $\pm$ 2.3; 0.0716 $\pm$ 0.0016; 149.4 $\pm$ 3.7; 0.3810 $\pm$ 0.0124	78.9 $\pm$ 3.0; 0.0670 $\pm$ 0.0054; 123.3 $\pm$ 0.6; 0.3408 $\pm$ 0.0624	82.4 $\pm$ 3.6; 0.0614 $\pm$ 0.0002; 122.6 $\pm$ 8.9; 0.2997 $\pm$ 0.0101	41.3 ( $n = 1$ ); 0.0351; 42.1; 0.0440
Dynamic load (0.125–0.25 N, 1 Hz)		93.6 $\pm$ 2.1; 0.0680 $\pm$ 0.0036; 155.7 $\pm$ 11.8; 0.3793 $\pm$ 0.0610	75.1 $\pm$ 3.9; 0.0627 $\pm$ 0.0039; 121.1 $\pm$ 8.4; 0.3748 $\pm$ 0.0292	70.1 $\pm$ 8.0; 0.0611 $\pm$ 0.0013; 81.3 $\pm$ 24.5; 0.1380 $\pm$ 0.1202	41.0 $\pm$ 5.1; 0.0357 $\pm$ 0.0011; 43.0 $\pm$ 4.2; 0.0674 $\pm$ 0.0226





*Figure 60.* The percent crystallinity ( $X_c$ ) changes with equivalent degradation time.

A significant interaction between load and time was observed. \* $p < 0.05$  compared to the dynamic load group within the same time point. # $p < 0.05$  compared to the small load group within the same time point. + $p < 0.05$  compared to the 6-month time point of that loading group. & $p < 0.05$  compared to the 9-month time point of that loading group. ^ $p < 0.05$  compared to the 15-month time point of that loading group.

Table 25. *Average Values for Crystallinity and Peak Melting Temperature for all Static (n=2) and Dynamic (n=3) Loading*

*Groups*

	<i>t</i> = 0 months	6 months	9 months	12 months	15 months
No load (0 N)	$X_c = 40.2 \pm 2.0$ MPa ( <i>n</i> = 4); $T_m = 184.6 \pm 1.4$ °C	44.1 ± 0.2;	41.8 ± 1.1;	46.7 ± 1.9;	51.6 ± 4.3;
		181.3 ± 2.9	180.2 ± 1.4	179.2 ± 1.4	176.3 ± 0.2
Small static load (0.5 N)		44.4 ± 0.4;	46.6 ± 0.0;	48.9 ± 1.4;	45.0 ± 0.9;
		181.4 ± 0.2	181.7 ± 0.5	178.1 ± 0.1	175.7 ± 2.4
Large static load (1 N)		47.5 ± 1.6;	44.8 ± 0.0;	47.1 ± 0.7;	52.8 (n = 1); 174.3
		182.6 ± 1.2	180.7 ± 0.9	179.1 ± 1.0	
Dynamic load		43.4 ± 1.1;	47.2 ± 3.0;	46.8 ± 2.0;	48.6 ± 0.8;
(0.125–0.25 N, 1 Hz)		181.7 ± 0.8	179.6 ± 1.1	178.0 ± 2.0	173.2 ± 0.2

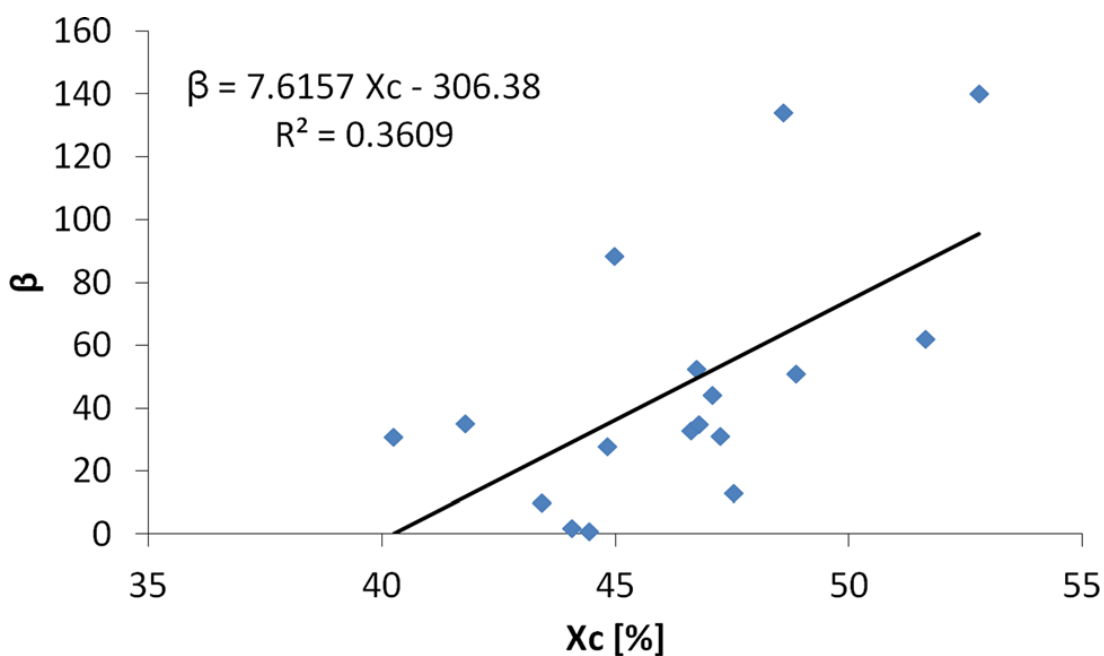


*Figure 61.* As the fiber degrades and percent crystallinity increases, the rigidity of the fiber also decreases. There is an approximate linear relationship between  $X_c$  and  $\beta$ .

The effect of dynamic loading on degradation was most noticeable at later time points and followed the trend observed in the large static load group. Specifically, the  $\beta$  value was significantly different from the no load group. Additionally the value of the deformation dependent reaction rate,  $K_\beta$  decreased compared to the no small static load group but was not different from the large static load group (Figure 62). These results indicate that the degradation rates, measured by  $K_\beta$ , were the same in the large static load group and the dynamic group despite the smaller average load applied to the dynamically degraded fibers (~20% of the large static load). The changes observed in this study indicate that dynamic loading increases degradation. Comparing our results to those from previous studies is

difficult because, to the best of our knowledge, this is the first study of dynamic loading on PLLA stent fibers in the literature. However, studies in other types of biodegradable polymers also indicate that dynamic loading increases degradation compared to unloaded controls (Thompson et al. 1996, Kang et al. 2009). At the same time, the level of loading in this study is low compared to other in vitro studies and is more similar to the loading applied to PLGA sutures, which produced no change in fiber degradation (Deng et al. 2005).

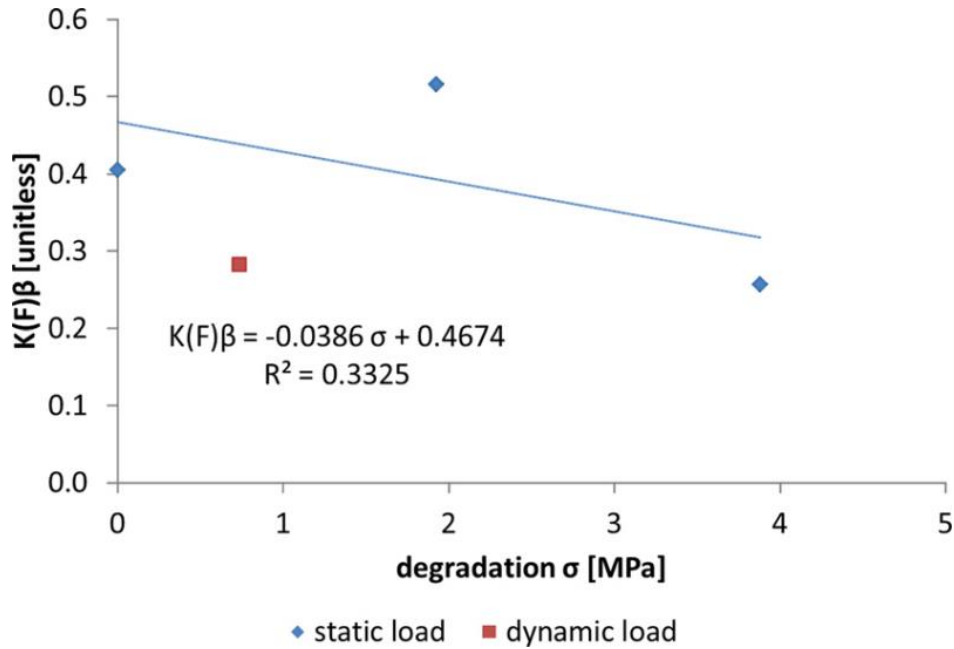


*Figure 62.* The model parameter  $K_\beta$  for each static loading group was fitted to a linear model. The values for the dynamic load are also shown (red square) but not included when determining the linear relationship between  $K_\beta$  and degradation stress.

While fiber degradation caused changes in mechanical behavior after 9 months, it is important to note that the fibers maintained their mechanical properties well during the initial stages of degradation. The changes in  $\beta$ , yield strain, and yield stress all indicate that

the bulk of the degradation of these properties occurred at later time points. PLLA constructs in the literature have also exhibited long-term maintenance of material properties before degradation begins to affect the mechanical behavior of the material (Fan et al. 2008, Tsuji et al. 2000). This suggests that the material is a good choice for biodegradable stent fibers, which must maintain their mechanical integrity while the artery remodels.

One of the main purposes of this study was to identify trends in the data, which could be used to predict the change in mechanical properties with degradation. Percent crystallinity was chosen as one possible factor to examine given that it has been shown to have an effect on both the mechanical behavior of a nondegraded polymer (Perego et al. 1996) and on the degradation of the molecular weight (Tsuji 2008, Tsuiji et al. 2000). We attempted to identify a relationship between the change in mechanical properties and the change in crystallinity. No relationship between  $\mu$  and percent crystallinity was observed; however, a linear relationship between crystallinity and  $\beta$  was observed. It is doubtful that percent crystallinity would provide a good prediction of material constant values during fiber degradation given the weakness of the correlation; however, this relationship does give some interesting insight into the degradation process. PLLA is a semicrystalline polymer consisting of both amorphous and crystalline regions. During the degradation process, the amorphous regions degrade first resulting in an increase in fiber crystallinity similar to that observed in our results (Tsuji 2008). In addition to the increase in fiber crystallinity, we observed a linear relationship between  $\beta$  and crystallinity. This is counterintuitive given that an increase in  $\beta$  corresponds with a decrease in overall fiber rigidity. This result suggests

that the change in  $\beta$  reflects something more than the change in crystallinity with degradation.

One limitation to this study is the long degradation time necessary to observe changes in these fibers. PLLA stents in vivo have a degradation time of approximately 2 years, and previous studies in this laboratory have shown that changes in mechanical properties of PLLA stent fibers do not begin to degrade until 12 months (Soares 2008, Onuma and Serruys 2011). In order to shorten the time necessary to perform these studies, they were carried out at 45°C in order to accelerate the degradation of the fibers and obtain a 15-month degradation profile in approximately half of that time. This approach is based on the approach used by Weir et al. (Weir et al. 2004). Other methods of accelerating degradation were also considered. However, increasing the degradation temperature while maintaining it below the glass transition temperature was the best option to conserve the original degradation and erosion mechanisms (Tsuji 2008). The Arrhenius equation was used to approximate the increased degradation rate in the unloaded samples at 45°C. There are some reservations expressed in the literature regarding the applicability of the Arrhenius equation to solids as the Maxwell–Boltzmann energy distribution function used to develop the relationship is not applicable to solids (Galwey and Brown 2002). However, there is currently no widely accepted alternative to the Arrhenius equation, which has been successfully used to predict temperature dependent behavior of polymers in the past (Weir et al. 2004, Galwey and Brown 2002). In addition, the energy distribution functions used to describe solids approximate to the same form as the Maxwell–Boltzmann energy

distribution function (Galwey and Brown 2002). One further limitation of increasing the degradation rate through an increase in temperature is that the total number of cycles experienced throughout the degradation period is less than what would be experienced by a nonaccelerated fiber. In this study, the loading was kept the same to more closely mimic the loading rate experienced in vivo and to preserve the original degradation and erosion mechanisms experienced during nonaccelerated degradation. In addition, we chose to keep the loading frequency at 1 Hz in part to avoid issues associated with the viscoelastic behavior of these polymers.

Another possible limitation of this study is the relatively simple mechanical environment to which the PLLA fibers were subjected. Although stents experience a more complex loading environment in vivo, this study represents a first and important step in understanding how loading will affect the material behavior. This is important for the development of a useful mathematical model, which necessitates first understanding the material's response to uniform loading conditions that can then be extrapolated to the more complex scenarios in vivo. Future studies will look at compressive loads and loads, which exceed the yield stress (as would be relevant for a balloon-expandable stent design).

The experimental results from this study were used to evaluate and further define the degradation model developed previously (Rajagopal et al. 2007, Soares et al. 2010, Soares et al., 2009). This model quantifies the change in degradation through the use of the degradation constant  $K_{\beta}$ , which is a function of deformation. While the model is able to

describe the degraded values of  $\beta$  with accuracy, it did have some limitations that caused difficulty when fitting the data. Processes at work in early time points lead to an initial increase in rigidity, which is reflected in the nonsignificant increase in  $\mu$  and decrease in  $\beta$  before the deterioration of the mechanical behavior. As it is currently constructed, the model does not account for these phenomena. Previous studies have also recorded an initial decrease in tensile modulus in degrading PLLA constructs. This has been attributed to swelling, which occurs when the polymer is initially submerged (Deng et al. 2005). Future work will focus on incorporating this behavior into the model. The statistical analysis is limited by the low number of samples in each group. In this case, the limited number of fibers made this unavoidable. However, these experiments provide an important first step in comparing the model to experimental data and in planning future studies of this kind.

In addition, the model assumes that the highest rates of degradation are observed at the earliest time points when the availability of unbroken bonds is highest (Rajagopal et al. 2007). However, our results indicate that higher rates of material constant degradation are observed at later time points. At the same time, the model assumes that, in the absence of loading, the degradation response will be trivial (Rajagopal et al. 2007). However, this assumption is only valid if the application of load decreases the degradation time scale significantly compared to the unloaded control. For the levels of loading observed in this study, the degradation time scales were similar between loaded and unloaded. Despite these limitations, the degradation model was still able to fit the values of  $\beta$  with accuracy and elucidate overall trends in the data.



Finally, although this model is able to describe the observed degradation behavior, it does not take into account the viscoelastic nature of the PLLA fiber. Although some initial modeling efforts have been made in this direction, more work is needed in this area (Soares 2008, Muliana and Rajagopal 2012).

### **Conclusion**

Overall, our results indicate that the type and magnitude of degradation load has some effect on fiber degradation rates; however, these changes are most apparent at later time points. In addition, our fitting of the degradation model to the experimental data indicate that it is a good predictor of material degradation behavior. However, we have also identified some areas of weakness in the model, which will help in its further development.

## CHAPTER V

### CANINE FRACTURE FIXATION DEVICE COMPARISON<sup>2</sup>

The author analyzed the data for the bending moment and angle calculations and worked closely with Caleb Davis, who was responsible for the data analysis for this study.

In Vitro Biomechanical Comparison of 3.5 mm LC-DCP/  
Intramedullary Rod and 5 mm Clamp-Rod Internal Fixator (CRIF)/  
Intramedullary Rod Fixation in a Canine Femoral Gap Model

The clamp rod internal fixation (CRIF) system was developed to provide veterinary orthopedists with a versatile and effective internal fracture fixation system requiring minimal implant and instrumentation inventory. Originally called the VetFix (Zahn et al. 2004), the CRIF system consists of cylindrical 316L stainless steel connecting rods available in a variety of lengths and diameters (2, 3, and 5 mm) that can be contoured in 3 dimensions with custom bending pliers. Each rod accepts 2 varieties of clamps, which are applied by sliding the clamps along the rod from either end using clamp-spreading forceps. Side

---

<sup>2</sup> Reprinted with permission from “In Vitro Biomechanical Comparison of 3.5 mm LC-DCP/Intramedullary Rod and 5 mm Clamp-Rod Internal Fixator (CRIF)/Intramedullary Rod Fixation in a Canine Femoral Gap Model” by Bonin, Baker, Davis, Bergerson, Hildebrandt, Hulse, Kerwin, Moreno and Saunders, 2014. *Veterinary Surgery*, 43(7)860-8, Copyright 2014 by The American College of Veterinary Surgeons.

clamps placed along the length of the rod accept traditional bone screws, whereas end clamps accept traditional bone screws at the end of connecting rods. End clamps are manufactured with interference rings that prevent clamp sliding and capture each end of the connecting rod. The ability to select rod length, shape, clamp number, clamp position, and clamp orientation provide substantial versatility to this unique fixation system.

Although the CRIF is currently used clinically, there are relatively few reports describing the biomechanical properties and clinical outcome of this system. In 2004, Zahn described the use of the CRIF for stabilization of a variety of appendicular and axial fractures in 120 dogs and cats (Zahn et al. 2004). Of the 90 animals available for follow-up, 86 (95%) had successful fracture healing. In 2008, Zahn and colleagues evaluated the mechanical properties of 18 different bone plates and the CRIF in vitro using a gap model and Canevasit bone substitute (Zahn et al. 2008). The 5mm CRIF system (which accepts 3.5 mm bone screws) had increased bending stiffness ( $0.85 \text{ N m}^\circ$ ) compared to 3.5 mm Dynamic Compression Plates (DCP;  $0.71 \text{ N m}^\circ$ ) or Limited Contact-Dynamic Compression Plates (LC-DCP;  $0.57 \text{ N m}^\circ$ ). However, when evaluated in torsion, the CRIF had decreased torsional stiffness ( $0.41 \text{ N m}^\circ$ ) when compared to 3.5 mm DCPs ( $0.48 \text{ N m}^\circ$ ) or LC-DCPs ( $0.42 \text{ N m}^\circ$ ). It was hypothesized that either structural properties of the CRIF system or mode of application to the Canevasit bone substitutes may have explained the decreased torsional stiffness. It was suggested that increasing the friction interface between clamps and connecting rods along with slightly contouring the rod in 3-dimensions would improve torsional stiffness. Based on this recommendation,

the surface of the current CRIF rod is roughened to increase the friction between the rod and clamps. Plate/rod fixation, or the combination of a bone plate with an intramedullary (IM) pin, is a common and effective technique for stabilization of comminuted long-bone fractures (Reems et al. 2003, Hulse et al. 1997, Hulse et al. 2000, Goh et al. 2009). A previous report described clinical use of the CRIF system in combination with IM pins and is referred to as CRIF/ rod fixation (Kerwin et al. 2004). In this small case series, 7 dogs treated with CRIF/rod fixation had successful fracture healing. Whereas this case series suggests that CRIF/rod fixation may be a suitable alternative to plate/rod fixation, biomechanical studies comparing the CRIF system to bone plates in combination with intramedullary pins are lacking. Thus, our purpose was to compare the in vitro biomechanical properties of a 3.5 mm LC-DCP/rod construct to a 5 mm CRIF/rod construct using a canine femoral gap model. Based on the structural properties and previous reports of 3.5 mm LC-DCP and 5 mm CRIF systems, we hypothesized that when compared to a 3.5 mm LC-DCP/rod construct, the 5 mm CRIF/rod construct would demonstrate increased construct stiffness and strength when examined in bending and decreased construct stiffness and strength in torsion.

### **Materials and Methods**

Canine femora (n=10 pair; 20 total limbs) were collected from healthy, skeletally mature large breed dogs (35–45 kg) euthanatized for reasons unrelated to this project. Each femur was dissected free of surrounding soft tissues, wrapped in isotonic saline (0.9% NaCl) solution soaked towels, double sealed in plastic specimen bags, and stored at 20°C until

testing. Left and right femora from each dog were randomly assigned to either LC-DCP/rod or CRIF/rod treatment groups using a randomization chart. Bone specimens were thawed overnight at room temperature and orthogonal view digital radiographs were obtained of each femur to screen for pre-existing trauma or other radiographic abnormalities. Femoral pairs with radiographic abnormalities were excluded from further analysis. A 10 cm radiographic calibration marker (10 cm marker, Biomedtrix, Boonton, NJ) was positioned adjacent to each femur and equidistant from the radiographic detector to allow digital calibration and measurement of each specimen. Digital radiographic images were stored on a local and off-site picture archiving and communication system (PACS) and evaluated with commercially available software (eFilm version 3.3, Sound-Eklin, Carlsbad, CA).

The mid-diaphysis of each femur was located using pre-implantation radiography and confirmed by direct measurement of each specimen. A 40 mm osteotomy was centered on the mid-diaphysis of each femur. Next, a 5/32 in. (3.175 mm) IM pin (Imex™ Veterinary, Inc., Longview, TX) was placed in a retrograde fashion using a battery powered drive system (Small Battery Drive System, SynthesVet®, West Chester, PA). Intramedullary pin size was selected to ensure that 35–40% of the endosteal diameter of each bone was filled by the IM pin based on previously published work (Hulse et al. 2000). Whereas small variations in endosteal diameter existed between bone pairs, IM pin size remained constant across all specimens. IM pins were retrograded along the caudomedial cortex of proximal bone segments and driven proximally to exit within the craniolateral aspect of the

trochanteric fossa. A 40 mm spacer was used to maintain a 40 mm gap while IM pins were inserted into the distal bone segment. Pins were driven along the caudomedial aspect of the distal bone segments until seated into the cancellous bone of the medial femoral condyle. Gaps were measured again to confirm the 40 mm defect.

For femora assigned to the LC-DCP/rod group, a 9 hole, 119 mm long, 3.5 mm stainless steel LC-DCP (SynthesVet®) was contoured to the lateral aspect of the femur using a bending template and hand-held bending pliers. LC-DCP were placed along the lateral aspect of each bone so that 3 plate holes were positioned over the proximal bone segment, 3 holes were positioned over the gap, and 3 holes were positioned over the distal bone segment (Figure 63). Three 3.5 mm bicortical bone screws were used to secure the plate to each bone fragment using standard AO/ASIF technique (Koch et al. 2005). Each screw hole was prepared with a 2.5 mm drill bit using a 3.5 mm LC-DCP drill guide in bridge mode, followed by manual insertion of a 3.5 mm tap. Screws were subsequently inserted with a small hexagonal screwdriver and manually tightened. Bone screws and all instrumentation were acquired from SynthesVet®. Femoral gaps were again measured to confirm a final 40 mm defect.

For femora assigned to the CRIF/rod group, a 5 mm diameter CRIF connecting rod (length=120 mm) was contoured to the lateral aspect of each femur using custom CRIF bending pliers. Six clamps were placed along each rod with 3 clamps positioned along the proximal aspect of the rod and 3 clamps positioned along the distal aspect of the rod. Four

side clamps and 2 end clamps were used for each specimen. To ensure that the working length of both LC-DCP/rod and CRIF/ rod constructs were equal, the side clamps adjacent to the gap were positioned 53 mm apart, the same distance as the 2 innermost LC-DCP bone screws. End clamps were secured to the end of each connecting rod 120 mm apart, a distance similar to the length of the LC-DCPs. Bicortical bone screws (3.5 mm) were placed through each CRIF clamp in the same order for each specimen (Figure 63); the number 1 screw (most proximal) was placed 1st, followed by the number 6 screw (most distal), then the 3rd, 4th, 2nd, and 5th screws. Screw placement was performed in a manner identical to the LC-DCP/rod constructs, with the exception that drill holes were prepared using a 3.5 m universal drill guide. All CRIF materials and instrumentation were acquired from SynthesVet®. Once the CRIF was secured to each femur, the gap was again measured to confirm the 40 mm gap was maintained. All implants were placed by a single investigator (G.A.B.). Implant/bone constructs were radiographed to confirm proper implant placement. Constructs were individually wrapped in isotonic saline-soaked towels, double sealed in specimen bags, and stored at 4°C overnight in preparation for mechanical testing.

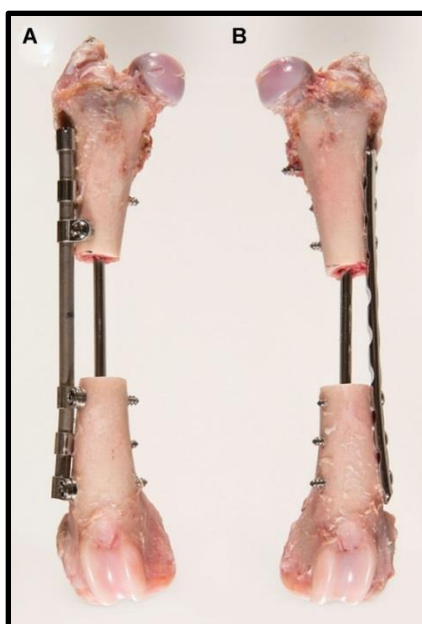


*Figure 63.* Representative photograph of paired canine femora implanted with either CRIF/rod (A) or LC-DCP/rod (B) fixation before potting for mechanical testing.

Endosteal diameter, IM pin diameter, and percentage IM pin canal fill were determined for each implant/bone construct using post-implantation radiographs and eFilm software. After calibration to the 10 cm marker, endosteal diameter, and IM pin diameter were measured at both the proximal and distal aspect of the defect using the craniocaudal radiographic projection (2 measurements/specimen/radiograph). Accurate measurements of endosteal and IM pin diameter were not possible on mediolateral projections because of the summation of LC-DCP or CRIF implants, the IM pin, and bone. Percentage canal fill was determined at the proximal and distal aspect of the defect by the following formula:  $\text{IM pin diameter} / \text{endosteal diameter} \times 100$ . Mean canal fill values were subsequently generated to represent a percentage canal fill for each specimen. Percentage canal fill values were



reported for each treatment group (LC-DCP/rod vs. CRIF/rod) as mean ( $\pm$ SD) and compared using Student t tests. Statistical significance was set at  $P \leq .05$ .

#### **Four-Point Bending Load Tests**

Five of the 10 pairs of femora (10 implant/bone specimens) were evaluated under 4-point bending loading conditions. Before testing, the ends of each specimen were potted in polyvinylchloride (PVC) and secured to aluminum housings using West System Epoxy Resin 105 with Extra Slow Hardener 209 (West System, Inc., Bay City, MI). A custom jig was designed to ensure the samples were potted such that the IM pin was aligned perpendicular to the direction of motion of the load frame crosshead. To ensure the working length of each construct was approximately the same for all specimens, the bone-device constructs were potted such that the ends of the fracture fixation device were 1 cm from the surface of the potting material. During the potting process, samples were maintained in saline soaked towels to prevent moisture loss. Potted specimens and associated housings were then mounted to a TestResources 830-36 Dual Column Axial/Torsion Load Frame outfitted with a custom made 4-point bending fixture. The constructs were oriented so that the fixation devices were on the tension side or outer radius of curvature when loaded. In conventional 4-point bend loading, the ends of the test specimen are free to translate toward each other as bending is induced and the ends of the specimen rotate about the inner bend points. A linear bearing and hinge combination was used to accommodate this tendency and facilitate free bending motion of the potted specimens.

Aluminum prongs attached to the load frame crosshead were used to apply the respective loads to the potted specimens. The prongs contacted 2 aluminum housings that were attached to the testing frame with hinges. This allowed each housing to rotate as load was applied (Figure 64). The hinges served as the outer bend points for the specimen, while the surface of the potting material near the sample was considered the inner bend point. The crosshead was lowered until the aluminum prongs made contact with the surface of the aluminum housings used to secure the specimens. A manual measurement protocol was used to adjust the system components to ensure a balanced symmetrical alignment of the applied load.

A single load to failure 4-point bending protocol was then initiated. A stroke control method was used wherein the crosshead was lowered at a rate of 10 mm/min as previously described by Zahn et al. (Zahn et al. 2008). The constructs were loaded to failure, which was defined as 1 of the following: (1) observable evidence (visual or auditory) of bone fracture; or (2) a sudden drop in load indicative of yielding. Load and displacement data were recorded and analyzed to determine construct stiffness, strength, and bending angle at failure using a modified form of the methods described by Zahn et al. (Zahn et al. 2008) (Figure 65). The load required to achieve the specified stroke position was recorded at a sample rate of 100 Hz.

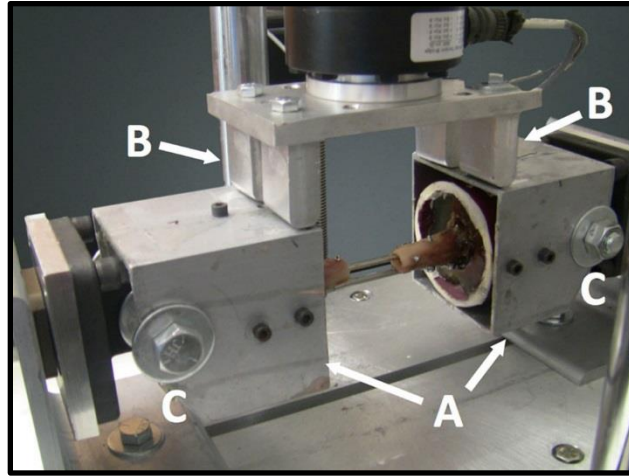


*Figure 64.* Four-point bending fixture.

Specimens were potted in PVC and secured to aluminum housings (A) using a jig designed to align the long axis of the IM pin perpendicular to the cross-head axis. CRIF or LC- DCP implants were oriented on the outer radius of the 4-point bend. A custom fixture was designed to contact the innermost aspects of each housing, thus serving as the innermost points of the 4-point bend (B). The aluminum housings containing potted specimens were secured to hinges (C), which served as the outermost points of the 4-point bend.

The moment arm and angle calculations took into account the axial translation of the loading points because of the influence of the linear bearings (Figure 65). Data were extracted at each integer degree of bending and the bending moment versus bend angle data were plotted for each construct. A linear curve fit was applied to the bending moment versus bend angle data for each construct to determine the construct stiffness, that is, the slope of the bending moment versus bend angle curve.

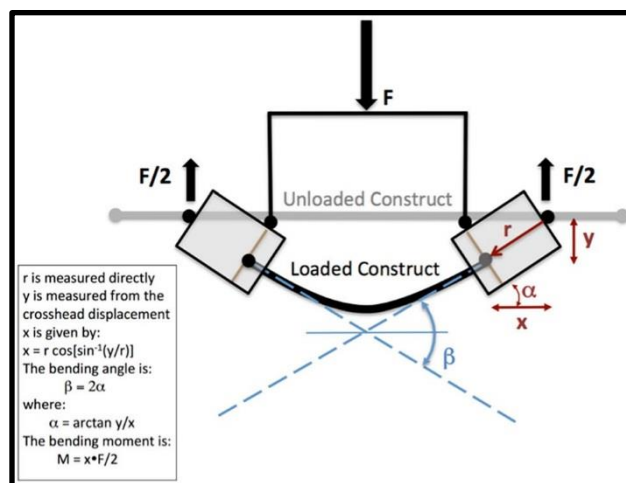


Figure 65. Geometry of the 4-point bending testing device.

Recorded data during testing included load ( $F$ ) and the vertical displacement ( $y$ ). The horizontal distance ( $x$ ) between the outer and inner 4-point bend contact points was calculated based on the known radius ( $r$ ) and vertical displacement data ( $y$ ) using the following equation:  $x = r \cos[\sin^{-1}(y/r)]$ . The bending moment ( $M = x \times F/2$ ) and bending angle ( $\beta = 2\alpha$ ) were determined as illustrated.

Mean ( $\pm$ SD) construct stiffness was calculated for LC-DCP/ rod and CRIF/rod treatment groups. Construct strength, defined as the bending load at construct failure, was also determined for each specimen and averaged for each treatment group. Paired Student  $t$ -tests were used to determine if differences in stiffness and strength existed between treatment groups. Statistical significance was set at  $P \leq 0.05$ .

### Torsional Load Tests

The other 5 pairs of femora were evaluated under torsional loading conditions. Before testing, the ends of each specimen were potted in PVC housings following the same protocol described for the 4-point bend tests (Figure 66). A custom jig was designed to ensure the

samples were potted such that the IM pin was aligned with the axis of rotation. Potted samples were then mounted to the load frame. Application of torsional loads results in twisting of the specimen, as one end is rotated with respect to the other. Thus, twist refers to the angular deformation resulting from the application of a torsional load. As the specimen is twisted there is a tendency to shorten in the axial direction, which results in increasing tensile stresses if the test construct is fixed in the axial direction. For this reason, a load control method was used with the vertical displacement motor on the load frame, wherein a small constant 10 N compressive load was maintained in the axial direction during torsional loading to mitigate the effects of increasing tension in a system that is deformed in torsion (Walsh et al. 2002). The small axial load ensured that the aluminum potting housings moved closer to each other as the implant/bone specimen shortened during twisting. This prevented the constructs being pulled from the potting material. A displacement control method was used with the torsion motor on the load frame wherein the samples were twisted 30° at a rate of 12°/min (Zahn et al. 2008). A twist angle of 30° was chosen as the endpoint as it is consistent with substantial clinical failure. Once 30° of twist was achieved, the torsional load required to achieve the target twist angle was removed and the constructs were allowed to recoil freely. Residual twist was then recorded as permanent angular deformation. Rotation of the CRIF rod within the CRIF clamps was anticipated under torsional loading conditions given the cylindrical geometry of the rod and the orientation of the rod with respect to the applied torsional load. As such, an index marking was created on each CRIF/rod construct such that rotation of the connecting rod within the CRIF clamps could be identified (Figure 67). The purpose of the index markings was strictly to provide

visual evidence whether slippage of the rod occurred, not to quantify such slippage, as the resolution of the markings was not sufficient for such a purpose.

During torsional loading, torque versus twist angle data were acquired for each specimen at a sample rate of 100 Hz. Torque (Nm) data at each integer degree of twist were then extracted for analysis. A linear curve fit was applied to the torque versus twist angle data to determine torsional stiffness of each construct, that is, the slope of the torque versus twist angle curve. Mean  $\pm$  SD torsional stiffness for both LC- DCP/rod and CRIF/rod treatment groups was calculated.



---

*Figure 66.* Torsion testing fixture. Specimens were potted in PVC housings using a jig designed to center the long axis of the IM pin within the torsional axis.

Torsional “strength” was defined and recorded for each specimen as the torque measured at 30° twist. These data were also averaged for each treatment group (mean  $\pm$  SD). Paired Student t-tests were used to identify significant differences in torsional stiffness, strength, and permanent angular deformation between treatment groups with  $P \leq 0.05$ .

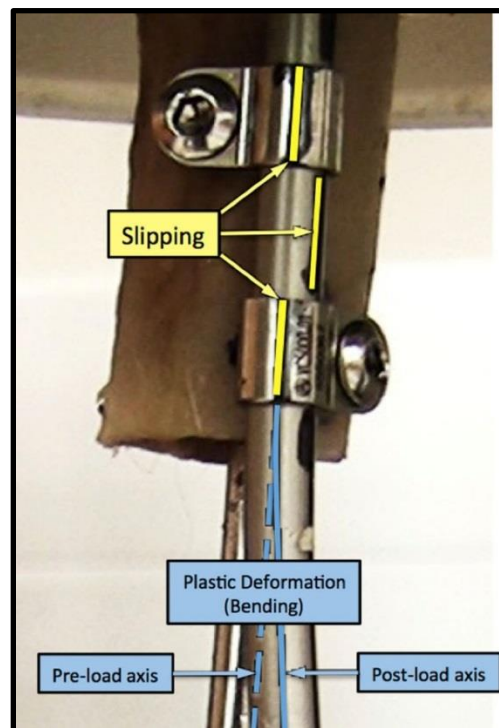


*Figure 67.* Representative photograph of a CRIF/Rod specimen upon completion of torsional testing.

Index markings (yellow) were placed on each CRIF clamp and connected by index markings placed on the lateral aspect of the CRIF connecting bar. Upon completion of torsion testing, index markings on clamps were no longer aligned with the adjacent markings on the connecting bar, demonstrating clamp slippage occurred during torsional testing. In addition, plastic deformation of the CRIF connecting rod was evident, as illustrated by the pre- and post-load connecting rod axis (dashed blue line and solid blue line, respectively).

## Results

### Four-Point Bending

LC-DCP/rod constructs and CRIF/rod constructs performed similarly when subjected to 4-point bend loading conditions (Table 26). LC-DCP/rod constructs had slightly higher bending strength ( $134.51 \pm 78.29$  N m) when compared with CRIF/rod constructs ( $94.34 \pm 13.46$  N m); however, these differences were not significant ( $P=0.277$ ). Differences in stiffness between LC-DCP/rod constructs ( $2.54 \pm 0.82$  N m/ $^{\circ}$ ) and CRIF/rod constructs ( $2.56 \pm 0.71$  N m/ $^{\circ}$ ) were not significantly different ( $P=0.97$ ; Figure 68). Lastly, differences in the bending angle at failure between the LC-DCP/rod constructs ( $37.35 \pm 4.69^{\circ}$ ) and the CRIF/rod constructs ( $35.40 \pm 4.93^{\circ}$ ) were not significantly different ( $P=0.599$ ). Implant/bone constructs failed by acute bone fracture. Differences in the percentage IM pin canal fill for LC-DCP/rod ( $36.2 \pm 4.5\%$ ) and CRIF/rod ( $36.6 \pm 4.7\%$ ) treatment groups were not significantly different ( $P=0.374$ ).

### Torsional Analysis

Performance of CRIF/rod constructs and LC-DCP/rod constructs was similar at torsional loads  $<4.92$  N m, but significantly different at loads  $>4.92$  N m (Table 27). Below the 4.92 N m threshold ( $10^{\circ}$  twist), there was no difference in the torsional stiffness of LC-DCP/rod constructs ( $0.553 \pm 0.134$  N m/ $^{\circ}$ ) and CRIF/rod constructs ( $0.543 \pm 0.056$  N m/ $^{\circ}$ ;  $P=0.819$ ). However, above the 4.92 N m threshold, LC-DCP/rod constructs had significantly greater torsional stiffness ( $0.303 \pm 0.079$  N m/ $^{\circ}$ ) than CRIF/rod constructs ( $0.06 \pm 0.013$  N m/ $^{\circ}$ ;  $P=0.003$ ). Torsional stiffness of both constructs decreased with



increasing torsional loading (Figure 69), with the CRIF/rod constructs experiencing an 89% decrease in torsional stiffness when subjected to torsional loads  $>4.92$  Nm compared with torsional loads  $<4.92$  Nm. In comparison, the LC-DCP/rod constructs experienced a smaller 46% decrease in torsional stiffness under similar torsional loading conditions.

Table 26. *Mean  $\pm$  SD Values for 4-Point Bending*

	LC-DCP	CRIF	<i>P</i> -Value
Four Point Bending Results			
Construct Stiffness [Nm/°]	2.54 $\pm$ 0.82	2.56 $\pm$ 0.72	.967
Ultimate Strength [Nm]	134.51 $\pm$ 78.29	94.34 $\pm$ 13.46	.277
Bending Angle at Failure [°]	37.35 $\pm$ 4.69	35.40 $\pm$ 4.93	.599

Lastly, the CRIF/rod constructs had significantly higher permanent angular deformations ( $23.1 \pm 0.89^\circ$ ) compared with LC-DCP/rod constructs ( $7.47 \pm 2.08^\circ$ ), when torsional loads were removed at the end of the loading cycle ( $P < 0.001$ ). As evidenced by visual inspection of the CRIF connecting rod and the index markings on the rod and clamps, the permanent angular deformation of the CRIF/rod constructs was the consequence of rod slippage and rotation within the clamps as well as plastic deformation of the rod itself (Figure 67). Differences in the percentage IM pin canal fill for LC-DCP/rod ( $37.6 \pm 3.3\%$ ) and CRIF/rod ( $37.6 \pm 2.8\%$ ) treatment groups were not significant ( $P=0.967$ ).

## Discussion

We compared the biomechanical properties of LC-DCP/rod and CRIF/rod constructs in a canine femoral gap model. Zahn and colleagues previously reported that the 5 mm diameter than both 3.5 mm DCP and LC-DCP (Zahn et al. 2008) however, LC-DCP and CRIF were evaluated in a gap model using Canevasit bone substitute and examined under

bending or torsion in a single load to failure experimental design. We commonly use both LC-DCP and CRIF systems in conjunction with IM pins to stabilize comminuted femur fractures. Therefore, our objective was to determine the biomechanical properties of these implant systems when combined with an IM pin in a canine femoral gap model. In contrast to the Zahn study, we did not find a significant difference in bending stiffness, strength, or bending angle at failure for LC-DCP/rod or CRIF/rod treatment groups. Based on structural properties of a 5 mm diameter CRIF connecting rod and a 3.5 mm LC-DCP plate, the cylindrical CRIF connecting rod is predicted to resist load more than a prismatic plate when evaluated in bending. The area moment of inertia, which is a property of shapes used to predict stress and deflections in beams, for the 5 mm diameter CRIF (30.66 mm<sup>4</sup>) is larger than the 3.5 mm LC-DCP (18.2 mm<sup>4</sup> between plate holes, 13.4 mm<sup>4</sup> through plate holes (personal communication, Horan TJ, SynthesVet® design engineer, June 2013). However, our experimental design combined the CRIF system and LC-DCP with IM pins, which have been shown to dramatically reduce implant strain and increase construct stiffness in bending (Hulse et al. 1997, Hulse et al. 2000). The addition of the IM pin to our experimental design likely explains the discrepancy between our bending result and those reported by Zahn et al. (Zahn et al. 2008).

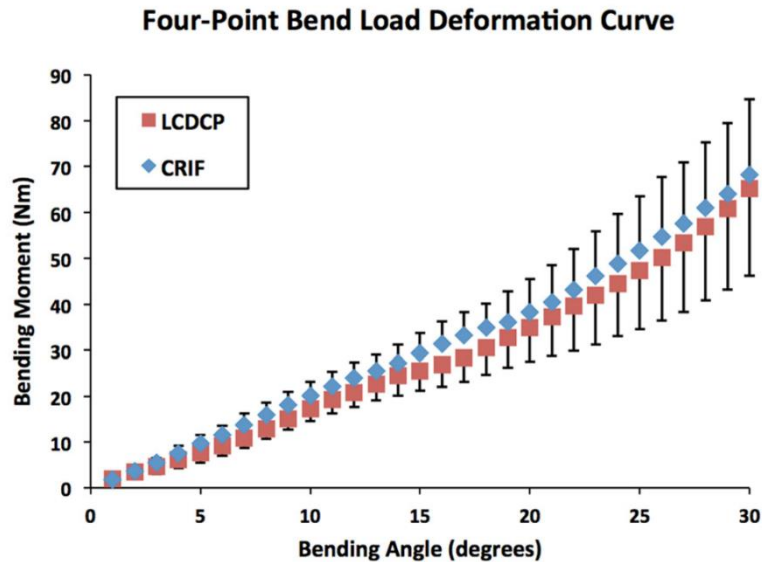


Figure 68. Four-point bend load deformation curve.

For each construct, data were extracted at each integer degree of bending and plotted as mean bending moment versus bending angle  $\pm$  SD (n=5 specimens/ group). A linear curve fit was applied to the bending moment versus bending angle data for each construct to determine the construct stiffness (Table 26).

We selected IM pin size based on previously published recommendations. Whereas there were small variations in endosteal diameter between cadaver specimens, we used an IM pin with a diameter of 5/32 in. (3.175 mm) for all specimens, because this pin filled 35–40% of the endosteal diameter for most of our specimens. When using an IM pin of this size, construct stiffness in bending increases a minimum of 40% when compared with a construct lacking an IM pin (Hulse et al. 2000). Mode of failure under bending loads for both treatment groups was generally bone fracture. Thus, the addition of an IM pin to both LC-DCP and CRIF treatment groups likely resulted in both device configurations being stronger than bone, that is, inclusion of the IM pin relegated the bone as the weakest component in

each implant/bone construct. Because the effect of IM pin diameter on construct stiffness has been adequately described (Hulse et al. 1997, Hulse et al. 2000), we maintained a uniform IM pin size across all cadaver specimens. Importantly, there were no significant differences in percentage canal fill for either LC-DCP/rod or CRIF/rod treatment groups when evaluated in 4-point bend or torsional testing.

We performed Student t-tests on torsional stiffness values at each degree of twist for all CRIF/rod and LC-DCP/rod constructs. Below 10° twist (4.92 Nm) there was no statistical difference in torsional stiffness between treatment groups. However, when the magnitude of twist exceeded 10° (>4.92 N m), a statistical difference was present between 2 constructs (Figure 69). This difference was primarily a consequence of the change in torsional stiffness of the CRIF/rod system, which had biphasic behavior and became much less resistant to torsional loading when the loads exceed 4.92 Nm (Figure 69, Table 27).

Table 27. *Mean ± SD Values for Torsional Testing*

	LC-DCP	CRIF	P-Value
Torsion Results			
Torsional Stiffness below 4.92 Nm [Nm/°]	0.553±0.134	0.543±0.056	.819
Torsional Stiffness above 4.92 Nm [Nm/°]	0.303±0.079	0.06±0.013	0.003*
Strength at 30° [Nm]	11.546±2.79	6.078±0.527	0.012*
Permanent angular deformation after 30° torsion [°]	7.47±2.08	23.1±0.89	<.001*

\*Denotes statistically significant differences between treatment groups at  $p \leq .05$ .

We hypothesize that as torsional loads are increased, the frictional forces between the CRIF rod and clamp are eventually exceeded, and slippage of the connecting rod within the connecting clamps occurs. This hypothesis is supported by previous reports and also by our results (Figure 67; Zahn et al. 2008). Based on previous recommendations by Zahn and colleagues, the CRIF connecting rods we used were textured to increase the frictional interface between the connecting rod and underside of the connecting clamps. This frictional interface is the primary mode of fixation between the rod and clamps. Under torsional loads, the frictional forces holding the rod in place within connecting clamps are exceeded and the rod simply slips within the clamp, resulting in an apparent decrease in construct torsional stiffness. Visual inspection of the CRIF/rod construct index markings (Figure 67) provided conclusive evidence that there is a combination of plastic deformation (bending) of the connecting rod, as well as slippage of the rod within connecting clamps.

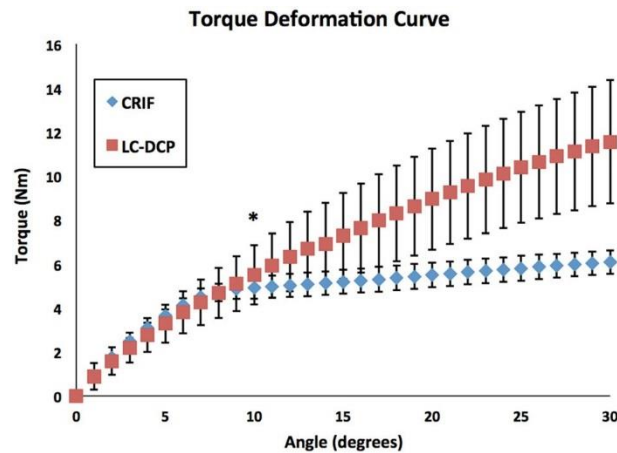


Figure 69. Torque deformation curve.

For each construct, data were extracted at each integer degree of twist and plotted as mean torque versus angle  $\pm$  SD (n=5 specimens/group). A linear curve fit was applied to the torque versus twist angle data to determine torsional stiffness (Table 27). While torsional stiffness was not different below 4.92 Nm of load ( $10^\circ$  twist), torsional stiffness was significantly greater for LC-DCP constructs above 4.92 Nm of load. Denotes  $10^\circ$  of twist, which corresponds to 4.92 Nm torsional load and the point at which statistically significant differences were present between treatment groups.

The torsional results we report are similar to those described by Zahn and colleagues. As described in our methods, the IM pin was aligned with the axis of rotation for torsional testing. For this reason, it was unlikely that the IM pin component of our test constructs contributed to torsional stiffness, because it is known that IM pins poorly resist torsional loads (Vasseur et al. 1984, Johnston et al. 2012). Whereas our results suggest that CRIF/rod fixation would thus provide inferior clinical results, we use CRIF/rod fixation successfully to stabilize comminuted femur fractures in dogs. The clinical significance of the 4.92 Nm separation point we detected should be interpreted with caution, because it has been demonstrated that the femur of a 36 kg dog experiences 0.56 Nm of torque at a

controlled leash- walk (Carter et al. 1981). When evaluated in this context, both CRIF/rod and LC-DCP/rod implant systems are likely suitable for repair of comminuted femur fractures in dogs, which is more consistent with our clinical experience with both implant systems. However, the torque applied to a femur of a 36 kg dog during rising, sitting, and uncontrolled activity remains unknown. Furthermore, in a clinical setting both bending and torsional loads are applied simultaneously. As such, initiation of the biphasic torsional behavior of CRIF/rod fixation may occur differently in vivo.

It is also worth noting that LC-DCP/rod constructs had superior recovery from torsional loads as evidenced by the permanent angular deformation data for each treatment group. After an initial twist of 30°, the CRIF/rod constructs remained twisted by  $23.1 \pm 0.89^\circ$  when loads were removed, whereas LC-DCP/rod constructs remained twisted by only  $7.47 \pm 2.08^\circ$  under similar conditions. This disparity in performance is partially a consequence of the slipping of the CRIF rod within connecting clamps. Once the rod slips as the construct is twisted to 30°, it maintains this slipped position upon load removal because of frictional forces between CRIF rod and clamps.

Both bending and torsional stiffness values of the LC- DCP/rod and CRIF/rod constructs evaluated in this study were higher than the stiffness values previously reported for CRIF and LC-DCP implant systems. Two possible explanations exist for these findings. As detailed above, addition of an IM pin dramatically increases a construct's bending stiffness, which explains the higher bending stiffness and strength values we report (Hulse et al. 1997,



Hulse et al. 2000). However, the increased torsional stiffness values we report cannot solely be explained by the presence of the IM pin. The increased torsional stiffness values we describe are likely explained by the constant 10 N compressive load applied to each construct during torsional tests and/or direct interactions between the IM pin and implant-associated bone screws.

There were several limitations to our study. Our experimental design used a single load to failure approach for both bending and torsional experiments. Bending is the most important biomechanical force sustained by the femur during both walking and running in both dogs and people (Hulse et al., 2003, Shahar et al., 2003). For this reason it was important that we evaluate both the LC- DCP/rod and CRIF/rod constructs under bending loads. However, the previous study describing the biomechanical properties of the CRIF highlighted important differences between the 5 mm CRIF and 3.5 mm LC-DCP under torsional loads (Zahn et al. 2008). Based on this work, it was necessary to determine the biomechanical properties of the LC-DCP/rod and CRIF/rod constructs in response to torsional loads. Thus we examined the LC-DCP and CRIF in combination with an IM pin under either bending or torsional loads. Our clinical experience with occasional failure of CRIF/rod stabilization suggests that this implant combination typically fails because of acute mechanical overload during early to mid-stages of fracture healing, as would occur when a post-surgical fracture dog suddenly breaks leash confinement. Our single load to failure experimental design was selected to mimic this clinical scenario. Our results demonstrate important differences in the torsional stiffness of LC-DCP/rod and CRIF/rod constructs, which may explain, from a

biomechanical perspective, acute clinical CRIF/rod failure. The contribution of cyclical loading to the biomechanical properties of LC-DCP/rod and CRIF/rod constructs was not evaluated in our study. Thus, while our study represents an important advance in the understanding of CRIF/rod constructs, additional studies are necessary to evaluate the biomechanical properties of CRIF/rod fixation in response to cyclical loads.

We used digital radiography to evaluate cadaveric bones for pre-implantation abnormalities. Ideally both digital radiography and Dual-energy X-ray Absorptiometry (DEXA or DXA) scanning would have been used to evaluate cadaveric specimens before implantation. DEXA scanning is a validated and widely accepted technique to detect small variations in bone quality (Boer et al. 1999, Gorman et al. 2005, Wahner et al. 1988); however, this equipment was not available. Lastly, as with any cadaveric study, there was variation in the size of bone specimens tested. As detailed above, all bones were from dogs weighing 35–45 kg. The 5 mm CRIF, 3.5 mm LC-DCP, and 5/32 in. (3.175 mm) IM pin were appropriately sized implants for the paired femora examined in our study. In addition, implant/bone/IM pin construct working length was normalized across all specimens by controlling the distance from the surface of the potting material to the end of the CRIF or LC-DCP implants as well as the distance between the outermost and innermost pairs of bone screws.

### **Conclusion**

We concluded that there were no significant differences in the bending stiffness or strength of LC-DCP/rod and CRIF/rod constructs. There were no significant differences in the

torsional stiffness of these systems below 10° of twist (4.92 N m torsion). However, above 10° of twist (>4.92 N m), LC-DCP/rod constructs had significantly higher torsional stiffness, whereas CRIF/rod constructs were not as stiff and had significantly greater permanent angular deformation. Additional cyclical studies are necessary to determine the response of the CRIF/rod system to repetitive physiologic loads.

**Disclosure**

The authors report no financial or other conflicts related to this report.

## CHAPTER VI

### DEVELOPMENT OF AN ELECTROSPINNING SYSTEM FOR THE PRODUCTION OF PARALLEL FIBERS

Congestive heart failure (CHF) is a major public health issue in the developed and developing world. In the U.S., CHF affects more than 5.3 million people with 550,000 new cases diagnosed each year. Approximately 20% of hospitalizations are due to acute CHF, incurring a health-care system cost of \$34.4 billion (Heart Disease and Stroke Statistics 2008). For the 300,000 Americans in end-stage failure transplant is the preferred treatment; however, with less than 3,000 hearts available this treatment plan is epidemiologically trivial (Bennett et al. 2000). The development of a therapeutic option targeting recovery of cardiac function is a substantial advancement in the treatment of heart failure and a great benefit to the healthcare economy, medical science, and society.

Current clinical practice of stem cell related therapies involves injecting the stem cells near the site of the damage and waiting for growth and remodeling to occur. There are several routes the clinician can use to deposit cells including injection directly into the heart muscle, administration via the vascular system and intracoronary injection. Out of these, direct injection is the most widely used (Kaushal et al. 2009, Heldman and Hare 2008). The intracoronary approach involves delivery of the stem cells via a balloon catheter and has the advantage of facilitating flow of the cells to both the infarct and the peri-infarct regions. One of the problems these types of delivery methods are seeing is an inability of the cells to navigate to the dyskinetic region (Kaushal et al. 2009, Paul et al. 2009). Despite this,

improvement in the patient's condition is routinely seen with stem cell therapies (Kaushal et al. 2009, Paul et al. 2009, Braun and Martire 2007, Heldman and Hare 2008, Guan and Hasenfuss 2007, Carmichael 2005, Passier et al. 2008). This is now speculated to come from a paracrine effect in which the presence of the hMSCs alerts the autoimmune system to the infarct region and recruits antiapoptotic factors and angiogenic cytokines (Guan and Hasenfuss 2007), but these benefits are marginal and are not seen at time points longer than 18 months. (Paul et al. 2009). Cell tracking studies have shown that after inducing this autoimmune response, the surviving undifferentiated stem cells exit the body via the bladder with very few cells ever finding the region of interest (Guan and Hasenfuss 2007). Stem cell therapies in large animal models have shown exemplary results, but those results are not being realized in a clinical setting (Paul et al. 2009, Heldman and Hare 2008, Carmichael 2005). Stem cell therapies would benefit from efforts towards confirming the necessary cues for their stimulating differentiation and using that knowledge to establish an effective treatment protocol (Braun and Martire 2007, Heldman and Hare 2008, Passier et al. 2008).

### **Innovation**

The present goal of stem cell therapy is cardiac regeneration. Though stem cell therapy for the treatment of heart failure remains promising, results of stem cell studies have collectively been inconclusive, and perhaps even controversial. Some crucial observations have not been reproducible and conclusions from similar findings have been conflicting (Braun and Martire 2007). Presently, cell-tracking studies are insufficient to answer questions definitively. To accomplish cardiac regeneration, generally three types of tissue generation

are required (1) angiogenesis, (2) arteriogenesis, and (3) cardiomyogenesis. Given this fact, bone marrow derived cells are likely the best cell type to use in meeting the cardiac regeneration objective. Bone marrow contains the endothelial progenitor cells (EPC) necessary for angiogenesis and arteriogenesis; and the mesenchymal precursor cells (MPC) necessary for arteriogenesis and cardiomyogenesis.

The prospect of inducing cardiac regeneration via cell cycle activation, cell transplantation, or stem cell mobilization is greater now than at any previous time (Wollert and Drexler 2010). One important obstacle to be overcome involves establishing the conditions under which transplanted cells may integrate, differentiate and function in harmony with the native tissue. The cues required to drive the transplanted cells through the appropriate processes are largely mechanical in nature. Mechanical cues are transduced by cells which respond biochemically, initiating a variety of potential responses, i.e. proliferation, migration, contraction, alignment, etc. Cardiac muscle fiber alignment can be highly disorganized in the failing heart and disrupted by fibrosis. Transplantation of progenitors in the absence of cues to drive alignment with native heart tissue may not improve global heart function. Therapies based on the direct introduction of cardiomyocytes into the failing heart assume transplanted cells will align, differentiate, and functionally integrate into the host tissue in the absence of the cues that normally drive these processes (Kaushal et al. 2009, Paul et al. 2009, Braun and Martire 2007, Heldman and Hare 2008, Guan and Hasenfuss 2007, Passier et al. 2008, Wollert and Drexler 2010). In cardiogenesis, mechanics play an important role in the appropriate pathfinding, differentiation, and ultimate function of embryonic

progenitors (Lui et al. 2012). In disease, mechanics has also been shown to play an important role in morphogenesis. The “biomechanical model” of heart failure developed by Mann et al. (Mann and Bristow 2005), predicts that when the deleterious changes in cardiac function and cardiac remodeling are sufficiently advanced, they become self-sustaining and hence are capable of driving disease progression independently of the neurohormonal status of the patient.

The heart is essentially a biomechanical pump and the important pillars of biomechanics, i.e. force (stress) and motion (strain), play a fundamental role in the mechanobiology and development of physiologic and pathologic states. The influence of mechanical stimuli on biological processes such as growth and remodeling remains a prominent research interest. Efforts towards unraveling the mechanisms of the disease process require innovative pursuit and are critical to understanding appropriate treatment plans. CHF typically advances following some index cardiac event, e.g. myocardial infarction and the mechanical environment in the infarct region; a region typically targeted for stem cell intervention is highly dyskinetic, emanating aberrant mechanical cues. Marginal success with stem cells has been observed in the infarct border-zone region, where mechanical cues remain somewhat intact. It is proposed that the promise of stem cell therapy as a means of treating heart failure may not be fully realized until we fully understand the effects of the local mechanical environment on stem cell function.

## **Design**

The purpose of this project is to establish a connection between mechanical cues and the differentiation of stem cells, with or without the influence of cardiomyocytes. This will be accomplished using a standard electrospinning setup, a custom designed strain module and various cell culture resources. The subjects of interest in this study are human mesenchymal stem cells and human cardiomyocytes. This project is a collaboration between Texas A&M University and University of Alabama at Birmingham.

### **Strain Module Creation**

This specific aim concerns the development of an in vitro model of a myocardial infarct including healthy, border-zone, and scarred regions that is constructed with fibers of known orientation and cyclic loading, and capable of serving as a cellular scaffold.

This research was focused around building the strain module and was considered met once the proper strains and gradients were achieved and the material was proven to be suitable for cellular seeding. The healthy region was defined as the region exhibiting physiologic strain with no strain gradient, the border zone region showed strain varying from healthy to none and the scarred region had no strain with no strain gradient, representative of scar tissue. This research was crucial to the completion of the study; creating an environment that is physiologically accurate is the foundation for validating this infarct model and its results.



## Methods

To create this model we first created the material. A standard electrospinning setup consisting of a high voltage power supply, a syringe pump, and a conductive receptor for the material was constructed. The first generation of the setup used to spin polycaprolactone polymer dissolved in a dichloromethane/dimethylformamide solution can be seen in Figure 70.

Electrospinning is a well-research procedure that has gained popularity in tissue engineering space. A hemispherical drop of solution suspended on the tip of a syringe needle can be pulled into a conical shape, or Taylor cone, if exposed to an electric field. The drop will continue to extend and distort until a threshold voltage is exceeded, at which point a stable jet of liquid is ejected from the cone tip. At this point, the liquid can either break up into droplets after ejection from the tip or remain as a stream and travel to a grounded target, depending on the viscosity of the solution. The first case, breaking up into droplets, is seen in low viscosity solutions and results in the popular ‘electrospraying’ procedure. The second case, traveling in an intact stream, is only seen with high viscosity solutions, which allow true electrospinning of continuous fibers which have diameters in the sub-micron range (Dietzel et al. 2001) which is the interest of this project. As the stream nears the collector, electrostatic forces cause it to whip back and forth, further thinning the fiber before it finally deposited on the collector. For successful electrospinning, it is important that the rate that the solution is being introduced into the Taylor cone match the rate at which solution is being removed, or else the Taylor cone will collapse (Taylor 1964, Taylor 1969). As the jet

exits the Taylor cone and streams towards the grounded target, the solution evaporates leaving only polymer remaining. Because of this, the solution the material being spun is dissolved in must be quite volatile. Including the rate of solution injection and the composition of the dissolving solution, the other factors important to successful electrospinning are the tip-to-target distance, the voltage applied and environmental factors including humidity (Dietzel et al. 2001).

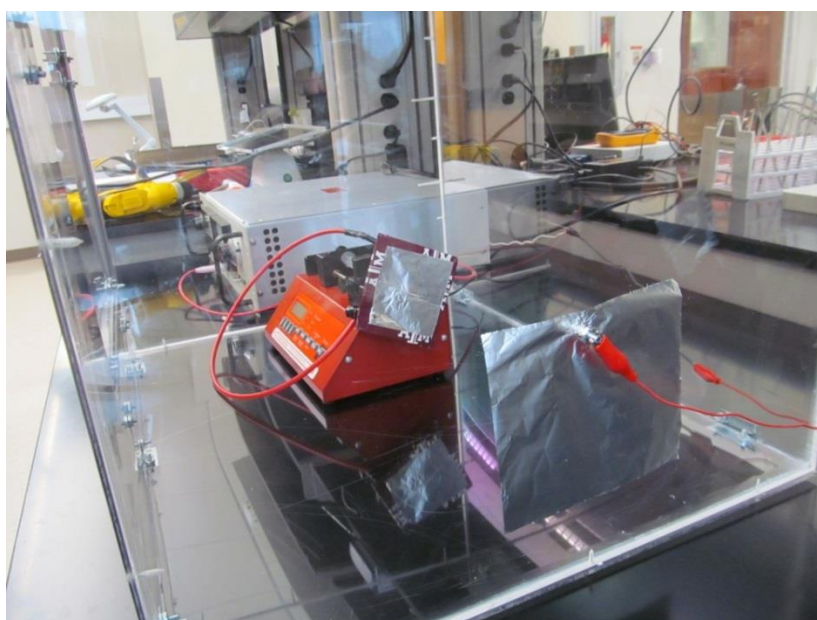


---

*Figure 70.* Generation 1 of the electrospinning set-up. Very generally, this setup contains a high voltage power supply on the left, a syringe pump in the middle and a collector plate on the right.

The material properties of the fibers will have to meet certain specifications as outlined by the strain module. The ideal setup will allow for variation of the feed rate of material, current introduced, voltage introduced, humidity within the spinning chamber, distance to

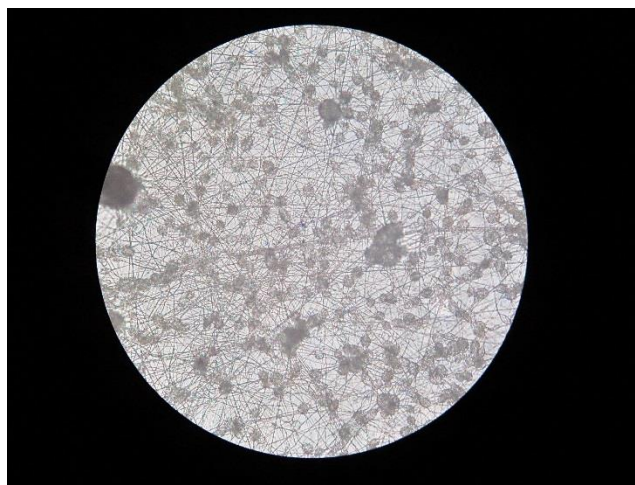
receptor and temperature, all of which have been found to influence the electrospinning process (Fee 2012), as well as providing a containment strategy for the volatile gases. Because of these concerns, the Generation 2 electrospinning set-up was created (Figure 71). Using this setup, we were able to tune the desired properties. The humidity was controlled by adding petri dishes of silica crystals (not pictured) inside containment system, which is sealed. A great deal of effort, both in our lab and in the literature, has gone into electrospinning fibers that are continuous and free from beading. Briefly, the method for creating the PCL/DCM/DMF solution involves adding equal parts DCM and DMF to a 20 mL beaker and dissolving the desired amount of PCL into it through use of a rocker table overnight with parafilm covering the beaker to prevent evaporation. DCM and DMF are both hazardous chemicals that should only be handled by trained lab employees. DCM and DMF will react to plastic, so glass serological pipettes are required for transfer. The researcher must wear the proper personal protective equipment during their interaction with this solution, including a lab coat, durable gloves and eye protection, and all work must be performed in a fume hood or within the containment system of the electrospinning setup.



---

*Figure 71.* Generation 2 of the electrospinning set-up as seen from two views: directly in front (top) and from behind the collector (bottom).

During initial experimentation with solution, the percent solution of PCL, the voltage applied and feed rate of the syringe pump were identified as the most important variables to a successful outcome and were optimized in turn. Fresh dessicant was always present in the containment system and the tip-to-target distance was set at 16 cm. The optimal voltage was found to be 7.2 kV with a feed rate of 4.0 mL/hour. A 12% PCL solution, meaning 0.24g of PCL added to 1 mL of DCM and 1 mL of DMF produced continuous fibers with appreciable beading (Figure 72). This beading is due to low surface tension in the solution and was corrected by increasing the concentration of PCL to 16%, or 0.32g of PCL added to 1 mL of DCM and 1 mL of DMF. The high voltage power supply settings were adjusted to get the same response at a lower potential by varying the current and the fibers seen in Figure 73 were produced.



---

*Figure 72.* 12% PCL/DMF/DCM solution spun at 24 kV with a feed rate of 4.0 mL produces continuous fibers with significant beading.

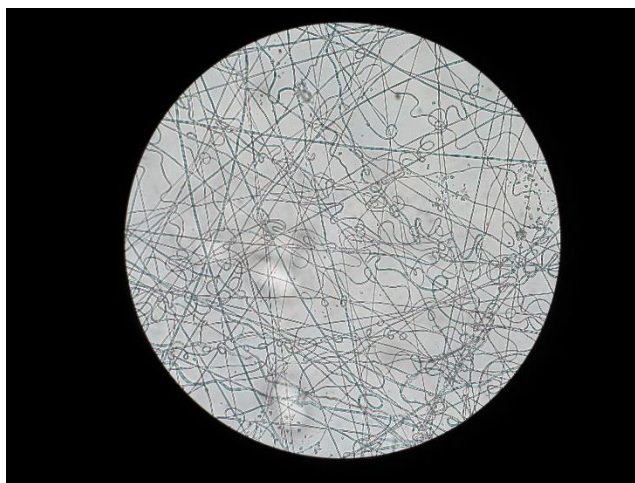
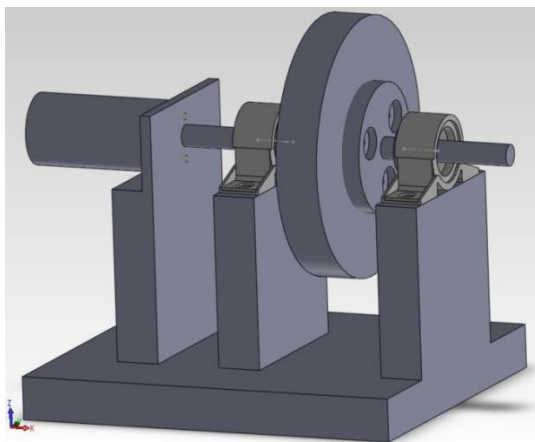


*Figure 73.* 16% PCL/DCM/DMF solution spun at 7.2 kV with a feed rate of 4.0 mL produces the ideal fiber geometry.

Our goal is to be able to electrospin fibers of a known orientation, which for our purposes will be parallel. This has been achieved before but with so many factors affecting the quality of the fibers, the recreation of this setup is nontrivial. We have a rudimentary way of aligning the fibers that involves physically placing them on the jig which is reliable and reproducible, but efforts were put towards finding a more elegant and reliable solution. The material used is a polycaprolactone (PCL) polymer dissolved in a dichloromethane/dimethylformamide (DCM/DMF) solution, a popular blend for these applications and can be sterilized by soaking in 70% EtOH for cell culture. It has been proven to be non-cytotoxic and cells have been cultured on such scaffolds previously, though not in our lab (Fee 2012). The possibility of electrospinning organic material, such as collagen, instead of the biodegradable polycaprolactone is an opportunity for advancement of the field. Organic electrospin fibers would be a novel addition to the

existing technology and therefore pose a considerable challenge. Inability to achieve suitable organic material composition would not hamper the progress of this study, but the ability to create such a material would be beneficial to both this model and the field as a whole.

After reviewing the literature, a spinning wheel was chosen as the collector plate that would produce the most suitable aligned fibers for our eventual goal and current setup. Based on the investigation by Liao et al., a system capable of rotational speeds reaching 4000 RPMs would likely be necessary, as would the ability to ground or negatively charge the wheel in an effort to increase the voltage potential between the tip of the syringe and the collector plate (Liao et al. 2008). A one inch wide spinning surface was chosen as it would produce material sections large enough for both cell culture and hypothesized installation on the straining device. A SolidWorks rendering of the collection wheel can be seen in Figure 74.

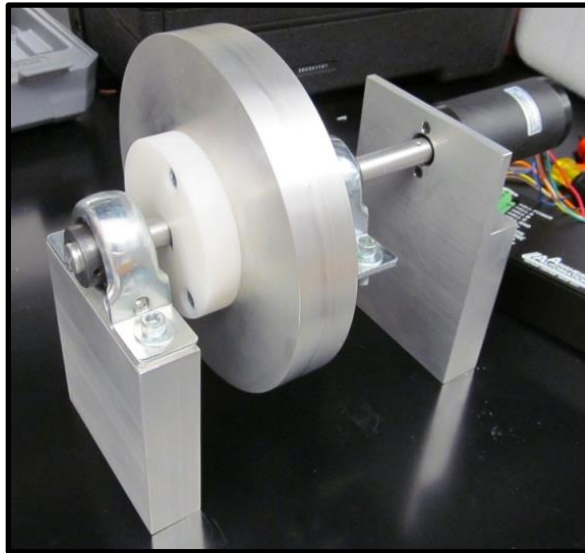


---

*Figure 74.* Solidworks model of the electrospinning wheel, for use in the creation of aligned fibers.



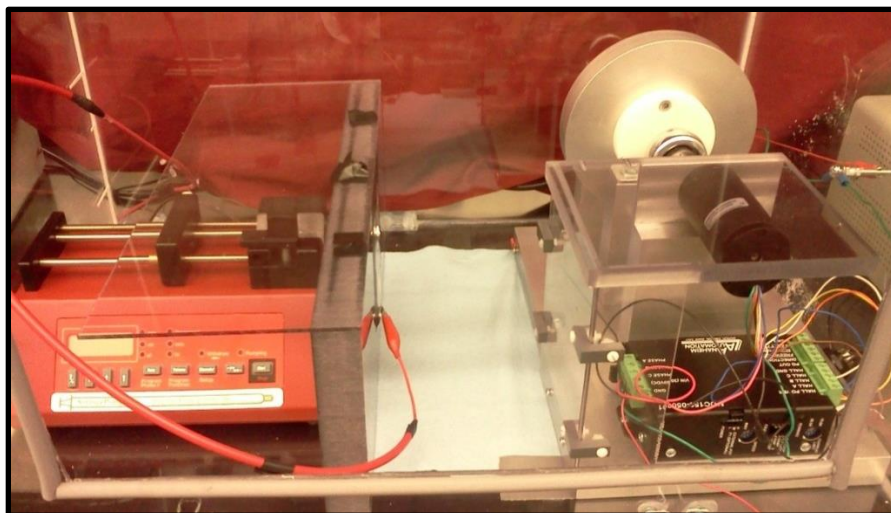
With the help of Carl Johnson, the spinning wheel system was created using the equipment in the machine shop of the Department of Biomedical Engineering at Texas A&M University and can be seen in Figure 75. The entire Generation 3 setup can be seen in Figure 76, and photographic proof of the ability to align fibers can be seen in Figure 77. Unfortunately, work on this project stopped before refinement of the alignment capabilities could occur. The image in Figure 77 was the result of a purely exploratory test in which details as to the percentage PCL, voltage applied, tip-to-target distance and feed rate were not recorded.



---

*Figure 75.* The completed spinning wheel system.





---

*Figure 76.* Generation 3 of the electrospinning setup, capable of creating aligned fibers.



---

*Figure 77.* An example of fiber alignment possible with the Generation 3 setup.

Unfortunately, this work has not yet received funding. As of publication of this dissertation, this system is currently in use to spin suture material housing a drug eluting core.

## CHAPTER VII

### CONCLUSION

The theories of biomechanics were applied in six different investigations in an effort to strengthen the design of medical devices still in the proof of concept stage, create computational packages to allow the appropriate geometric features when subjected to physiologic mechanics and to develop benchtop systems that will allow the investigation of complex research initiatives and the development of future technology.

The first project concerned the design, verification and validation of a novel bone-implant interface for a total knee replacement tibial tray. The findings were encouraging enough to engender support for funding this project through FDA clearance and into clinical trials, after which this technology could someday become commercially available.

The second project involved a novel fracture fixation device that regenerates the bone before biodegrading away. Again, this project had very encouraging results and is currently under consideration for DARPA funding, which would take it through the development stage and toward an investigational device exemption with the FDA.

The third project detailed the generation of a computational model for the biodegradation of materials *in vivo*. The basis for a robust model were laid and, though more work is necessary to refine the parameters, a model for the biodegradation for medical devices such as stents *in vivo* is closer to realization.

The fourth project was an investigation of fracture fixation technology for the veterinary field. This study found that the CRIF system might not perform as well in torsion as the gold standard, but the point of difference between the two is well above what a canine would experience during a controlled leash walk and its versatility in the operating suite could justify its continued use.

Finally, the fifth project detailed the iterative development of an electrospinning system for the lab. The system went through three iterations and is fully capable of spinning continuously aligned fibers that are free from beading. Should funding for this project materialize, it is well positioned for immediate use.

## REFERENCES

- ASTM D695-02a. (2002). *Standard test method for compressive properties of rigid plastics*. West Conshohocken, PA: ASTM International. Retrieved from [www.astm.org](http://www.astm.org)
- ASTM F1044-05. (2005). *Standard test method for shear testing of calcium phosphate coatings and metallic coatings*. West Conshohocken, PA: ASTM International. Retrieved from [www.astm.org](http://www.astm.org)
- ASTM F1160-05. (2005). *Standard test method for shear and bending fatigue testing of calcium phosphate and metallic medical and composite calcium phosphate/metallic coatings*. West Conshohocken, PA: ASTM International. Retrieved from [www.astm.org](http://www.astm.org)
- ASTM F1223-08. (2008). *Standard test method for determination of total knee replacement constraint*. West Conshohocken, PA: ASTM International. Retrieved from [www.astm.org](http://www.astm.org)
- ASTM F1800-12. (2012). *Standard practice for cyclic fatigue testing of metal tibial tray components of total knee joint replacements*. West Conshohocken, PA: ASTM International. Retrieved from [www.astm.org](http://www.astm.org)

- Aerssens, J., Boonen, S., Lowet, G., & Dequeker, J. (1998). Interspecies differences in bone composition, density, and quality: potential implications for in vivo bone research 1. *Endocrinology* 139(2), 663-70.
- Agostinho, F. S., Rahal, S. C., Araujo, F. A P., Conceicao, R. T., Hussni, C. A., El-Warrak, A. O., & Monteiro, F. O. B. (2012). Gait analysis in clinically healthy sheep from three different age groups using a pressure-sensitive walkway. *BMC Veterinary Research* 8(87), 1-7.
- Agrawal, C. M., Huang, D., Schmitz, J. P., & Athanasiou, K. A. (1997). Elevated temperature degradation of a 50:50 copolymer of PLA-PGA. *Tissue Engineering*, 3(4), 345-352.
- An, Y. H., & Friedman, R. J. (1998). Animal selections in orthopaedic research. In Y. H. An & R. J. Friedman (Eds.), *Animal models in orthopaedic research* (pp. 39-57). Boca Raton, FL: CRC Press.
- Au, A. G., Liggins, A. B., Raso, V. J., & Amirfazli, A. (2005). A parametric analysis of fixation post shape in tibial knee prostheses. *Med Eng Phys*, 27, 123- 34.
- Bedoya, J., Meyer, C. A., Timmins, L. H., Moreno, M. R., & Moore, J. E. (2006). Effects of stent design parameters on normal artery wall mechanics. *ASME J. Biomech. Eng.*, 128(5), 757-765.

- Bunger, C. M., Grabow, N., Sternberg, K., Goosmann, M., Schmitz, K. P., Kreutzer, H. J., Ince, H., ... & Schareck, W. (2007). A Biodegradable stent based on poly(lactide) and poly(4-hydroxybutyrate) for peripheral vascular application: Preliminary experience in the pig. *J. Endovasc. Ther.*, 14(5), 725-733.
- Beillas, P., Papioannou, G., Tashman, S., & Yang, K. H. (2004). A new method to investigate in vivo knee behavior using a finite element model of the lower limb. *J Biomech.*, 37(7), 1019-1030.
- Bennett, L. E., Keck, B. M., Daily, O. P., Novick, R. J., & Hosenpud, J. D. (2000). Worldwide thoracic organ transplantation: A report from the UNOS/ISHLT International Registry for Thoracic Organ Transplantation. *Clinical Transplant*, 31-44.
- Bhimji, S., & Meneghini, R. M. (2012). Micromotion of cementless tibial baseplates under physiological loading conditions. *The Journal of Arthroplasty*, 27(4), 648-654.
- Bloemers, F. W., Blokhuis, T. J., Patka, P., Bakker, F. C., Wippermann, B. W., & Haarman H. J. Th. M. (2003). Autologous bone versus calcium-phosphate ceramics in treatment of experimental bone defects. *Journal of Biomedical Materials Research*, 66B(2), 526-531. doi:10.1002/jbm.b.10045
- Boerckel, J. D., Kolambkar, Y. M., Stevens, H. Y., Lin, A. S.p., Dupont, K. M., & Guldberg, R. E. (2011). Effects of in vivo mechanical loading on large bone defect regeneration. *Journal of Orthopaedic Research*, 30(7), 1067-1075.

- Braun, T., & Martire, A. (2007). Cardiac stem cells: paradigm shift or broken promise? A View from developmental biology. *Trends in Biotechnology*, 25(10), 441-447.
- Bryant, B. J., Tilan, J. U. , McGarry, M. H. , Takenaka, N. , Kim, W. C. , & Lee, T. Q. . (2014). The biomechanical effect of increased valgus on total knee arthroplasty: A cadaveric study. *The Journal of Arthroplasty*, 29(4), 722-726.
- Cai, Z.-Y., De- Yang, A., Zhang, N., Ji, C.-G., Zhu, L., & Zhang, T. (2009). Poly(propylene fumarate)/(calcium sulphate/ $\beta$ -tricalcium phosphate) composites: Preparation, characterization and in vitro degradation. *Acta Biomaterialia*, 5(2), 628-635.
- Callaghan, J. J., O'Rourke, M. R., & Saleh, K. J. . (2004). Why knees fail. *The Journal of Arthroplasty*, 19(4), 31-34.
- Callister, W. D., Rethwisch, D. G. (2010). *Materials science and engineering*. (8<sup>th</sup> ed.). New York, NY: Wiley.
- Carlsson, A., Bjorkman, A. , Besjakov, J. , & Onsten, I. (2005). Cemented tibial component fixation performs better than cementless fixation. *Acta Orthopeda*, 76(3), 362-369.
- Carmicheal, M. (2005, October 3). Rebuilding the heart; stem cells seem to rejuvenate failing hearts. The trouble is, doctors still don't understand how. *Newsweek*.

- Carter, D. R., Vasu, R., Spengler, D. M., & Dueland, R. T. (1981). Stress fields in the unplated and plated canine femur calculated from in vivo strain measurements. *J Biomech*, 14, 63-70.
- Chong, Y. R., Hansen, U. N., & Amis, A. A. (2010). Analysis of bone–prosthesis interface micromotion for cementless tibial prosthesis fixation and the influence of loading conditions. *Journal of Biomechanics*, 43(6), 1074-1080.
- Cook, S. D., Thongpreda, N., Anderson, R. C., & Haddad, R. J., Jr. (1988). The effect of post-sintering heat treatments on the fatigue properties of porous coated Ti-6Al-4V alloy. *Journal of Biomedical Materials Research*, 22, 287-302.
- Completo, A., Fonseca, F., Simoes, J. A. (2008). Strain shielding in proximal tibia of stemmed knee prosthesis: experimental study. *J Biomech*, 41(3), 560-566.
- Cristofolini, L., & Viceconti, M. (2000). Mechanical validation of whole bone composite tibia models. *Journal of Biomechanics*, 33(3), 279-288.
- Deitzel, J. M., Kleinmeyer, J., Harris, D., & Tan, N. C. B. (2001). The effect of processing variables on the morphology of electrospun nanofibers and textiles. *Polymer*, 42(1), 261-272.



- den Boer, F. C., Patka, P., Bakker, F. C., Wipperman, B. W., van Lingen, A., Vink, G. Q., ... & Haarman, H. J. (1999). New segmental long bone defect model in sheep: quantitative analysis of healing with dual energy X-ray absorptiometry. *J Orthop Res*, 17(5), 654-660.
- Deng, M., Zhou, J., Chen, G., Burkley, D., Xu, Y., Jamiolkowski, D., & Barbolt, T. (2005). Effect of load and temperature on in vitro degradation of poly(glycolide-co-l-lactide) multifilament braids. *Biomaterials*, 26(20), 4327–4336.
- Diletti, R., Serruys, P. W., Farooq, V., Sudhir, K., Dorange, C., Miquel-Hebert, K., Veldhof, S., Rapoza, R., Onuma, Y., Garcia-Garcia, H. M., and Chevalier, B. (2012). Absorb II randomized controlled trial: A clinical evaluation to compare the safety, efficacy, and performance of the absorb everolimus-eluting bioresorbable vascular scaffold system against the Xience Everolimus-Eluting Coronary Stent System in the treatment of subjects with ischemic heart disease caused by de novo native coronary artery lesions: Rationale and study design. *Am. Heart J.*, 164(5), 654-663.
- Donahue, T., Hull, M., Rashid, M., and Jacobs, C.(2002). A finite element model of the human knee joint for the study of 584 tibio-femoral contact. *J Biomech Eng.*, . 124(3), . 273-280.
- Fan, Y., Li, P., & Yuan, X. (2010). *Influence of Mechanical loads on degradation of scaffolds*. WCB 2010, IFMBE Proceedings, 31, 549-552.

- Fan, Y.-B., Li, P., Zeng, L., & Huang, X.-J. (2008). Effects of mechanical load on the degradation of poly(D,L-lactic acid) foam. *Polym. Degrad. Stabil.*, 93(3), 677-683.
- Fitzgerald, S. J., & Trousdale, R. T. (2011). Why knees fail in 2011: Patient, surgeon or device? *Orthopedics*, 34, 513-515.
- Food and Drug Administration (FDA),. Center for Devices and Radiological Health. (2003). *Knee joint patellofemoral and femoral metal/polymer porous-coated uncemented prostheses*. .
- Fee, T. (2012). *Mechanics of Electrospun Nanofibers* (Unpublished master's of science thesis proposal). University of Alabama at Birmingham.
- Galwey, A. K., & Brown, M. E. (2002). Application of the arrhenius equation to solid state kinetics: Can this be justified? *Thermochim. Acta*, 386(1), 91-98.
- Gao, T., Tuominen, T. K., Lindholm, T. Kommonen, S. B., & Lindholm, T. C. (1997). Morphological and Biomechanical difference in healing in segmental tibial defects implanted with Biocoral® or tricalcium phosphate cylinders. *Biomaterials*, 18(3), 219-223.
- Goh, C. S. S., Santoni, B. G., Puttlitz, C. M., & Palmer, R. H. (2009). Comparison of the mechanical behaviors of semicontoured, locking plate-rod fixation and anatomically contoured, conventional plate-rod fixation applied to experimentally induced gap fractures in canine femora. *Am J Vet Res*, 70(1), 23-29.

- Gorman, S. C., Kraus, K. H., Keating, J. H., Tidwell, A. S., Rand, W. M., Parkington, J. D., & Boudrieau, R. J. (2005). In vivo axial dynamization of canine tibial fractures using the Securos external skeletal fixation system. *Vet Comp Orthop Traumatol*, 18, 199-207.
- Goodheart, J. R., Miller, M. A., & Mann, K. A. . (2014). In vivo loss of cement-bone interlock reduces fixation strength in total knee arthroplasties. *Journal of Orthopedic Research*, 32, 1052-1060.
- Gopferich, A. (1996). Mechanisms of polymer degradation and erosion. *Biomaterials*, 17(2), 103–114.
- Grabow, N., Bünger, C. M., Sternberg, K., Mews, S., Schmohl, K., & Schmitz, K.-P. (2007). Mechanical properties of a biodegradable balloon- expandable stent from poly(L-lactide) for peripheral vascular applications. *ASME J. Med. Devices*, 1(1), 84-88.
- Grizzi, I., Garreau, H., Li, S., & Vert, M. (1995). Hydrolytic degradation of devices based on poly(DL-lactic acid) size-dependence. *Biomaterials*, 16(4), 305-311.
- Guan, K., & Hasenfuss, G. (2007). Do Stem Cells in the Heart Truly Differentiate into Cardiomyocytes? *Journal of Molecular and Cellular Cardiology*, 43(4), 377-387. \
- Haider, H., & Walker, P. S. (2005). Measurements of Constraint of Total Knee Replacement. *Journal of Biomechanics*, 38(2), 341-348.

Heart Disease and Stroke Statistics – 2008 Update. (2008). *Circulation*. 117, e25-e146. doi: 10.1161/CIRCULATIONAHA.107.187998

Hedberg, E. L., Shih, C. K., Lemoine, J. J., Timmer, M. D., Liebschner, M. A., Jansen, J. A., & Mikos, A. G. (2005). In Vitro Degradation of Porous Poly(propylene Fumarate)/poly(dl-lactic-co-glycolic Acid) Composite Scaffolds. *Biomaterials*, 26(16), 3215-3225.

Heiner, A. D., & Brown, T. D. (2001). Structural Properties of a New Design of Composite Replicate Femurs and Tibias. *Journal of Biomechanics*, 34(6), 773-781.

Heldman, A. W., & Hare, J. M. (2008). Cell Therapy for Myocardial Infarction: Special Delivery. *Journal of Molecular and Cellular Cardiology*, 44(3), 473-476.

Hulse, D., Ferry, K., Fawcett, A., Gentry, I., Hyman, W., Geller, S., & Slater, M. (2000). Effect of intramedullary pin size on reducing bone plate strain. *Vet Comp Orthop Traumatol*, 13, 185-190.

Hulse, D., Hyman, W., Nori, M., & Slater, M. (1997). Reduction in plate strain by addition of an intramedullary pin. *Vet Surg* 26, 451-459.

Hulse, D. A., & Hyman, W. (2003). Fracture biology and biomechanics. In D. Slatter (Ed.), *Textbook of small animal surgery* (3<sup>rd</sup> ed., Vol. 2, pp. 1785-1792). Philadelphia, PA: Saunders.

Humphrey, J. D. (2002). *Cardiovascular solid mechanics: Cells, tissues, and organs*.

New York, NY: Springer.

Hutmacher, D. W. (2000). Scaffolds in tissue engineering bone and cartilage.

*Biomaterials*, 21(24), 2529-2543.

Hutmacher, D. W., Schantz, J. T., Lam, C. X. F., Tan, K. C., & Lim, T. C. (2007). State

of the Art and Future Directions of Scaffold-based Bone Engineering from a

Biomaterials Perspective. *Journal of Tissue Engineering and Regenerative*

*Medicine*, 1(4), 245-260.

ISO 14879-1. (2000). Implants for surgery: Total knee-joint prostheses—Part 1:

Determination of endurance properties of knee tibial trays.

Johnston, S. A., von Pfeil, D. J. F., & Dejardin, L. M. (2012). Internal fracture fixation In

K. M. Tobias & S. A. Johnston (Eds.), *Veterinary surgery: Small animal* (Vol. 1,

pp 576-607). St. Louis, MO: Elsevier/Saunders.

Kang, Y., Yao, Y., Yin, G., Huang, Z., Liao, X., Xu, X., & Zhao, G. (2009). A Study on

the in vitro Degradation Properties of Poly(L-Lactic Acid)/Beta- Tricalcuim

Phosphate (PLLA/Beta-TCP) Scaffold Under Dynamic Loading. *Med. Eng. Phys.*,

31(5), 589-594.

- Kaushal, S., Jacobs, J. P., Gossett, J. G., Steele, A., Steele, P., Davis, C. R., Pahl, E., ... & Wold. (2009). Innovation in basic science: stem cells and their role in the treatment of paediatric cardiac failure: Opportunities and challenges. *Cardiology in the Young*, 19(S2), 74.
- Kerwin, S. C. (2004, October 6–9). Clinical experience with the clamp rod internal fixator. *Proceedings of the 14th Annual American College of Veterinary Surgeons Symposium*, Denver, CO, 260-262.
- Kiapour, A., Kiapour, A. M., Kaul, V., Quatman, C., Wordeman, S., Hewett, T., Demetropoulos, C., Goel, V. (2014a). Finite element model of the knee for investigation of injury mechanisms: development and validation. *Journal of Biomechanical Engineering*. , 136(1).
- Kiapour, A. M., Quatman, C. E., Goel, V. K., Wordeman, S., Hewett, T., Demetropoulos, C., (2014b). Timing sequence of multi-planar knee kinematics revealed by physiologic cadaveric simulation of landing: implications for ACL injury mechanism. *Clinical Biomechanics*. 29(1), 75-82.
- Kiapour, A. M., Wordeman, S. C., Paterno, M. V., Quatman, C., Levine, J., Goel, V., Demetropoulos, C., Hewett, T. (2014c). Diagnostic value of knee arthrometry in the prediction of anterior cruciate ligament strain during landing. *The American Journal of Sports Medicine*. , 42(2), 312-319.

- Kim, J., & Breur, G. J. (2008). Temporospacial and kinetic characteristics of sheep walking on a pressure sensing walkway. *The Canadian Journal of Veterinary Research*, 72, 50-55.
- Kleinschmidt, J. C., & Hollinger, J. O. (1992). Animal models in bone research. In M. B. Habal, & A. H. Reddi (Eds.), *Bone grafts and bone substitutes* (pp. 133-146). Philadelphia, PA: W.B. Saunders Co.
- Knowles, J. K. (1977). The finite anti-plane shear field near the tip of a crack for a class of incompressible elastic solids. *Int. J. Fract.*, 13(5), 611-639.
- Koch, D. (2005). Implants: description and application. In A. Johnson, J. E. F. Houlton, & R. Vannini (Eds.), *AO principles of fracture management in the dog and cat* (pp. 27-52). Davos, Switzerland: AO Publishing.
- Lanckohr, C., Torsello, G., Scheld, H., Schieffer, B., & Theilmeier, G. (2012). Drug-eluting stents and perioperative risk—More than matters of the heart? *Vasa*, 41(6), 410–418.
- Lee, S. Y., & Gallagher, D. (2008). Assessment methods in human body composition. *Current Opinion in Clinical Nutrition and Metabolic Care*, 11(5), 566-572.
- Leenslag, J. W., Pennings, A. J., Bos, R. R., Rozema, F. R., & Boering, G. (1987). Resorbable materials of poly(L-lactide) VII in vivo and in vitro degradation. *Biomaterials*, 8(4), 311-314.

- Li, S. (1999). Hydrolytic degradation characteristics of aliphatic polyesters derived from lactic and glycolic acids. *J. Biomed. Mater. Res.*, 48(3), 342-353.
- Lickorish, D., Guan, L., & Davies, J. E. (2007). A Three-phase, fully resorbable, polyester/calcium phosphate scaffold for bone tissue engineering: Evolution of scaffold design. *Biomaterials*, 28(8), 1495-1502.
- Lui, K. O., Bu, L., Li, R. A., & Chan, C. W. (2012). Pluripotent stem cell-based heart regeneration: From the development and immunological perspectives. *Birth Defects Research Part C, Embryo Today: Reviews*, 96(1), 98-108.
- Łysiak-Drwal, K., Dominiak, M., Solski, L., Żywicka, B., Pielka, S., Konopka, T., & Gerber, H. (2008). Early histological evaluation of bone defect healing with and without guided bone regeneration techniques: Experimental animal studies. *Postepy Hig Med Dosw*, 62, 282-288.
- Lyu, S., Schley, J., Loy, B., Lind, D., Hobot, C., Sparer, R., & Untereker, D. (2007). Kinetics and time-temperature equivalence of polymer degradation. *Biomacromolecules*, 8(7), 2301-2310.
- Mann, D. L., & Bristow, M. R. (2005). Mechanisms and Models in Heart Failure: The Biomechanical Model and Beyond. *Circulation*, 111(21), 2837-2849.



- Mano, J. F., Ribelles, J. L. G., Alves, N. M., & Sanchez, M. S. (2005). Glass Transition Dynamics and Structural Relaxation of PLLA Studied by DSC: Influence of Crystallinity. *Polymer*, 46(19), 8258–8265.
- Martin, R. B. (1999, October 23). *A Genealogy of Biomechanics*. Presidential lecture presented at the 23rd Annual Conference of the American Society of Biomechanics. Pittsburgh, PA: Washington University Course Bioen 520.
- Martini, L., Fini, M., Giavaresi, G., & Giardino, R. (2001). Sheep model in orthopedic research: A literature review. *Comparative Medicine*, 51(4 ), 292-299.
- Mastrogiamco, M., Corsi, A., Francioso, E., Di Comite, M., Monetti, F., Scaglione, S., Favia, A., ... & Cancedda, R. (2006). Reconstruction of extensive long bone defects in sheep using resorbable bioceramics based on silicon stabilized tricalcium phosphate. *Tissue Engineering*, 12(5), 1261-1273.
- Meling, T., Harboe, K., & Søreide, K. (2009). Incidence of traumatic long-bone fractures requiring in-hospital management: A prospective age- and gender-specific analysis of 4890 fractures. *Injury*, 40(11), 1212-1219.
- Mills, L. A., & Simpson, A. H. R. W. (2012). In vivo models of bone repair. *The Bone & Joint Journal*, 94-B(7), 865-874.
- Minnesota Community Measurement. (2010, June). Total knee replacement. *Impact and Recommendation Document*.

- Moran, M. F., Bhimji, S., Racanelli, J., & Piazza, S. J. . (2008). Computational assessment of constraint in total knee replacement. *Journal of Biomechanics*, 41(9), 2013-2020.
- Muliana, A., & Rajagopal, K. R. (2012). Modeling the response of nonlinear viscoelastic biodegradable polymeric stents. *Int. J. Solids Struct.*, 49, 989-1000.
- Murase, K., Crowninshield, R. D., Pederson, D. R., & Chang, T. S. (1982). An analysis of tibial component design in total knee arthroplasty. *J Biomech*, 16, 13-22.
- National Joint Registry for England and Wales (2010). 7<sup>th</sup> annual report. . Retrieved from <http://www.njrcentre.org.uk/NjrCentre/Portals/0/NJR%207th%20Annual%20Report%202010.pdf>
- Nishio, S., Kosuga, K., Igaki, K., Okada, M., Kyo, E., Tsuji, T., Takeuchi, E.,... & Ikeguchi, S. (2012). Long-term (>10 years) clinical outcomes of first-in-human biodegradable poly-L-lactic acid coronary stents: Igaki-Tamai stents. *Circulation*, 125(19), 2343-2353.
- Nyman, R., Magnusson, M., Sennerby, L., Nyman, S., & Lundgren, D. (1995). Membrane-guided bone regeneration: segmental radius defects studied in the rabbit. *Acta Orthop Acta Orthopaedica*, 66(2), 169-173.

- Okamura, T., Garg, S., Gutierrez-Chico, J. L., Shin, E. S., Onuma, Y., Garcia-Garcia, H. M., Rapoza, R. J., ... & Serruys, P. W. (2010). In vivo evaluation of stent strut distribution patterns in the bioabsorbable everolimus-eluting device: An OCT ad hoc analysis of the revision 1.0 and revision 1.1 stent design in the absorb clinical trial. *EuroIntervention*, 5(8), 932-938.
- O'Neill, D. (2015). Measuring obesity in the absence of a gold standard. *Economics & Human Biology*, 17, 116-128.
- Onuma, Y., & Serruys, P. W. (2011). Bioresorbable Scaffold: The advent of a new era in percutaneous coronary and peripheral revascularization? *Circulation*, 123(7), 779-797.
- Onuma, Y., Serruys, P. W., Gomez, J., De Bruyne, B., Dudek, D., Thuesen, L., Smits, P., ... & Ormiston, J. A. (2011). Comparison of in vivo acute stent recoil between the bioresorbable everolimus-eluting coronary scaffolds (revision 1.0 and 1.1) and the metallic everolimus-eluting stent. *Cathet. Cardiovasc. Interv.*, 78(1), 3-12.
- Park, J.-H., Gu, L., Von Maltzahn, G., Ruoslahti, E., Bhatia, S. N., Sailor, M. J. (2009). Biodegradable luminescent porous silicon nanoparticles for in vivo applications. *Nat Mater*, 8(4), 331-336.
- Passier, R., Van Laake, L. W., & Mummery, C. L. (2008). Stem-cell-based therapy and lessons from the heart. *Nature*, 453(7193), 322-329.

- Paul, D., Samuel, S. M., & Maulik, N. (2009). Mesenchymal stem cell: Present challenges and prospective cellular cardiomyoplasty approaches for myocardial regeneration. *Antioxidants & Redox Signaling*, 11(8), 1841-1855.
- Peter, S. J., Kim, P., Yasko, A. W., Yaszemski, M. J., & Mikos, A. G. . (1999). Crosslinking characteristics of an injectable poly(propylene fumarate)/beta-tricalcium phosphate paste and mechanical properties of the crosslinked composite for use as a biodegradable bone cement. *Journal of Biomedical Materials Research*. . . , 44(3), 314-321.
- Perego, G., Cella, G. D., & Bastioli, C. (1996). Effect of molecular weight and crystallinity on poly(lactic acid) mechanical properties. *J. Appl. Polym. Sci.*, 59(1), 37-43.
- Puppi, D., Chiellini, F. A., Piras, M., & Chiellini, E. . (2010). Polymeric materials for bone and cartilage repair. *Progress in Polymer Science*, 35(4), 403-440.
- Radu, D. R., Lai, C.-Y., Jeftinija, K., Rowe, E. W., Jeftinija, S., Lin, V. S. Y. (2004). A polyamidoamine dendrimer-capped mesoporous silica nanosphere-based gene transfection reagent. *Journal of the American Chemical Society* 126(41), 13216-13217.
- Rajagopal, K. R., Srinivasa, A. R., & Wineman, A. S. (2007). On the shear and bending of a degrading polymer beam. *Int. J. Plasticity*, 23(9), 1618-1636.

- Ramakrishna, S., Mayer, J., Wintermantel, E., & Leong, K. W. . (2001). Biomedical applications of polymer-composite materials: A review. *Composites Science and Technology*, 61(9), 1189-1224.
- Ramirez-Zea, M., Torun, B., Martorell, R., & Stein, A. D. (2006). Anthropometric predictors of body fat as measured by hydrostatic weighing in Guatemalan adults. *American Journal of Clinical Nutrition*, 83, 795-802.
- Rawlinson, J. L., Peters, L. E., Campbell, D. A., Windsor, R., Wright, T., Bartel, D. (2005). Cancellous bone strains indicate efficacy of stem augments in constrained condylar knees. *Clin Orthop Relat Res*, 440, 107-116.
- Reems, M., Beale, B., & Hulse, D. (2003). Use of a plate-rod construct and principles of biological osteosynthesis for repair of diaphyseal fractures in dogs and cats: 47 cases (1994–2001). *J Am Vet Med Assoc*, 223, 330-335.
- Reilly, D., Walker, P. S., Ben-Dov, M., & Ewald, F. C. (1982, May). Effects of tibial components on load transfer in the upper tibia. *Clin Orthop Relat Res*, 65, 273-282.
- Rezwan, K., Chen, Q. Z., Blaker, J. J., & Boccaccini, A. R. (2006). Biodegradable and bioactive porous polymer/inorganic composite scaffolds for bone tissue Engineering. *Biomaterials*, 27(18), 3413-3431.

- Scantlebury, T., & Ambruster, J. (2012). The development of guided regeneration: Making the impossible possible and the unpredictable predictable. *Journal of Evidence Based Dental Practice*, 12(3), 101-117.
- Scott, C. E. H., & Biant, L. C. (2012). The role of the design of tibial components and stems in knee replacement. *The Bone & Joint Journal*, 94-B(8), 1009-1015.
- Shahar, R., Banks-Sills, L., & Eliasy, R. (2003). Stress and strain distribution in the intact canine femur: finite element analysis. *Med Eng Phys*, 25, 387-395.
- Slowing, I., Trewyn, B. G., & Lin, V. S. Y. (2006). Effect of surface functionalization of mcm-41-type mesoporous silica nanoparticles on the endocytosis by human cancer cells. *Journal of the American Chemical Society*, 128(46), 14792-14793.
- Smith, J. D., & Abramson, M. . (1974). Membranous vs endochondral bone autografts. *Archives of Otolaryngology—Head and Neck Surgery*, 99(3), 203-205.
- Soares, J. S., Moore, J. E., & Rajagopal, K. R. (2010). Modeling of Deformation-Accelerated Breakdown of Polylactic Acid Biodegradable Stents. *ASME J. Med. Devices*, 4(4), 041007.
- Soares, J. S., Rajagopal, K. R., & Moore, J. E. (2009). Deformation-induced hydrolysis of a degradable polymeric cylindrical annulus. *Biomech. Model.Mechanobiol.*, 9(2), 177-186.

- Soares, J. S., Moore, J. E., & Rajagopal, K. R. (2008). Constitutive framework for biodegradable polymers with applications to biodegradable stents. *ASAIO J.*, 54(3), 295-301.
- Soares, J. S. (2008). *constitutivemodeling for biodegradable polymers for application in endovascular stents* (Doctoral dissertation). Retrieved from Texas A&M, College Station, TX.
- Su, S. H., Chao, R. Y., Landau, C. L., Nelson, K. D., Timmons, R. B., Meidell, R. S., & Eberhart, R. C. (2003). Expandable bioresorbable endovascular stent. I. fabrication and properties. *Ann. Biomed. Eng.*, 31(6), 667–677.
- Szivek, J. A., Cutignola, L., & Volz , R. G. (1995). Tibiofemoral contact stress and stress distribution evaluation of total knee arthroplasties. *The Journal of Arthroplasty*, 10(4), 480-491.
- Szivek, J. A., Anderson, P. L., & Benjamin, J. B. (1996). Average and peak contact stress distribution evaluation of total knee arthroplasties. *The Journal of Arthroplasty*, 11(8), 952-963.
- Taylor, G. I. (1964). *Proceedings of the Royal Society of London, Series A.* 280, 383-397.
- Taylor, G. I. (1969). *Proceedings of the Royal Society of London, Series A.* 313, 453-475.

- Timmer, M. D., Shin, H., Horch, R. A., Ambrose, C. G., & Mikos, A. G. . (2003). In vitro cytotoxicity of injectable and biodegradable poly(propylene fumarate)-based networks: Unreacted macromers, cross-linked networks, and degradation products. *Biomacromolecules*, 4(4), 1026-1033.
- Tamai, H., Igaki, K., Kyo, E., Kosuga, K., Kawashima, A., Matsui, S., Komori, H., ... & Uehata, H. (2000). Initial and 6-month results of biodegradable poly-L-lactic acid coronary stents in humans. *Circulation*, 102(4), . 399–404.
- Thompson, D. E., Agrawal, C. M., & Athanasiou, K. (1996). The effects of dynamic compressive loading on biodegradable implants of 50-50% polylactic acid-polyglycolic acid. *Tissue Eng.*, 2(1), . 61-74.
- Tsuji, H. (2008). *Degradation of poly(lactide)-based biodegradable materials*. New York, NY: Nova Science Publishers, Inc.
- Tsuji, H., Akira, M., & Ikada, Y. (2000). Properties and morphology of poly(L-lactide). III. effects of initial crystallinity on long-term in vitro hydrolysis of high molecular weight poly(L-lactide) film in phosphate-buffered solution. *J. Appl. Polym. Sci.*, 77, . 1452-1464.
- Tsuji, H., & Ikada, Y. (2000). Properties and morphology of poly(L-lactide) 4. effects of structural parameters on long-term hydrolysis of poly(L-lactide) in phosphate buffered solution. *Polym. Degrad. Stabil.*, 67(1), . 179-189.



- Van Dijk, M., Tunc, D. C., Smit, T. H., Higham, P., Burger, E. H., & Wuisman, P. I. (2002). In vitro and in vivo Degradation of Bioabsorbable PLLA Spinal Fusion Cages. *J. Biomed. Mater. Res.*, 63(6), . 752-759.
- Vasseur, P., Paul, H. A., Crumley, L. (1984). Evaluation of fixation devices for prevention of rotation in transverse fractures of the canine femoral shaft: an in vitro study. *Am J Vet Res* 45, 1504-1507.
- Venkatraman, S. S., Tan, L. P., Joso, J. F. D., Boey, Y. C. F., & Wang, X. (2006). Biodegradable stents with elastic memory. *Biomaterials*, 27(8), . 1573-1578.
- Viateau, V., Guillemin, G., Yang, Y. C., Bensaid, W., Reviron, T., Oudina, K., Meunier, A., ... & Petite, H. (2004). A Technique for Creating Critical-size Defects in the Metatarsus of Sheep for Use in Investigation of Healing of Long-bone Defects. *American Journal of Veterinary Research*, 65(12), 1653-1657.
- Vogt, F., Stein, A., Rettemeier, G., Krott, N., Hoffmann, R., Vom Dahl, J., Bosserhoff, A. K., ... & Blindt, R. (2004). Long-term assessment of a novel biodegradable paclitaxel-eluting coronary polylactide stent. *Eur. Heart J.*, 25(15), . 1330-1340.
- Wahner, H. W., Dunn, W. L., Brown, M. L., Morin, R., Riggs, B. (1988). Comparison of dual-energy X-ray absorptiometry and dual photon absorptiometry for bone mineral measurements of the lumbar spine. *Mayo Clin Proc*, 63, 1075-1084.

- Walsh, W. R., Yu, Y., Yang, J. L. (2002). Biology and biomechanics of fracture healing, in Y. H. An (Ed.), *Internal fixation in osteoporotic bone* (pp. 22-29). New York, NY: Thieme Medical Publishers, Inc.
- Wan, Y. Z., Wang, Y. L., Zheng, L. Y., Zhou, F. G., Zhao, Q., & Cheng, G. X. (2001). Influence of external stress on the in vitro degradation behavior of C3d/Plu composites. *J. Mater. Sci. Lett.*, 20, . 1957-1959.
- Wei, M., Ruys, A. J., Swain, M. V., Kim, S. H., Milthrope, B. K., & Sorrell, C. C. (1999). Interfacial Bond strength of electrophoretically deposited hydroxyapatite coatings on metals. *Journal of Materials Science*, 10, 401-409.
- Weinstein, A. M., Klawitter, J. J., & Koeneman, J. B. (1977, April). Structure property relationships for porous Ti-6Al-4V. *Transaction of the Third Annual Meeting of the Society for Biomaterials*, New Orleans, Louisiana, p. 140.
- Weir, N. A., Buchanan, F. J., Orr, J. F., Farrar, D. F., & Dickson, G. R. (2004). Degradation of Poly-L-Lactide. Part 2: Increased Temperature Accelerated Degradation. *Proc. Inst. Mech. Eng., Part H*, 218(5), . 321-330.
- Willing, R., & Kim, I. Y. (2012). The development, calibration and validation of a numerical total knee replacement kinematics simulator considering laxity and unconstrained flexion motion. *Computer Models in Biomechanics and Biomedical Engineering*, 15(6), 585-593.

- Wollert, K. C., & Drexler, H. (2010). Cell therapy for the treatment of coronary heart disease: A critical appraisal. *Nature Reviews Cardiology*, 7(4), 204-215.
- Wu, Y., Shen, L., Wang, Q., Ge, L., Xie, J., Hu, X., Sun, A., & Ge, J. (2012). Comparison of acute recoil between bioabsorbable poly-L-lactic acid xinsorb stent and metallic stent in porcine model. *ASME Journal of Biomedicine and Biotechnology*, 413956. doi:10.1155/2012/413956.
- Yew, G. H., Yusof, A. M. M., Ishak, Z. A. M., & Ishiaku, U. S. (2005). Water absorption and enzymatic degradation of poly(lactic acid)/rice starch composites. *Polymer Degradation and Stability*, 90(3), . 488-500.
- Yuan, X., Mak, A. F. T., & Yao, K. (2002). Comparative Observation of Accelerated Degradation of Poly(L-Lactic Acid) Fibres in Phosphate Buffered Saline and a Dilute Alkaline Solution. *Polymer Degradation and Stability*, 75(1), . 45-53.
- Zahn, K., Frei, R., Wunderle, D., Linke, B., Schwieger, K., Guerguiev, B., Pohler, O., Matis, U. (2008). Mechanical properties of 18 different AO bone plates and the clamp-rod internal fixation system tested on a gap model construct. *Veterinary and Comparative Orthopedics and Traumatology*, 21, 185-194.
- Zahn, K., Matis, U. (2004). The clamp rod internal fixator—Application and results in 120 small fracture patients. *Veterinary and Comparative Orthopedics and Traumatology*, 17, 110-120.

## APPENDIX I

### NOMENCLATURE AND GREEK SYMBOLS

#### *Nomenclature*

$A$  = frequency factor  
 $B$  = left Cauchy–Green stretch tensor  
 $d$  = degradation  
 $E_a$  = activation energy  
 $k$  = Arrhenius equation rate constant  
 $K_x$  = deformation dependent reaction rate  
 $m$  = dimensionless material constant  
 $R$  = universal gas constant  
 $t$  = time  
 $T$  = temperature  
 $X_c$  = percent crystallinity  
 $W$  = strain energy function  
 $I_B$  = first strain invariant  
 $II_B$  = second strain invariant  
 $III_B$  = third strain invariant

#### *Greek Symbols*

$\beta$  = dimensionless material constant  
 $\Delta H_m$  = enthalpy of fusion  
 $\mu$  = shear modulus  
 $\sigma$  = Cauchy stress  
 $\sigma_n$  = nominal stress

## APPENDIX II

### BNS NANOCOMPOSITE SURFACE DEFECT ANALYSIS

#### Control

*Average Ultimate Strength: 1160.25 +/- 78.81 N*

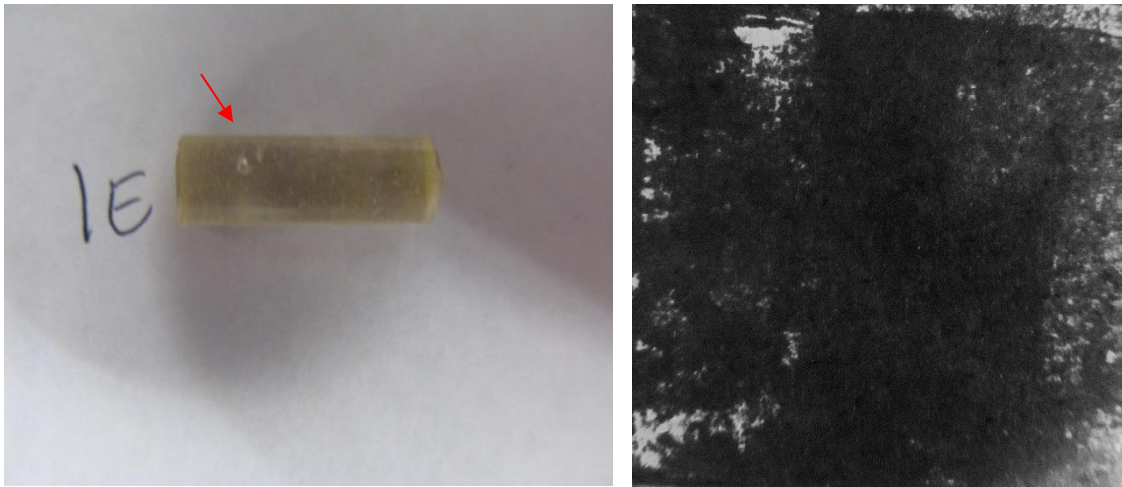


Figure A-1. Sample 1E

Density (kg/m<sup>3</sup>): 1250.58

% Surface Defects: 6.7

Ultimate Strength (N): 1104.52

Formulation: Control

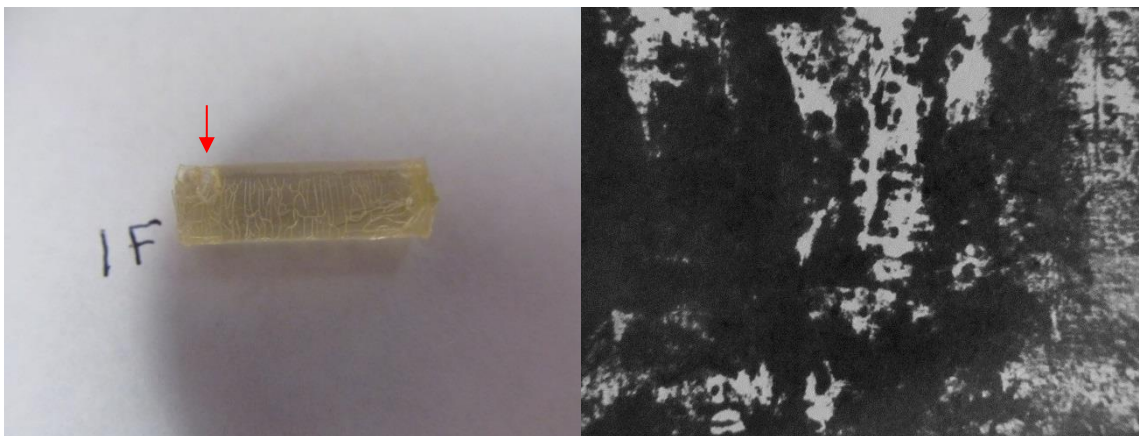


Figure A-2. Sample 1F

Density (kg/m<sup>3</sup>): 1270.54

% Surface Defects: 21.4

Ultimate Strength (N): 1215.98

Formulation: Control

**0.5% MSN**

*Average Ultimate Strength: 1057.667 +/- 168.16 N*

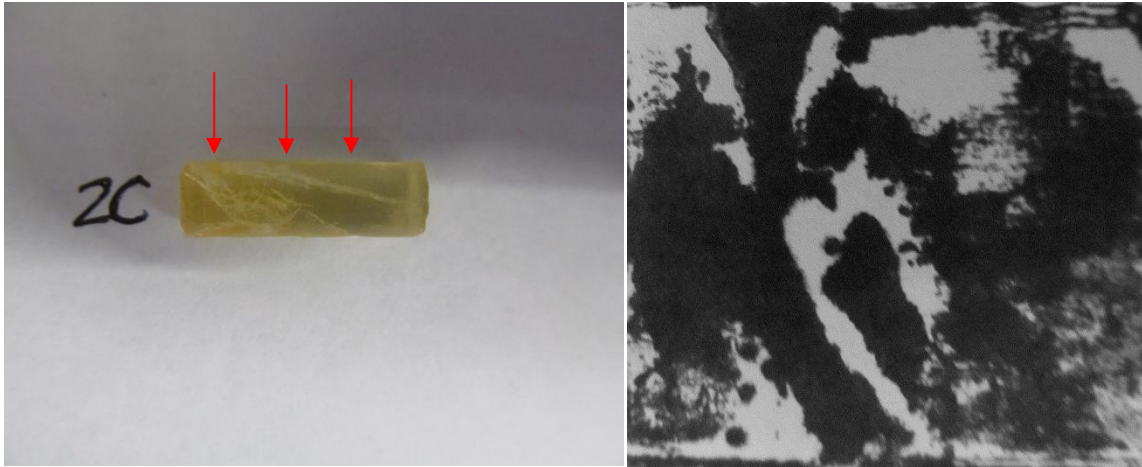


Figure A-3. Sample 2C

Density (kg/m<sup>3</sup>): 1179.05

% Surface Defects: 28.7

Ultimate Strength (N): 822.545

Formulation: 0.5% MSN

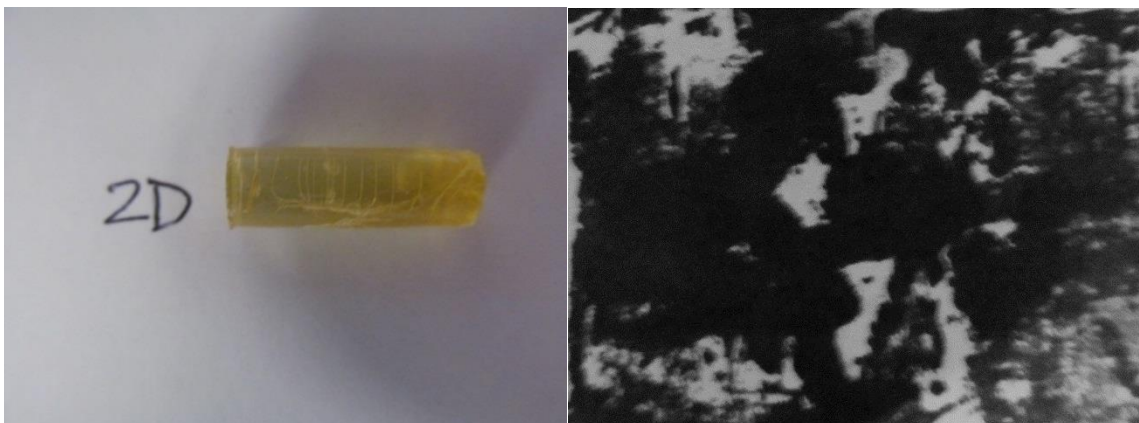


Figure A-4. Sample 2D

Density (kg/m<sup>3</sup>): 1259.99

% Surface Defects: 18.3

Ultimate Strength (N): 1038.28

Formulation: 0.5% MSN



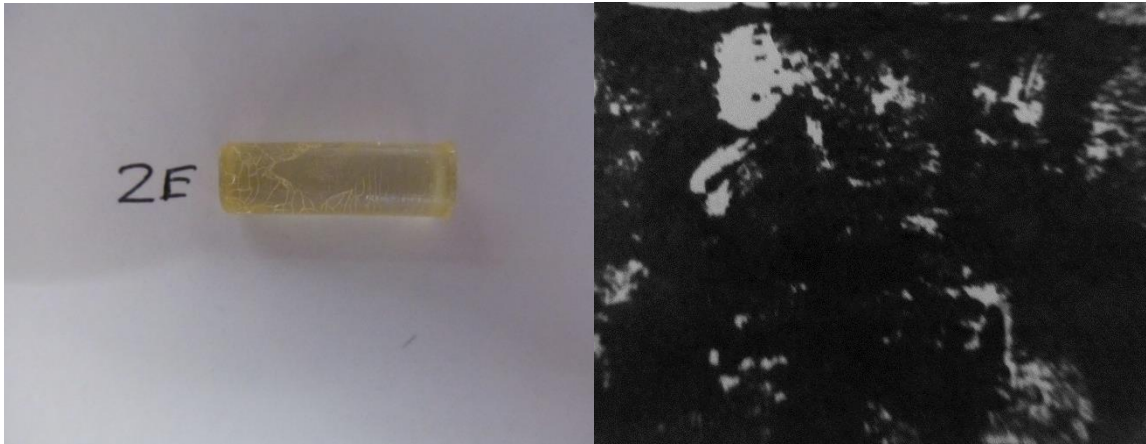


Figure A-5. Sample 2E

Density (kg/m<sup>3</sup>): 1217.04

% Surface Defects: 7

Ultimate Strength (N): 1153.86

Formulation: 0.5% MSN

**1% MSN**

*Average Ultimate Strength: 2000.75 +/- 657.06 N*

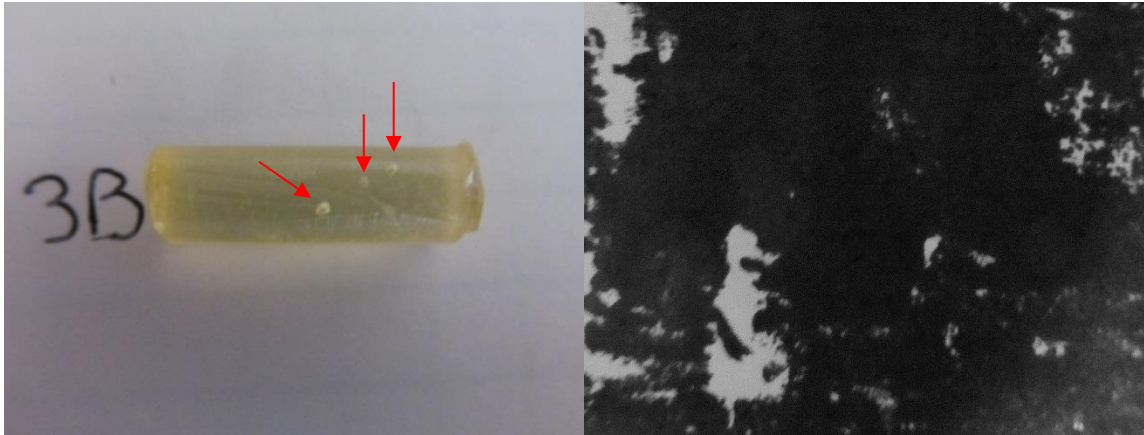


Figure A-6. Sample 3B

Density (kg/m<sup>3</sup>): 1251.49

% Surface Defects: 8.3

Ultimate Strength (N): 1184.85

Formulation: 1% MSN

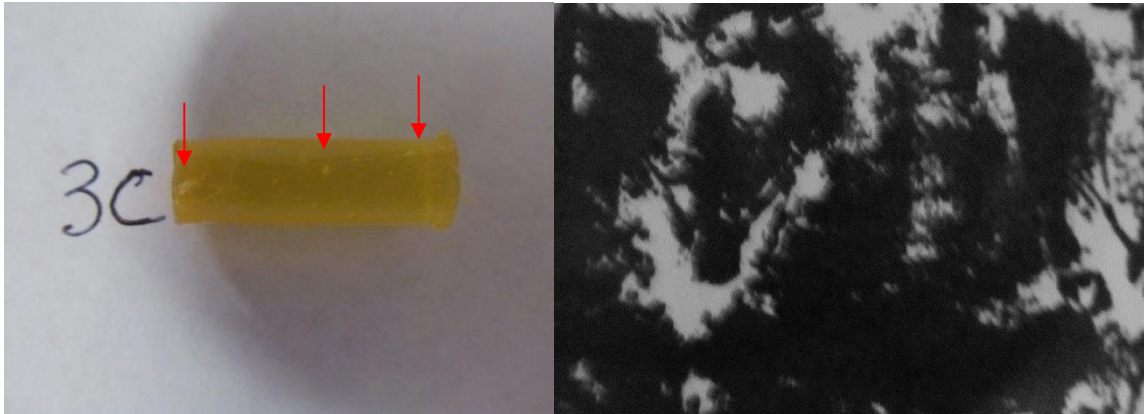


Figure A-7. Sample 3C

Density (kg/m<sup>3</sup>): 1225.39

% Surface Defects: 20.4

Ultimate Strength (N): 1751.48

Formulation: 1% MSN

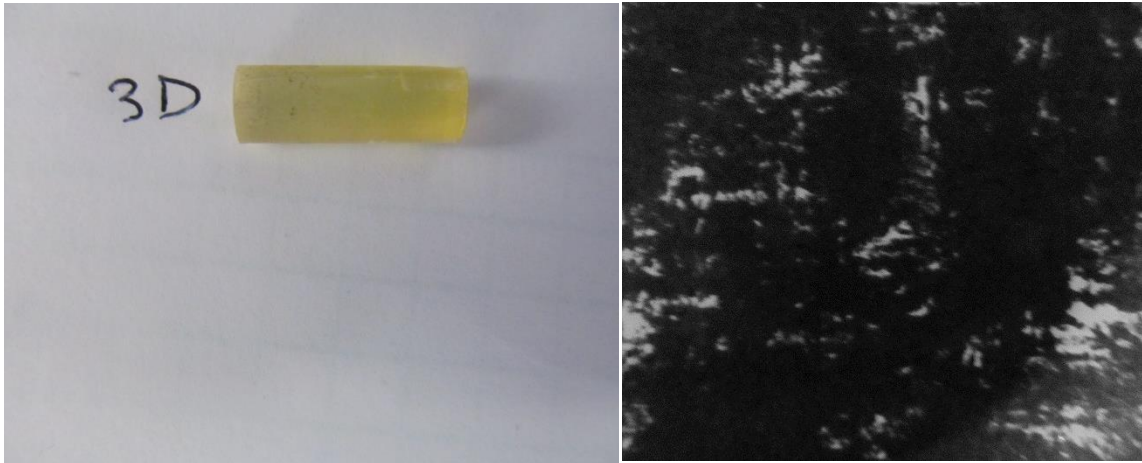


Figure A-8. Sample 3D

Density (kg/m<sup>3</sup>): 1225.39

% Surface Defects: 6.1

Ultimate Strength (N): 2527.7

Formulation: 1% MSN

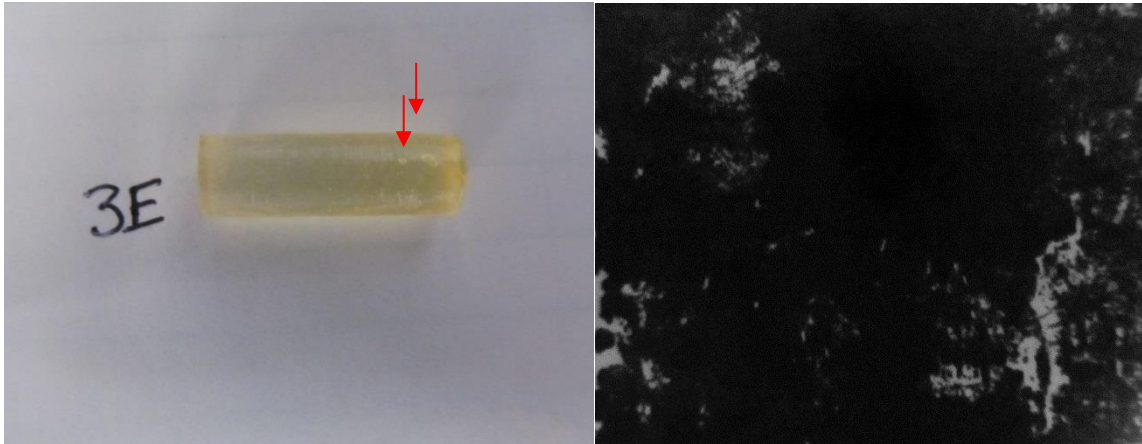


Figure A-9. Sample 3E

Density (kg/m<sup>3</sup>): 1226.96

% Surface Defects: 2.5

Ultimate Strength (N): 2538.96

Formulation: 1% MSN

**0.5% 3.5 Rod**

*Average Ultimate Strength: 1972.28 +/- 597.72 N*

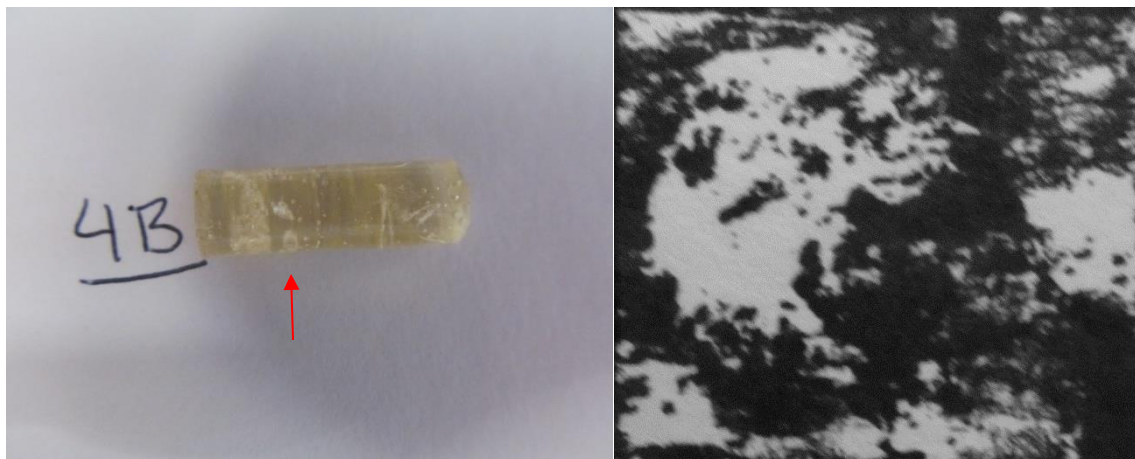


Figure A-10. Sample 4B

Density (kg/m<sup>3</sup>): 1245.63

% Surface Defects: 39.3

Ultimate Strength (N): 2022.62

Formulation: 0.5% 3.5 Rod

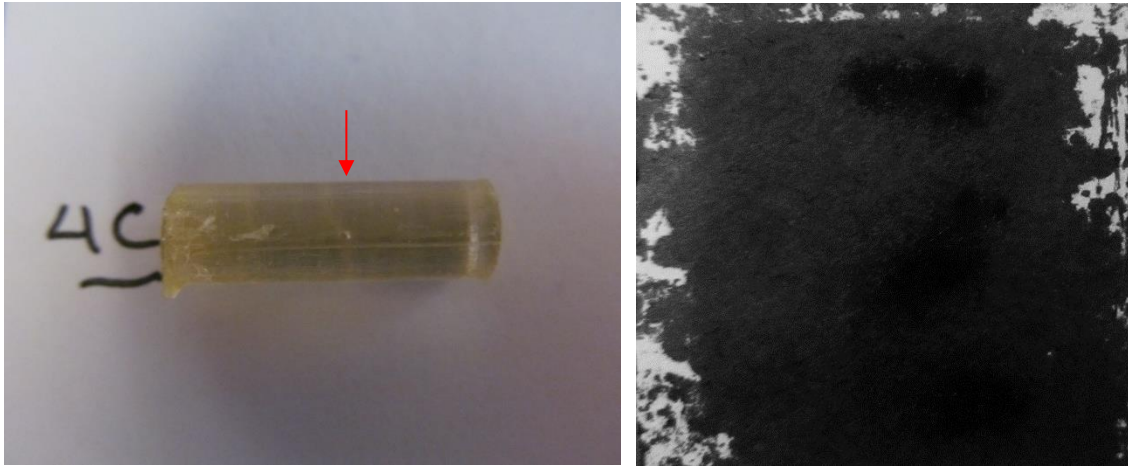


Figure A-11. Sample 4C

Density (kg/m<sup>3</sup>): 1261.08

% Surface Defects: 9.4

Ultimate Strength (N): 2590.42

Formulation: 0.5% 3.5 Rod

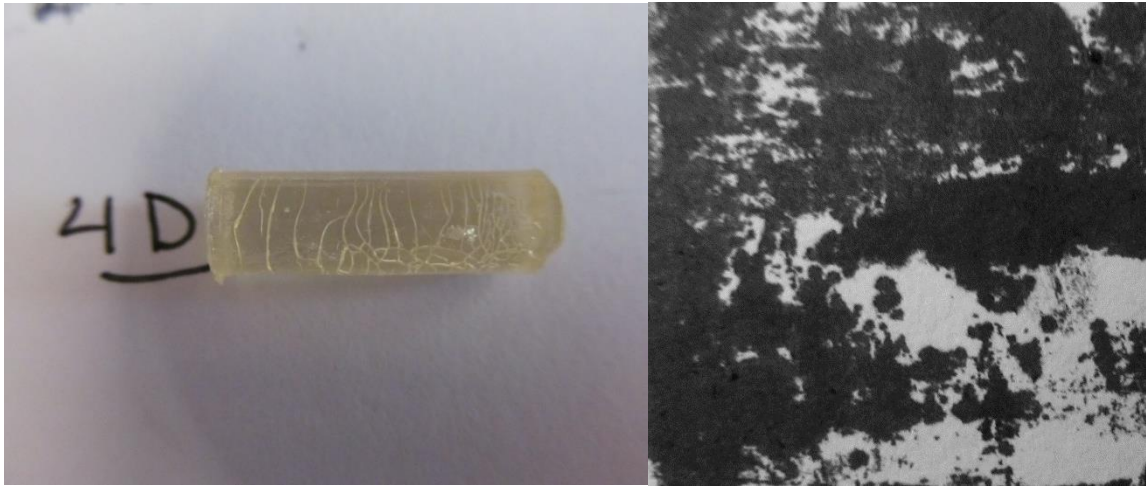


Figure A-12. Sample 4D

Density (kg/m<sup>3</sup>): 1231.01

% Surface Defects: 28.2

Ultimate Strength (N): 1156.51

Formulation: 0.5% 3.5 Rod



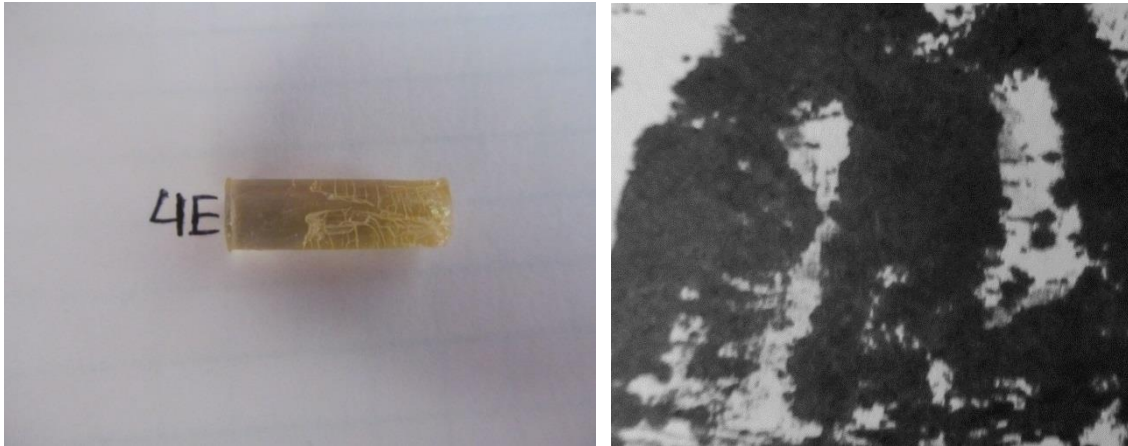


Figure A-13. Sample 4E

Density (kg/m<sup>3</sup>): 1244.44

% Surface Defects: 25.5

Ultimate Strength (N): 2119.57

Formulation: 0.5% 3.5 Rod

**1% 3.5 Rod**

*Average Ultimate Strength: 1817.16 +/- 808.06 N*

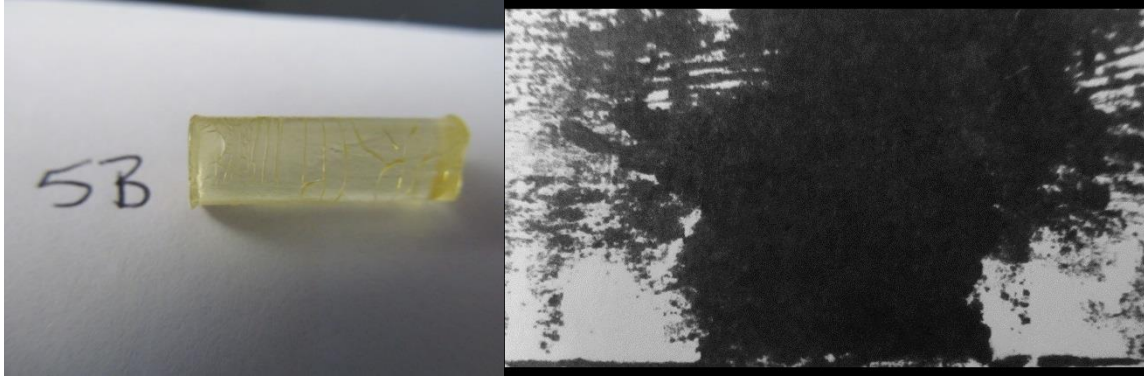


Figure A-14. Sample 5B

Density (kg/m<sup>3</sup>): 1255.98

% Surface Defects: 27.9

Ultimate Strength (N): 2112.95

Formulation: 1% 3.5 Rods

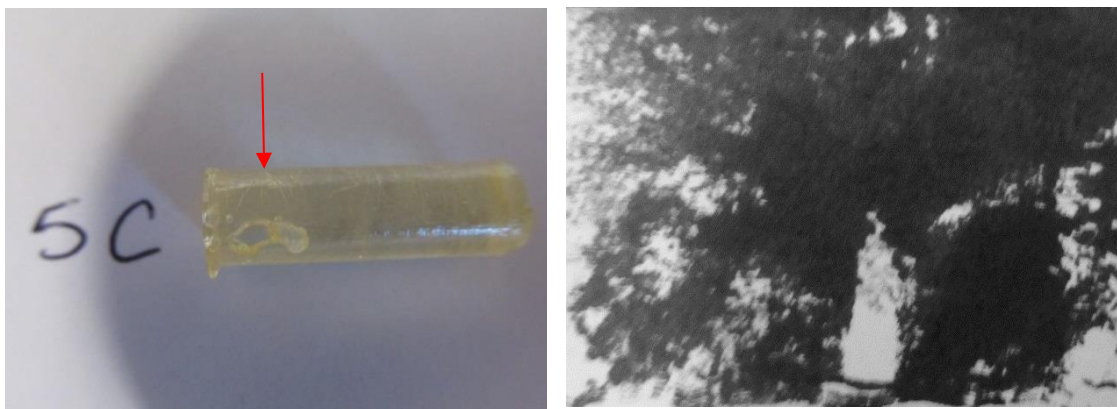


Figure A-15. Sample 5C

Density (kg/m<sup>3</sup>): 1228.26

% Surface Defects: 34.3

Ultimate Strength (N): 828.174

Formulation: 1% 3.5 Rod

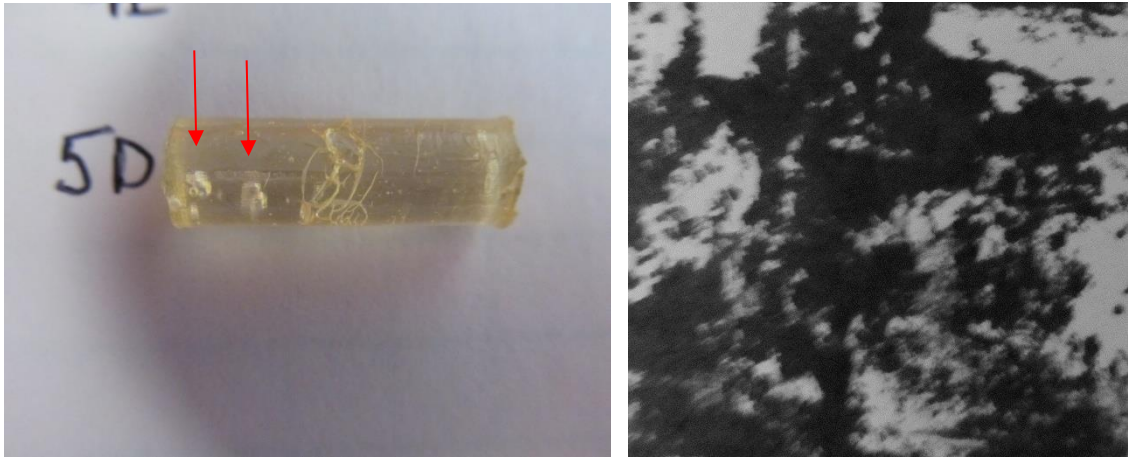


Figure A-16. Sample 5D

Density (kg/m<sup>3</sup>): 1229.53

% Surface Defects: 29.1

Ultimate Strength (N): 2735.17

Formulation: 1% 3.5 Rod

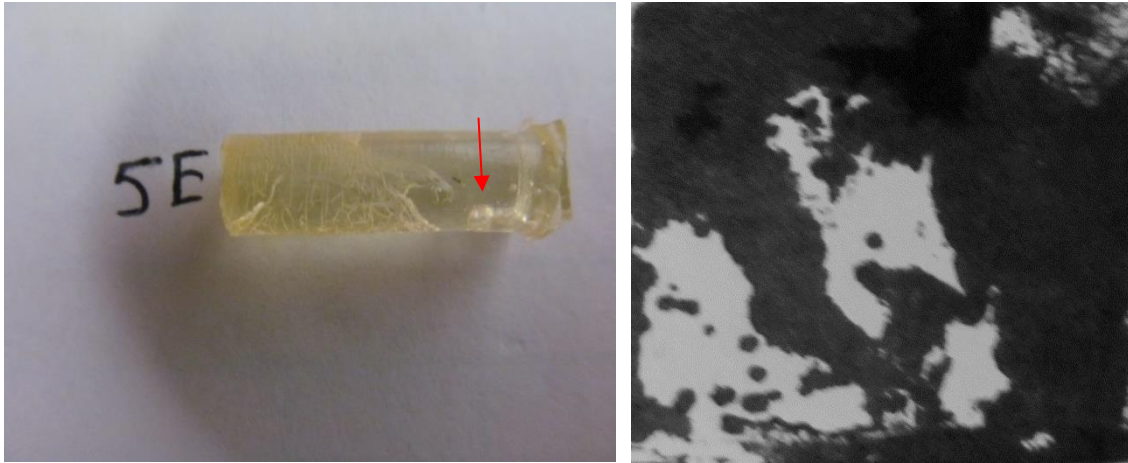


Figure A-17. Sample 5E

Density (kg/m<sup>3</sup>): 1247.63

% Surface Defects: 24.6

Ultimate Strength (N): 1592.36

Formulation: 1% 3.5 Rod

**0.5% 7.5 Rods**

*Average Ultimate Strength: 1616.8 +/- 801.6 N*

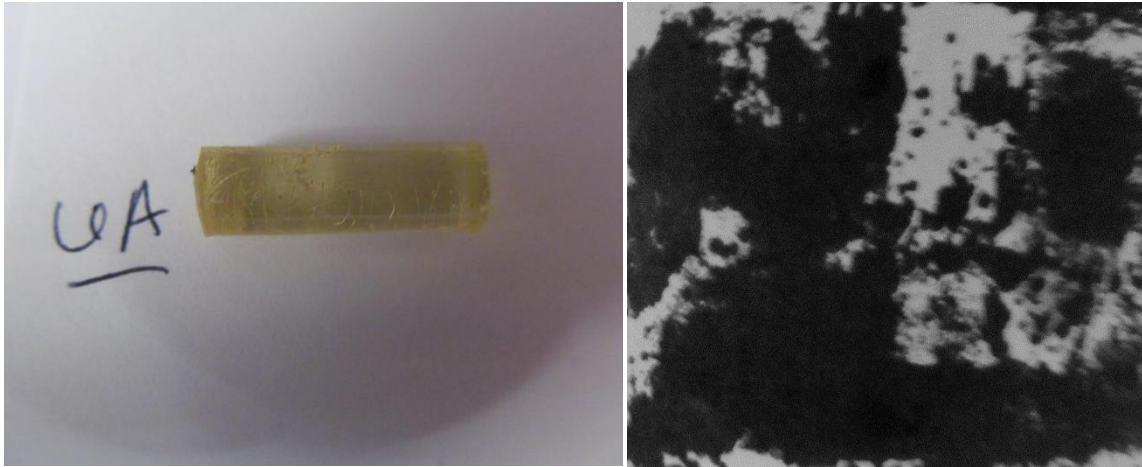


Figure A-18. Sample 6A

Density (kg/m<sup>3</sup>): 1241.34

% Surface Defects: 20.4

Ultimate Strength (N): 807.258

Formulation: 0.5% 7.5 Rod

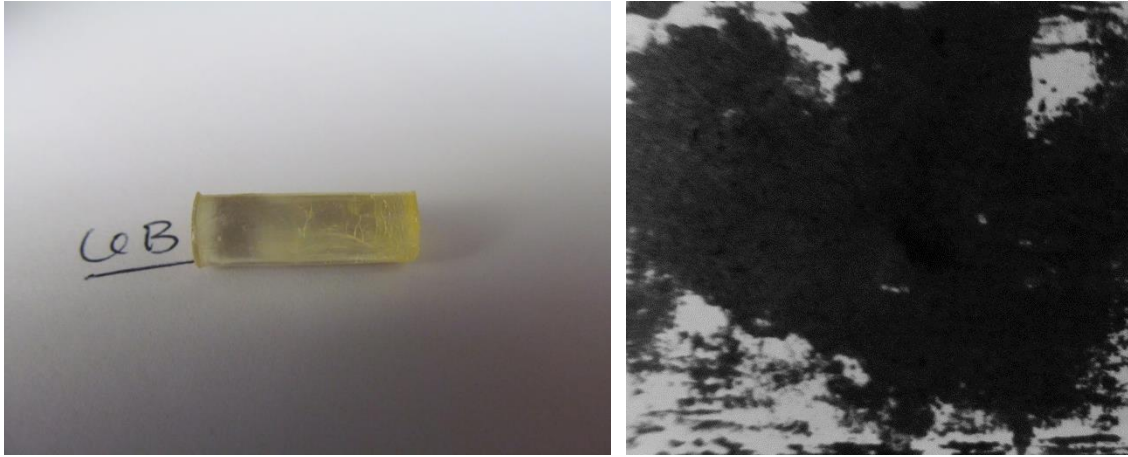


Figure A-19. Sample 6B

Density (kg/m<sup>3</sup>): 1246.9

% Surface Defects: 16.2

Ultimate Strength (N): 774.444

Formulation: 0.5% 7.5 Rod

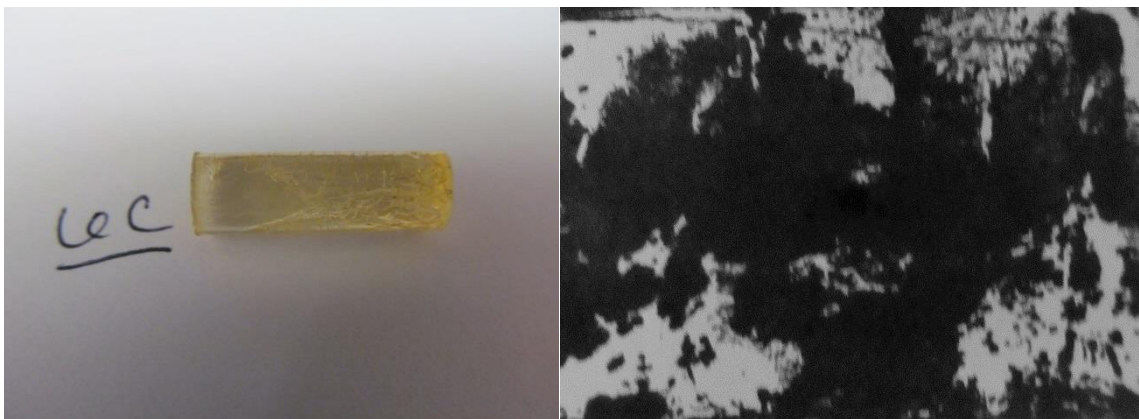


Figure A-20. Sample 6C

Density (kg/m<sup>3</sup>): 1261.97

% Surface Defects: 24.8

Ultimate Strength (N): 2415.51

Formulation: 0.5% 7.5 Rod



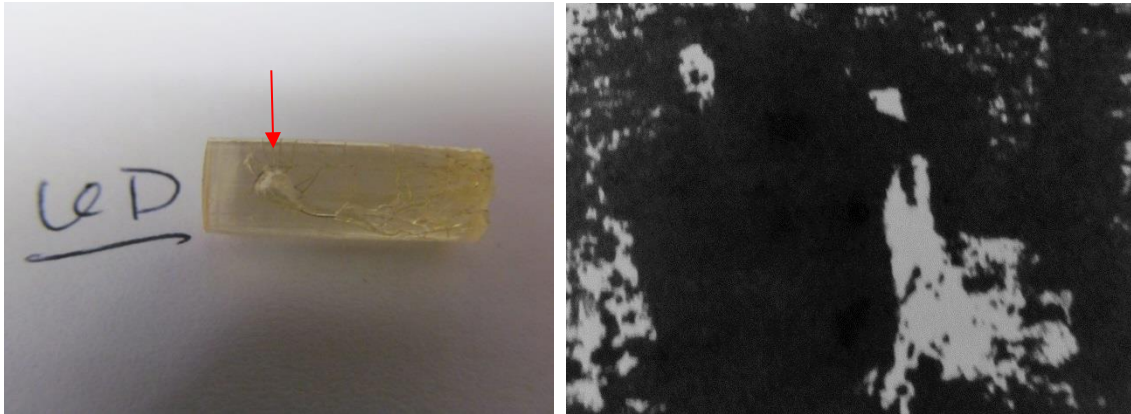


Figure A-21. Sample 6D

Density (kg/m<sup>3</sup>): 1242.6

% Surface Defects: 14.2

Ultimate Strength (N): 2362.34

Formulation: 0.5% 7.5 Rod

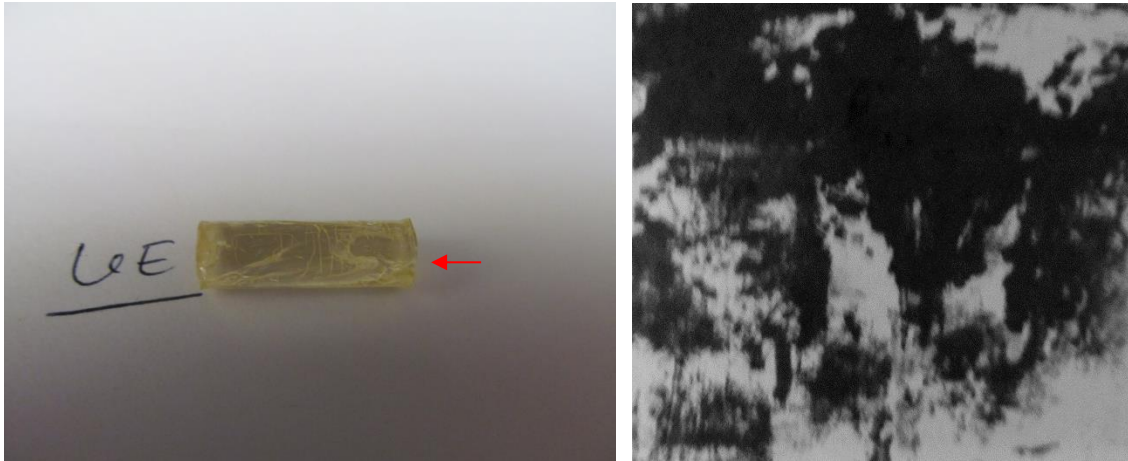


Figure A-22. Sample 6E

Density (kg/m<sup>3</sup>): 1243.53

% Surface Defects: 32.6

Ultimate Strength (N): 1724.46

Formulation: 0.5% 7.5 Rod

**1% 7.5 Rod**

*Average Ultimate Strength: 1694.58 +/- 867.67 N*

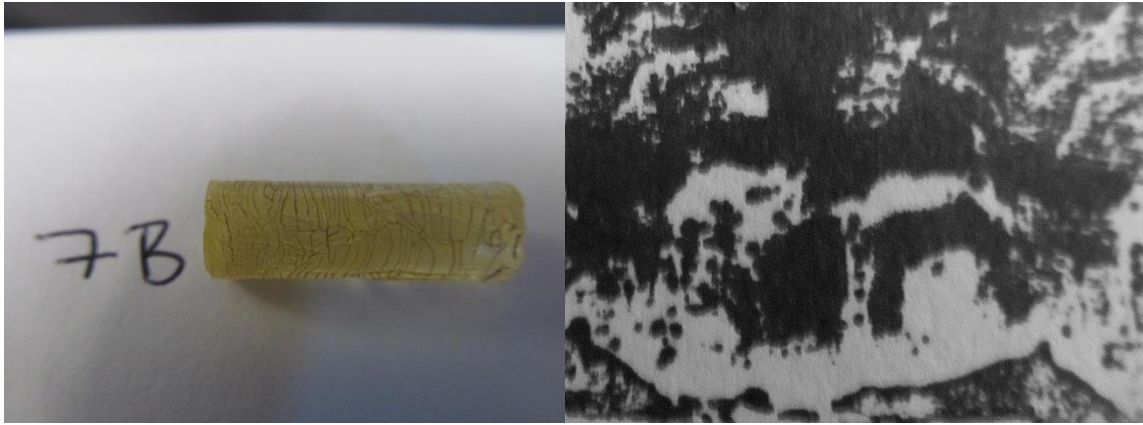


Figure A-23. Sample 7B

Density (kg/m<sup>3</sup>): 1211.99

% Surface Defects: 40.4

Ultimate Strength (N): 2693.92

Formulation: 1% 7.5 Rod

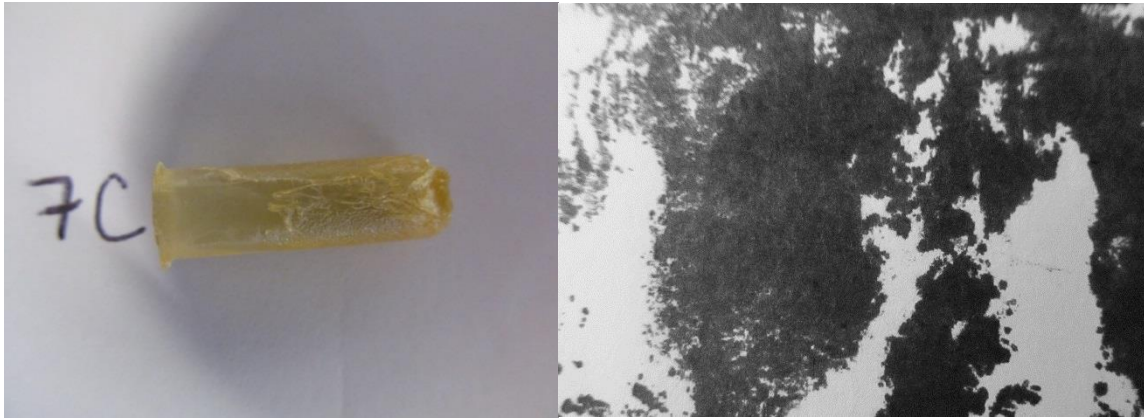


Figure A-24. Sample 7C

Density (kg/m<sup>3</sup>): 1172.03

% Surface Defects: 44.7

Ultimate Strength (N): 1256.87

Formulation: 1% 7.5 Rod

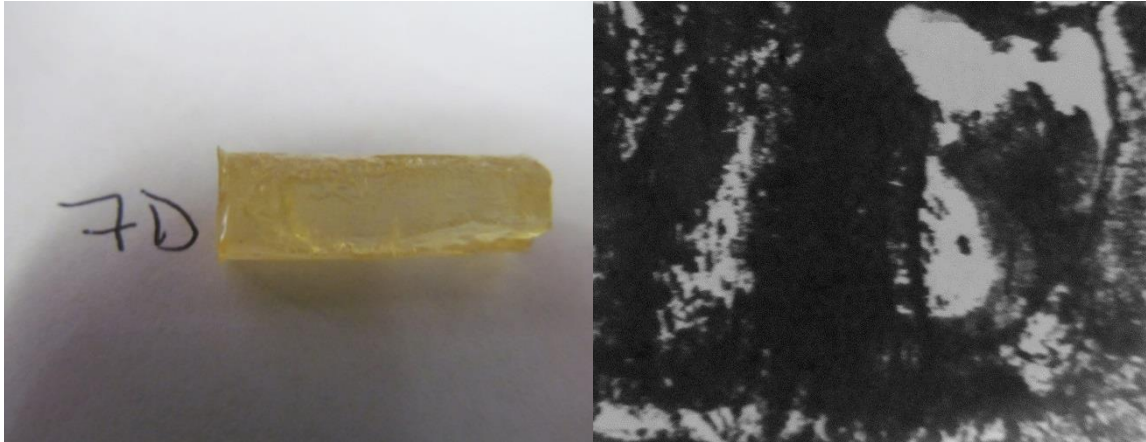


Figure A-25. Sample 7D

Density (kg/m<sup>3</sup>): 1287.73

% Surface Defects: 22.6

Ultimate Strength (N): 1132.95

Formulation: 1% 7.5 Rod

## APPENDIX III

### INDIVIDUAL FRACTURE ANALYSIS OF BNS NANOCOMPOSITES

#### Control Graphs

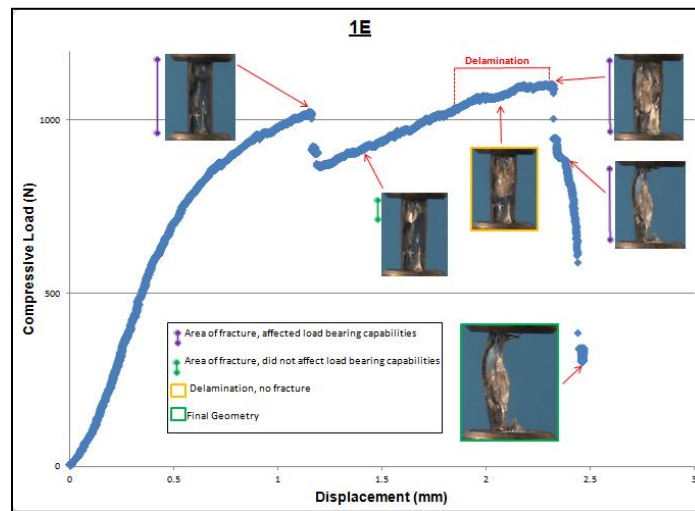


Figure A-26. Sample 1E Failure Analysis

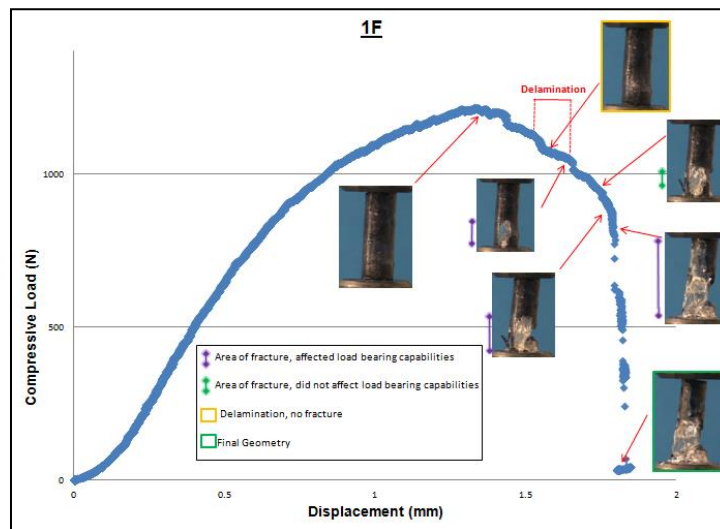


Figure A-27. Sample 1F Failure Analysis

### 0.5% MSN Graphs

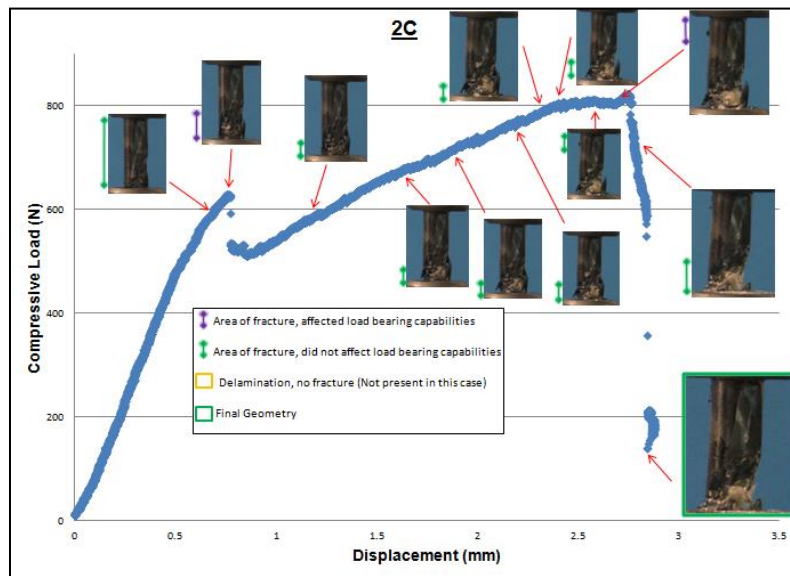


Figure A-28. Sample 2C Failure Analysis

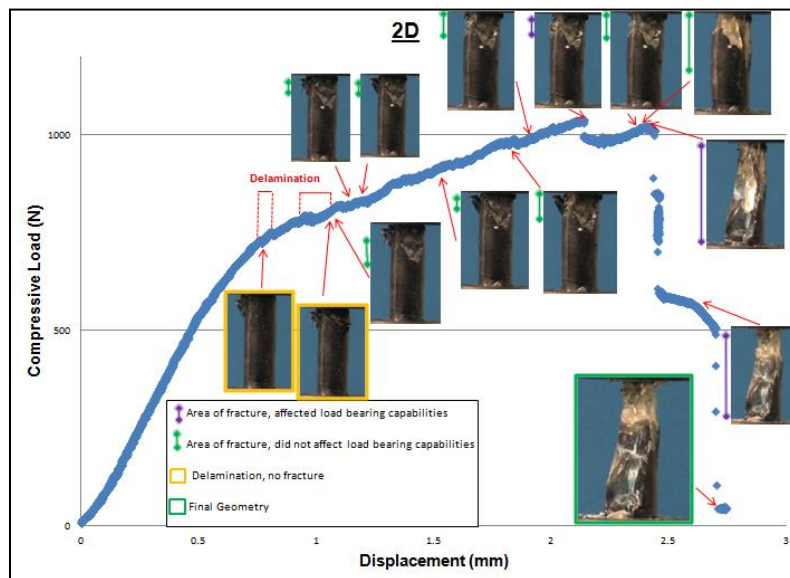


Figure A-29. Sample 2D Failure Analysis

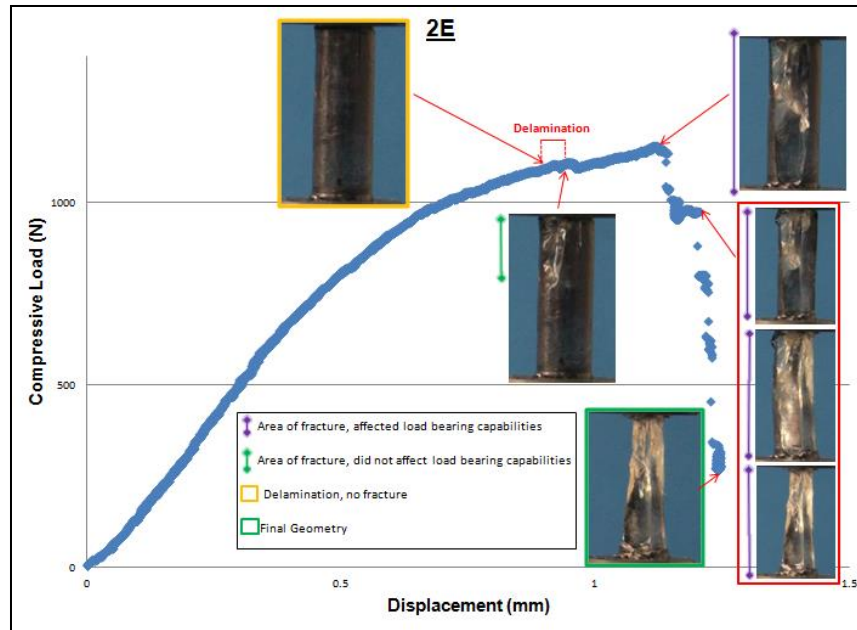


Figure A-30. Sample 2E Failure Analysis



### 1.0% MSN Graphs

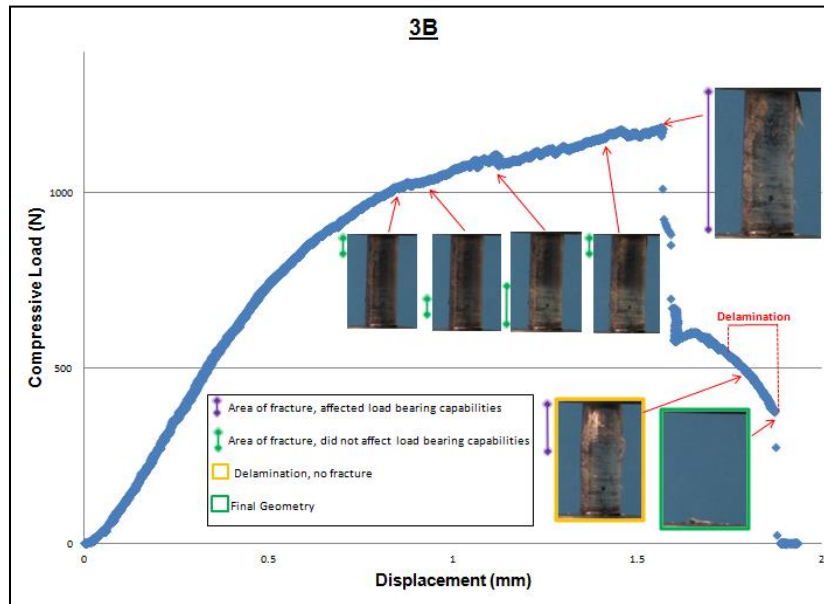


Figure A-31. Sample 3B Failure Analysis

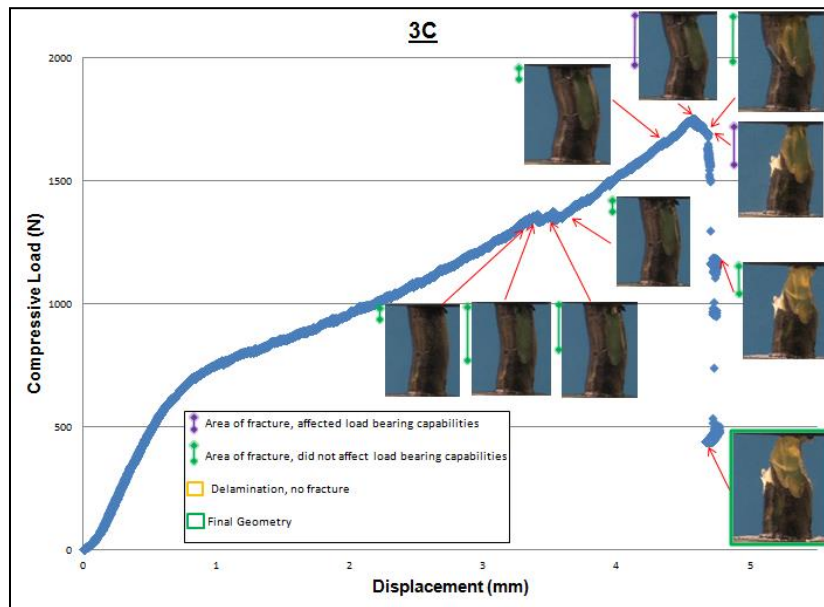


Figure A-32. Sample 3C Failure Analysis

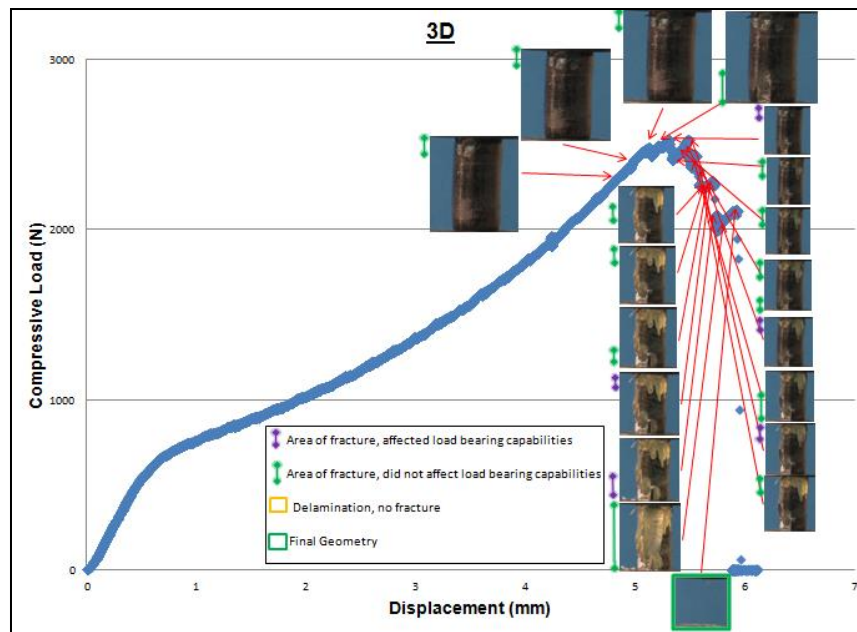


Figure A-33. Sample 3D Failure Analysis

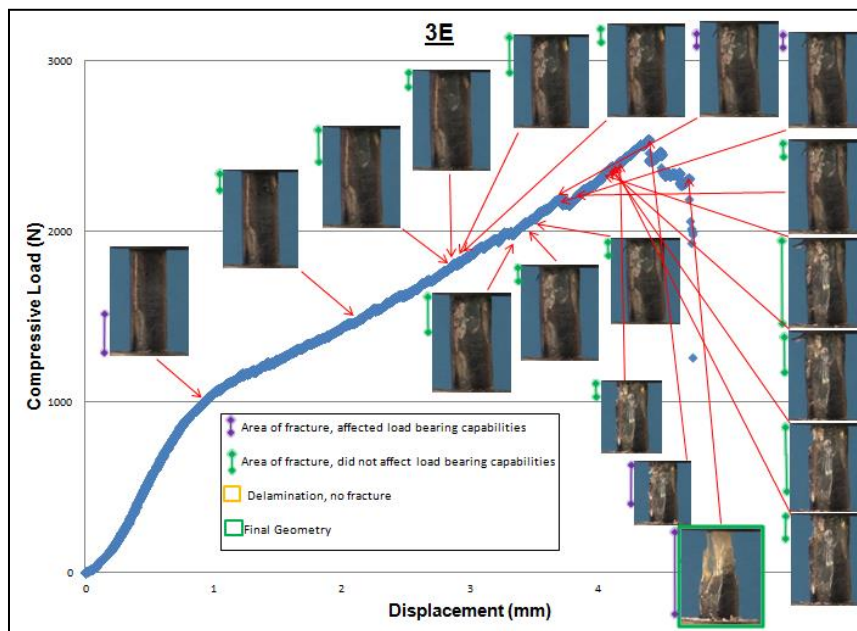


Figure A-34. Sample 3E Failure Analysis

### .5% 3.5 Rod Graphs

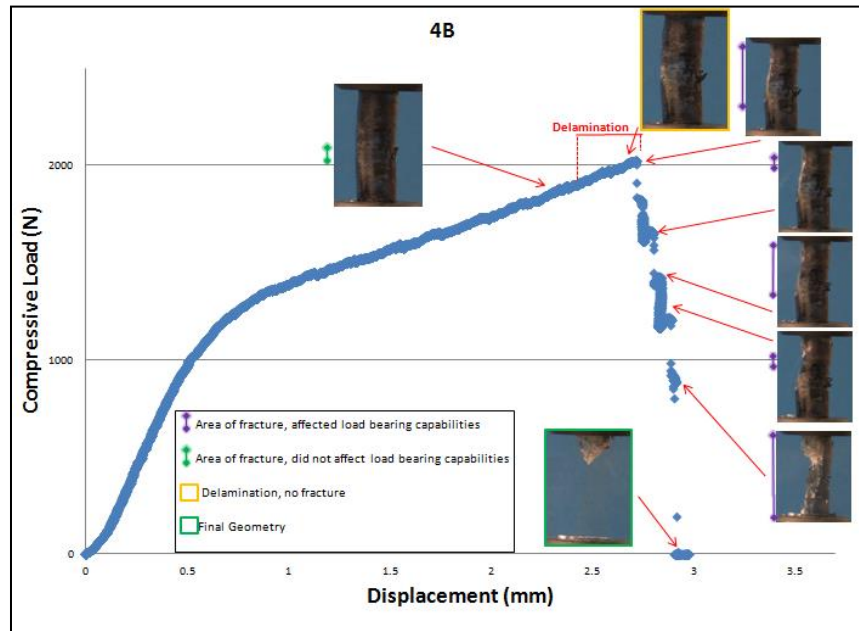


Figure A-35. Sample 4B Failure Analysis

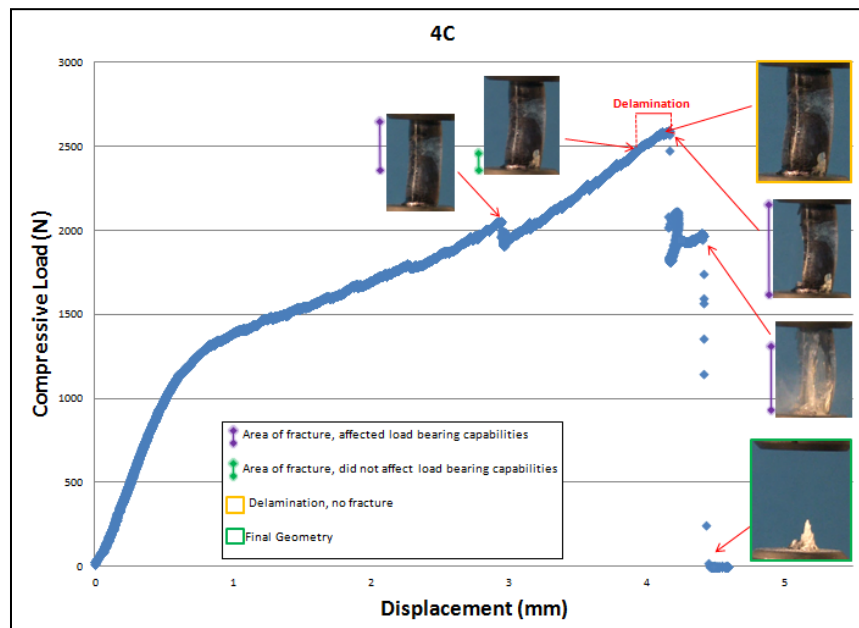


Figure A-36. Sample 4C Failure Analysis

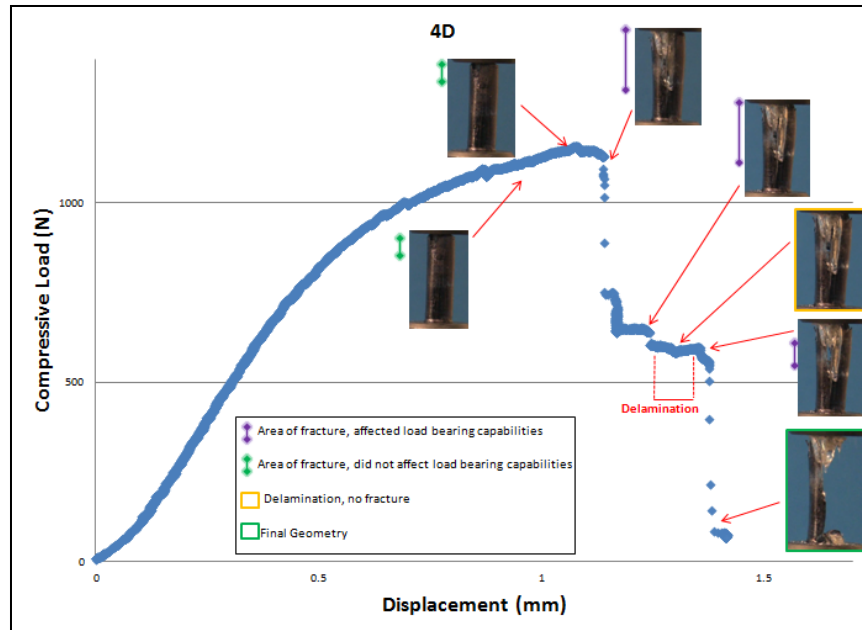


Figure A-37. Sample 4D Failure Analysis

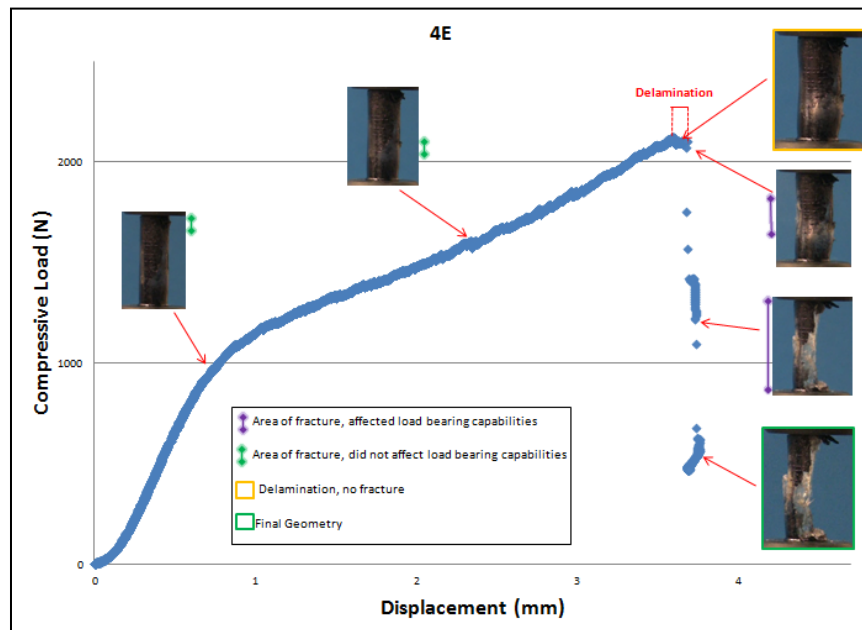


Figure A-38. Sample 4E Failure Analysis

### 1.0% 3.5 Rod Graphs

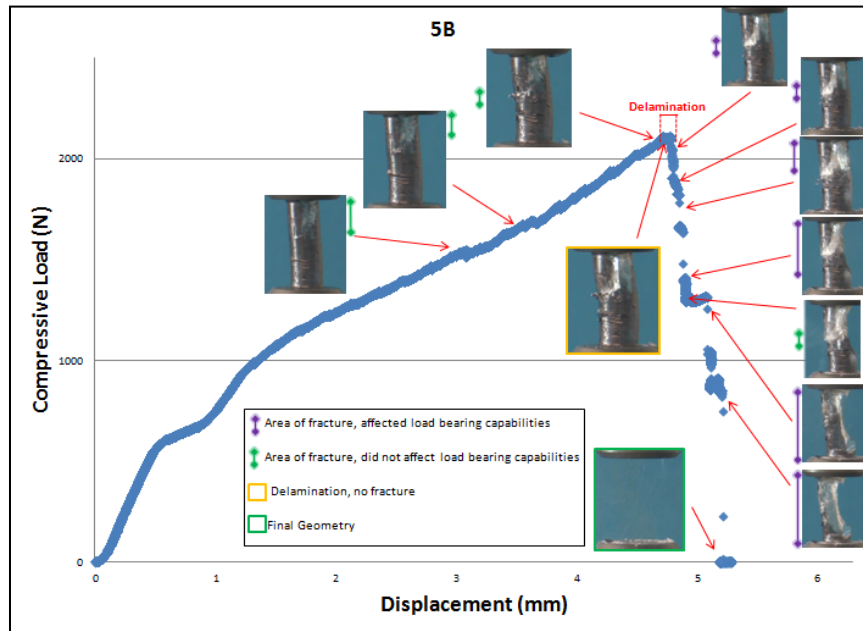


Figure A-39. Sample 5B Failure Analysis

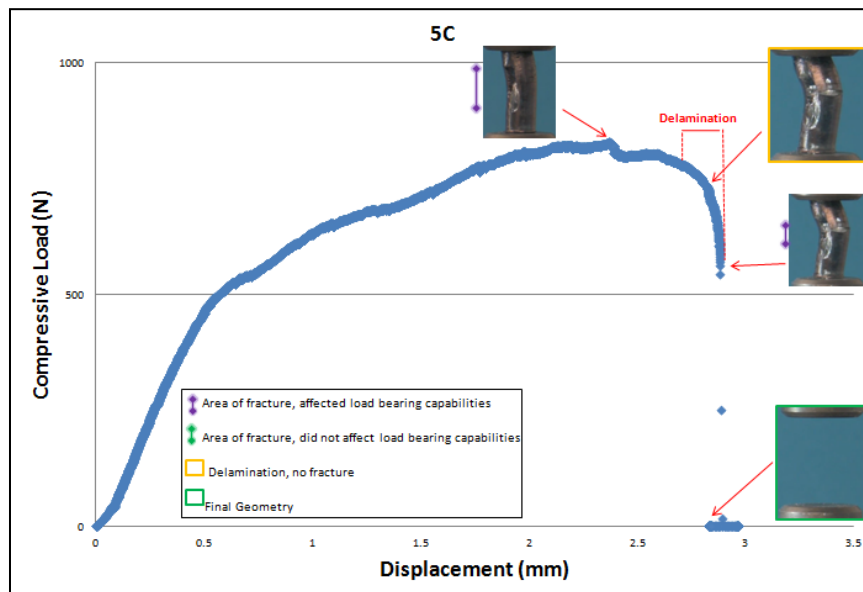


Figure A-40. Sample 5C Failure Analysis

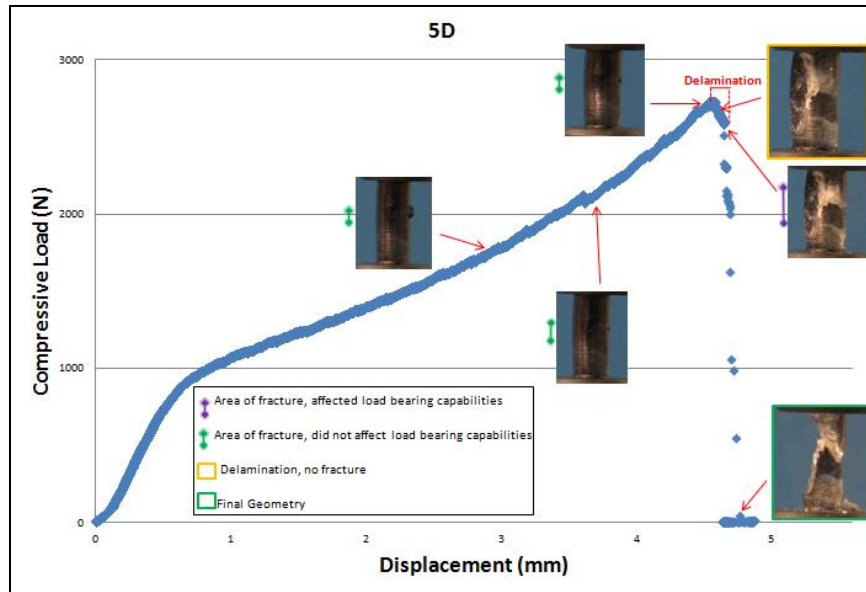


Figure A-41. Sample 5D Failure Analysis

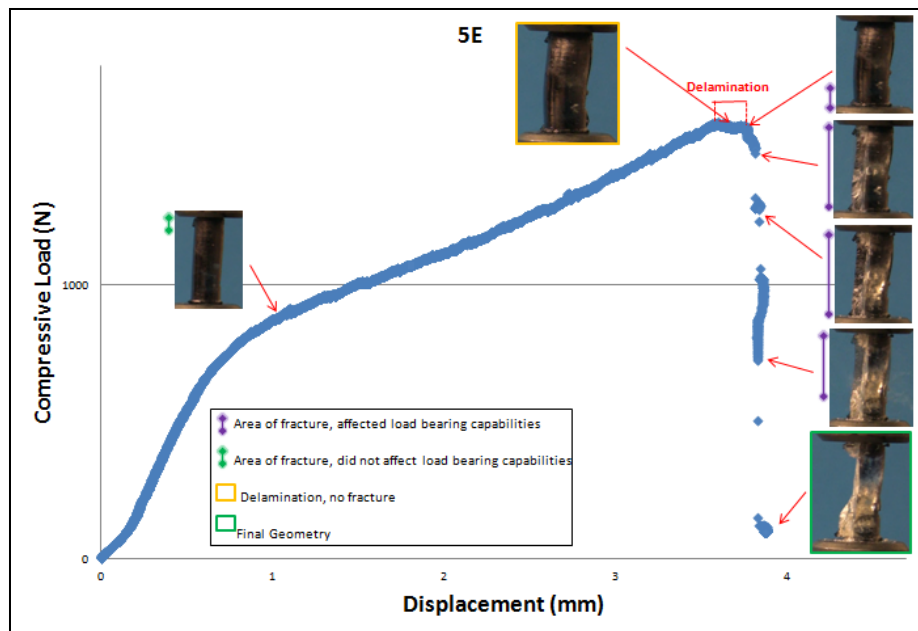


Figure A-42. Sample 5E Failure Analysis

### 0.5% 7.5 Rod Graphs

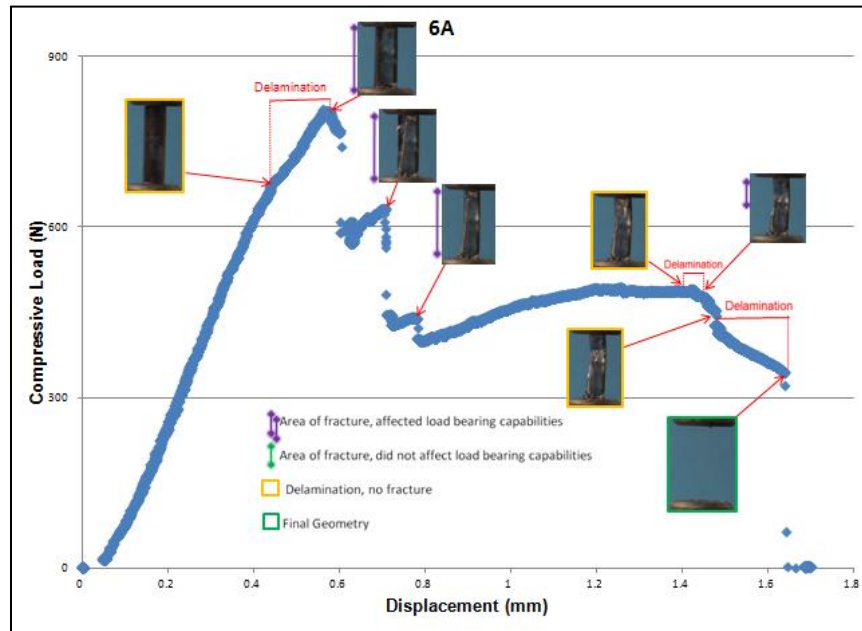


Figure A-43. Sample 6A Failure Analysis

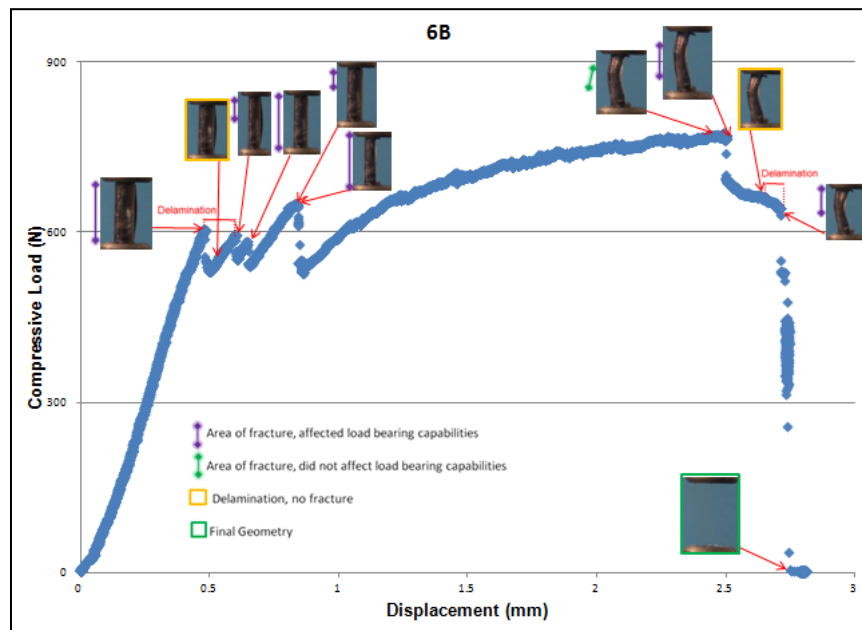


Figure A-44. Sample 6B Failure Analysis

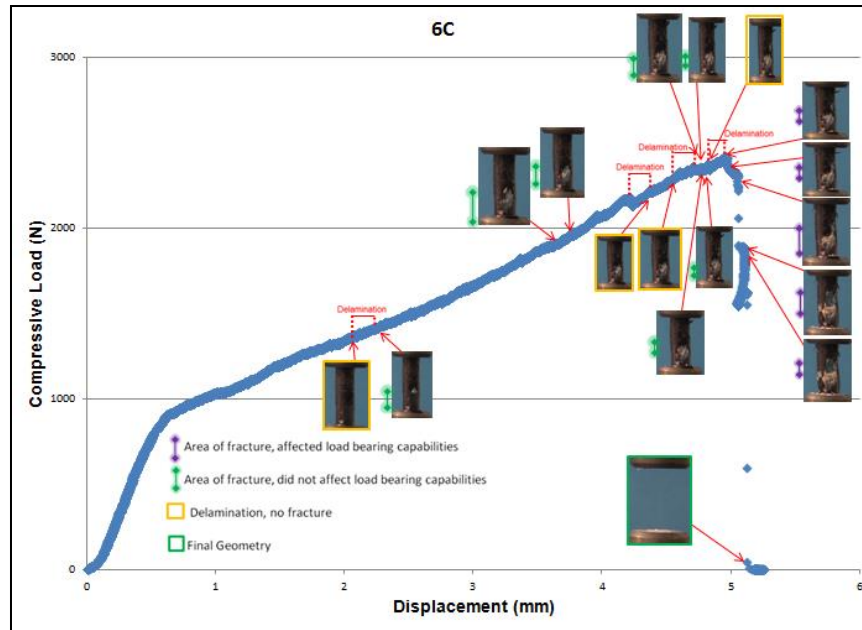


Figure A-45. Sample 6C Failure Analysis

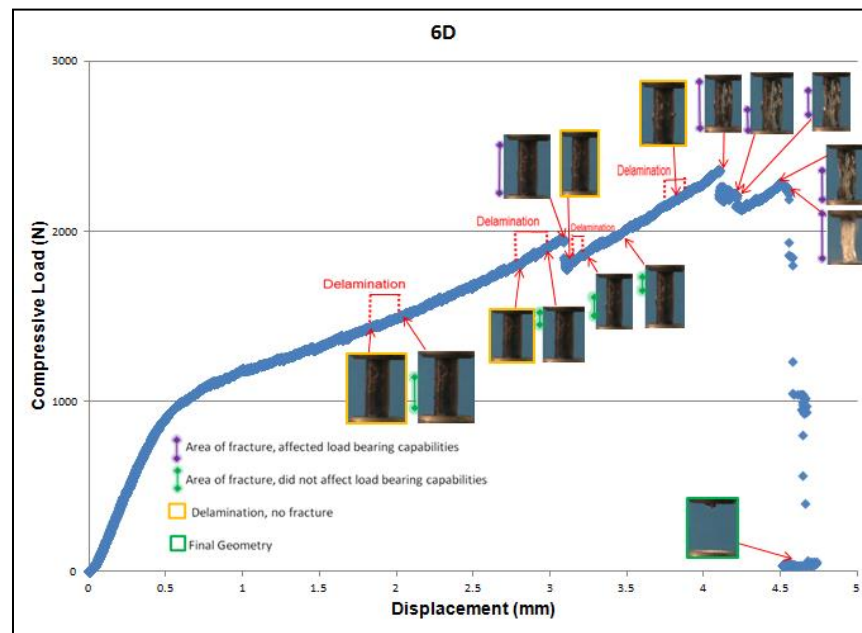
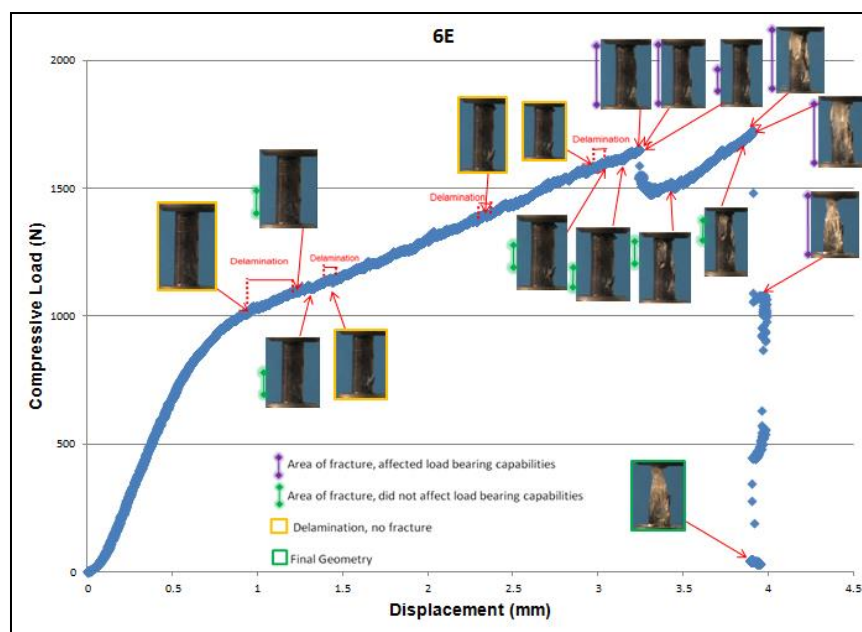


Figure A-46. Sample 6D Failure Analysis





### 1.0% 7.5 Rod Graphs

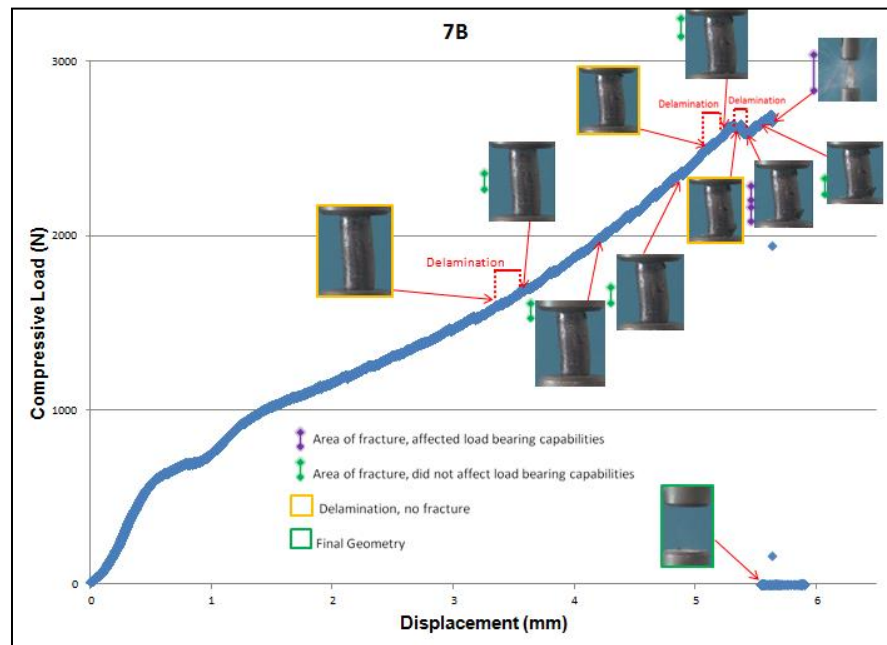


Figure A-48. Sample 7B Failure Analysis

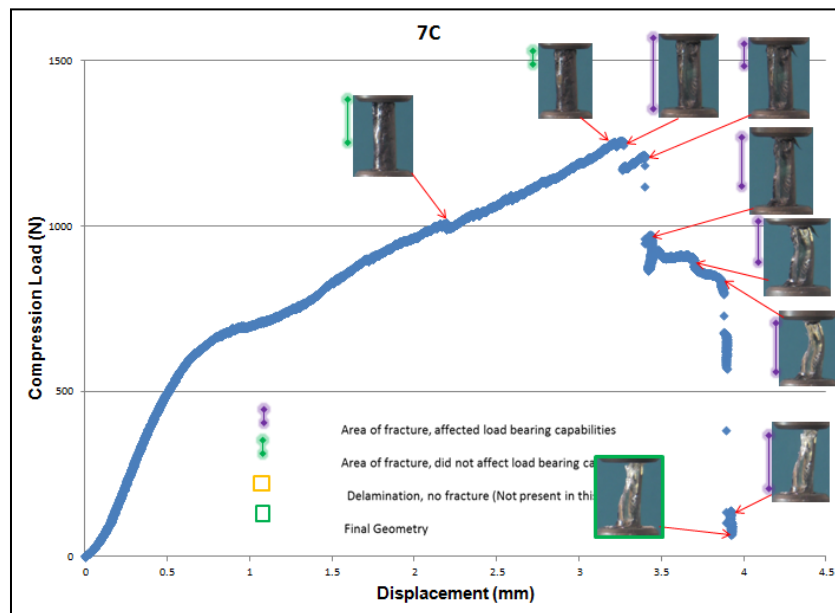


Figure A-49. Sample 7C Failure Analysis

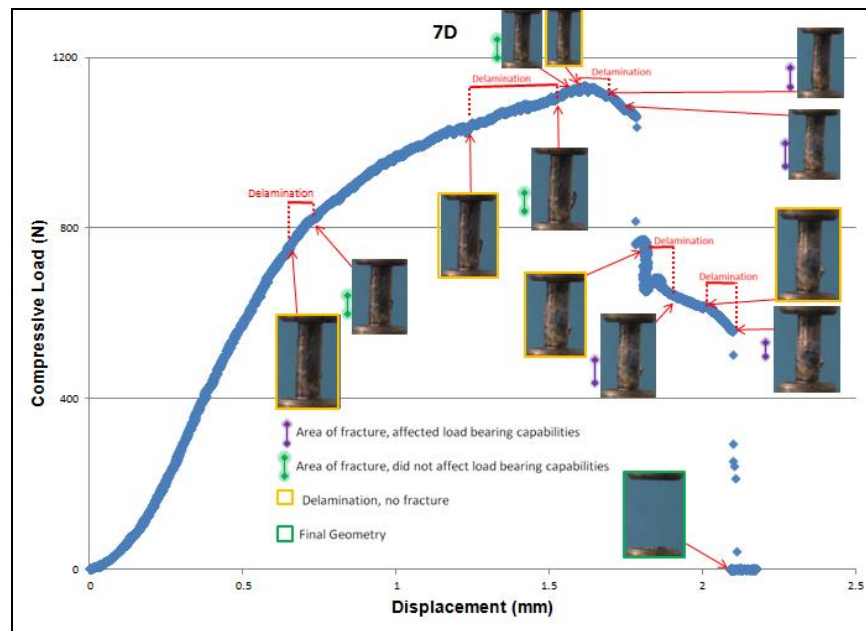


Figure A-50. Sample 7D Failure Analysis